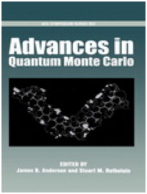

ACS SYMPOSIUM SERIES [illegible]

Advances in Quantum Monte Carlo

EDITED BY
James B. Anderson and Stuart M. Rothstein

Downloaded by 89.163.35.42 on July 3, 2012 | http://pubs.acs.org
Publication Date: December 31, 2006 | doi: 10.1021/bk-2007-0953.fw001

Advances in Quantum Monte Carlo

In Advances in Quantum Monte Carlo; Anderson, J., et al.;
ACS Symposium Series; American Chemical Society: Washington, DC, 2006.

Downloaded by 89.163.35.42 on July 3, 2012 | http://pubs.acs.org
Publication Date: December 31, 2006 | doi: 10.1021/bk-2007-0953.fw001

ACS SYMPOSIUM SERIES **953**

Advances in Quantum Monte Carlo

James B. Anderson, Editor
Pennsylvania State University

Stuart M. Rothstein, Editor
Brock University

Downloaded by 89.163.35.42 on July 3, 2012 | http://pubs.acs.org
Publication Date: December 31, 2006 | doi: 10.1021/bk-2007-0953.fw001

American Chemical Society, Washington, DC

Downloaded by 89.163.35.42 on July 3, 2012 | http://pubs.acs.org
Publication Date: December 31, 2006 | doi: 10.1021/bk-2007-0953.fw001

Library of Congress Cataloging-in-Publication Data

Advances in quantum Monte Carlo / James B. Anderson, editor, Stuart M. Rothstein,
editor.

p. cm.—(ACS symposium series ; 953)

Includes bibliographical references and index.

ISBN 13: 978-0-8412-7416-7 (alk. paper)

ISBN 10: 0-8412-7416-9 (alk. paper)

1. Monte Carlo method—Congresses. 2. Quantum chemistry—Congresses. 3. Quantum theory—Congresses.

I. Anderson, James B., 1935–. II. Rothstein, Stuart M.

QD462.6.M66A38 2006
530.1201′518282—dc22
2006042924

The paper used in this publication meets the minimum requirements of American National Standard for Information Sciences—Permanence of Paper for Printed Library Materials, ANSI Z39.48–1984.

Copyright © 2007 American Chemical Society

Distributed by Oxford University Press

All Rights Reserved. Reprographic copying beyond that permitted by Sections 107 or 108 of the U.S. Copyright Act is allowed for internal use only, provided that a per-chapter fee of $33.00 plus $0.75 per page is paid to the Copyright Clearance Center, Inc., 222 Rosewood Drive, Danvers, MA 01923, USA. Republication or reproduction for sale of pages in this book is permitted only under license from ACS. Direct these and other permission requests to ACS Copyright Office, Publications Division, 1155 16th Street, N.W., Washington, DC 20036.

The citation of trade names and/or names of manufacturers in this publication is not to be construed as an endorsement or as approval by ACS of the commercial products or services referenced herein; nor should the mere reference herein to any drawing, specification, chemical process, or other data be regarded as a license or as a conveyance of any right or permission to the holder, reader, or any other person or corporation, to manufacture, reproduce, use, or sell any patented invention or copyrighted work that may in any way be related thereto. Registered names, trademarks, etc., used in this publication, even without specific indication thereof, are not to be considered unprotected by law.

PRINTED IN THE UNITED STATES OF AMERICA

Foreword

The ACS Symposium Series was first published in 1974 to provide a mechanism for publishing symposia quickly in book form. The purpose of the series is to publish timely, comprehensive books developed from ACS sponsored symposia based on current scientific research. Occasionally, books are developed from symposia sponsored by other organizations when the topic is of keen interest to the chemistry audience.

Before agreeing to publish a book, the proposed table of contents is reviewed for appropriate and comprehensive coverage and for interest to the audience. Some papers may be excluded to better focus the book; others may be added to provide comprehensiveness. When appropriate, overview or introductory chapters are added. Drafts of chapters are peer-reviewed prior to final acceptance or rejection, and manuscripts are prepared in camera-ready format.

As a rule, only original research papers and original review papers are included in the volumes. Verbatim reproductions of previously published papers are not accepted.

ACS Books Department

Downloaded by 89.163.35.42 on July 3, 2012 | http://pubs.acs.org
Publication Date: December 31, 2006 | doi: 10.1021/bk-2007-0953.fw001

Downloaded by 89.163.35.42 on July 3, 2012 | http://pubs.acs.org
Publication Date: December 31, 2006 | doi: 10.1021/bk-2007-0953.pr001

Preface

Quantum Monte Carlo provides an ab initio solution to the Schrödinger Equation by virtue of performing a random walk through configuration space in imaginary time. Recent benchmark calculations suggest that its most commonly employed variant, fixed-node Monte Carlo, estimates energies with an accuracy comparable to those from high-level coupled-cluster calculations. Each has its advantages and disadvantages, but arguably, at present, the quantum Monte Carlo and coupled-cluster approaches are complementary "gold-standards" of quantum chemistry.

The chapters in this monograph are contributions from the *Advances in Quantum Monte Carlo* Symposium held at Pacifichem 2005, International Chemical Congress of Pacific Basin Societies. The Theoretical and Physical Chemistry Division of the Canadian Society for Chemistry (CSC) sponsored the symposium, whose objectives were: (1) to gather together experts to discuss current challenges in the field, and their latest approaches to addressing them; (2) to highlight applications of quantum Monte Carlo to a myriad of chemical and physical problems, ranging from isolated atoms and molecules to clusters, biomolecules, and condensed matter; and (3) to facilitate an exchange of ideas with students and researchers in related fields.

We extend special thanks to Professor Shigenori Tanaka, our colleague in coorganizing the symposium. Acknowledgment is made to the Donors of The Petroleum Research Fund, administered by the American Chemical Society (ACS), for providing partial financial support to the symposium. In addition, we are grateful for the assistance of Ms. Margaret Brown at the ACS Books Department in preparing this volume.

James B. Anderson
Department of Chemistry
Pennsylvania State University
University Park, PA 16802

Stuart M. Rothstein
Department of Chemistry
Brock University
St. Catharines, Ontario L2S 3A1
Canada

Downloaded by 89.163.35.42 on July 3, 2012 | http://pubs.acs.org
Publication Date: December 31, 2006 | doi: 10.1021/bk-2007-0953.pr001

Advances in Quantum Monte Carlo

Downloaded by 89.163.35.42 on July 3, 2012 | http://pubs.acs.org
Publication Date: December 31, 2006 | doi: 10.1021/bk-2007-0953.pr001

Downloaded by 89.163.35.42 on July 3, 2012 | http://pubs.acs.org
Publication Date: December 31, 2006 | doi: 10.1021/bk-2007-0953.ch001

Chapter 1

Quantum Monte Carlo Calculations for Helium Dimers and Trimers

Matthew C. Wilson[1] and James B. Anderson[2,*]

**Departments of [1]Physics and [2]Chemistry, Pennsylvania State University,
University Park, PA 16802**

We report fixed-node diffusion quantum Monte Carlo (QMC) calculations of the potential energies of interaction of helium atoms in helium dimers and trimers. Statistical errors are lower by a factor of two to ten than for earlier diffusion calculations. Node location errors are expected to be very small for these systems, and comparisons with exact calculations for the dimer indicate they are negligible at intermolecular distances beyond a few bohr. The calculations for the trimers reveal interaction energies very nearly pairwise-additive for internuclear distances near the dimer equilibrium distance of 5.6 bohr and longer. At shorter distances the Axilrod-Teller-Muto third-order expression for trimers fails badly. The results confirm earlier QMC calculations as well as thoses of an extended group function model (Røeggen and Almlöf) and have implications for predictions of the properties of small helium clusters as well as the properties of the bulk liquids and solids.

In Advances in Quantum Monte Carlo; Anderson, J., et al.;
ACS Symposium Series; American Chemical Society: Washington, DC, 2006.

Introduction

For the helium trimer with internuclear distances close to the equilibrium distance of the helium dimer, 5.6 bohr, the interaction is expected to be very close to the sum of the interaction between the three pairs of atoms. The higher order terms are thought to be very small and comprise the "nonadditive" contribution to the total energy of the cluster. In this paper, we present results for the interaction potential of a helium dimer and a helium trimer in symmetric linear and equilateral triangle configurations.

Attractive forces between helium atoms are due to fluctuating electric moments, which induce dipoles in nearby atoms (London dispersion forces). A potential curve for the interaction between two helium atoms was first calculated by Slater (*1*) in 1928 and gave a minimum of -8.9 K at a distance of 5.6 bohr. Since then, various methods have been used to calculate the energies of different helium clusters with interesting and varied results. For example, early SCF calculations for the dimer with small basis sets predicted no attraction. As larger basis sets were able to be used, attractive wells in agreement with experiment were predicted. This was followed by the prediction of again no attraction with even larger basis sets. This odd behavior was largely the result of basis set superposition error, a difficulty encountered in many types of calculations for weak interactions. Modern high-level calculations by a variety of methods, including 'exact' QMC, have given highly accurate and consistent predictions of the potential energy curve for the dimer (*2*).

The first perturbative calculations for the trimer were done by Axilrod and Teller (*3*) and Muto (*4*) in 1943. Their third-order perturbation expansion is known as the Axilrod-Teller-Muto (ATM) expression. In 1953, Rosen (*5*) used the valence bond method to calculate the repulsive part of the interaction. Shostak (*6*) calculated the interaction energy of the linear helium trimer with the self-consistent LCAO method in 1955. The effect of nonadditive three-body forces on the third virial coefficient was estimated in 1966 by Sherwood, De Rocco, and Mason (*7*). Novaro and Beltran-Lopez (*8*) tested the pairwise additivity in the helium trimer at short ranges by predicing the potential energy surface using SCF-LCAO-MO calculations in 1972. More recently, in 1993, Parish and Dykstra (*9*) carried out calculations at the coupled cluster level with double substitutions using very large basis sets to investigate the many-body contributions to interaction potentials and the second-order exchange-dispersion energy. In 1995, Røeggen and Almlöf (*10*) used an extended group function model for calculations of the three-body potential to obtain results more accurate than those previously available.

Several types of quantum Monte Carlo calculations have been repoted earlier. In 1990, Mohan and Anderson (*11*) reported diffusion QMC calculations for the equilateral triangle configuration of the trimer. In 1992,

Downloaded by 89.163.35.42 on July 3, 2012 | http://pubs.acs.org
Publication Date: December 31, 2006 | doi: 10.1021/bk-2007-0953.ch001

Tawa et al. (*12*) reported variational QMC calculations of similar accuracies for trianglular configurations. 'Exact' QMC calculations, without node location error, were reported by Bhattacharya and Anderson (*13*). In the present work, diffusion Monte Carlo was used for both helium dimers and trimers.

The energies calculated are with respect to separated atoms. For clusters of more than two helium atoms, the energy can be thought of as consisting of two terms, the energy of the pairs of atoms and a multibody correction. Specifically, for a trimer:

Monomer: E_1
Dimer: $E_2 = \Sigma_2 E_1 + \Delta E_2$
Trimer: $E_3 = \Sigma_3 E_1 + \Sigma_3 \Delta E_2 + \Delta E_3$

In this research, the energies of helium dimers and trimers relative to separated atoms were calculated, along with the correction to the pairwise-additive energy, ΔE_3.

Calculation Procedure

The calculations were done with the fixed-node diffusion quantum Monte Carlo (DQMC) method. For the dimer calculations, the trial function used was that due to Lowther and Coldwell (*14*) having the form:

$$\Psi_T = \varphi_{A13}\,\varphi_{B24}e^{-U1324/2} - \varphi_{A14}\,\varphi_{B23}e^{-U1423/2} - \varphi_{A23}\,\varphi_{B14}e^{-U2314/2} + \varphi_{A24}\,\varphi_{B13}e^{-U2413/2}$$

where φ_{Nij} is a 189-term Hylleraas-like function and U_{ijkl} contains cross-terms for the electron-electron interactions. The trial function used for the trimer calculations was a similar 36-term function described by Bhattacharya and Anderson (*13*). The calculations were run for internuclear distances of 4.5, 5.6, 6.5, and 7.5 bohr. For each geometry calculations were run at three step sizes (0.010, 0.005, and 0.002 a.u.) and the results extrapolated to a step size of zero.

For comparisons, calculations using the Gaussian 03 suite of programs were run. The methods used were Hartree-Fock (HF), fourth-order Møller-Plesset (MP4), and coupled-cluster at the single and doubles level (CCSD). The HF and CCSD calculations used the 6-311G** basis set; the MP4 calculations used the aug-cc-pV5Z basis set. Also calculated were the energies predicted by the ATM expression:

$$\Delta E_3 = C\frac{3\cos\gamma_1\cos\gamma_2\cos\gamma_3 + 1}{r_{12}^3 r_{23}^3 r_{31}^3}$$

Downloaded by 89.163.35.42 on July 3, 2012 | http://pubs.acs.org
Publication Date: December 31, 2006 | doi: 10.1021/bk-2007-0953.ch001

where r_{12}, r_{23}, and r_{31} are the internuclear distances and γ_1, γ_2, and γ_3, are the included angles. C is a positive constant on the order $V\alpha^3$, where V is the ionization energy and α is the polarizability. Its value is 1.478 a.u. as given in (*10*). The Gaussian and ATM calculations were run for internuclear distances of 2.5, 3.5, 4.5, 5.6, 6.5, and 7.5 bohr.

Results

The potential energies for the helium dimer relative to the exact value for a pair of separated atoms were calculated for four internuclear distances between 4.5 and 7.5 bohr at three different time steps: 0.002, 0.005, and 0.010 au. The data from the calculations for each distance are presented in Figures 1-4 and the results are listed in Table I. The error bars indicate 1σ statistical error as determined from repeated calculations.

The DQMC calculations for the equilateral triangle form of the helium trimer were calculated at the same four internuclear distances as the helium dimer and with the same time steps. The data from the calculations for each distance are shown in Figures 5-8 and the results are listed in Table II.

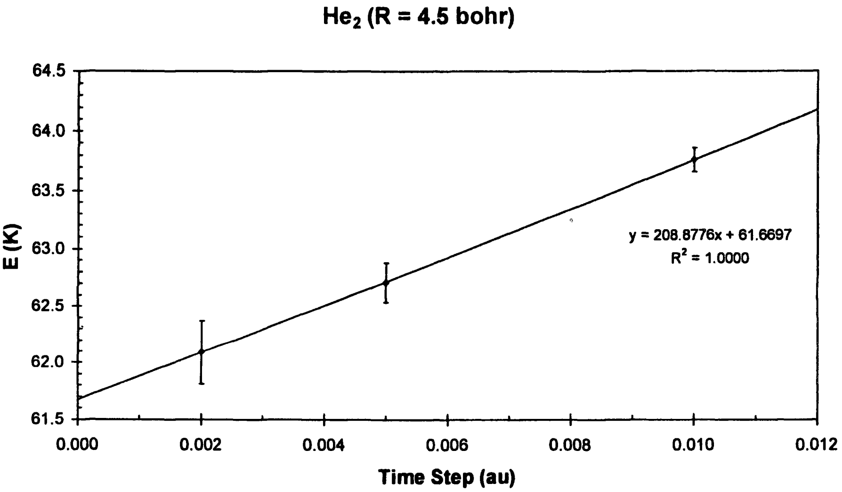

Figure 1. Calculated interaction energy ΔE_2 for the helium dimer at a distance of 4.5 bohr at three time step sizes.

Downloaded by 89.163.35.42 on July 3, 2012 | http://pubs.acs.org
Publication Date: December 31, 2006 | doi: 10.1021/bk-2007-0953.ch001

Downloaded by 89.163.35.42 on July 3, 2012 | http://pubs.acs.org
Publication Date: December 31, 2006 | doi: 10.1021/bk-2007-0953.ch001

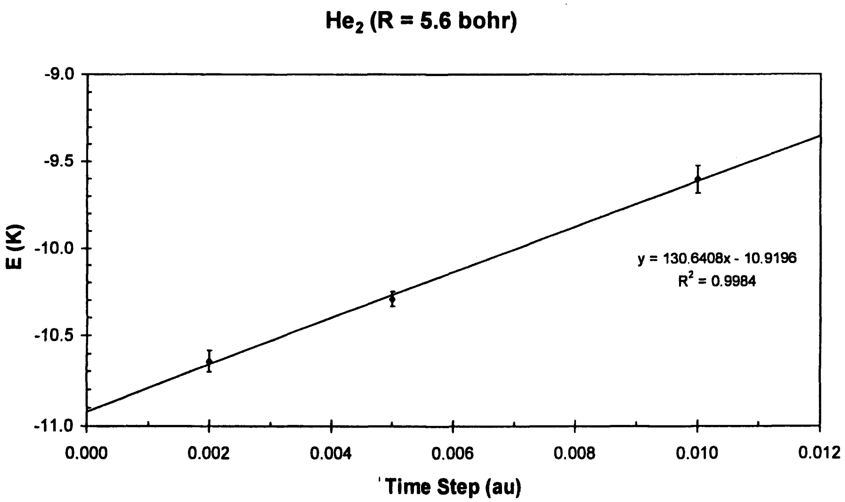

Figure 2. Calculated interaction energy ΔE_2 for the helium dimer at a distance of 5.6 bohr at three time step sizes.

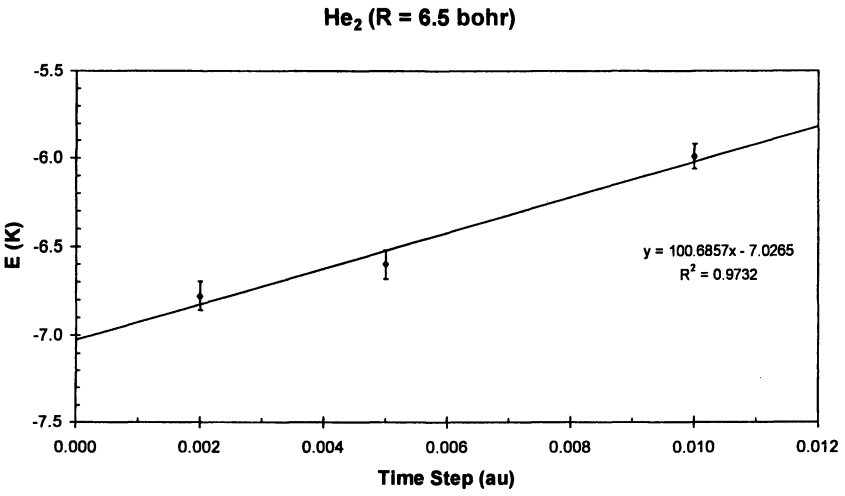

Figure 3. Calculated interaction energy ΔE_2 for the helium dimer at a distance of 6.5 bohr at three time step sizes.

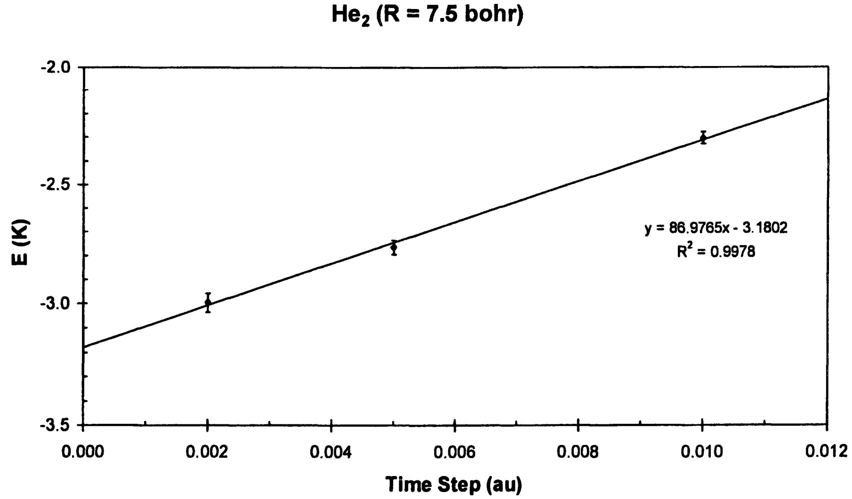

Figure 4. Calculated interaction energy ΔE_2 for the helium dimer at a distance of 7.5 bohr at three time step sizes.

TABLE I. Interaction energy calculated for the helium dimer by the diffusion quantum Monte Carlo method.

Internuclear distance R (bohr)	*Interaction Energy ΔE_2 (K)*	
	Exact QMC[a]	*DQMC (present work)*
4.5	58.3(5)	61.7(4)
5.6	-10.998(5)	-10.92(8)
6.5	-6.930(5)[b]	-7.03(5)
7.5	-3.073(3)	-3.18(4)

[a] Reference 2
[b] Interpolated

Downloaded by 89.163.35.42 on July 3, 2012 | http://pubs.acs.org
Publication Date: December 31, 2006 | doi: 10.1021/bk-2007-0953.ch001

Downloaded by 89.163.35.42 on July 3, 2012 | http://pubs.acs.org
Publication Date: December 31, 2006 | doi: 10.1021/bk-2007-0953.ch001

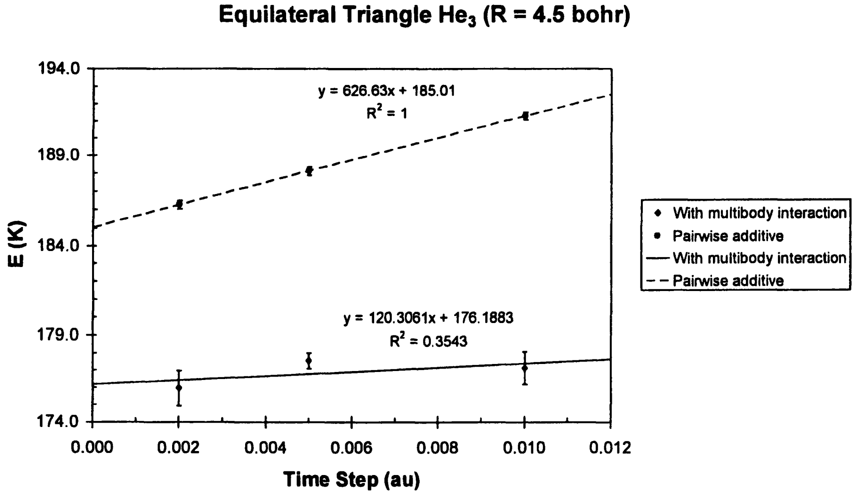

Figure 5. Interaction energy for the helium trimer in equilateral triangle configuration with sides of 4.5 bohr at three time step sizes and the corresponding pairwise-additive energy.

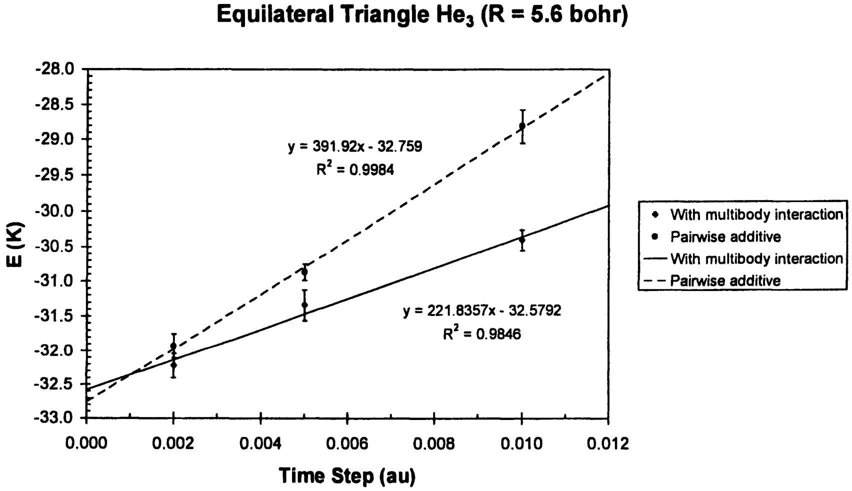

Figure 6. Interaction energy for the helium trimer in equilateral triangle configuration with sides of 5.6 bohr at three time step sizes and the corresponding pairwise-additive energy.

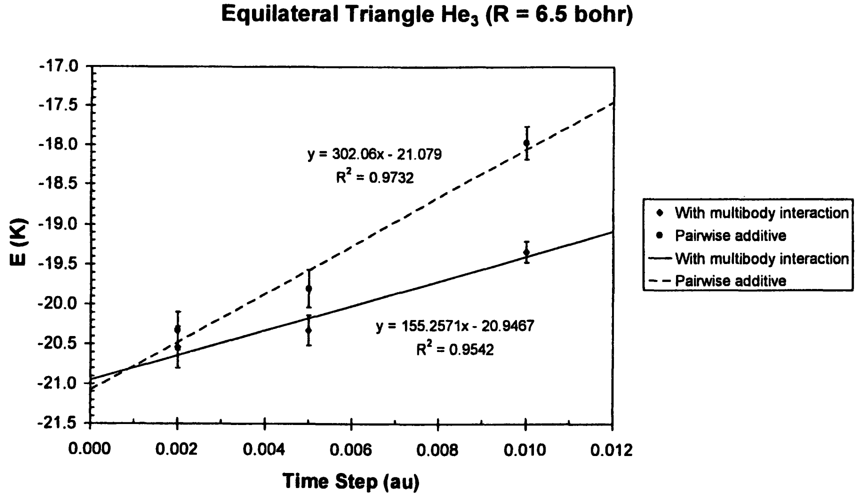

Figure 7. Interaction energy for the helium trimer in equilateral triangle configuration with sides of 6.5 bohr at three time step sizes and the corresponding pairwise-additive energy.

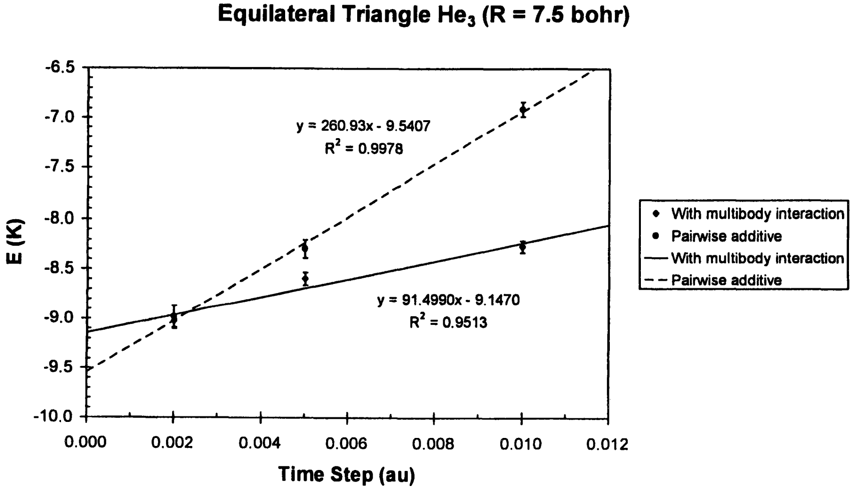

Figure 8. Interaction energy for the helium trimer in equilateral triangle configuration with sides of 7.5 bohr at three time step sizes and the corresponding pairwise-additive energy.

Downloaded by 89.163.35.42 on July 3, 2012 | http://pubs.acs.org
Publication Date: December 31, 2006 | doi: 10.1021/bk-2007-0953.ch001

TABLE II. Results for the diffusion quantum Monte Carlo calculations for the helium trimer with equilateral triangle configuration.

R (bohr)	*E* (a.u.)	$E-3E_1$ (K)	ΔE_2 (K)	ΔE_3 (K)	
				Present work	*Mohan and Anderson*[a]
2.5[a]	-8.6062(5)	33190(160)	13040(60)		-5930(240)
3.5[a]	-8.70088(13)	3260(40)	1169(30)		-247(100)
4.5	-8.7106058(15)	176.19(7)	61.7(4)	-8.8(12)	-4(30)
5.6	-8.7112727(6)	-32.58(17)	-10.92(8)	0.2(4)	1(10)
6.5	-8.7112395(3)	-20.95(14)	-7.03(5)	0.13(28)	-9(10)
7.5	-8.71120211(19)	-9.15(6)	-3.18(4)	0.39(18)	

[a]Reference 11

Downloaded by 89.163.35.42 on July 3, 2012 | http://pubs.acs.org
Publication Date: December 31, 2006 | doi: 10.1021/bk-2007-0953.ch001

The DQMC calculations for the symmetric linear form of the helium trimer were calculated at the same four intenuclear distances as the helium dimer and with the same time steps. The data from the calculations for each distance are shown in Figures 9-12 and the results are listed in Table III.

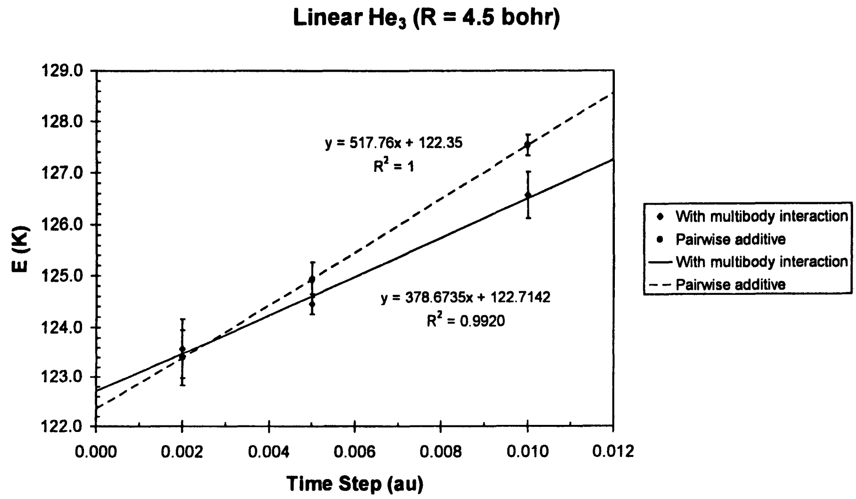

Figure 9. Interaction energy for the helium trimer in symmetric linear configuration with sides of 4.5 bohr at three time step sizes and the corresponding pairwise-additive energy.

Downloaded by 89.163.35.42 on July 3, 2012 | http://pubs.acs.org
Publication Date: December 31, 2006 | doi: 10.1021/bk-2007-0953.ch001

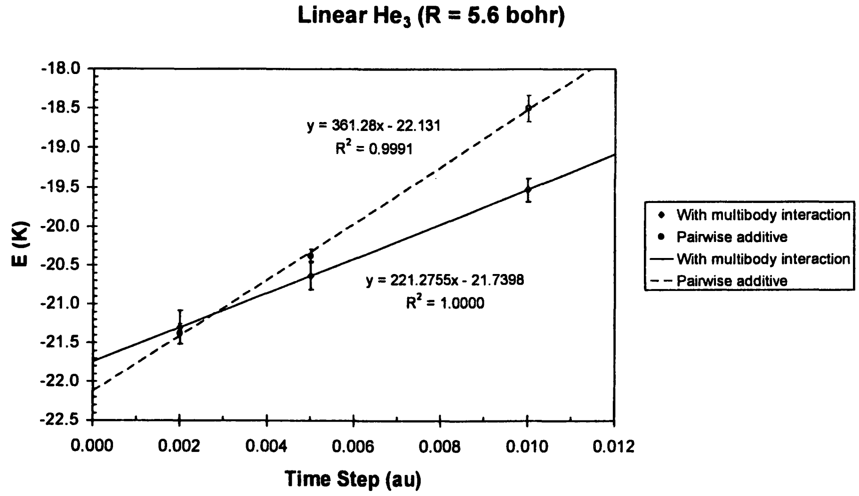

Figure 10. Interaction energy for the helium trimer in symmetric linear configuration with sides of 5.6 bohr at three time step sizes and the corresponding pairwise-additive energy.

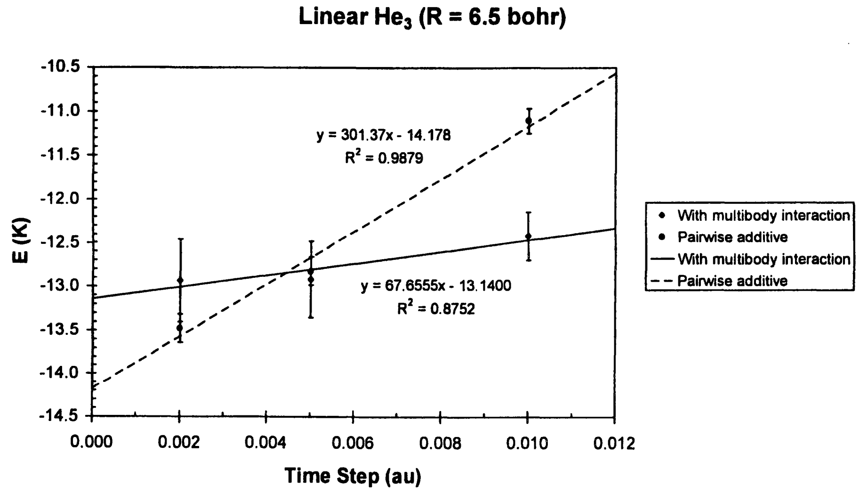

Figure 11. Interaction energy for the helium trimer in symmetric linear configuration with sides of 6.5 bohr at three time step sizes and the corresponding pairwise-additive energy.

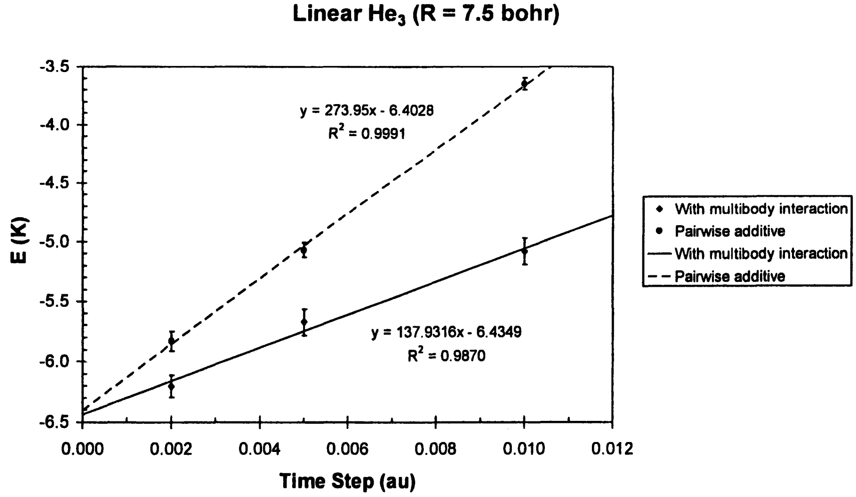

Figure 12. Interaction energy for the helium trimer in symmetric linear configuration with sides of 7.5 bohr at three time step sizes and the corresponding pairwise-additive energy.

TABLE III. Results for the diffusion quantum Monte Carlo calculations for the helium trimer with symmetric linear configuration.

R	*E*	*$E - 3E_1$*	*ΔE_2*	*ΔE_3 (K)*	
(bohr)	*(a.u.)*	*(K)*	*(K)*	*Present work*	*Bhattacharya and Anderson*[a]
3.5[b]	-8.70417(19)	2200(60)	2225(7)		-20(70)
4.5	-8.7107846(16)	122.7(5)	61.7(4)	0.4(12)	-13(12)
5.6	-8.7112418(10)	-21.7(3)	-10.92(8)	0.3(5)	0.7(21)
6.5	-8.7112146(19)	-13.1(6)	-7.03(5)	1.0(7)	0.8(13)
7.5	-8.71119349(29)	-6.43(9)	-3.18(4)	-0.03(18)	

[a] Reference 13

Downloaded by 89.163.35.42 on July 3, 2012 | http://pubs.acs.org
Publication Date: December 31, 2006 | doi: 10.1021/bk-2007-0953.ch001

The results of the Gaussian 03 calculations and the ATM three-body correction term for six interatomic distances between 2.5 and 7.5 bohr are listed in Table IV for the equilateral triangle geometry and Table V for the symmetric linear geometry.

Discussion

The results of our calculations are in good agreement with previous quantum Monte Carlo calculations. We have reduced the statistical errors in the quantum Monte Carlo calculations of the equilateral triangle helium trimer by Mohan and Anderson (*11*) by more than a factor of ten. The errors in the quantum Monte Carlo calculations of Bhattacharya and Anderson (*13*) for the symmetric linear geometry of the helium trimer were reduced by factors of two to ten. We find again that the three-body interaction of helium trimers in both configurations is very small for internuclear distances of 5.6 bohr and larger. We also find again that the ATM expression fails badly for internuclear distances of less than 4.5 bohr, and for the equilateral triangle, even the sign is wrong. An explanation for this is given by the analysis of Bulski and Chalasiński (*15*), where the three-body correction is split into three contributions, of which the ATM expression is only a fraction of one, and the other two predominate at close distances. For internuclear distances of 5.6 bohr and greater, both the DQMC and the ATM values are both small, but the statistical error in the DQMC values prevents further comparisons.

The DQMC results are entirely compatable witht the extended group function model (EGFM) results of Røeggen and Almlöf (*10*). This is particularly evident for the smaller internuclear distances of the trianglular case. In all cases, however, the DQMC values fall within one or two standard deviations of the EGFM values. In this sense, the DQMC calculations confirm the EGFM results.

For the smaller internuclear distances, the several standard types of calculations (HF, CCSD, and MP4) give remarkably good agreement with each other and with the DQMC calculations for the three-body corrections despite poor values for the two-body interactions. This was observed in the earlier DQMC calculations.

In one of the first calculations to use accurate pair potentials of the properties of liquid helium, Kalos *et al.* (*16*) found that predictions gave better agreement with experiment when the ATM correction was omitted than when it was included. Since then, a number of other calculations have been made for solid and liquid helium(^{3}He and ^{4}He) using several different three-body correction terms, some good and some bad, but most without any three-body correction term (*17*). Results of our current calculations, together with those of the best prior calculations, give consistent predictions of three-body corrections and should lead to more accurate first principle calculations of the properties of solid and liquid helium and helium clusters.

Acknowledgement is made to the National Science Foundation: IGERT grant No. DGE 9987589.

Downloaded by 89.163.35.42 on July 3, 2012 | http://pubs.acs.org
Publication Date: December 31, 2006 | doi: 10.1021/bk-2007-0953.ch001

Downloaded by 89.163.35.42 on July 3, 2012 | http://pubs.acs.org
Publication Date: December 31, 2006 | doi: 10.1021/bk-2007-0953.ch001

TABLE IV. Correction to the pairwise-additive energy calculated for helium trimers in an equilateral triangle geometry by various methods.

R	*Three-body Interaction Energy ΔE_3 (K)*					
(bohr)	*HF*	*CCSD*	*MP4*	*ATM*	*EGFM*[a]	*DQMC*
2.5	-5708.46	-5902.54	-5610.95	168.32		-5930(240)[b]
3.5	-284.26	-317.42	-288.90	8.15	-285	-274(100)[b]
4.5	-7.67	-9.13	-10.70	0.85	-9.8	-8.8(12)
5.6	0.22	0.19	-0.25	0.12	-0.05	0.2(4)
6.5	0.06	0.06	-0.03	0.03	0.04	0.13(28)
7.5	0.00	0.09	0.03	0.01	0.01	0.39(18)

[a] Reference 10

[b] Reference 11

TABLE V. Correction to the pairwise-additive energy calculated for helium trimers in a symmetric linear geometry by various methods.

R	*Three-body Interaction Energy ΔE_3 (K)*					
(bohr)	*HF*	*CCSD*	*MP4*	*ATM*	*EGFM*[a]	*DQMC*
2.5	601.58	638.05	638.53	-30.60		
3.5	11.87	12.28	13.39	-1.48	16.2	-20(70)[b]
4.5	0.03	-0.3	-0.13	-0.15	0.26	0.4(12)
5.6	0.03	0.0	-0.03	-0.02	-0.010	0.3(5)
6.5	0.03	0.3	-0.06	-0.01	-0.005	1.0(7)
7.5	0.00	0.1	0.00	0.00	-0.001	-0.03(18)

[a] Reference 10

[b] Reference 13

References

1. J. C. Slater, Phys. Rev. **32**, 349 (1928).
2. J. B. Anderson, J. Chem. Phys. **120**, 9886 (2004).
3. B. M. Axilrod and E. Teller, J. Chem. Phys. **6**, 299 (1943).
4. Y. Muto, Nippon Sugaku-Buturigakukai-si **17**, 629 (1943), as reported in Ref. 2
5. D. Rosen, J. Chem. Phys. **21**, 1007 (1953).
6. A. Shostak, J. Chem. Phys. **23**, 1808 (1955).
7. A. E. Sherwood, A. G. De Rocco, and E. A. Mason, J. Chem. Phys. **44**, 2984 (1966).
8. O. A. Novaro and V. Beltran-Lopez, J. Chem. Phys. **56**, 815 (1972).
9. C. A. Parish and C. E. Dykstra, J. Chem. Phys. **98**, 437 (1993).
10. I. Røeggen and J. Almlöf, J. Mol. Struct. **388**, 331 (1996).
11. V. Mohan and J. B. Anderson, J. Chem. Phys. **92**, 6971 (1990).
12. G. J. Tawa, P. Whitlock, K. E. Schmidt, and J. E. Moskowitz, Mol. Phys. **77**, 477 (1992).
13. A. Bhattacharya and J. B. Anderson. J. Chem. Phys. **100**, 8999 (1994).
14. R. E. Lowther and R. L. Coldwell, Phys. Rev. A **22**, 14 (1980).
15. M. Bulski and G. Chalasiński, J. Chem. Phys. **86**, 937 (1987).
16. M. H. Kalos, M. A. Lee, P. A. Whitlock, and G. V. Chester, Phys. Rev. B **24**, 115 (1981).
17. S. Baroni and S. Moroni, Phys. Rev. Lett. **82**, 4745 (1999). S. Moroni, F. Pederiva, S. Fantoni, and M. Boninsegni, Phys. Rev. Lett. **84**, 2650 (2000). J. Cuervo, P.-N. Roy, and M. Boninsegni, J. Chem. Phys. **122**, 114504 (2005).

Downloaded by 89.163.35.42 on July 3, 2012 | http://pubs.acs.org
Publication Date: December 31, 2006 | doi: 10.1021/bk-2007-0953.ch001

Downloaded by CORNELL UNIV on July 3, 2012 | http://pubs.acs.org
Publication Date: December 31, 2006 | doi: 10.1021/bk-2007-0953.ch002

Chapter 2

Energies and Properties of the Hydrogen Molecular Ion

S. A. Alexander[1] and R. L. Coldwell[2]

[1]Department of Physics, Southwestern University, Georgetown, TX 78626
[2]Department of Physics, University of Florida, Gainesville, FL 32611

Using variational Monte Carlo techniques we calculate the rovibrational energy and a number of rovibrationally averaged properties of several of the lowest vibrational and rotational levels of the hydrogen molecular ion.

Introduction

The hydrogen molecular ion has the unique distinction of being the only molecular system whose Born-Oppenheimer energy can be determined to arbitrary accuracy (1). In order to compare with experiment, however, this energy must be corrected for relativistic effects, non-adiabatic effects and even radiative effects. A wide variety of theoretical methods have been used to produce highly converged values for these corrections. In this paper we show that variational Monte Carlo techniques can produce very accurate energies and properties for this system. We begin by optimizing a simple wavefunction form at 26 internuclear distances. Using these molecular wavefunctions we then calculate the Born-Oppenheimer energy, the diagonal correction to the Born-Oppenheimer approximation, the lowest-order relativistic corrections and the radiative corrections at each distance. All of these results are discussed in the second section. With our wavefunctions we also calculate nine molecular properties at each internuclear distance. These calculations are described in the third section. In the fourth section we construct four potential energy surfaces and then optimize a set of rapidly convergent wavefunctions for several of the lowest rotational and vibrational levels of this system. With these rovibrational wavefunctions we then compute the rovibrational energy and a number of rovibrationally averaged properties for each level. The former calculations are described in the fifth section and the latter calculations in the sixth section. Wherever possible we compare our results to earlier ones in the literature. Unless otherwise indicated, all values in this paper are given in atomic units.

Downloaded by CORNELL UNIV on July 3, 2012 | http://pubs.acs.org
Publication Date: December 31, 2006 | doi: 10.1021/bk-2007-0953.ch002

Calculating the Molecular Energy and its Corrections

Variational Monte Carlo is a method of computing the expectation value of an operator

$$<A> = \sum_i [\Psi_i A \Psi_i / w_i] / \sum_i [\Psi_i^2 / w_i] \qquad (1)$$

and its standard deviation (i.e., statistical error)

$$\sigma^2 = \sum_i [(A\Psi_i - <A>\Psi_i)^2 \Psi_i^2 / w_i^2] / \{\sum_i [\Psi_i^2 / w_i]\}^2 \qquad (2)$$

using Monte Carlo integration. Here $\Psi_i = \Psi_T(x_i)$ is the value of the trial wavefunction at the Monte Carlo integration point x_i and the weight function $w_i = w(x_i)$ is the relative probability of choosing this point. In a variational Monte Carlo calculation the adjustable parameters in the trial wavefunction are often optimized with respect to a functional, usually some combination of the energy and its standard deviation (2,3). The Monte Carlo integration points used in these calculations are generated from a guiding function that can also be optimized with respect to the standard deviation of the local energy or any other property (4).

In Ref. 5 we showed that the trial wavefunction form

$$\Psi_T = (1+P_{AB}) \exp(\sum_k a_k q_{1A}^i q_{1B}^j - \alpha r_{1A}) \qquad (3)$$

produces rapidly convergent energies for the H_2^+ ground state. Here P_{AB} is the operator that interchanges the two nuclei and $q_x = r_x/(1 + cr_x)$ is a coordinate transformation that allows terms in the exponential to go smoothly to the asymptotic limit. The exponents i and j are integers (0, 1,...) which have been preselected for each value of k. All exponents that add up to N=i+j=4 are included in the trial wavefunction. Using a set of 4,000 Monte Carlo integration points we optimized all 16 adjustable parameters in Eqn. 3 so as to minimize the statistical error in the local energy. This step was repeated at 26 internuclear distances. Once these trial wavefunctions were determined, we computed the Born-Oppenheimer energies using 65,536,000 Monte Carlo integration points in order to obtain a low statistical error. As shown in Table I, our values are all within a few nanohartrees of earlier calculations (6,7).

Handy and others have demonstrated that the diagonal energy correction to the Born-Oppenheimer approximation can easily be evaluated from the expression (8-11)

$$E_{non} = -\sum_N \frac{1}{2M_N} \int [\Psi_T \frac{d^2\Psi_T}{dX_N} + \Psi_T \frac{d^2\Psi_T}{dY_N} + \Psi_T \frac{d^2\Psi_T}{dZ_N}] d^3 r_1 \ \dots \quad (4)$$

In a variational Monte Carlo calculation the derivatives in Eqn. 4 can be computed by moving each atom by some small amount in each direction, reoptimizing the wavefunction and then numerically differentiating the wavefunction with respect to the nuclear coordinates. As in several earlier calculations these numerical derivatives are computed over the same Monte Carlo integration points to substantially reduce their statistical error (5,12-14). This correlated sampling works best when all the wavefunctions have been optimized to about the same statistical error. The values in Table I were computed using $M_N = 1836.152693$ for the mass of the proton and 65,536,000 Monte Carlo integration points. For comparison, we also list the values obtained by Bishop and Wetmore (6). At all values of R the difference between these values is less than a microhartree.

The lowest-order relativistic corrections for the ground state of H_2^+ are given by the expectation value (15)

$$\overset{4}{}$$

$$E_{rel} = \langle \Psi | -\frac{1}{4c^2} + \frac{2\pi}{c^2} \delta(\mathbf{r}_{1A}) | \Psi \rangle \quad (5)$$

Downloaded by CORNELL UNIV on July 3, 2012 | http://pubs.acs.org
Publication Date: December 31, 2006 | doi: 10.1021/bk-2007-0953.ch002

Table 1. Potential energy surface of the H_2^+ ground state. All values are in a.u. and have been computed with 65,536,000 Monte Carlo integration points. The number in the parenthesis is the statistical error.

R	Born-Oppenheimer Energy	Non-Adiabatic Energy	Relativistic Energy	Radiative Energy
0.2	+3.071379733(54) +3.071379703 [6]	0.00054357(9) 0.000542648 [6]	-0.000076765(87) -0.000076624 [17]	0.0000107983(13)
0.4	+0.699246016(38) +0.699245941 [6]	0.00049530(9) 0.000501166 [6]	-0.000049508(54) -0.000049442 [17]	0.0000074934(9)
0.6	-.004817997(24) -0.004818048 [6]	0.00044939(8) 0.000449446 [6]	-0.000033292(36) -0.000033252 [17]	0.0000055757(7) 0.0000055751 [19]
0.8	-.304480005(15) -0.304480094 [6]	0.00040222(8) 0.000402704 [6]	-0.000023667(26) -0.000023637 [17]	0.0000042107(5) 0.0000042101 [19]
1.0	-.451786273(11) -0.451786313 [6]	0.00036372(7) 0.000363940 [6]	-0.000017714(20) -0.000017691 [17]	0.0000033297(4) 0.0000033293 [19]
1.4	-0.569983491(6) -0.569983528 [6]	0.00030763(6) 0.000307598 [6]	-0.000011302(14) -0.000011287 [17]	0.0000023165(3)
1.5	-0.582323174(5) -0.582323205 [6]	0.00029707(6) 0.000297039 [6]	-0.000010336(12) -0.000010322 [17]	0.0000021537(3) 0.0000021536 [19]
1.6	-0.590937199(5) -0.590937225 [6]	0.00028760(6) 0.000287614 [6]	-0.000009528(12) -0.000009515 [17]	0.0000020142(2)
1.7	-0.596696250(4) -0.596696270 [6]	0.00027919(6) 0.000279207 [6]	-0.000008849(11)	0.0000018941(2)
1.8	-0.600253616(4) -0.600253634 [6]	0.00027170(6) 0.000271718 [6]	-0.000008276(10) -0.000008265 [17]	0.0000017902(2) 0.0000017902 [19]
1.9	-0.602105768(3) -0.602105783 [6]	0.00026504(5) 0.000265189 [6]	-0.000007790(10)	0.0000016999(2) 0.0000016999 [19]
2.0	-0.602634202(3) -0.602634214 [6]	0.00025918(5) 0.000259144 [6]	-0.000007376(9) -0.000007366 [17]	0.0000016211(2) 0.0000016211 [19]

Downloaded by CORNELL UNIV on July 3, 2012 | http://pubs.acs.org
Publication Date: December 31, 2006 | doi: 10.1021/bk-2007-0953.ch002

Downloaded by CORNELL UNIV on July 3, 2012 | http://pubs.acs.org
Publication Date: December 31, 2006 | doi: 10.1021/bk-2007-0953.ch002

Table 1. Continued.

R	Born-Oppenheimer Energy	Non-Adiabatic Energy	Relativistic Energy	Radiative Energy
2.1	-0.602134935(3) -0.602134946 [6]	0.00025390(5) 0.000253912 [6]	-0.000007024(9)	0.0000015522(2) 0.0000015522 [19]
2.2	-0.600839617(3) -0.600839627 [6]	0.00024929(5) 0.000249296 [6]	-0.000006723(8) -0.000006715 [17]	0.0000014918(2) 0.0000014918 [19]
2.3	-0.598930879(3) -0.598930886 [6]	0.00024524(5) 0.000245244 [6]	-0.000006467(8)	0.0000014387(2)
2.4	-0.596553632(3) -0.596553639 [6]	0.00024170(5) 0.000241708 [6]	-0.000006248(8) -0.000006240 [17]	0.0000013920(2)
2.5	-0.593823505(2) -0.593823511 [6]	0.00023858(5) 0.000238643 [6]	-0.000006062(8) -0.000006054 [17]	0.0000013509(2)
2.6	-0.590833192(2) -0.590833196 [6]	0.00023601(5) 0.000236011 [6]	-0.000005904(7) -0.000005897 [17]	0.0000013147(2)
3.0	-0.577562861(2) -0.577562864 [6]	0.00022911(5) 0.000229166 [6]	-0.000005488(7) -0.000005482 [17]	0.0000012088(1) 0.0000012088 [19]
4.0	-0.546084882(2) -0.546084884 [6]	0.00023640(5) 0.000229470 [6]	-0.000005311(6) -0.000005305 [17]	0.0000011080(1) 0.0000011080 [19]
5.0	-0.524420296(2) -0.524420295 [6]	0.00024521(6) 0.000241202 [6]	-0.000005631(6) -0.000005625 [17]	0.0000011147(1) 0.0000011147 [19]
6.0	-0.511969049(1) -0.511969048 [6]	0.00025358(6) 0.000253543 [6]	-0.000006020(7) -0.000006014 [17]	0.0000011521(1) 0.0000011520 [19]
7.0	-0.505594004(1) -0.505594004 [6]	0.00026223(6) 0.000262174 [6]	-0.000006312(7)- 0.000006306 [17]	0.0000011861(1)
8.0	-0.502570388(1) -0.502570389 [6]	0.00026720(6) 0.000267142 [6]	-0.000006485(7) -0.000006479 [17]	0.0000012086(1)
9.0	-0.501195452(1) -0.501195453 [6]	0.00026980(6) 0.000269735 [6]	-0.000006576(7) -0.000006569 [17]	0.0000012213(2)
10.0	-0.500578728(1) -0.500578729 [6]	0.00027109(6) 0.000271025 [6]	-0.000006620(7) -0.000006614 [17]	0.0000012279(2)

where $c = 137.0359895$ is the speed of light. The first term in this expression is the mass-velocity operator and the second is the one-body Darwin term. We have evaluated Eqn. 5 at each internuclear distance using using 65,536,000 Monte Carlo integration points. Our results are listed in Table I and are in excellent agreement with earlier calculations (16,17).

For a one-electron system the radiative correction to the ground state energy (of order $Z^2 \alpha^3$) is simply the lowest order Lamb shift (15)

$$E_{rad} = \frac{8}{3c^3} \left[2\,\mathrm{Ln}(c) - 2\,\mathrm{Ln}(2) + \frac{19}{30} - \mathrm{Ln}(K_0) \right] \langle \Psi | \delta(\mathbf{r}_{1A}) | \Psi \rangle \qquad (6)$$

where $\mathrm{Ln}(K_0)$ is a quantity normally referred to as the Bethe logarithm. This function depends on the internuclear distance and is notoriously difficult to evaluate accurately. Following the example of Bishop and Cheung (18) we interpolate the values of the Bethe logarithm computed by Bukowski et al. (19) and combine these with the same values for the electronic density that were used to evaluate Eqn 5. Our results are listed in Table I and, not surprisingly, are in excellent agreement with the calculations of Ref. 19.

Calculating Molecular Properties

Once a trial waveunction has been optimized it is relatively easy to calculate the expectation value of even complicated operators using Monte Carlo methods (12). We have used the molecular wavefunctions computed in the previous section to evaluate nine geometrical properties at each internuclear distance using 65,536,000 Monte Carlo integration points. Here the permanent quadrupole moment is defined as $Q_2 = (R^2 + r_1^2 - 3z_1^2)/2$ for a molecule oriented along the z-axis. As Table II shows, almost all of our properties are determined to several significant digits. Only a few of these properties have been calculated using other theoretical methods and our values are in excellent agreement with these earlier results (7,18,20).

Calculating Rovibrational Energies

The rovibrational energies of a diatomic are the solutions of the radial Schrodinger equation (1)

Downloaded by CORNELL UNIV on July 3, 2012 | http://pubs.acs.org
Publication Date: December 31, 2006 | doi: 10.1021/bk-2007-0953.ch002

Downloaded by CORNELL UNIV on July 3, 2012 | http://pubs.acs.org
Publication Date: December 31, 2006 | doi: 10.1021/bk-2007-0953.ch002

Table 2. Selected properties of the H_2^+ ground state as a function of the internuclear distance R. All values are in a.u. and have been computed with 65,536,000 Monte Carlo integration points. The number in the parenthesis is the statistical error.

R	r_{1A}	r_{1A}^2	r_{1A}^{-1}	r_{1A}^{-2}	x^2	z^2	r^2	Q_2	$\delta(r_{1A})$
0.2	0.7841(1)	0.8120(1)	1.8711(3)	6.615(2)	0.26974(6)	0.26614(6)	0.8020(1)	0.02179(6)	1.6020(2)
0.4	0.8556(1)	0.9503(2)	1.6680(3)	5.077(1)	0.31287(7)	0.29876(7)	0.9104(1)	0.08704(7)	1.0470(1)
0.6	0.9430(1)	1.1360(2)	1.4855(2)	3.9783(9)	0.37035(8)	0.33784(8)	1.0460(2)	0.19623(8)	0.73628(9)
0.8	1.0382(2)	1.3595(2)	1.3349(2)	3.2146(7)	0.43970(9)	0.37997(9)	1.1996(2)	0.3498(1)	0.55111(7)
1.0	1.1377(2)	1.6175(3)	1.2123(2)	2.6730(6)	0.5204(1)	0.4236(1)	1.3676(2)	0.5483(1)	0.43358(5)
1.4	1.3434(2)	2.2313(4)	1.0291(2)	1.9836(4)	0.7169(1)	0.5123(1)	1.7414(3)	1.0822(2)	0.30022(4)
1.5	1.3956(2)	2.4049(4)	0.9930(2)	1.8638(4)	0.7738(1)	0.5344(1)	1.8425(3)	1.2446(2)	0.27895(3)
1.6	1.4480(2)	2.5864(4)	0.9600(2)	1.7587(4)	0.8341(2)	0.5563(1)	1.9466(3)	1.4188(2)	0.26076(3)
1.7	1.5005(2)	2.7761(5)	0.9296(2)	1.6661(3)	0.8978(2)	0.5781(1)	2.0538(3)	1.6047(3)	0.24513(3)
1.8	1.5532(3)	2.9739(5)	0.9018(2)	1.5842(3)	0.9650(2)	0.5996(1)	2.1641(3)	1.8026(3)	0.23162(3)
1.9	1.6059(3)	3.1799(5)	0.8761(1)	1.5116(3)	1.0360(2)	0.6209(2)	2.0124(3)	2.0124(3)	0.21989(3)
2.0	1.6588(3)	3.3942(6)	0.8524(1)	1.4470(3)	1.1109(2)	0.6419(2)	2.3944(4)	2.2344(4)	0.20967(3)
2.1	1.7116(3)	3.6168(6)	0.8305(1)	1.3893(3)	1.1897(2)	0.6625(2)	2.5145(4)	2.4685(4)	0.20073(2)
2.2	1.7646(3)	3.8478(7)	0.8102(1)	1.3379(3)	1.2728(2)	0.6828(2)	2.6381(4)	2.7148(4)	0.19290(2)
2.3	1.8176(3)	4.0874(7)	0.7915(1)	1.3601(2)	1.3601(2)	0.7027(2)	2.7652(5)	2.9736(5)	0.18602(2)
2.4	1.8705(3)	4.3355(8)	0.7741(1)	1.2506(3)	1.4519(3)	0.7221(2)	2.8959(5)	3.2447(5)	0.17997(2)
2.5	1.9236(3)	4.5924(8)	0.7579(1)	1.2136(2)	1.5483(3)	0.7411(2)	3.0303(5)	3.5284(6)	0.17465(2)
2.6	1.9766(3)	4.8581(9)	0.7430(1)	1.1805(2)	1.6496(3)	0.7596(2)	3.1686(5)	3.8248(6)	0.16996(2)
3.0	2.1886(4)	6.012(1)	0.6929(1)	1.0788(2)	2.1060(4)	0.8283(2)	3.7623(6)	5.1386(8)	0.15623(2)
4.0	2.7169(5)	9.571(2)	0.6172(1)	0.9621(2)	3.6611(6)	0.9560(3)	5.5726(9)	9.352(1)	0.14310(2)
5.0	3.2405(6)	14.174(3)	0.5830(1)	0.9429(2)	5.890(1)	1.0184(3)	7.926(1)	14.936(2)	0.14384(2)
6.0	3.7576(7)	19.848(4)	0.5687(1)	0.9576(2)	8.786(1)	1.0332(3)	10.852(2)	21.876(3)	0.14856(2)
7.0	4.2682(8)	26.550(5)	0.5619(1)	0.9763(2)	12.253(2)	1.0264(3)	14.306(2)	30.113(4)	0.15295(2)
8.0	4.7736(9)	34.232(7)	0.5572(1)	0.9895(2)	16.208(3)	1.0159(3)	18.239(3)	39.596(6)	0.15584(2)
9.0	5.276(1)	42.871(9)	0.5528(1)	0.9968(2)	20.615(3)	1.0079(3)	22.630(4)	50.303(7)	0.15746(2)
10.0	5.776(1)	52.47(1)	0.5486(1)	1.0003(2)	25.475(4)	1.0032(3)	27.481(4)	62.236(9)	0.15830(2)

$$\frac{-1}{2\mu}\frac{d^2\Psi_{vJ}(R)}{dR^2} + [\, V(R) - \frac{J(J+1)}{2\mu\, R^2} \,]\, \Psi_{vJ}(R) = E_{vJ} \quad \Psi_{vJ}(R) \qquad (7)$$

where μ is the reduced mass of the molecule and V(R) is the potential energy surface as a function of the internuclear distance R. For these calculations we use the energies in section 2 to form four slightly different potential energy surfaces: PES1 is simply the Born-Oppenheimer energy, PES2 is the sum of the PES1 and the diagonal non-adiabatic energy, PES3 is the sum of PES2 and the relativistic energy, PES4 is the sum of PES3 and the radiative energies. In Ref. 21 we found that an 11-term Lagrange interpolation of $V(R)^*R^2$ provides an accurate estimate of points everywhere on the potential energy surface. We also showed that an exponential Pade is a rapidly convergent trial wavefunction for diatomics

$$\text{for } v=0: \; \Psi_T(R) = \exp\left(\frac{\sum_{k=0}^{n} a_k\, (R-R_e)^k}{\sum_{k=0}^{n} b_k\, (R-R_e)^k} \right)$$

$$\text{for } v=1: \; \Psi_T(R) = (R-a)\exp\left(\frac{\sum_{k=0}^{n} a_k\, (R-R_e)^k}{\sum_{k=0}^{n} b_k\, (R-R_e)^k} \right) \qquad (8)$$

$$\text{for } v=2: \; \Psi_T(R) = (R-a)(R-b)\exp\left(\frac{\sum_{k=0}^{n} a_k\, (R-R_e)^k}{\sum_{k=0}^{n} b_k\, (R-R_e)^k} \right)$$

Downloaded by CORNELL UNIV on July 3, 2012 | http://pubs.acs.org
Publication Date: December 31, 2006 | doi: 10.1021/bk-2007-0953.ch002

$$\text{for } v=3:\ \Psi_T(R) = (R-a)(R-b)(R-c)\exp\left(\frac{\sum_{k=0}^{n} a_k (R-R_e)^k}{\sum_{k=0}^{n} b_k (R-R_e)^k}\right)$$

where R_e is the equilibrium distance. For each of the lowest several rotational and vibrational levels of this system we optimized a unique n=4 wavefunction using variance minimization and 4,000 Monte Carlo integration points. All rotational levels have the same wavefunction form - only the value of J in Eqn. 7 is changed. Because we are interested in the effect of the different corrections on the rovibrational energies and on the rotationally-averaged properties, this process was repeated for each potential energy surface.

There are two sources of error in the evaluation of Eqn. 7 - the integration error and the error caused by our interpolation procedure. We evaluated the energy of each optimized wavefunction using 1,024,000 Monte Carlo integration points. This resulted in a set of energies that had a very low statistical error. We can estimate the grid error by omitting one point in V(R), reoptimizing the trial wavefunction and then recalculating E_{vJ}. This process was repeated until each point in V(R) had been omitted. The grid error in each rotational-vibrational energy level is just the standard deviation between our original value and these new energies. For all of the energies considered here we found that the grid error is many times larger than the integration error. To decrease it we will need to use a grid with many more points.

In Table III we list the final rovibrational energies for each potential energy surface. These are in excellent agreement with those computed using other theoretical methods (23-26). As expected, the diagonal energy correction to the Born-Oppenheimer approximation produces the largest change in the rovibrational energies - on average about 253 microhartrees. In contrast, the average relativistic correction is 7 microhartrees and the average radiative correction is 1 microhartree.

Downloaded by CORNELL UNIV on July 3, 2012 | http://pubs.acs.org
Publication Date: December 31, 2006 | doi: 10.1021/bk-2007-0953.ch002

Calculating Rovibrationaly Averaged Properties

Once a set of rovibrational wavefunctions have been determined, the vibrationally averaged values of a property can be computed from the expression

$$\langle A \rangle_{vJ} = \int \Psi_{vJ}(R)\ A(R)\, \Psi_{vJ}(R)\ dR \,/ \int \Psi_{vJ}^2(R)\ dR \qquad (9)$$

Downloaded by CORNELL UNIV on July 3, 2012 | http://pubs.acs.org
Publication Date: December 31, 2006 | doi: 10.1021/bk-2007-0953.ch002

Table 3. Rovibrational energies (in a.u.) of the H_2^+ ground state computed using four different potential energy surfaces. The number in the parenthesis is the estimated error.

v	J	PES1	PES2	PES3	PES4
0	0	-0.597395894(6)	-0.59713844(2)	-0.59714574(2)	-0.59714414(1)
0	1	-0.597130415(5)	-0.59687311(2)	-0.59688040(2)	-0.59687880(1)
0	2	-0.596601584(5)	-0.59634456(2)	-0.59635182(2)	-0.59635022(2)
0	3	-0.595813570(5)	-0.59555696(2)	-0.59556419(2)	-0.59556260(2)
1	0	-0.58740831(3)	-0.5871541(1)	-0.5871613(1)	-0.5871597(1)
1	1	-0.58715681(3)	-0.5869028(1)	-0.5869099(1)	-0.5869083(1)
1	2	-0.58665585(3)	-0.5864021(1)	-0.5864092(1)	-0.5864076(1)
1	3	-0.58590943(3)	-0.5856560(1)	-0.5856631(1)	-0.5856615(1)
2	0	-0.5780009(2)	-0.5777495(6)	-0.5777564(6)	-0.5777549(6)
2	1	-0.5777629(2)	-0.5775116(6)	-0.5775186(6)	-0.5775170(6)
2	2	-0.5772888(2)	-0.5770378(6)	-0.5770447(6)	-0.5770432(6)
2	3	-0.5765826(2)	-0.5763318(6)	-0.5763388(6)	-0.5763373(6)
3	0	-0.5691543(5)	-0.568905(2)	-0.568912(2)	-0.568910(2)
3	1	-0.5689294(5)	-0.568680(2)	-0.568687(2)	-0.568686(2)
3	2	-0.5684815(5)	-0.568233(2)	-0.568239(2)	-0.568238(2)
3	3	-0.5678142(5)	-0.567566(2)	-0.567572(2)	-0.567571(2)

As in our earlier discussion of Eqn. 7 this expectation value will have two sources of error - the integration error and the use of a finite grid to represent A(R). Here we use a 5-term Lagrange interpolation of all the properties in Table II to provide an accurate estimate of A(R) at all values of R. In all our calculations we found that a relatively small number of integration points produces a result that is converged to many significant digits. Using the same procedure described in the previous section, we computed the grid error for each property and found that it is many times larger than the integration error.

In Table IV we list a number of vibrationally averaged properties for several of the lowest vibrational and rotational levels of this system. These were computed using the properties in Table II, the rovibrational wavefunctions from our most accurate potential (PES4) and 1,024,000 Monte Carlo integration points. When we repeated these calculations using our other rovibrational wavefunctions, we found that the influence of the potential energy surface on our vibrationally averaged properties is roughly the same as on our rovibrational energies. If we compare each set of properties with the values produced by the Born-Oppenheimer potential, the diagonal energy correction to the Born-Oppenheimer approximation produces the largest change (averaging about 0.04%). Relativistic and radiative corrections produce average changes of about 0.001% and 0.0003% respectively.

Downloaded by CORNELL UNIV on July 3, 2012 | http://pubs.acs.org
Publication Date: December 31, 2006 | doi: 10.1021/bk-2007-0953.ch002

Conclusions

Using variational Monte Carlo and a simple wavefunction form that contains only 16 adjustable parameters we calculated the Born-Oppenheimer energy, the diagonal correction to the Born-Oppenheimer approximation, the lowest order relativistic energy, an estimate of the radiative energy and nine molecular properties of the ground state of the hydrogen molecular ion at 26 internuclear distances. These properties were then combined with rapidly convergent rovibrational wavefunctions to produce rovibrationally averaged properties for several of the lowest rotational and vibrational levels of this system. Our results are in excellent agreement with previous values found in the literature (27,28). Since all of the techniques used here can easily be generalized to polyatomics, we believe that the calculations in this paper are a necessary first step toward using Monte Carlo methods to evaluate rovibrationally averaged properties for a wide variety of molecules.

Acknowledgments

We wish to thank Dr. R.E. Moss for several valuable discussions and the staff of the Northeast Regional Data Center for their support in running our program on the University of Florida IBM NERSP.

Downloaded by CORNELL UNIV on July 3, 2012 | http://pubs.acs.org
Publication Date: December 31, 2006 | doi: 10.1021/bk-2007-0953.ch002

Table 4. Rovibrationally averaged properties (in a.u.) of the H_2^+ ground state computed using the values in Table 2 and the rovibrational wavefunctions obtained from PES4. The number in the parenthesis is the estimated error.

v	J	R	R^2	R^{-1}	R^{-2}	r_{1A}	r_{1A}^2
0	0	2.063888985(1)	4.313187737(1)	0.4907144(3)	0.243931(5)	1.69267502(8)	3.5579693(5)
0	1	2.066595112(1)	4.324440169(1)	0.4900641(3)	0.243281(5)	1.69410578(8)	3.5640656(5)
0	2	2.071997371(1)	4.346947342(1)	0.4887709(3)	0.241990(4)	1.69696212(8)	3.5762544(5)
0	3	2.080076999(1)	4.380719448(1)	0.4868496(2)	0.240080(4)	1.70123436(9)	3.5945304(5)
1	0	2.199109261(1)	4.999228015(1)	0.471614(2)	0.23110(2)	1.7644390(5)	3.915137(3)
1	1	2.201928688(1)	5.011866168(1)	0.470989(1)	0.23047(2)	1.7659297(5)	3.921891(3)
1	2	2.207559369(1)	5.037156377(1)	0.469746(1)	0.22924(2)	1.7689069(5)	3.935400(3)
1	3	2.215980666(1)	5.075100735(1)	0.467900(1)	0.22741(2)	1.7733599(6)	3.955657(4)
2	0	2.339747597(1)	5.754395860(1)	0.453099(4)	0.21871(7)	1.839034(3)	4.30574(2)
2	1	2.342697269(1)	5.768609536(1)	0.452497(4)	0.21811(6)	1.840593(3)	4.31325(2)
2	2	2.348588883(1)	5.797055117(1)	0.451300(4)	0.21692(6)	1.843708(3)	4.32827(2)
2	3	2.357403441(1)	5.839748162(1)	0.449521(4)	0.21517(5)	1.848368(3)	4.35082(2)
3	0	2.486630585(1)	6.588113256(1)	0.435075(9)	0.2067(1)	1.916887(9)	4.73483(5)
3	1	2.489753407(1)	6.604266325(1)	0.434491(9)	0.2061(1)	1.918538(9)	4.74329(5)
3	2	2.495937970(1)	6.636283926(1)	0.433336(8)	0.2050(1)	1.921807(9)	4.76006(5)
3	3	2.505204540(1)	6.684415589(1)	0.431618(8)	0.2033(1)	1.92670(1)	4.78525(5)

v	J	r_{1A}^{-1}	r_{1A}^{-2}	x^2	z^2	r^2	Q_2	$\delta(r_{1A})$
0	0	0.84273830(2)	1.4267836(2)	1.1718487(9)	0.6541540(6)	2.4799106(5)	2.4153182(7)	0.2069895(1)
0	1	0.84214773(2)	1.4252152(2)	1.1740261(9)	0.6547075(6)	2.4831945(5)	2.4217561(7)	0.2067441(1)
0	2	0.84097248(2)	1.4220986(2)	1.1783818(9)	0.6558117(6)	2.4897579(5)	2.4346351(7)	0.2062569(1)
0	3	0.83922410(2)	1.4174733(2)	1.1849192(8)	0.6574611(6)	2.4995931(5)	2.4539647(7)	0.2055348(1)
1	0	0.8232088(2)	1.386128(1)	1.306947(2)	0.679474(2)	2.665632(2)	2.813220(2)	0.2015619(3)
1	1	0.8226450(3)	1.384657(1)	1.309433(2)	0.680028(2)	2.669227(3)	2.820505(2)	0.2013322(3)
1	2	0.8215229(3)	1.381733(1)	1.314410(2)	0.681135(2)	2.676416(3)	2.835085(2)	0.2008762(3)
1	3	0.8198537(3)	1.377394(1)	1.321880(2)	0.682787(2)	2.687190(3)	2.856965(2)	0.2002004(4)
2	0	0.804552(2)	1.348243(7)	1.458603(3)	0.704596(9)	2.86752(2)	3.254063(6)	0.196545(2)
2	1	0.804013(2)	1.346863(7)	1.461454(3)	0.705150(9)	2.87148(2)	3.262318(6)	0.196330(2)
2	2	0.802941(2)	1.344120(7)	1.467161(3)	0.706256(9)	2.87940(2)	3.278841(6)	0.195903(2)
2	3	0.801346(2)	1.340051(7)	1.475732(3)	0.70791(1)	2.89127(2)	3.303647(6)	0.195272(2)
3	0	0.786699(6)	1.31293(2)	1.629640(3)	0.72946(2)	3.08828(5)	3.74400(1)	0.191910(6)
3	1	0.786181(6)	1.31163(2)	1.632951(3)	0.73002(2)	3.09270(5)	3.75345(1)	0.191709(6)
3	2	0.785157(7)	1.30906(2)	1.639516(3)	0.73112(2)	3.10147(5)	3.77219(1)	0.191311(6)
3	3	0.783631(7)	1.30525(2)	1.649391(3)	0.73277(3)	3.11463(5)	3.80037(1)	0.190721(6)

Downloaded by CORNELL UNIV on July 3, 2012 | http://pubs.acs.org
Publication Date: December 31, 2006 | doi: 10.1021/bk-2007-0953.ch002

References

1. Pauling, L.; Wilson Jr., E.B. *Introduction to Quantum Mechanics*, McGraw-Hill, New York, 1935.
2. Coldwell, R.L. Int. J. Quantum Chem. **1977**, *S11*, 215-222.
3. Alexander, S.A.; Coldwell, R.L.; Monkhorst, H.J.; Morgan III, J.D. J. Chem. Phys. **1991**, *95*, 6622-6633.
4. Alexander, S.A.; Coldwell, R.L.; Morgan III, J.D. J. Chem. Phys. **1992**, *97*, 8407-8414.
5. Alexander, S.A.; Coldwell, R.L. Chem. Phys. Lett. **2005**, *413*, 253-257.
6. Bishop, D.M.; Wetmore, R.W. Mol. Phys. **1973**, *26*, 145-157.
7. Montgomery Jr., H.E. Chem. Phys. Lett. **1977**, *50*, 455-458.
8. Handy, N.C.; Yamaguchi, Y.; Schaefer III, H.F. J. Chem. Phys. **1986**, *84*, 4481-4484.
9. Handy, N.C.; Lee, A.M. Chem. Phys. Lett. **1996**, *252*, 425-430.
10. Kutzelnigg, W. Mol. Phys. **1997**, *90*, 909-916.
11. Cencek, W.; Kutzelnigg, W. Chem. Phys. Lett. **1997**, *266*, 383-387.
12. Alexander, S.A.; Coldwell, R.L.; Aissing, G.; Thakkar, A.J. Int. J. Quantum Chem. **1992**, *S26*, 213-227.
13. Alexander, S.A.; Coldwell, R.L. Int. J. Quantum Chem. **2004**, *100*, 851-857.
14. Alexander, S.A.; Coldwell, R.L. J. Chem. Phys. **2004**, *121*, 11557-11561.
15. Bethe, H.A.; Salpeter, E.E. *Quantum Mechanics of One- and Two-Electron Systems*, Springer-Verlag, Berlin, 1957.
16. Bishop, D.M. J. Chem. Phys. **1977**, *66*, 3842-3843.
17. Howells, M.H.; Kennedy, R.A. J. Chem. Soc. Faraday Trans. **1990**, *86*, 3495-3503.
18. Bishop, D.M.; Cheung, L.M. J. Phys. B. **1978**, *11*, 3133-3144.
19. Bukowski, R.; Jeziorski, B.; Moszynski, R.; Kolos, W. Int. J. Quantum Chem. **1992**, *42*, 287-319.
20. Laaksonen, L.; Pykko, P.; Sundholm, D. Int. J. Quantum Chem. **1983**, *23*, 309-317.
21. Alexander, S.A.; Coldwell, R.L. Int. J. Quantum Chem. **2006**, *106*, 1820-1826.
22. Beckel, C.L.; Hansen III, B.D.; Peek, J.M. J. Chem. Phys. **1970**, *53*, 3681-3690.
23. Hunter, G.; Yau, A.W.; Pritchard, H.O. Atomic Data and Nuclear Data Tables **1974**, *14*, 11-20.
24. Bishop, D.M.; Cheung, L.M. Phys. Rev. A. **1977**, *16*, 640-645.
25. Wolniewicz, L.; Orlikowski, T. Mol. Phys. **1991**, *74*, 103-111.
26. Moss, R.E. Mol. Phys. **1993**, *80*, 1541-1554.
27. Bishop, D.M.; Cheung, L.M. Mol. Phys. **1978**, *36*, 501-507.
28. Babb, J.F.; Shertzer, J. Chem. Phys. Lett. **1992**, *189*, 287-290.

Downloaded by CORNELL UNIV on July 3, 2012 | http://pubs.acs.org
Publication Date: December 31, 2006 | doi: 10.1021/bk-2007-0953.ch002

Chapter 3

Accuracy of a Random Walk-Based Approach in the Determination of Equilibrium Bond Lengths and Harmonic Frequencies for Some Doublet First-Row Diatomic Radicals

Shih-I Lu

**Department of Applied Chemistry, Fooyin University, 151 Chinhsueh Road,
Ta-Liao Hsiang, Kaohsiung Hsien, 831 Taiwan**

Downloaded by UNIV OF GUELPH LIBRARY on July 4, 2012 | http://pubs.acs.org
Publication Date: December 31, 2006 | doi: 10.1021/bk-2007-0953.ch003

The accuracy of equilibrium bond lengths and harmonic frequencies for 12 doublet first-row diatomic radicals is presented as predicted by the fixed-node diffusion quantum Monte Carlo method based on the Ornstein-Uhlenbeck random walk guided by a floating-spherical-Gaussian-orbital and spherical-Gaussian-geminal-type of trial wave function. Compared to the experimental determined values, the random walk based approach gives the absolute mean deviations of 0.0019 Å and 18 cm^{-1} for the equilibrium bond length and harmonic frequency, respectively. We also compare the random-walk-based results with BD(TQ) and CCSD(T) calculated values with a basis set of cc-pVQZ.

In Advances in Quantum Monte Carlo; Anderson, J., et al.;
ACS Symposium Series; American Chemical Society: Washington, DC, 2006.

Downloaded by UNIV OF GUELPH LIBRARY on July 4, 2012 | http://pubs.acs.org
Publication Date: December 31, 2006 | doi: 10.1021/bk-2007-0953.ch003

Introduction

This study presents a comparison to experimental values of equilibrium bond distances and harmonic frequencies of 12 doublet first-row diatomic radicals to investigate the performance of a random walk based approach in solving the many-electron Schrödinger equation for open-shell radicals. Recently Beran et al. *(1)* reported some sophisticated coupled-cluster based results using the basis sets of cc-pVTZ and cc-pVQZ for the same set of molecules that are CH, OH, FH^+, BO, CN, CO^+, N_2^+, CF, NO, O_2^+, OF, and F_2^+.

The random walk based method employed in this work is the fixed-node (FN) diffusion quantum Monte Carlo (DQMC) method *(2-5)* implemented with the Ornstein-Uhlenbeck (OU) random walks guided by a trial wave function constructed from floating spherical Gaussian orbitals (FSGO) and spherical Gaussian geminals (SGG). This approach was designated as the OUDQMC/FSGO-SGG *(6,7)*. This work reports a further application of the method and results described in earlier papers *(8,9)*. Part of calculated results was published in the Journal of Chemical Physics *(10)*.

Computational details

Trial wave function

The most popular form of trial wave function is the so-called Jastrow-Slater wave function *(2)* that consists of a correlation factor, usually exp(u(R)), where u(R) is some function which is totally symmetric in the electron coordinates, multiplied by a Slater determinant. The Slater determinant is usually obtained in a mean-field calculation like Hartree-Fock or Kohn-Sham density function theory. For some cases in which the non-dynamical correlation is important, a sum of a few determinants has proven to be useful.

In our approach, another type of trial wave function, the FSGO-SGG-type trial wave function, was introduced. The FSGO-SGG-type trial wave function (φ_F) for ab N-electron system is a linear combination of many-configuration wave functions. The configuration wave function taking care of a two-electron correlation between the two electrons occupied the spin-orbitals of i_1 and i_2, respectively, can be read as

$$\psi_{i_1,i_2} = b_{i_1,i_2} \sum_{1 \le j_1 < j_2 \le N} \phi_{i_1,i_2}(j_1,j_2) \times \tilde{\phi}_{i_1,i_2}(j_1,j_2) \times g_{i_1,i_2}(j_1,j_2),$$

in which b_{i_1,i_2} is the coefficient, (j_1, j_2) is the electron pair in the two spin-orbitals, i_1 and i_2, $\phi_{i_1,i_2}(j_1, j_2)$ is the 2×2 sub-matrix of ϕ that lies on the intersection of rows i_1 and i_2 with columns j_1 and j_2, and $\tilde{\phi}_{i_1,i_2}(j_1, j_2)$ is the signed minor determinant of ϕ in which the rows i_1 and i_2 and columns j_1 and j_2 are deleted from ϕ. The ϕ is a Slater determinant constructed from spin-orbital that is a product of spatial orbital based on the FSGOs and an electron spin eigenfunction. Each configuration wave function correlates different pair of spin-orbitals, thus the nature and the FSGOs of ϕ for different configuration wave function might be different. The correlation term, $g_{i_1,i_2}(j_1, j_2)$, being an expansion of the SGGs that is symmetric with respect to the exchange of two electrons might be different for different configuration wave functions. With the independent particle wave function, ψ_0, the FSGO-SGG-type trial wave function for a N-electron system can be written as $\varphi_F = \psi_0 + \sum_{1 \le i_1 < i_2 \le N} \psi_{i_1,i_2}$.

For the independent particle wave function, the basis set of the 1s orbital of hydrogen is an expansion of six spherical Gaussian orbitals proposed by Stewart *(11)*, and the basis set for atoms except hydrogen is taken from the well-tempered Gaussian-type-function basis set of (14s9p) of Huzinaga and Klobukowski *(12)*. The 2p-type functions are expanded by a linear combination of two spherical Gaussians referred to as the lobe functions proposed by Whitten *(13)* in which the two spherical Gaussians are located at different points in space in order to give the proper orbital symmetry. In the optimization of ψ_0, all spherical Gaussians are allowed to adjust their positions and sizes. For the correlated state configuration wave function, ψ_{i_1,i_2}, the determinant parts are constructed from the 1s and 2s orbitals that are expanded by 3 spherical Gaussian orbitals proposed by Stewart *(11)*, and as well the 2p orbital that is expanded in two lobe functions proposed by Whitten *(13)*. The correlation part, $g_{i_1,i_2}(j_1, j_2)$, is a linear combination of six SGGs.

An evaluation of matrix elements over configurations results in many-electron integrals, and formulas for closed form evaluation of them have been given earlier *(14,15)*. We make use of the quasi-Newton technique *(16)* with analytical first energy derivatives to optimize the variational parameters of ψ_0. The SIMPLEX technique *(17)* that requires the functional values only is used to optimize the variational parameters of ψ_{i_1,i_2}. To simplify the task of

Downloaded by UNIV OF GUELPH LIBRARY on July 4, 2012 | http://pubs.acs.org
Publication Date: December 31, 2006 | doi: 10.1021/bk-2007-0953.ch003

optimization of trial wave functions, we optimized one configuration wave function at a time. After finishing the optimization of all configuration wave functions, we repeated the procedure again. It usually took five or six steps to obtain a converged trial wave function. In practical calculation here, however, we dropped the configuration with a weight of less than 0.0001 to reduce the number of configuration state functions to save the computational demanding.

The FSGO-SGG-type trial wave function has some characteristics interested. Firstly, it has a MCSCF-like expansion but the correlated configuration wave function has a freedom in choosing basis functions. The correlated configuration wave function is not constructed from a simple replacement of one or two spin-orbitals of the independent particle wave function. Secondly, it describes bonding and lone-pair electrons more efficiently than an atom-centered basis functions. Thirdly, it gives an analytical energy functional although a very complicated one. This offers an opportunity in the optimization of trial wave function by means of deterministic approaches in addition to Monte Carlo optimization techniques. Fourthly it takes the difference in the correlation strength between two electrons occupying different paris of spin-orbitals into account in construction of trial wave function. Fifthly, it enables the OU procedure in the DQMC simulations. This is described in the appendix.

Downloaded by UNIV OF GUELPH LIBRARY on July 4, 2012 | http://pubs.acs.org
Publication Date: December 31, 2006 | doi: 10.1021/bk-2007-0953.ch003

Diffusion quantum Monte Carlo

The imaginary time Schrödinger equation implemented with the importance sampling technique with a trial wave function, φ_F, appears as a diffusion-drift equation with branching term as *(18)*

$$\frac{\partial f}{\partial t} = \frac{1}{2}\nabla^2 f - \vec{\nabla}(f\vec{\nabla}\ln|\varphi_F|) - (\frac{\hat{H}\varphi_F}{\varphi_F} - E_T)f,$$

where $f(R,t)$ is a product of the trial wave function and the exact solution of Schrödinger equation within the fixed-node approximation, E_T is the reference energy adjusted in the simulation process, and $\hat{H}$ is the usual Hamiltonian operator. The ground-state energy can then be obtained as an average value of the local energies, $\hat{H}\varphi_F / \varphi_F$. The first two terms and the third term of $\partial f / \partial t$ in this equation are simulated, respectively, by the OU process while using the FSGO-SGG-type trial wave function and by the technique of cumulated weights proposed by East et al. *(19)* The details about the OU random walks are given in the appendix.

A cut-off term for the local energies as suggested by DePasquale et al. *(20)* was used to control the branching of the random walkers in the Monte Carlo simulation. For $| E_L(R) - E_V | \geq \frac{2}{\sqrt{\tau}}$, one uses

$$E_L(R) = E_V + sign[\frac{2}{\sqrt{\tau}}, E_L(R) - E_V],$$

and the branching factor is taken to be

$$\begin{aligned} b(R,R') &= \exp\{-\tau \frac{[E_L(R) + E_L(R')]}{2} + \tau \cdot E_T\} \\ &\approx 1 - \tau \frac{[E_L(R) + E_L(R')]}{2} + \tau \cdot E_T \end{aligned}$$

In which E_V and E_T are the variational energy of the trial wave function and the reference energy adjusted in the propagation, respectively; R and R' are the last and present positions of random walkers, respectively. A small size of time step of 0.0002 a.u. was used to avoid a zero size of time-step extrapolation. In order to make accurate comparisons with experiment, the all-electron OUDQMC/FSGO-SGG computations were performed for sufficiently long time to yield statistical error bars less than 0.01 kcal/mol for electronic energies and less than 10^{-4} hartree/bohr for energy gradients.

Geometry optimization

Accurate and efficient calculation of energy gradient with regard to geometrical parameters is a basic requirement for a modern electronic structure theory to be one of the mainstream approaches in the field of quantum chemistry. In the development of DQMC, the finite difference technique is a useful method to determine energy gradient. For a D-dimensional system, the computational requirement is at least D+1 times of single Monte Carlo calculation. This prevents the finite difference technique from implementing into DQMC for a large system. The other choice is to implement the Hellmann-Feynman (H-F)

Downloaded by UNIV OF GUELPH LIBRARY on July 4, 2012 | http://pubs.acs.org
Publication Date: December 31, 2006 | doi: 10.1021/bk-2007-0953.ch003

theorem in the DQMC simulation. However, there was a big challenge in accurate calculation of H-F energy gradient in DQMC. Difficulty of the calculated variances growing rapidly arises in the direct evaluation of H-F energy gradients in the Monte Carlo simulation due to terms involving the third order of the reciprocal of electron-nuclear distances, $1/r_{i\alpha}^3$ *(2)*. In order to avoid the problem related to the infinite variance of the H–F force estimator, a renormalized technique suggested by Assaraf and Caffarel was used to modify the H–F force estimator *(21)*. For a particular component q, the renormalized expression is

$$\overline{F}(q) = \bar{F}(q) + [\frac{\overline{H}\overline{\varphi}_F}{\overline{\varphi}_F} - \frac{\overline{H}\varphi_F}{\varphi_F}]\frac{\overline{\varphi}_F}{\varphi_F},$$

where $\overline{H}$ is some rather arbitrary Hermitian operators and $\overline{\varphi}_F$ an arbitrary auxiliary wave function (supposed to be square-integrable). The auxiliary function for a diatomic molecule having N electrons considered here is introduced as

$$\overline{\varphi}_F(x_A) = \varphi_F \times Z_A \sum_{i=1}^{N} \frac{(x_i - X_A)}{\left|\vec{r}_i - \vec{R}_A\right|},$$

to remove the infinite variance in the X-component of the H-F energy gradient exerted on the atom A whose location and charge are $\vec{R}_A$ and Z_A, respectively.

In the geometry optimization procedure, the search direction was chosen using the quasi-Newton method implemented with the Broyden-Fletcher-Goldfarb-Shanno (BFGS) Hessian updating formula *(16)* based on the renormalized H-F VMC energy gradients and the FN-DQMC electronic energies. The systems studied in this work are diatomic molecules, so the degree of freedom involved is one. Hence, after a simple arithmetic, the updating formula for geometry in an one-dimensional case can be rewritten as $x_{k+1} = x_k - g_k/H_k = x_k - g_k \times (x_k - x_{k-1})/(g_k - g_{k-1})$, in which k is the step and x, g, and H are the coordinate, gradient, and Hessian, respectively.

The trial wave functions for geometries other than the initial geometry in the geometry optimization procedure have the same parameters as the initial one but

Downloaded by UNIV OF GUELPH LIBRARY on July 4, 2012 | http://pubs.acs.org
Publication Date: December 31, 2006 | doi: 10.1021/bk-2007-0953.ch003

Downloaded by UNIV OF GUELPH LIBRARY on July 4, 2012 | http://pubs.acs.org
Publication Date: December 31, 2006 | doi: 10.1021/bk-2007-0953.ch003

the coordinates are relative to the new nuclear positions. A self-consistent field procedure with a convergence criterion of 10^{-8} with regard to changes in the density matrix is then used to obtain the coefficients of spherical Gaussians constructing determinants for every configuration wave function while keeping other parameters frozen. Finally, the coefficients of all configuration wave functions were obtained by solving a Secular equation about all configuration wave functions.

The harmonic frequency at the stationary molecular geometry was calculated from the renormalized H-F DQMC energy gradient *(21)*

$$\tilde{F}^{DQMC}(q) = \tilde{F}^{VMC}(q) + [E_L - < E_L >][w - < w >]$$

in which $w \equiv \overline{\varphi}_F / \varphi_F$, based on the second-order approximation *(22)*

$$< \hat{F} >_{EXACT} \approx < \hat{F} >_{SOA} = 2 < \hat{F} >_{DQMC} - < \hat{F} >_{VMC} .$$

To obtain reliable results, the Monte Carlo simulations in the determination of harmonic frequencies were performed sufficiently long to reduce the statistical uncertainties of energy gradient and electronic energy to less than 10^{-6} hartree/bohr and 10^{-8} hartree, respectively.

The elements of the Hessian, h_{ij}, are obtained from the difference of the two energy derivatives ($\vec{F}_i$) and the step size (Δ_j) based on the central finite-difference approximation,

$$h_{ij} = \frac{1}{2}\left[\frac{(\vec{F}_i)_{+0.5\Delta_j} - (\vec{F}_i)_{-0.5\Delta_j}}{\Delta_j} + \frac{(\vec{F}_j)_{+0.5\Delta_i} - (\vec{F}_j)_{-0.5\Delta_i}}{\Delta_i}\right]$$

to reduce the errors that occur in the calculation of the energy gradient.

Calculated results and discussion

We constructed the FSGO-SGG-type trial wave function at the B3LYP/aug-cc-pVDZ calculated geometries for all diatomic radicals. In search of the equilibrium bond lengths, we also constrained one atom on the origin and the other atom on the positive X-axis. The B3LYP/aug-cc-pVDZ, BD(TQ)/cc-pVQZ and CCSD(T)/cc-pVQZ calculations were carried out by the Gaussian 03 program *(23)*.

Table I lists the experimental values of equilibrium bond lengths taken from the literature (24-26) and the calculated values from the OUDQMC/FSGO-SGG, BD(TQ)/cc-pVQZ, and CCSD(T)/cc-pVQZ calculations. Comparing the experimental values, the OUDQMC/FSGO-SGG calculation gives the absolute mean deviations of 0.0019 Å compared with the results from BD(TQ)/cc-pVQZ and CCSD(T)/cc-pVQZ calculations, 0.0021 Å and 0.0025 Å, respectively.

Table II lists the experimental values of harmonic frequencies taken from the literatures (24,27,28) and the calculated values from the OUDQMC/FSGO-SGG, BD(TQ)/cc-pVQZ, and CCSD(T)/cc-pVQZ calculations. Comparing the experimental values, the OUDQMC/FSGO-SGG calculation gives the absolute mean deviations of 18 cm^{-1} compared with the results from BD(TQ)/cc-pVQZ and CCSD(T)/cc-pVQZ calculations, 21 cm^{-1} and 43 cm^{-1}, respectively.

The Monte Carlo calculation gave a high quality in the determination of equilibrium bond lengths and harmonic frequencies for the 12 doublet radicals that is consistent with a sophisticated BD(TQ)/cc-pVQZ calculation that used a large basis set and added triples and quadruples contributions to a Brueckner Doubles. Considering the Monte Carlo approach has a better scaling behavior relative to the BD(TQ) and CCSD(T) calculations, our study demonstrated the competence of the random walk based approach for open-shell radicals.

Downloaded by UNIV OF GUELPH LIBRARY on July 4, 2012 | http://pubs.acs.org
Publication Date: December 31, 2006 | doi: 10.1021/bk-2007-0953.ch003

Acknowledgments

Acknowledgment is made to the donors of The American Chemical Society Petroleum Research Fund for partial support of this research. The author also thanks the National Science Council, Taiwan (Grant No. NSC 93-2113-M-242-004 and 94-2113-M-242-002) for financial support and the molecular simulation laboratory at Fooyin University and the National Center for High-performance Computing, Taiwan, for a huge amount of computer time.

Appendix

Consider a one-dimensional random walk under an harmonic velocity field generated by one spherical Gaussian function, the corresponding Fokker-Planck equation is obtained by a simple arithmetic,

$$\frac{\partial f}{\partial \tau}=\frac{1}{2}\frac{\partial^2 f}{\partial x^2}+2\alpha\frac{\partial}{\partial x}(x\cdot f), \tag{A1}$$

in which f is a product of the trial wave function, φ_F, and the exact ground-state wave function. This equation that is the Fokker-Planck equation for one variable for an Ornstein-Uhlenbeck process describes a Brownian motion under an external harmonic velocityfield with a force constant 2α *(29)*. There is an analytical solution for this simple equation,

$$f(x_0,x,t)=[\frac{2\alpha}{\pi(1-e^{-4\alpha t})}]^{\frac{1}{2}}\exp[-2\alpha\frac{(x-x_0e^{-2\alpha t})^2}{(1-e^{-4\alpha t})}].$$

This analytical solution gives the time-dependent behavior of averages of x and x^2 for the random walkers under an external harmonic velocity field with a force constant 2α,

$$<x_t>=x_0e^{-2\alpha t} \tag{A2}$$

and

$$<x_t^2>=\frac{1}{4\alpha}+(x_0^2-\frac{1}{4\alpha})e^{-4\alpha t}. \tag{A3}$$

Therefore, it is not necessary to implement a Monte Carlo procedure to simulate the behavior of particles under this situation.

However, for a more complex system, there is no analytical solution to the corresponding Fokker-Planck equation. To describe time-dependent behavior of particles in a more complex velocity fileds, a Monte Carlo scheme is a powerful strategy. In conventional DQMC simulation, the Langevin-based approach was implemented and gave many accurate calculated values *(2)*. In our approach, we proposed an alternative. Consider the one-dimensional case, we design a Markov procedure, $x_{k+1}=ax_k+g_k\sigma$, in which a and σ are parameters depending on the positions of random walkers, g_k is a Gaussian random number with mean of zero and variance of one, and k and $k+1$ are two successive steps in the simulation. Repeating this Markov procedure after n steps leads to the averages of x and x^2 for the random walkers,

Downloaded by UNIV OF GUELPH LIBRARY on July 4, 2012 | http://pubs.acs.org
Publication Date: December 31, 2006 | doi: 10.1021/bk-2007-0953.ch003

$$<x_n>=x_0 a^n \tag{A4}$$

and

$$<x_n^2>=\frac{\sigma^2}{1-a^2}+a^{2n}(x_0^2-\frac{\sigma^2}{1-a^2}). \tag{A5}$$

After a comparison between Eqs. (A2) and A(3) and Eqs. (A4) and A(5), the analytical solution and our Markov procedure give the same average values of x and x^2, while the two conditions in which δ is the size of time step satified:

$$a=e^{-2\alpha\delta} \text{ and } \sigma^2=\frac{1-a^2}{4\alpha}.$$

Hence, we can use this simple Markov procedure, to simulate the Fokker-Planck equation without splitting the diffusion and drift parts. For a more complex system, there is no analytical solution, however, a similar Markov algorithm can also be used to describe the corresponding Fokker-Planck equation for a complex system.

Now, we took the ground state of H_2^+ molecule as an example to illustrate how to implement the Markov procedure to DQMC simulation. There is only one electron in this simple system. We write the trial wave function as a sum of two spherical Gaussians located at the two hydrogen atoms, $\varphi_F=\chi_A(1)+\chi_B(1)$. Hence, the harmonic velocity fields generated by this simple trial wave function have the following form,

$$\begin{aligned}\frac{\nabla\varphi_F}{\varphi_F}&=\frac{\nabla\chi_A(1)+\nabla\chi_B(1)}{\chi_A(1)+\chi_B(1)}\\&=\frac{\chi_A(1)\nabla\ln\chi_A(1)+\chi_B(1)\nabla\chi_B(1)}{\chi_A(1)+\chi_B(1)}\\&=\frac{\chi_A(1)}{\chi_A(1)+\chi_B(1)}\nabla\ln\chi_A(1)+\frac{\chi_B(1)}{\chi_A(1)+\chi_B(1)}\nabla\ln\chi_B(1)\end{aligned}.$$

This equation has two harmonic velocity fields located on the two hydrogen atoms. Random walker chooses one of the two harmonic velocity fields according to a probability proportional to the prefactor of each harmonic velocity field.

Downloaded by UNIV OF GUELPH LIBRARY on July 4, 2012 | http://pubs.acs.org
Publication Date: December 31, 2006 | doi: 10.1021/bk-2007-0953.ch003

For a more complex system, there are many harmonic velocity fileds generated by a trial wave function constructed by spherical Gaussians. Random walker chooses one of the harmonic velocity fields according to a probability proportional to the prefactor of each harmonic velocity field. The key to enable OU random walkers in DQMC simulation is a trial wave function constructed by spherical Gaussians. The basis functions used to construct the FSGO-SGG-type trial wave function are spherical Gaussians.

Table I. Absolute mean deviations in calculated equilibrium bond distances (in Å) of OUDQMC, BD(TQ) and CCSD(T) methods relative to experimental values.

Molecule	Expt.[a]	OUDQMC[b]	BD(TQ)/cc-pVQZ	CCSD(T)/cc-pVQZ
CH	1.1199	1.1202(3)	1.1204	1.1199
OH	0.9697	0.9697(5)	0.9697	0.9697
FH^+	1.001	1.0013(6)	1.0003	1.0004
BO	1.205	1.2069(6)	1.2060	1.2082
CN	1.1718	1.1730(4)	1.1733	1.1702
CO^+	1.1283	1.1222(5)	1.1154	1.1146
N_2^+	1.11642	1.1176(5)	1.1176	1.1185
CF	1.272	1.2727(7)	1.2727	1.2749
NO	1.1508	1.1512(5)	1.1512	1.1499
O_2^+	1.1164	1.1170(7)	1.1170	1.1169
OF	1.354[c]	1.3492(8)	1.3526	1.3520
F_2^+	1.305[d]	1.3099(7)	1.3099	1.3078
Absolute mean deviation		0.0019	0.0021	0.0025

a: Reference 24.

b: Reference 10.

c: Reference 25.

d: Reference 26.

Downloaded by UNIV OF GUELPH LIBRARY on July 4, 2012 | http://pubs.acs.org
Publication Date: December 31, 2006 | doi: 10.1021/bk-2007-0953.ch003

Table II. Absolute mean deviations in calculated harmonic frequencies (in cm^{-1}) of OUDQMC, BD(TQ) and CCSD(T) methods relative to experimental values.

Molecule	Expt.	OUDQMC[a]	BD(TQ)/cc-pVQZ	CCSD(T)/cc-pVQZ
CH	2859[b]	2853(8)	2852	2857
OH	3738[c]	3750(12)	3748	3749
FH^+	3090[d]	3126(18)	3121	3119
BO	1886[d]	1906(16)	1908	1889
CN	2069[c]	2082(19)	2081	2126
CO^+	2170[c]	2218(17)	2244	2291
N_2^+	2207[d]	2212(20)	2212	2211
CF	1308[d]	1324(18)	1324	1311
NO	1904[c]	1922(21)	1932	2106
O_2^+	1905[c]	1928(22)	1931	1933
OF	1053[d]	1067(19)	1067	1089
F_2^+	1104[b]	1109(22)	1109	1120
Absolute mean deviation		18	21	43

a: Reference 10.

b: Reference 24.

c: Reference 27.

d: Reference 28.

Downloaded by UNIV OF GUELPH LIBRARY on July 4, 2012 | http://pubs.acs.org
Publication Date: December 31, 2006 | doi: 10.1021/bk-2007-0953.ch003

References

1. Beran, G. J. O.; Gwaltney, S. R.; Head-Gordon, M. *Phys. Chem. Chem. Phys.* **2003,** *5,* 2488.
2. Hammond, B. L.; Lester, W. A.; Reynolds, P. J. *Monte Carlo Methods in Ab Initio Quantum Chemistry;* World Scientific: Singapore, 1994.
3. Lüchow, A.; Anderson, J. B. *Annu. Rev. Phys. Chem.* **2000,** *51,* 501.
4. Foulkes, W, M. C.; Mitas, L; Needs, R. J.; Rajagopal G. *Rev. Mod. Phys.* **2001,** *73,* 33.
5. Aspuru-Guzik, A.; Lester, W. A. In *Handbook of Numerical Analysis: Computational Chemistry*; Ciarlet P. G.; LeBris C., Eds.; North Holland: Amsterdam, 2003, Vol. 10, pp 485.
6. Leu, S. Y; Mou, C. Y *J. Chem. Phys.* **1994,** *101,* 5910.
7. Lu, S. -I. *J. Chem. Phys.* **2001,** *114,* 3898.
8. Lu, S. -I. *J. Chem. Phys.* **2004,** *120,* 14.
9. Lu, S. -I. *J. Chem. Phys.* **2004,** *120,* 3185.
10. Lu, S. -I. *J. Chem. Phys.* **2005,** *123,* 074104.
11. Stewart, R. F. *J. Chem. Phys.* **1970,** *52,* 431.
12. [Huzinaga S.; Klobukowski M. *Can. J. Chem.* **1985,** *63,* 1812.
13. Whitten, J. L. *J. Chem. Phys.* **1963,** *39,* 349.

14. Boys, S. F. *Proc. R. Soc. London Ser. A* **1960,** *258,* 402.
15. Karunakaran K. M.; Christoffersen R. E. *Int. J. Quantum Chem.* **1982,** *22,* 1.
16. Dennis, J. E.; Schnabel, R. B. *Numerical Methods for Unconstrained Optimization and Nonlinear Equations;* Prentice Hall, Inc.: NJ, 1983.
17. Press, W. H.; Flanery, B. P.; Teukowsky, S. A.; Vetterling, W. T. *Numerical Recipes;* Cambridge University Press: Cambridge, 1986.
18. Reynolds, P.J.; Ceperley, D.M.; Alder, B.J.; Lester, W.A. *J. Chem. Phys.* **1982,** *77,* 5593.
19. East, A. L. L.; Rothstein, S. M.; Vrbik, J. *J. Chem. Phys.* **1988,** *89,* 4880.
20. DePasquale, M. F.; Rothstein, S. M.; Vrbik, J. *J. Chem. Phys.* **1988,** *89,* 3629.
21. Assaraf R.; Caffarel, M. *J. Chem. Phys.* **2000,** *113,* 4028.
22. Ceperley, D. M.; Kalos, M. H. in *Monte Carlo Methods in Statistical Physics*, Binder, K., Ed.; Springer: Berlin, 1979, pp 145–194.
23. Gaussian 03, Revision C.02, Frisch, M. J.; Trucks, G. W.; Schlegel, H. B. et al. Gaussian Inc., Wallingford CT, 2004.
24. Huber, K. P.; Herzberg, G. *Molecular Spectra and Molecular Structure. IV. Constants of Diatomic Molecules*; Van Nostrand: NY, 1979.
25. Burkholder, J. B.; Hammer, P. D.; Howard, C. J.; McKellar, A. R. W. *J. Mol. Spectrosc.* **1986,** *118,* 471.
26. Tuckett, R. P.; Dale, A. R.; Jaffey, D. M.; Jarrett, P. S.; Kelly, T. *Mol. Phys.* **1983,** *49,* 475.
27. Cormack, A. J.; Yencha, A. J.; Donovan, R. J.; Lawley, K. P.; Hopkirk, A.; King, G. C. *Chem. Phys.* **1996,** *213,* 439.
28. Herzberg, G. *Molecular Spectra and Molecular Structure. I. Constants of Diatomic Molecules*, 2nd ed.; Van Nostrand: NY, 1950.
29. Risken, H. *The Fokker-Planck Equation*, 2nd ed.; Springer-Verlag: Berlin, 1996.

Downloaded by UNIV OF GUELPH LIBRARY on July 4, 2012 | http://pubs.acs.org
Publication Date: December 31, 2006 | doi: 10.1021/bk-2007-0953.ch003

Chapter 4

Rydberg States with Quantum Monte Carlo

Annika Bande and Arne Lüchow

**Institut für Physikalische Chemie, RWTH Aachen University,
52056 Aachen, Germany**

Calculations on Rydberg states are performed using quantum Monte Carlo methods. Excitation energies and singlet-triplet splittings are calculated for the carbon atom. Wave functions constructed from open-shell localized Hartree-Fock orbitals are used as trial and guide functions. The fixed-node diffusion quantum Monte Carlo (FN-DMC) method depends strongly on the wave function's nodal hypersurface. The nodal regions confined by antisymmetry, excitation, and spurious nodes are investigated for selected cases. Their effect on the FN-DMC calculations is analyzed and a novel approach for excited states calculations with FN-DMC is proposed.

In Advances in Quantum Monte Carlo; Anderson, J., et al.;
ACS Symposium Series; American Chemical Society: Washington, DC, 2006.

Electronic structure quantum Monte Carlo methods (QMC) are versatile and applicable to atoms and molecules of single-reference or multi-reference character, strong and weak interactions, as well as ground and excited states. The accurate calculation of excitation energies usually requires a method that accounts for the correlation energy because the correlation energy is generally smaller in the excited than in the ground state. The calculation of excited states with QMC is straightforward, but a few new features arise. In this paper, the calculation of Rydberg states with fixed-node diffusion quantum Monte Carlo (FN-DMC) and variational quantum Monte Carlo (VMC) is demonstrated for the carbon atom. Furthermore, we perform a topological analysis of the wave functions with the purpose of properly describing the Rydberg states' electron distributions with FN-DMC.

The emphasis of this work is on using simple guide or trial wave functions that allow one to keep the favorable scaling of the QMC methods for Rydberg state calculations. To this end, we use one- or two-determinant guide functions whereas most excited state calculations require a multi-determinant ansatz. If one- or two-determinant functions are to be sufficient, the orbitals, and in particular the Rydberg orbitals, need to be accurate. Kohn-Sham orbitals of the open-shell localized Hartree-Fock method (OSLHF) by Görling and Della Sala (*1-7*) are used here, since Hartree-Fock or standard DFT orbitals are generally not suitable as Rydberg orbitals. This work extends a previous study of Rydberg states where VMC and DMC were used with OSLHF orbitals to calculate atoms and molecules (*8,9*).

The fixed-node diffusion quantum Monte Carlo method (FN-DMC) is predominantly discussed here. In this approach, the energy is calculated in regions defined by the nodal hypersurface of the guide function. While the regions of the ground state are due to antisymmetry nodes and thus equivalent, non-equivalent regions arising from excitation nodes are found in excited states. In general they yield different energies, and the correct calculation of excitation energies from regional energies is not obvious. For approximate wave functions it has recently been demonstrated that non-equivalent regions and energies can even occur in the ground state due to spurious nodes arising from limited basis sets (*10,11*). These nodal artefacts have first been observed for H_2 by Barnett et al. (*12*).

While excited state calculations with QMC have been considered as early as 20 years ago (*13-16*), several applications of QMC methods to excited states of small molecules have appeared in the last few years (*17-22*). The exact nodal structure of the wave function has been the focus of only a few papers (*23-26*). In this work, we analyze the wave function's nodal structure with respect to antisymmetry, excitation, and spurious nodes for singlet (^1P) and triplet (^3P) carbon Rydberg states with the configuration $2s^22pns$ (with $n = 3 - 6$) and the ground state. We discuss the effect of non-equivalent nodal regions on the FN-DMC energies.

Quantum Monte Carlo Methods for Rydberg States

Both the FN-DMC and the VMC methods are described in detail elsewhere (*27*) and will be discussed here only briefly. In the VMC method, the energy is calculated from the Rayleigh-Ritz quotient using Monte Carlo integration and Metropolis sampling:

$$E_R[\Psi_T] = \int E_L(r)\frac{\Psi_T(r)^2}{\int \Psi_T(r)^2 d\tau} d\tau = \langle E_L(r) \rangle \tag{1}$$

with the local energy $E_L(\mathbf{r}) = \Psi_T(\mathbf{r})^{-1} H \Psi_T(\mathbf{r})$. The trial wave function $\Psi_T = \Sigma_i a_i \Phi_i^{(SD)} e^U$ consists of one or more Slater determinants $\Phi_i^{(SD)}$ and a positive symmetric correlation or Jastrow factor e^U. The all-electron fixed-node diffusion quantum Monte Carlo calculations are carried out using the VMC trial function as a guide function Ψ_G in importance sampling. Branching and weighting is done as suggested by Umrigar et al. (*28*). The energy is calculated with the mixed estimator (*28,29*).

Formally, fixed-node DMC solves (numerically) exactly the electronic Schrödinger equation with the nodes of Ψ_G as additional boundary condition:

$$\begin{aligned} H\Psi_0^{(j)}(r) &= E_0^{(j)}(r)\Psi_0^{(j)}(r) \quad \text{for } r \in \Omega_j \\ \text{and} \quad \Psi_0^{(j)}(r) &= 0 \quad \text{for } r \notin \Omega_j \end{aligned} \tag{2}$$

The Hamiltonian is defined in $\mathbb{R}^{3N}$ for an N-electron system. The $3N$-1 dimensional nodal hypersurface given by Ψ_G=0 partitions $\mathbb{R}^{3N}$ in K regions Ω_j, $j = 1...K$ that are defined as disjoint connected open sets (with either $\Psi > 0$ or $\Psi < 0$). Two regions are considered equivalent if they are related by an electron permutation. A unique FN-DMC solution exists only if all regions Ω_j yield the same ground state energy $E_0^{(j)}$ from $H \Psi^{(j)} = E^{(j)} \Psi^{(j)}$. Particularly important is Ceperley's proof of the tiling theorem (*23*), which says that for the exact ground state all Ω_j are equal in shape and size and are related by electron exchange. In this case, a FN-DMC calculation can be started with walkers either in one region or in many regions. All calculations would yield statistically the same energy. Not every approximate ground state function has only equivalent regions, and we denote the additional regions "spurious" as they are due to spurious nodes that eventually vanish as the guide function converges toward the exact wave function. Non-equivalent regions even in exact wave functions are expected for excited states. They arise from excitation nodes. The non-equivalent regions necessarily yield the same energy if the nodes are exact, but in general different regional energies $E_0^{(j)}$ are obtained if the nodal hypersurface is only approximate.

In the case of different regional energies $E_0^{(j)}$, FN-DMC is in principle capable of determining all $E_0^{(j)}$ by starting the calculation with walkers in region Ω_j only. The standard FN-DMC calculation starts with walkers distributed over all space. In this case, the lowest energy of all regions initially populated is obtained: $E_0^{(FN)} = \min_j E_0^{(j)}$.

The excitation nodes of atomic Rydberg states are easier to rationalize than other excitation nodes. If the nodes are defined by a Slater determinant and one electron has a much larger distance from the nucleus than the others (the "Rydberg electron"), the Slater determinant can be factorized approximately into the Rydberg orbital and a Slater determinant of the other electrons by using Laplace's expansion:

$$\Psi_N \approx \Psi_{N-1}\phi_{Ryd}(N) \tag{3}$$

The excitation nodes can thus be described at least approximately by the nodes of the orbital ϕ_{Ryd} which is of s-type for the carbon Rydberg states considered here.

The Rydberg excitation energies into the ^1P and ^3P 2p*n*s states of the carbon atom (with $n = 3 - 6$) and the singlet-triplet splittings were calculated using the variational and the diffusion Monte Carlo algorithms of the program amolqc by the authors (*30*).

The Jastrow factors applied in the VMC calculations were indeed variationally optimized for all the states, but to minimize the error introduced by different Jastrow parameters all the excited states were calculated using both an optimized singlet and an optimized triplet Jastrow factor. Excited state energies are then represented as the mean value from the two VMC energies, singlet-triplet splittings are evaluated for triplet and singlet states with the same Jastrow parameters and then averaged. Large steps with low acceptance ratios were employed to improve the spatial sampling when one electron has a large distance to the nucleus.

Furthermore we performed a regional analysis. Based on prior work (*8,9*) DMC runs were performed using an initial walker that is known to force the calculation to come out with a higher energy than the expected $E_0^{(j)}$. In every step the geometrical data of the walkers are collected and analyzed after a certain interval (here: every 25 blocks of 250). It turned out to be most meaningful to characterize nodal regions Ω_j by their energy $E_0^{(j)}$ and the mean distances $\langle r \rangle$ of all the electrons. A similar distance analysis has been done previously by Glauser et al. for atomic ground states (*24*).

To answer the question about the significance of these different regions in excited state FN-DMC calculations, a natural way to calculate the FN-DMC energy for excited states is to weight the regional energies $E_0^{(j)}$ according to Ψ^2. We sample this walker distribution in a VMC calculation with 50 random walkers using an initial walker at a certain distance. Subsequently 50 DMC calculations were performed using the final walker positions from VMC as initial walker positions each for one calculation. It should be noted that long runs were required to obtain converged VMC results for the excited states. We are not aware of any excited state calculation that has been done in this fashion, so we denote this novel procedure here FN-DMC(n) to distinguish it from the standard method, designated here FN-DMC(s). By default the initial walker ensemble in FN-DMC(s) is distributed according to Ψ^2, where thus most regions Ω_j are initially populated. The weighting or branching process in DMC results in the decay of the walker population in all high energy regions. Therefore, the final FN-DMC result is $\Psi_0^{(1)}$ with $E_0^{(1)}$ (assuming regions ordered with increasing energy) if Ω_1 is initially populated. This procedure may lead to unsatisfactory results if Ω_1 is not one of the most probable regions.

Computational Details

In the FN-DMC calculations $5 \cdot 10^8$ random walk steps were made with a time step of 0.003 a.u. For VMC we employed $4 \cdot 10^8$ random walk steps. The Jastrow parameters were variationally optimized for each state under consideration. Each state was calculated at least five times for both methods to obtain statistically independent data.

The wave functions used in all calculations were derived previously (*8,9*). The OSLHF calculations (*6,31*) were performed using a special version of the program package Turbomole (*32-36*). The Lee-Yang-Parr (LYP) (*37*) correlation functional was employed.

As basis set we used a modified version of the Dunning cc-pVTZ basis (*38,39*) augmented with several diffuse functions (*9*). To correct for the missing electron nucleus cusp of contracted GTOs a method of one of the authors was used (*30*).

The singlet state requires two determinants constructed from OSLHF Kohn-Sham orbitals, for the triplet we calculated the $M_S = 1$ state with one determinant. The trial and guide functions are products of these configuration state functions and variance optimized Schmidt-Moskowitz Jastrow factors of the nine-term type (*40*).

Results and Discussion

The excitations of the carbon atom into the four lowest ^3P and ^1P Rydberg states with the electron configuration 2p*n*s (with $n = 3 - 6$) have been calculated with VMC and FN-DMC.

In our previous calculations (*9*) the excitation energies and singlet-triplet splittings have been obtained in very good agreement with experimental data, but the FN-DMC splittings have been found qualitatively wrong for several electron configurations.

The VMC results indicated that the OSLHF wave function extended by a Schmidt-Moskowitz Jastrow factor is entirely suitable for Rydberg excited states. It appeared that the main difficulty was the nodal structure of excited state wave functions.

Nodal Regions of the Carbon Atom

For the Rydberg states of the carbon atom we have to consider excitation nodes as well as nodal artefacts. The latter have been found by Hachmann et al. in Hartree-Fock wave functions of Be and Be^{2+} to be dependent on the size and flexibility of the basis set (*10,11*).

We attempted to better understand the OSLHF wave function of the ^3P ground state, denoted here G, and the highly excited states ^3P (2p6s), here T4, and ^1P (2p6s), S4, by characterizing their nodal regions Ω_j as described before. The Tables I to III display examples of different regions Ω_j.

In all three cases the region lowest in energy (Ω_1) is the one in which the electrons are closest to the nucleus. Note that in S4 the electrons are all at the same mean distance demonstrating the possible exchange of “core” and “valence” electrons. *Per contra* the two down-spin electrons (5 and 6) in the triplet states are separated by a node (in this case exactly $r_5 = r_6$, because the spin down electrons occupy 1s and 2s orbitals only (*41*)).

For the two excited states S4 and T4, the regions Ω_2 to Ω_4 are characterized by one large average electron-nucleus distance. The distances are very similar for the singlet and the triplet state and can be understood well when evaluating the excitation nodes according to Eq. 3. The radial distribution functions $p(r) = 4\pi r^2 \phi_{6s}(r)^2$ for the OSLHF 6s orbitals are shown in Figure 1 for the S4 and T4 states.

Table I. Nodal regions of the ^3P ground state (G)

Ω_j	$E_0^{(j)}$	$\langle r_1\rangle$	$\langle r_2\rangle$	$\langle r_3\rangle$	$\langle r_4\rangle$	$\langle \bar{r}_5\rangle$	$\langle \bar{r}_6\rangle$
Ω_1	-37.8301(4)	1.4	1.4	1.4	1.4	1.6	0.3
Ω_2	-37.4161(9)	47	1.2	1.2	1.2	1.6	0.3
Ω_3	-37.1368(5)	1.3	1.3	1.3	1.3	24	0.3
Ω_4	-34.837(1)	44	43	26	0.3	1.4	0.3
Ω_5	-26.3212(6)	1.1	1.1	1.1	1.1	24	2.2

NOTE: Regional energies are given in E_h, electron-nucleus distances $\langle r\rangle$ for up-spin and $\langle \bar{r}\rangle$ for down-spin electrons in bohr.

Table II. Nodal regions of the ^3P 2p6s state (T4).

Ω_j	$E_0^{(j)}$	$\langle r_1 \rangle$	$\langle r_2 \rangle$	$\langle r_3 \rangle$	$\langle r_4 \rangle$	$\langle \bar{r}_5 \rangle$	$\langle \bar{r}_6 \rangle$
Ω_1	-37. 4332(4)	1.8	1.7	1.7	1.7	1.5	0.3
Ω_2	-37. 4315(5)	41	1.1	1.1	1.1	1.5	0.3
Ω_3	-37. 4281(6)	20	1.1	1.1	1.1	1.5	0.3
Ω_4	-37. 4276(5)	10	1.1	1.1	1.1	1.5	0.3
Ω_5	-36. 4630(6)	1.6	1.6	1.6	1.6	15	0.3

NOTE: Regional energies are given in E_h, electron-nucleus distances ⟨r⟩ for up-spin and $\langle \bar{r} \rangle$ for down-spin electrons in bohr.

Table III. Nodal regions ofthe ^1P 2p6s state (S4).

Ω_j	$E_0^{(j)}$	$\langle r_1 \rangle$	$\langle r_2 \rangle$	$\langle r_3 \rangle$	$\langle \bar{r}_4 \rangle$	$\langle \bar{r}_5 \rangle$	$\langle \bar{r}_6 \rangle$
Ω_1	-37.4378(5)	1.5	1.5	1.5	1.5	1.5	1.5
Ω_2	-37.4311(4)	43	1.5	0.3	1.1	1.1	1.1
Ω_3	-37.4280(3)	20	1.5	0.3	1.1	1.1	1.1
Ω_4	-37.4249(4)	10	1.5	0.3	1.1	1.1	1.1
Ω_5	-36.563(1)	38	1.0	0.7	35	1.4	0.3
Ω_6	-36.5537(8)	46	1.4	0.3	46	1.4	0.3

NOTE: Regional energies are given in E_h, electron-nucleus distances ⟨r⟩ for up-spin and $\langle \bar{r} \rangle$ for down-spin electrons in bohr.

The observed average distances coincide well with the three highest maxima of that function suggesting the interpretation of the nodes between Ω_2, Ω_3, and Ω_4 being excitation nodes. Even the larger average of the highest peak of the radial distribution function for the S4 state is found as a slightly larger $\langle r_1 \rangle$ in Ω_2. The regions Ω_1 correspond analogously to the first maximum of Figure 1. According to the radial distribution function, Ω_2 is the most important region for S4 and T4 and should contribute to the FN-DMC result, whereas Ω_1 is not expected to be important at all. It should be emphasized that Ω_2 does not have the lowest energy, as might have been anticipated.

The higher regions Ω_5 and above cannot be explained by excitation nodes with Eq. 3 and are thus due to spurious nodes. The energy in these regions is substantially higher. Neglecting these regions we are left with regional energies that span 5 mE_h (T4) or even 13 mE_h (S4). For the ground state there is only one way to explain the different regions Ω_2 and higher and this is by spurious nodes. So we offer here an alternative method for detection of nodal artefacts in ground state wave functions.

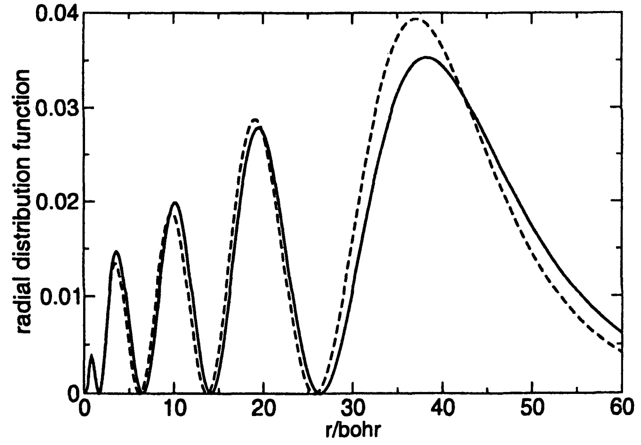

Figure 1. Radial distribution function for OSLHF 6s Rydberg atomic orbital (solid for S4, dashed for T4).

With these results we can now understand our previous calculations with the FN-DMC(s) approach (*9*). Since all regions have been populated in the initial walker ensemble we have consistently obtained $E_0^{(1)}$ and thus a singlet energy 5 mE_h below the corresponding triplet energy (see Tables II and III). Calculating instead the singlet-triplet splitting with Ω_2, we obtain 0.4(6) mE_h consistent with the experimental value of 0.4 mE_h (*42*). On the other hand, the excitation energy is increased for Ω_2 (10.89 eV) although the excitation energy for Ω_1 in T4 (10.80 eV) is larger than the experimental value (10.70 eV). This investigation demonstrates that seemingly good FN-DMC excitation energies might be due to unimportant regions with erroneously low energies.

Rydberg Excitations of the Carbon Atom

The observations discussed before make clear that excited states need to be treated in more detail according to the walker distribution in the nodal regions Ω_j resulting from the excitation and spurious nodes. A way to do this is to perform the previously described FN-DMC(n) calculation. This approach is discussed here for three examples: the ground (G), and the highest triplet (T4) and singlet (S4) state. Proceeding with a regional topological analysis and based on themean energies in the observed regions, the histograms (Fig. 2) for T4 and S4 can be plotted.

As expected for S4, region Ω_2 is the most important with a frequency of appearance of 67 % followed by Ω_3 (29 %) and Ω_4 (4 %).

T4 is similar as can be seen in Figure 2 with 53 % occupation of Ω_2, 29 % Ω_3, 16 % Ω_4 and 2 % Ω_1. Here the regions Ω_3 and Ω_4 are unequivocally distinguishable by geometry but not by energy.

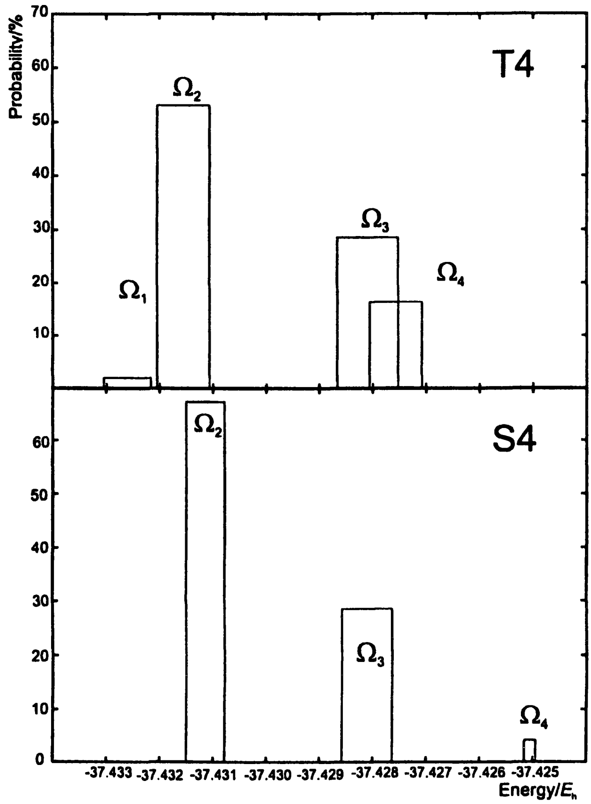

Figure 2. Histograms for the T4 (up) and the S4 (below) states. The width of the boxes represents twice the standard deviation.

In the ground state the region Ω_1 is occupied by 100 %. The regions due to spurious nodes have neither been populated in the ground state nor in the excited states investigated here with a Ψ^2 sample.

A proof for convergence of the VMC calculation and thus the Ψ^2 distribution is the fact that distant electrons have changed positions with near core electrons which is only possible if Ω_1 has temporarily been occupied. The same way of execution is now employed for all states and Rydberg excitation energies and singlet-triplet splittings are recalculated in Table IV from weighted averages of the absolute energies. The error given is the standard deviation of the mean of all FN-DMC calculations. This error increases with higher excitations of the Rydberg electron, because there more regions with different energies are populated. In order to obtain the same error as in FN-DMC(s), more FN-DMC steps are required.

The FN-DMC(n) excitation energies are compared to OSLHF, VMC, FN-DMC(s), and experimental values, the same is done for the singlet-triplet splittings. Experimental data are corrected for spin-orbit coupling. Note that the ground state energy actually remained unchanged since only Ω_1 was sampled here.

OSLHF overestimates the excitation energy by about 0.25 eV and the singlet-triplet splittings by 0.01 eV to 0.03 eV. FN-DMC(s) improves it, especially for the higher states and the singlets (-0.02 eV to 0.22 eV). The ^1P (2p6s) configuration is the only one where the excitation energy is found smaller than in the experiment. This behavior unfortunately causes too small and even negative singlet-triplet splittings.

Table IV. Rydberg excitation energies and singlet-triplet splittings.

	OSLHF	*VMC*	*DMC(s)*	*DMC(n)*	*Expt.(42)*
^3P (2p3s)	7.71	7.60(1)	7.716(4)	7.716(2)	7.48
^1P (2p3s)	7.93	7.78(1)	7.884(4)	7.890(2)	7.68
^3P (2p4s)	9.90	9.67(1)	9.815(5)	9.847(2)	9.68
^1P (2p4s)	9.96	9.71(1)	9.780(6)	9.904(4)	9.71
^3P (2p5s)	10.65	10.39(1)	10.505(5)	10.546(4)	10.38
^1P (2p5s)	10.67	10.40(1)	10.408(4)	10.547(5)	10.40
^3P (2p6s)	10.99	10.79(1)	10.803(7)	10.890(7)	10.70
^1P (2p6s)	11.01	10.80(1)	10.668(7)	10.891(7)	10.71
2p3s	0.22	0.18(1)	0.168(3)	0.178(3)	0.20
2p4s	0.06	0.04(1)	-0.035(6)	0.056(4)	0.03
2p5s	0.03	0.01(1)	-0.096(4)	0.021(6)	0.01
2p6s	0.02	0.01(1)	-0.136(8)	0.00(1)	0.01

NOTE: Energies for the excitations from the ^3P carbon atom ground state to Rydberg states and singlet-triplet splittings in eV. The standard deviation for the last digit is given in parentheses.

Since the results for the FN-DMC excitation energies with OSLHF wave functions looked rather promising, we performed VMC calculations of a similar type. With independence of the complicated Rydberg states nodal structure, it was possible to improve all the calculated energy differences again. Excitation energies deviate by at most 0.12 eV from experiment, some exactly reproduce it. The singlet-triplet splittings are in excellent agreement with experiment.

For FN-DMC(n) the excitation energies are not improved over the FN-DMC(s) results for the reason discussed above, whereas the singlet-triplet splittings are now as good as those of the VMC calculations. Reliable FN-DMC calculations of excited states require therefore a careful analysis of the nodal regions and their energies. As a practical approach, we suggest the procedure employed here, i.e. starting several short independent FN-DMC runs from the individual walkers of a Ψ^2 VMC distribution.

Conclusions

Rydberg states of the carbon atom have been studied. Using guide functions described in terms of configuration state functions from OSLHF orbitals, the OSLHF excitation energies can be improved with VMC and with both discussed FN-DMC approaches, respectively. Standard fixed-node DMC is not able to describe the singlet-triplet splitting reliably for the carbon Rydberg states whereas VMC and the novel FN-DMC method for excited states produce good agreement with experiment.

The nodal regions of the ground state and the 2p6s triplet and singlet wave functions and their effect on FN-DMC calculations were investigated. Different regional energies $E_0^{(i)}$ have been observed depending on the initial walker. It was demonstrated that cases where $E_0^{(i)} > E_0^{(FN)}$ can occur. In the ground states they must be due to spurious nodes and are qualitatively shown not to play a role for standard FN-DMC calculations.

Contrarily the excitation nodes observed in the two 2p6s states that separate the regions in which one electron only is at higher distance from the nucleus influence the FN-DMC result. We propose to include regional energies $E_0^{(i)}$ of these cases weighted according to a Ψ^2 distribution.

Acknowledgements

A.L. gratefully acknowledges support of travel by the Petroleum Research Fund and financial support by the Deutsche Forschungsgemeinschaft (DFG) in the DFG priority program SPP 1145. The OSLHF calculations have been performed by A. Görling and F. Della Sala.

References

1. Görling, A. *Phys. Rev. A* **1993**, *47*, 2783.
2. Görling, A. *Phys. Rev. A* **1999**, *59*, 3359.
3. Görling, A. *Phys. Rev. Lett.* **2000**, *85*, 4229.

4. Della Sala, F.; Görling, A. *J. Chem. Phys.* **2003,** *118*, 10439.
5. Vitale, V.; Della Sala, F.; Görling, A. *J. Chem. Phys.***2005,** *122*, 244102.
6. Della Sala, F.; Görling, A. *J. Chem. Phys.* **2002,** *116*, 5375.
7. Della Sala, F.; Görling, A. *Phys. Rev. Lett* **2002,** *89*, 033003.
8. Bande, A. diploma thesis; RWTH Aachen University: Aachen, 2004.
9. Bande, A.; Lüchow, A.; Della Sala, F.; Görling, A. *J. Chem. Phys.* **2006,** *124*, 114114.
10. Hachmann, J.; Galek, P. T. A.; Yanai, T.; Chan, G. K.-L.; Handy, N. C. *Chem. Phys. Lett.* **2004,** *392*, 55.
11. Handy, N. C. *Mol. Phys.* **2004,** *102*, 2399.
12. Barnett, R. N.; Reynolds, P. J.; Lester, Jr., W. A. *J. Chem. Phys.* **1985,** *82*, 2700.
13. Grimes, R. M.; Hammond, B. L.; Reynolds, P. J.; Lester, Jr., W. A. *J. Chem. Phys.* **1986,** *85*, 4749.
14. Reynolds, P. J.; Barnett, R. N.; Hammond, B. L.; Lester, Jr., W. A. *J. Stat. Phys.* **1986,** *43*, 1017.
15. Barnett, R. N.; Reynolds, P. J.; Lester, Jr., W. A. *Int. J. Quantum Chem.* **1992,** *42*, 837.
16. Reynolds, P. J.; Dupius, M.; Lester, Jr., W. A. *J. Chem. Phys.* **1985,** *82*, 1983.
17. El Akramine, O.; Kollias, J. A. C.; Lester, Jr., W. A. *J. Chem. Phys.* **2003,** *119*, 1483.
18. Aspuru-Guzik, A.; El Akramine, O.; Grossman, J. C.; Lester, Jr., W. A. *J. Chem. Phys.* **2004,** *120*, 3049.
19. Sokolova, S.; Lüchow, A. *Chem. Phys. Lett.* **2000,** *320*, 421.
20. Schautz, F.; Filippi, C. *J. Chem. Phys.* **2004,** *120*, 10931.
21. Schautz, F.; Buda, F.; Filippi, C. *J. Chem. Phys.* **2004,** *121*, 5836.
22. Grossman, J. C.; Rohlfing, M.; Mitas, L.; Louie, S. G.; Cohen, M. L. *Phys. Rev. Lett.* **2001,** *86*, 472.
23. Ceperley, D. M. *J. Stat. Phys.* **1991,** *63*, 1237.
24. Glauser, W. A.; Brown, W. R.; Lester, Jr., W A.; Bressanini, D.; Hammond, B. L.; Koszykowski, M. L. *J. Chem. Phys.* **1992,** *97*, 9200.
25. Bressanini, D.; Ceperley, D. M.; Reynolds, P. J.; *Recent Advances in Quantum Monte Carlo Methods, Part II*; World Scientific: Singapore, 2002; p 3.
26. Bajdich, M.; Mitas, L.; Drobny, G.; Wagner, L. W. *Phys. Rev. B* **2005,** *72*, 075131.
27. Hammond, B. L.; Lester, Jr., W. A.; Reynolds, P.~J. *Monte Carlo Methods in Ab Initio Quantum Chemistry*; World Scientific: Singapore, 1994.
28. Umrigar, C. J.; Nightingale, M. P.; Runge, K. J. *J. Chem. Phys.* **1993,** *99*, 2865.
29. Grimm, R. C.; Storer, R. G. *J. Comput. Phys.* **1971,** *7*, 134.
30. Manten, S.; Lüchow, A. *J. Chem. Phys.* **2001,** *115*, 5362.

31. Della Sala, F.; Görling, A. *J. Chem. Phys.* **2001**, *115*, 5718.
32. Turbomole. Ahlrichs, R.; Bär, M.; Baron, H.-P.; Bauernschmitt, R.; Böcker, S.; Ehrig, M.; Eichkorn, K.; Elliot, S.; Furche, F.; Haase, F.; Häser, M.; Horn, H.; Huber, C.; Huniar, U.; Kattaneck, M.; Kölmel, C.; Kollwitz, M.; Kay, K.; Ochsenfeld, C.; Öhm, H.; Schäfer, A.; Schneider, U.; Treutler, O.; v. Arnim, M.; Weigend, F.; Weis, P.; Weiss, H.; *Turbomole*; University of Karlsruhe: Karlsruhe, Germany, since 1988.
33. Ahlrichs, R.; Bär, M.; Häser, M.; Horn, H.; Kölmel, C. *Chem. Phys. Lett.* **1989**, *162*, 165.
34. Häser, M.; Ahlrichs, R. *J. Comput. Chem.* **1989**, *10*, 104.
35. Horn, H.; Weiss, H.; Häser, M.; Ehrig, M.; Ahlrichs, R. *J. Comput. Chem.* **1991**, 1*2*, 1058.
36. Treutler, O.; Ahlrichs, R. *J. Chem. Phys.***1995**, *102*, 346.
37. Lee, C.; Yang, W.; Parr, R. G. *Phys. Rev. B* **1988**, *37*, 785.
38. Dunning, Jr., T. H. *J. Chem. Phys.* **1989**, *90*, 1007.
39. Gaussian basis set order form; Basis sets were obtained from the Extensible Computational Chemistry Environment Basis Set Database, Version 02/25/04, as developed and distributed by the Molecular Science Computing Facility, Environmental and Molecular Sciences Laboratory which is part of the Pacific NorthwestLaboratory, P.O. Box 999, Richland, Washington 99352, USA, and funded by the U.S. Department of Energy. The Pacific Northwest Laboratory is a multi-program laboratory operated by Battelle Memorial Institute for the U.S. Department of Energy under contract DE-AC06-76RLO 1830. Contact David Felleror Karen Schuchardt for further information. , Feb. 2004.
40. Schmidt, K. E.; Moskowitz, J. W. *J. Chem. Phys.* **1990**, *93*, 4172.
41. Anderson, J. B. *Phys. Rev. A* **1987**, *35*, 3550.
42. Atomic spectra database, version 2.0; http://physics.nist.gov.PhysRevData/ASD/index.html.

Downloaded by PENNSYLVANIA STATE UNIV on July 4, 2012 | http://pubs.acs.org
Publication Date: December 31, 2006 | doi: 10.1021/bk-2007-0953.ch005

Chapter 5

Linear-Scaling Evaluation of the Local Energy in Quantum Monte Carlo

Brian Austin[1,2], Alán Aspuru-Guzik[1], Romelia Salomón-Ferrer[1,2], and William A. Lester, Jr.[1,2]

[1]Kenneth S. Pitzer Center for Theoretical Chemistry, Department of Chemistry, University of California at Berkeley, Berkeley, CA 94720–1460
[2]Chemical Sciences Division, Lawrence Berkeley National Laboratory, Berkeley, CA 94720

For atomic and molecular quantum Monte Carlo calculations, most of the computational effort is spent in the evaluation of the local energy. We describe a scheme for reducing the computational cost of the evaluation of the Slater determinants and correlation function for the correlated molecular orbital (CMO) ansatz. A sparse representation of the Slater determinants makes possible efficient evaluation of molecular orbitals. A modification to the scaled distance function facilitates a linear scaling implementation of the Schmidt-Moskowitz-Boys-Handy (SMBH) correlation function that preserves the efficient matrix multiplication structure of the SMBH function. For the evaluation of the local energy, these two methods lead to asymptotic linear scaling with respect to the molecule size.

In the quantum Monte Carlo (QMC) method (*1-7*), the expectation value of the Hamiltonian ⟨H⟩ is computed as a statistical average of the local energy of a trial wave function, $\Psi_T(\mathbf{R})$, where **R** denotes the 3N coordinates of the N-particle system.

$$E_L(\mathbf{R}) \equiv \frac{\hat{H}\Psi_T(\mathbf{R})}{\Psi_T(\mathbf{R})}. \tag{1}$$

Averages of this quantity provide an estimator of the energy of the system,

$$E \approx \langle E_L \rangle = \lim_{N_s \to \infty} \frac{1}{N_s} \sum_i^{N_s} E_L(\mathbf{R}_i), \tag{2}$$

where N_s is the number of sample points $\mathbf{R}_i$ and the local energy is evaluated during the random walk. The points $\mathbf{R}_i$ are sampled from a probability function $f(\mathbf{R}, \tau)$, such as $\Psi_T^2(\mathbf{R})$ for variational Monte Carlo (1). Presently, the more commonly used QMC version is the diffusion Monte Carlo (DMC) that yields time-independent solutions of the Schrödinger equation from an imaginary time stochastic formalism (8).

For most molecular applications, the correlated molecular orbital (CMO) wave function form is used.

$$\Psi_T = \mathbf{D} \times \mathbf{F} = \left[\sum c_k \cdot D_k^\alpha D_k^\beta\right] \times \left[e^{U(\mathbf{r}_{ij})}\right] \tag{3}$$

Here **D** is a linear combination of Slater determinants and **F** is a correlation function that depends on inter-particle distances. The determinants $\mathbf{D}^\sigma{}_i$, where σ denotes α or β spin, are usually constructed with molecular orbitals (MOs) obtained from a previous ab initio calculation such as Hartree-Fock (HF), multi-configuration self consistent field theory (MCSCF), or density functional theory (DFT). Interactions between electrons in a molecule diminish exponentially as the distance between them increases (*9*). In recent years, linear diffusion Monte Carlo (LDMC) methods (*10-12*) have been introduced to take advantage of this property to reduce the computational demands of QMC to linear dependence on system size. Williamson et al. (*10*) developed a linear-scaling method in a plane-wave basis expansion for periodic systems and applied the approach in several studies (*13-15*). Alfè and Gillan (*12*) developed a method that employs non-orthogonal localized orbitals in a plane-wave basis expansion that further improves efficiency.

Manten and Luchow (ML) (*11, 16*) have presented a similar method that uses Gaussian-type orbitals (GTOs). ML have also shown how parts of the DMC algorithm, including the evaluation of the Coulomb potential and inter-particle correlation function, can be made to scale linearly with system size (*11, 16*). In the present work, we address the two most important contributions to the computational cost of wave function evaluation, namely, the evaluation of the

Downloaded by PENNSYLVANIA STATE UNIV on July 4, 2012 | http://pubs.acs.org
Publication Date: December 31, 2006 | doi: 10.1021/bk-2007-0953.ch005

Slater determinant (*17*) and that of the correlation function. We will describe a fast implementation of these two steps in the following two sections. Progress towards deeper understanding of results from QMC is described in the last section.

Fast evaluation of the Slater determinant

One purpose of LDMC is to decrease computational time by reducing computation associated with wave function evaluation. The approach of Williamson et al. (*10*) has the potential of near-optimal efficiency because only a single three-dimensional spline (3DS) evaluation is required for a given molecular orbital (MO). Maximally-localized Wannier (MLW) functions of systems using effective core potentials (ECPs) are smooth functions that can be described accurately with 3DS. All-electron MOs expressed in a Slater or Gaussian basis set are rapidly-varying with distance, and their representation with 3DS is memory intensive due to the cubic scaling of 3DS memory requirements with MO complexity. On the other hand, Gaussian or Slater basis sets are more compact than plane waves and therefore amenable to being evaluated explicitly without substantially increasing computational cost as proposed by ML (*11, 16*). We improve upon the work of ML by introducing a sparse representation of the Slater matrix and cutoff criteria that derive from the sparse representation. The method proposed here can be extended to 3DS-based methods to achieve further computational efficiency.

Evaluation of **D** of Eq. 3 requires the construction of Slater matrices, $\mathbf{D}^{\sigma}_{i}$, and the corresponding determinants $D^{\sigma}_{i} \equiv \det(\mathbf{D}^{\sigma}_{i})$. Note that naive construction of the Slater matrix leads to cubic scaling with system size.

The main feature of the method is the use of a three-dimensional grid to store the non-zero contributions to the Slater matrix. The use of the grid does not affect the accuracy of the wave function because the orbitals are evaluated using accurate one-dimensional representations of Slater basis functions. The memory requirements for the grid are of the order of a few megabytes for the polyalanine systems studied (*17*).

Evaluation of determinants D^{σ}_{i} involves an additional cubic step associated with the inversion of $\mathbf{D}^{\sigma}_{i}$ (*18*). Although ML proposed using a sparse linear algebra routine for this purpose, an optimized algorithm for dense matrices (*19*) is used in the present approach because inversion of $\mathbf{D}^{\sigma}_{i}$ is not a computational bottleneck for the size of systems treated here.

Slater matrices require evaluation of MOs for all electrons of a given spin σ. An MO ϕ is expanded in a basis of atom-centered functions, typically GTOs or Slater-type orbitals (STOs),

Downloaded by PENNSYLVANIA STATE UNIV on July 4, 2012 | http://pubs.acs.org
Publication Date: December 31, 2006 | doi: 10.1021/bk-2007-0953.ch005

$$\phi_i(\mathbf{r}) = \sum_{\mu=1}^{Nbas} C_{\mu i}\chi_\mu(\mathbf{r}) \tag{4}$$

The $C_{\mu i}$ elements form the coefficient matrix **C**. The atom-centered functions χ are usually expressed as linear combinations of primitive functions φ,

$$\chi_\mu(\mathbf{r}) = \sum_{k=1}^{Ncont} c_{\mu k} \cdot \varphi_k(\mathbf{r}). \tag{5}$$

It may seem that construction of a Slater matrix is cubic scaling, because the evaluation of Eq. 5 requires iteration over basis functions, MOs and positions. However, MO evaluation can be made linear with system size by the use of localized MOs (LMOs) coupled with a sensible cutoff of LMO spatial extent. These two steps are essential for achieving linear scaling with system size.

Most ab initio computer programs employ orthogonal LMOs. The orthogonalization restriction has the disadvantage of producing orthogonalization tails, i.e., small contributions to the LMOs at centers that lie far from the main contribution to the LMO (20). To accelerate the onset of linear scaling, ML removed the orthogonalization tails (11). In this study, we chose not to do so in order to preserve fully the nodal characteristics of the LMOs.

We next present a brief explanation of the steps involved in the calculation of the Slater matrix. The first step required for the sparse representation of the Slater matrix is to generate a pre-sorted coefficient matrix. For CMOs of the form of Eq. 3, Slater matrices are constructed separately for α and β electrons leading to sorted coefficient matrices, $\mathbf{K}^\beta_i$ and $\mathbf{K}^\beta_i$, built from $\mathbf{C}^\beta_i$ and $\mathbf{C}^\beta_i$, respectively. The rows of $\mathbf{K}^\alpha_i$ run over the basis functions, while the columns run over the LMO coefficients sorted by their absolute value,

$$|\mathbf{K}_{1i}| \geq |\mathbf{K}_{2i}| \geq \ldots \geq |\mathbf{K}_{N_{mos}i}| \tag{6}$$

It is convenient to construct an auxiliary array that maps indexes of $\mathbf{K}^\alpha_i$ and $\mathbf{K}^\beta_i$ to the indexes of the Slater matrices $\mathbf{D}^\sigma_i$. This step facilitates filling the columns of the Slater matrices in the correct order.

Grid Generation

For an electron located at **r**, the value of a LMO $\phi_i(\mathbf{r})$ is a sum of products $p_{\mu i}$ of basis functions and LMO coefficients for each LMO,

$$\phi(\mathbf{r}) = \sum_{\mu=1}^{N_{bas}} p_{\mu i} = \sum_{\mu=1}^{N_{bas}} C_{\mu i}\chi_\mu(\mathbf{r}) \tag{7}$$

In the present LDMC approach, we only sum over products that are greater than a numerical threshold ε_c. This threshold is directly connected to the numerical

Downloaded by PENNSYLVANIA STATE UNIV on July 4, 2012 | http://pubs.acs.org
Publication Date: December 31, 2006 | doi: 10.1021/bk-2007-0953.ch005

precision of the truncated trial wave function. This is the single most important parameter for the onset of linear scaling.

When an electron is evaluated at position **r**, the nearest point from a 3D grid is referenced. Each 3D grid element is associated with a compressed representation of the Slater matrix that describes the non-zero elements of a column of the Slater matrix evaluated at the particular volume element. The compression scheme is depicted in Figure 1.

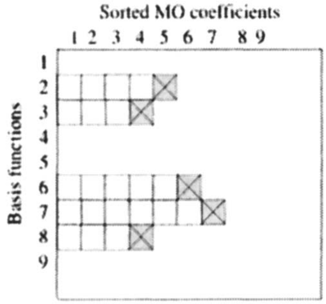

Figure 1: The compressed matrix representation used for this work. The non-zero basis function index is stored along with the index of the smallest LMO coefficient that multiplies the basis function. These pairs of indexes are designated by an x *and for the example correspond to (2,5)(3,4)(6,6)(7,7)(8,4).*

Besides the numerical threshold ε_c, a second parameter is introduced. It is the fraction (*f*) of products $p_{\mu i}$ retained. The parameters *f* and ε_c are related. For small thresholds, a higher fraction of products can be discarded without change in the value of the wave function. At higher thresholds, a smaller fraction of products can be removed from the calculation.

Determinant Evaluation Algorithm

In DMC electrons can be moved one at a time (8), or all at the same time (21). For this discussion, we assume that the electrons are moved one at a time. On this basis we present a procedure for the construction of a column of a Slater matrix corresponding to an electron located at a position **r**.

With CMO wave functions, electrons have a given spin σ throughout the simulation. As soon as one specifies the electron index, and therefore spin, one can use the grid and sorted coefficient matrix associated with the particular spin. With the electron spin specified, the grid element corresponding to the spatial location is identified, and then a sequence of doublets (μ_1, i_1), $(\mu_2, i_2)\ldots(\mu_n, i_n)$ is

Downloaded by PENNSYLVANIA STATE UNIV on July 4, 2012 | http://pubs.acs.org
Publication Date: December 31, 2006 | doi: 10.1021/bk-2007-0953.ch005

Downloaded by PENNSYLVANIA STATE UNIV on July 4, 2012 | http://pubs.acs.org
Publication Date: December 31, 2006 | doi: 10.1021/bk-2007-0953.ch005

```
Require: $x,y,z \subset$ Grid {ensure that the point is inside the grid.}
  $DoubletList = Grid^{\sigma}(x,y,z)$
  $SortedCoefficients = PresortedCoefficients^{\sigma}$
  $SortKey = SortKey^{\sigma}$
  $SlaterMatrix = SlaterMatrix^{\sigma}$
  while Doublet from DoubletList: do
    $(\mu, i_{max}) = Doublet$
    Evaluate $\chi_{\mu}(x,y,z)$
    for $i=0$ to $i=i_{max}$ do
      $c = SortedCoefficients(\mu, i)$
      $j = SortKey(\mu, i)$
      $SlaterMatrix(j,k) = \phi_j(x,y,z) = \phi_j(x,y,z) + c * \chi_{\mu}(x,y,z)$
    end for
  end while
```

Figure 2: Algorithm for the evaluation of a column k of the Slater matrix for an electron of spin σ at a point r = [*x*, *y*, *z*].

read. Here, μ_1, μ_2, ..., μ_n are the indexes of the *n* non-zero basis functions, and i_1, i_2, ..., i_n are the maximum LMO coefficient indexes needed to evaluate the products $p_{\mu i}$. The Slater matrix columns are updated in iterations over electrons. A pseudo-code representation of the algorithm is illustrated in Figure 2.

Rapid Evaluation of Primitive Basis Functions

STOs have been shown to be advantageous for QMC owing to their correct asymptotic behavior at short and long electron-nucleus distances. To employ wave functions expanded in an STO basis, we use the Amsterdam Density Functional (ADF) package (22). For rapid evaluation, the radial components of the contractions χ_j are interpolated using cubic splines, and cut-off at an appropriate distance from their center. Cut-off values are determined so that the local energy of a fixed sample of walkers changes by less than a prescribed percentage. Splines make possible the representation of a linear combination of all STOs belonging to a given contraction by a single spline function, with the result of reducing the computational cost. For the remainder of this discussion, we will refer to such representations of contracted STOs as basis functions.

Linear-Scaling Evaluation of the Correlation Function

Rapid evaluation of the correlation function is equally important to obtain a linear scaling QMC algorithm. The correlation function of Schmidt and Moskowitz (SM) (23), which stems from the form suggested by Boys and Handy (BH) (24) is displayed in Equation 8.

$$U=\sum_{\mu}\sum_{A}^{atoms} c_{\mu A}\sum_{i<j} U^{\mu}_{Aij}$$

where,

$$U^{\mu}_{Aij}=(\bar{r}_{Ai}^{\,l_\mu}\bar{r}_{Aj}^{\,m_\mu}+\bar{r}_{Aj}^{\,l_\mu}\bar{r}_{Ai}^{\,m_\mu})\bar{r}_{ij}^{\,n_\mu}; \qquad \bar{r}(r)=\frac{r}{1+br} \qquad (8)$$

An important step in accelerating evaluation of the SMBH correlation function was taken by ML. These authors changed the scaled distance function to $\bar{r}=1-\exp[-\alpha r]$, leading to a shorter cutoff distance in their linear scaling algorithm.

A further change to $\bar{r}$ is required for the present approach. This change is motivated by examining the asymptotic behavior of the three-body terms in the SMBH expansion. Consider the (lmn)=(011) term: $U_{ijA}=(1-\exp[-\alpha r_{ij}])(1-\exp[-\alpha r_{jA}])$. Because ML's $\bar{r}$ approaches unity at large distances, U_{ijA} reduces to the two- body (lmn)=(010) term when electron i is separated from the jA pair, leaving many nonzero terms in the SMBH function. To reduce the number of nonzero terms, we simply shift $\bar{r}$ so that its asymptotic value is zero: $\bar{r}=-\exp[-\alpha r]$.

The consequences of this change are simple to interpret. Although physical arguments would seem to favor an ansatz where three-body terms reduce to two-body terms, these extra terms are merely redundant descriptions of the two-body correlations included in the (lmn)=(010) term. For two-body terms, this changes only the normalization of the wavefunction. Linear dependence among all the terms is also reduced. Our modification to $\bar{r}$ may also be alternatively viewed as a generalization of the Sun-Lester correlation function (25), which is included as the (lmn)=(001) term of the SMBH expansion.

The next step in the development of our linear scaling algorithm requires recognition that the SMBH function can be rewritten as a trace over a matrix product,

$$U=\sum_{\mu}\sum_{A}\sum_{i\neq j} c_{\mu A}\bar{r}_{Ai}^{\,l_\mu}\bar{r}_{ij}^{\,n_\mu}\bar{r}_{jA}^{\,m_\mu}. \qquad (9)$$

Simpler terms where l, m, or n are zero can be handled by deleting the appropriate matrix from Equation 9. The term where m and l are swapped in

Downloaded by PENNSYLVANIA STATE UNIV on July 4, 2012 | http://pubs.acs.org
Publication Date: December 31, 2006 | doi: 10.1021/bk-2007-0953.ch005

Equation 8 is unnecessary in the matrix form because the sum over *i* and *j* is no longer lower triangular. It is easy to exclude terms where *i*=*j* by setting diagonal elements of the $\bar{r}_{ij}$ matrix to zero.

Because BLAS (26) libraries make matrix operations particularly efficient, we observed speedups of at least a factor of ten relative to our initial implementation after switching to a matrix-based implementation. Matrix multiplication, however, scales cubically with system size. To achieve linear scaling, we take advantage of the sparsity in the $\bar{r}$ matrices that was created by our modification to the scaled distance function.

Figure 3 sketches our sparse matrix multiplication routine. A distance-based cutoff is used to determine which $\bar{r}$ elements need to be computed. By limiting operations to electrons near each atom, we implicitly compress the nonzero elements of $\bar{r}_{iA}$ and $\bar{r}_{ij}$ into a set of three O(1) blocks ($\bar{r}_i^{m[A]}$, $\bar{r}_{ij}^{l[A]}$ and $\bar{r}_j^{l[A]}$) for each atom. The cost of the matrix operations for each atom is therefore O(1), yielding an overall linear scaling algorithm.

```
for each atom, A do
    Make a list of electrons near A.
    Build the vectors of e-n distances $\bar{r}_i^{m[A]}$ and $\bar{r}_j^{l[A]}$.
    Build the matrix of distances $\bar{r}_{ij}^{n[A]}$ for electrons near A.
    Perform the matrix operations: $U_A^{\mu} = \sum_{ij} \bar{r}_i^{m[A]} \bar{r}_{ij}^{n[A]} \bar{r}_j^{l[A]}$.
    Increment U: $U = U + c_{\mu A} U_A^{\mu}$.
end for
```

Figure 3: Algorithm for computing one term in the SMBH expansion using sparse matrices.

Application to Biological Systems

As an example of the capability of treating large systems, we show some results for calculations on two biomolecules present in Photosystem II, bacteriochorophyll (Bchl) and spheroidene (Spo), containing 304 and 314 electrons respectively. Under high light conditions, the generation of chlorophyll triplet states and singlet oxygen, $^1O_2$, can increase dramatically due to the fact that the light flux exceeds the amount of light that the reaction center is able to process (turn-over capacity). Carotenoids help protect the organism by non-photochemical quenching (NPQ), which dissipates the excess excitation energy of singlet oxygen. If carotenes are absent, chlorophyll is readily oxidized,

Downloaded by PENNSYLVANIA STATE UNIV on July 4, 2012 | http://pubs.acs.org
Publication Date: December 31, 2006 | doi: 10.1021/bk-2007-0953.ch005

leading to the organism's death. Several scientific questions about the photoprotection mechanism remain unanswered. The ground-state to lowest-triplet-state excitation energies of both molecules as well as the energy transfer rate between the systems have not been determined. At present, DFT is not sufficiently accurate to answer these questions. A rigorous electronic structure method that accurately treats electron correlation is needed, but, as noted, basis-set correlated methods scale too steeply with system size to be applicable. DMC presently offers the only feasible option for the accurate calculation of these quantities.

To understand chemical processes, it is useful to have information besides total energies. Electron localization methods provide insight on the behavior of electrons in molecules. Properties such as electron density, spin density and the electron pair localization function (EPLF) (27) can routinely be computed by post-processing. The EPLF provides a quantitative description of electron pairing in molecular systems and has similarities to the electron localization function (ELF) of Becke and Edgecombe (28). The QMC method is a particularly well suited approach for obtaining such information because the simple and general definition of EPLF is easily evaluated in QMC.

In the next section, some details on the speedup in calculating the local energy obtained by the application of the techniques mentioned above are presented. Results for spheroidene as well as other molecules of biological importance are given.

Results and Discussion

Local energies for the spheroidene molecule were computed with a series of different grid sizes. Our tests show a factor of 10 speedup with respect to a standard calculation for a grid of 2660 elements. The basis-function cut offs were in the 11.0-15.0 a.u range, following the criteria for STOs given above. The grid memory requirements are modest; for spheroidene, a 20520 element grid requires 3.4 MB of RAM.

CPU timings for a sample of eight molecules of biological interest have been obtained. We chose the series of 2-,4-,6- and 8-polyalanine in an alpha helix conformation. We also selected four other molecules with different conformations to show dependence on geometrical factors. For the calculation of the eight molecules, we used a grid element length of 2 a.u. and a cutoff threshold of $\varepsilon_c = 1\text{x}10^{-12}$. The whole fraction ($f = 1.0$) of products was preserved for all calculations.

Geometrical effects can be compared as well. With fewer basis functions per volume element, linear molecules require less computer time than 2D or 3D arrangements. For example, the spheroidene molecule required 75% of the CPU time of 8-alanine, which has the same number of electrons. A model bacteriochlorophyll with ten fewer electrons required 124% of the time 8-alanine.

Downloaded by PENNSYLVANIA STATE UNIV on July 4, 2012 | http://pubs.acs.org
Publication Date: December 31, 2006 | doi: 10.1021/bk-2007-0953.ch005

Downloaded by PENNSYLVANIA STATE UNIV on July 4, 2012 | http://pubs.acs.org
Publication Date: December 31, 2006 | doi: 10.1021/bk-2007-0953.ch005

The CPU timings for the evalution of the Slater determinant for 8 molecules are given in Figure 4. After around 80 electrons, the CPU time for filling the Slater matrices scales linearly with the number of electrons. A series of linear alkanes have been used to determine CPU scaling for evaluating the SMBH correlation function. Figure 5 presents timing data using a matrix-based algorithm with dense $\overline{r}$ matrices and the linear scaling algorithm with the present $\overline{r}$ .For these tests, we set $\alpha = 4.0$ and determined empirically that a cutoff of 4.0 a.u. affected local energies by less than 10^{-7} Hartrees. The sparse algorithm is linear scaling for all molecules studied and is faster than the dense algorithm for molecules with more than three carbon atoms.

Figure 6 presents slices of the EPLF function for spheroidene in the ground state singlet and the first excited triplet state in the z=0 plane. The different values represent the different levels of electron pair localization for that particular region, larger values indicate higher degree of localization. Most of the EPLF values obtained for this system are less than 0.1, which indicates a high level of delocalization in this system due to its conjugated polyene structure. Important differences can be seen between the singlet and the triplet state. While the singlet appears to have no spin-polarized (gray) regions, the triplet state does possess such regions near the outer boundary of the molecule. Grey regions show where excess alpha electron density is paired.

Conclusions

In this study, we have presented and demonstrated a novel approach in quantum Monte Carlo for the evaluation of the local energy of molecular systems described by atom-centered basis functions. Our approach exploits the structure of the wave function representation and evaluates the wave function using sparse linear-algebra methodologies. The product of basis functions and molecular orbital coefficients $p_{\mu i}$, truncated at $\varepsilon_c = 10^{-12}$ seems to be a good choice for retaining the high accuracy of the wave function while obtaining a significant speedup in the computation for the systems studied. For increasingly large molecules, the number of operations needed to evaluate the wave function and the local energy at each point of the simulation increases. In the past few years, major advances have been achieved in this laboratory that have made possible the treatment of systems considerably larger than those that could be addressed few years earlier. Development of more efficient codes and, in particular, codes that scale linearly with system size, will have significant impact on the kind of systems that will become feasible to study with QMC. The ability to complement the information given by the energy with electron distribution and electron localization functions obtained from a high accuracy method such as QMC should prove useful in providing further insight on chemical properties and processes.

Downloaded by PENNSYLVANIA STATE UNIV on July 4, 2012 | http://pubs.acs.org
Publication Date: December 31, 2006 | doi: 10.1021/bk-2007-0953.ch005

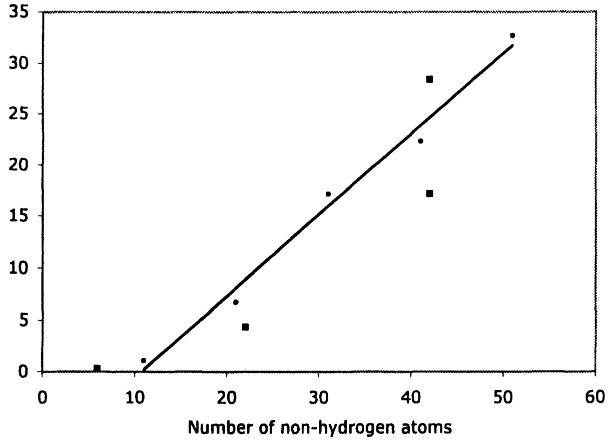

Figure 4: Computer time for filling the Slater matrices, $\mathbf{D}^{\alpha}_{i}$ and $\mathbf{D}^{\beta}_{i}$, as a function of the number of non-hydrogen atoms for different biological molecules. Data for a series of poly-alanine molecules (2-,4-,6- and 8-polyalanine) is plotted as circles. (1) hexatriene, (2) capsaicin, (3) bacteriochlorophyll and (4) spheroidene are designated by squares. The CPU time for polyalanine chains scales linearly with system size. Data are from reference (17).

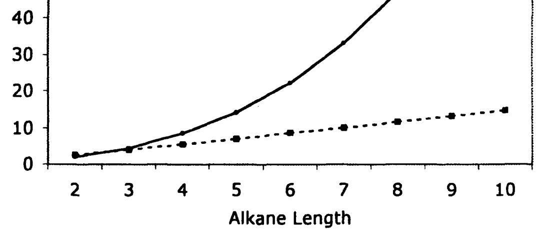

Figure 5: Computer time for evaluating the SMBH correlation function versus alkane length. The dense matrix-based algorithm (solid line) scales roughly cubically with system size. The sparse matrix based algorithm (dashed line) scales linearly.

Downloaded by PENNSYLVANIA STATE UNIV on July 4, 2012 | http://pubs.acs.org
Publication Date: December 31, 2006 | doi: 10.1021/bk-2007-0953.ch005

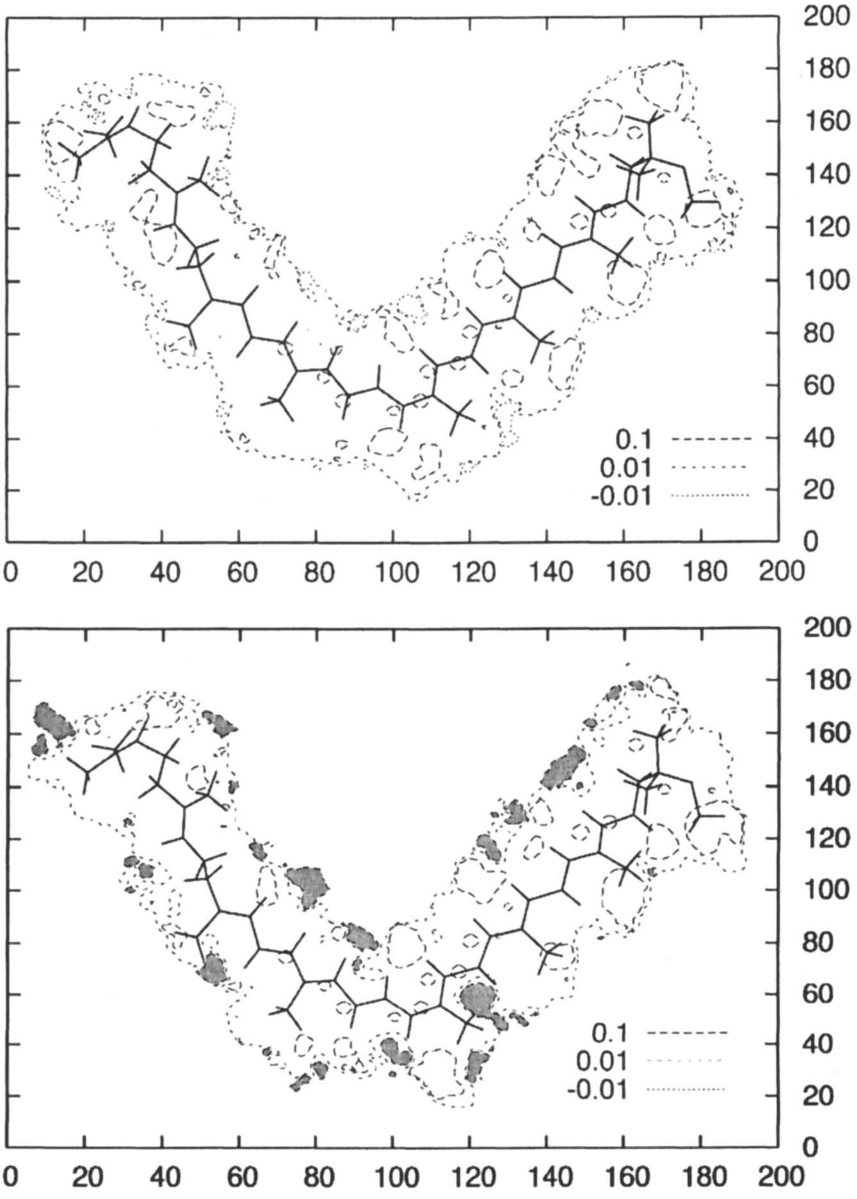

Figure 6: Plot of the z =0 plane of the EPLF function values for Spo in the ground state singlet (top), and the triplet state (bottom). The triplet state shows spin-polarized regions (dark grey) that are absent in the singlet state. The EPLF domain for both plots is [-0.1:0.1]

References

1. Hammond, B.L.; Lester, W. A., Jr.; Reynolds, P. J. Monte Carlo Methods in Ab Initio Quantum Chemistry, World Scientific, Singapore, 1994.
2. Ceperley, D. M.; Mitas, L. Quantum Monte Carlo Methods in Chemistry, in New Methods in Computational Quantum Mechanics, edited by Prigogine, I.; Rice, S. A. , volume XCIII of Adv. Chem. Phys., John Wiley and Sons, 1996.
3. Anderson, J. B. Quantum Monte Carlo: Atoms, Molecules, Clusters, Liquids and Solids, in Reviews in Computational Chemistry, edited by Lipkowitz, K. B. and Boyd, D. B., volume 13, p. 133, John Wiley and Sons, New York, 1999.
4. Lester, W. A., Jr.; Hammond, B. L. Annu. Rev. Phys. Chem. 41, 283 (1990).
5. Mitas, L. Comp. Phys. Comm. 97, 107 (1996).
6. Foulkes, M.; Mitas, L.; Needs, R.; Rajagopal, G. Rev. Mod. Phys. 73, 33 (2001).
7. Aspuru-Guzik, A.; Lester, W. A., Jr. Quantum Monte Carlo methods for the Solution of the Schrodinger equation for molecular systems, in Computational Chemistry, edited by Le Bris, C. volume X of Handbook of Numerical Analysis, p. 485, Elsevier, Amsterdam, The Netherlands, first edition, 2003.
8. Reynolds, P. J.; Ceperley, D. M.; Alder, B.; Lester, W. A., Jr. J. Chem. Phys. 77, 5593 (1982).
9. Maslen, P.; Ochsenfeld, C.; White, C.; Lee, M.; Head-Gordon, M.; J. Phys. Chem. A 102, 2215 (1998).
10. Williamson, A.; Hood, R.; Grossman, J. Phys. Rev. Lett. 8724 (2001).
11. Manten, S.; Luchow, A.; J. Chem. Phys. 119, 1307 (2003).
12. Alfè, D.; Gillan, M. Phys. Cond. Mat. 16, L305 (2004).
13. Williamson, A. J.; Grossman, J. C.; Hood, R. Q.; Puzder, A.; Galli, G. Phys. Rev. Lett. 89 (2002).
14. Puzder, A.; Williamson, A. J.; Grossman, J. C.; Galli, G. Phys. Rev. Lett. 88 (2002).
15. Puzder, A.; Williamson, A. J.; Grossman, J. C.; Galli, G. J. Chem. Phys. 117, 6721 (2002).
16. Manten, S.; Luchow, A. Improved Scaling in Diffusion Quantum Monte Carlo with Localized Molecular Orbitals, in Recent Advances in Quantum Monte Carlo Methods, Part II, edited by Rothstein, S. M.; Lester, W. A., Jr.; Tannaka, S. Singapore, 2002, World Scientific.
17. Aspuru-Guzik, A.; Salomon-Ferrer, R.; Austin, B.; Lester, W. A., Jr. J. Comp. Chem. 26, 708 (2005).
18. Ceperley, D.; Chester, G. V.; Kalos, M. H. Phys. Rev. B. 16, 3081 (1977).

Downloaded by PENNSYLVANIA STATE UNIV on July 4, 2012 | http://pubs.acs.org
Publication Date: December 31, 2006 | doi: 10.1021/bk-2007-0953.ch005

19. Whaley, R. C.; Petitet, A.; Dongarra, J. J. Parallel Computing 27, 3 (2001), Also available as University of Tennessee LAPACK Working Note #147, UT-CS-00-448, 2000 (www.netlib.org/lapack/lawns/lawn147.ps).
20. Liu, S.; Perez-Jorda, J.; Yang, W. J. Chem. Phys. 112, 1634 (2000).
21. Umrigar, C. J.; Nightingale, M. P.; Runge, K. J. J. Chem. Phys. 99, 2865 (1993).
22. Velde, G.; Bickelhaupt, F.; Baerends, E.; Guerra, C.; Gisber-Gen, S. V.; Snijders, J.; Ziegler, T. J. Comp. Chem. 22, 931 (2001).
23. Schmidt, K. E.; Moskowitz, J. W. J. Chem. Phys. 93 (1990).
24. Boys, S. F.; Handy, N. C. Proc. R. Soc. London Ser. A 310, 63 (1969).
25. Sun, Z.; Owen, R. K.; Reynolds, P. J.; Lester, W. A., Jr. Theo. Chim. Acta. 75, 353 (1989).
26. Lawson, C.; Hanson, R.; Kincaid, D.; Krogh, F. ACM Trans. Math. Software 5, 308 (1979).
27. Scemama, A.; Chaquin, P.; Caffarel, M. J. Chem. Phys 121, 1725 (2004).
28. Becke, A. D.; Edgecombe, K. E. J. Chem. Phys. 92, 5397 (1990).

Downloaded by PENNSYLVANIA STATE UNIV on July 4, 2012 | http://pubs.acs.org
Publication Date: December 31, 2006 | doi: 10.1021/bk-2007-0953.ch005

Downloaded by UNIV OF GUELPH LIBRARY on July 4, 2012 | http://pubs.acs.org
Publication Date: December 31, 2006 | doi: 10.1021/bk-2007-0953.ch006

Chapter 6

Electronic Quantum Monte Carlo Calculations of Energies and Atomic Forces for Diatomic and Polyatomic Molecules

Myung Won Lee[1], Massimo Mella[2], and Andrew M. Rappe[1,*]

[1]**The Makineni Theoretical Laboratories, Department of Chemistry, University of Pennsylvania, Philadelphia, PA 19104–6323**
[2]**School of Chemistry, Cardiff University, P.O. Box 912, Cardiff CF10 3TB, United Kingdom**

We calculated the energies and atomic forces of first-row monohydrides, carbon monoxide, and small organic polyatomic molecules using quantum Monte Carlo (QMC) method. Accurate forces were obtained with the method of Casalegno, Mella, and Rappe, combining the Hellmann-Feynman theorem forces calculated by the Assaraf-Caffarel method with a many-body Pulay correction. Improved algorithms for the minimization of the variational integral were useful in the force calculations.

In Advances in Quantum Monte Carlo; Anderson, J., et al.;
ACS Symposium Series; American Chemical Society: Washington, DC, 2006.

Introduction

While quantum Monte Carlo (QMC) has become quite successful in computing ground-state total energies, the calculation of properties other than energies has been less favorable. The accurate QMC calculation of atomic forces has been enabled through the recent developments by Assaraf and Caffarel (*1,2*), Filippi and Umrigar (*3*), Casalegno *et el.* (*4*), Chiesa *et al.* (*5*), and others.

The atomic force calculation can be extended to more complex systems (*6*), and we applied this method to all the first-row monohydrides, carbon monoxide, and small organic polyatomic molecules such as the methylene radical, the methyl radical, methane, and benzene. The first and second derivatives of the variational energy were analytically computed, and used to perform Newton's method parameter updates (*7*). For more efficient calculation of energies and forces, improved methods for optimizing variational Monte Carlo (VMC) wave functions were used (*6*). In general, the direct application of the variational principle yields significantly lower energies than variance minimization methods, so minimizing the energy is advantageous. The wave functions optimized in VMC were used as a guiding function in diffusion Monte Carlo (DMC) to compute more accurate energies.

Dissociation energies could be obtained from the total energy calculations of diatomic and polyatomic molecules. The computed results agree well with experiment. The dissociation energies from our VMC calculations give better results than the values obtained through the variance minimization technique reported in Ref. (*8*).

Downloaded by UNIV OF GUELPH LIBRARY on July 4, 2012 | http://pubs.acs.org
Publication Date: December 31, 2006 | doi: 10.1021/bk-2007-0953.ch006

Theoretical Background

The trial wave function we used is the product of Slater determinants of up-spin and down-spin electrons and a correlation factor containing the variational parameters ($c_{k\alpha}$),

$$\psi_T = D^{\uparrow} D^{\downarrow} \exp\left[\sum_{\alpha}^{N_{\mathrm{nuc}}} \sum_{i}^{N_{\mathrm{elec}}} \sum_{j>i}^{N_{\mathrm{elec}}} \sum_{k}^{N_{\alpha}} c_{k\alpha} \left(\overline{r}_{i\alpha}^{\,m_{k\alpha}} \overline{r}_{j\alpha}^{\,n_{k\alpha}} + \overline{r}_{j\alpha}^{\,m_{k\alpha}} \overline{r}_{i\alpha}^{\,n_{k\alpha}} \right) \overline{r}_{ij}^{\,o_{k\alpha}} \right],$$

where $\overline{r} = br/(1+br)$ with $b = 1$ inverse bohr and $m_{k\alpha}$, $n_{k\alpha}$, and $o_{k\alpha}$ are taken to be integers.

Newton's method was used to optimize the parameters in the VMC trial wave function. To improve the stability of the algorithm, we used the singular value decomposition (SVD). In addition, we used the steepest descent method in the initial stage of calculation and for the directions discarded in the SVD method for some calculations as described in Ref. (*6*).

Atomic forces can be calculated by taking the first derivative of energy with respect to the nuclear coordinates,

$$\langle F_{q\alpha}\rangle = -\frac{\partial}{\partial R_{q\alpha}}\frac{\langle \psi_{\mathrm{T}}|H|\psi_{\mathrm{T}}\rangle}{\langle \psi_{\mathrm{T}}|\psi_{\mathrm{T}}\rangle},$$

where q represents x, y, or z coordinate, α indexes the nuclei, and $R_{q\alpha}$ is a nuclear coordinate. For energy minimized trial wave functions, it can be shown that the force is given by $\langle F_{q\alpha}\rangle = \langle F_{q\alpha}^{\mathrm{HFT}}\rangle + \langle F_{q\alpha}^{\mathrm{Pulay}}\rangle$ as described in Ref. (*4*).

For VMC, $\langle F_{q\alpha}^{\mathrm{HFT}}\rangle$ can be calculated efficiently by using the following expression proposed by Assaraf and Caffarel (*1*),

$$\langle F_{q\alpha}^{\mathrm{HFT}}\rangle = \langle F_{q\alpha}^{\mathrm{AC}}\rangle = Z_{\alpha}\sum_{I\neq\alpha} Z_{I}\frac{(R_{q\alpha}-R_{qI})}{|\mathbf{R}_{I}-\mathbf{R}_{\alpha}|^{3}} - \left\langle \sum_{i=1}^{N_{\mathrm{elec}}} \nabla_{i} Q_{q\alpha}\cdot\frac{\nabla_{i}\psi_{\mathrm{T}}}{\psi_{\mathrm{T}}}\right\rangle,$$

where $Q_{q\alpha} = -Z_{\alpha}\sum_{i=1}^{N_{\mathrm{elec}}}(r_{qi}-R_{q\alpha})/|\mathbf{r}_{i}-\mathbf{R}_{\alpha}|$ and this term differs for each force component. A similar expression can be used in the DMC case (*1*).

The Pulay correction term for VMC is given by

$$\begin{aligned}\langle F_{q\alpha}^{\mathrm{Pulay}}\rangle &= -2\frac{\langle \partial\psi_{\mathrm{T}}/\partial R_{q\alpha}|H|\psi_{\mathrm{T}}\rangle}{\langle \psi_{\mathrm{T}}|\psi_{\mathrm{T}}\rangle} + 2\langle E_{\mathrm{L}}\rangle\frac{\langle \partial\psi_{\mathrm{T}}/\partial R_{q\alpha}|\psi_{\mathrm{T}}\rangle}{\langle \psi_{\mathrm{T}}|\psi_{\mathrm{T}}\rangle} \\ &= -2\left\langle \frac{\partial\psi_{\mathrm{T}}}{\partial R_{q\alpha}}\frac{E_{\mathrm{L}}}{\psi_{\mathrm{T}}}\right\rangle + 2\langle E_{\mathrm{L}}\rangle\left\langle \frac{\partial\psi_{\mathrm{T}}}{\partial R_{q\alpha}}\frac{1}{\psi_{\mathrm{T}}}\right\rangle,\end{aligned}$$

and a similar equation can be used for DMC (*4*).

Downloaded by UNIV OF GUELPH LIBRARY on July 4, 2012 | http://pubs.acs.org
Publication Date: December 31, 2006 | doi: 10.1021/bk-2007-0953.ch006

Results and Discussion

We calculated the energies and forces of first-row monohydrides and carbon monoxide at five different bond distances around the experimental bond length (0.90, 0.95, 1.00, 1.05, and 1.10 r_{exp}). We fitted the result to the Morse potential to take the anharmonicity into consideration.

Since the number of data points is small, we used the energy and force results simultaneously in the fitting to the Morse potential to get better results. With this fitting, various properties of diatomic molecules, such as equilibrium bond lengths, harmonic vibrational frequencies, and anharmonicity constants could be obtained (*6*).

Dissociation energies could also be calculated for these diatomic molecules by taking the differences between the energies of molecules and the energies of atoms. The dissociation energies and error bars obtained from our VMC and DMC calculations are summarized in Table I, together with the dissociation energies of our Hartree-Fock calculations. The VMC and DMC results and experimental values from Ref. (*8*) are also shown. Our VMC dissociation energies are closer to the experimental values than those given by L♦chow and Anderson (*8*), while our DMC results are similar to theirs. We think that better

Downloaded by UNIV OF GUELPH LIBRARY on July 4, 2012 | http://pubs.acs.org
Publication Date: December 31, 2006 | doi: 10.1021/bk-2007-0953.ch006

Table I. Dissociation energies of diatomic molecules in kcal/mol

	H-F	VMC	DMC	VMC[a]	DMC[a]	Exp[a]
LiH	34.2	54.7(1)	57.8(1)	45.7	57.8	58.0
BeH	50.3	57.9(2)	55.7(2)	49.4	52.1	49.8
BH	64.2	82.7(2)	84.7(3)	63	84.8	84.1
CH	56.9	81.1(3)	83.5(3)	81	83.9	83.9
NH	48.1	80.2(4)	82.3(4)	77	81.4	80.5-84.7
OH	68.6	105.1(5)	106.4(5)	86	106.4	106.6
HF	98.8	140.4(6)	141.4(6)	130	141.3	141.5
CO	177.6	218.1(6)	254.9(7)	-	-	258.7

[a] from Ref. (*8*)

VMC results in our calculation can be attributed to the energy minimization method, as compared to the variance minimization method used in Ref. (*8*).

The following compares the force components for the LiH molecule at the bond distance of 0.9 r_{exp}. First, the force on the hydrogen atom is displayed in Figure 1 (a) and (b). As can be seen in the figure, the Assaraf-Caffarel method reduces the noise considerably, enabling the efficient calculation of the Hellmann-Feynman theorem force. In the case of the force on the hydrogen atom, the Pulay correction was close to zero, so that the total force was quite similar to the Assaraf-Caffarel force, as can be seen in Figure 1 (b).

We also calculated the force on the lithium atom, which should be the negative of the force on the hydrogen atom, as LiH is a diatomic molecule, and it is shown in Figure 2 (a) and (b). The black horizontal line in the figure denotes the negative of the force on the hydrogen atom.

In the case of the force on the lithium atom, however, although the Assaraf-Caffarel method reduces the noise in the Hellmann-Feynman theorem force calculation, the Assaraf-Caffarel force does not agree with the negative of the force on the hydrogen atom. The total force on the lithium atom obtained by adding the Assaraf-Caffarel force and the Pulay correction agrees well with the negative of the force on the hydrogen atom, as can be clearly seen in Figure 2 (b).

For other hydrides, we calculated the atomic force only on the hydrogen atom. For all cases, the Pulay correction was very small. For carbon monoxide, however, the magnitude of the Pulay correction was larger than that of the Assaraf-Caffarel force, and was important in obtaining correct atomic forces. As can be seen in Figure 3, the total force on the carbon atom is similar to the total force on the oxygen atom in magnitude, and their directions are opposite, while for the Assaraf-Caffarel force, their magnitudes for the carbon atom and the oxygen atom are quite different. It seems that the Pulay correction is indispensable in the calculation of forces on nonhydrogen atoms.

We performed VMC and DMC calculation of energies for the methylene radical, the methyl radical, and the methane molecule at their experimental geometries and then obtained the dissociation energies. The result is summarized in Table II together with the Hartree-Fock result. The Hartree-Fock method shows poor results, as is the case for the dissociation energies of diatomic molecules, while the QMC method considerably corrects errors in the Hartree-Fock calculation, making it promising as an accurate method for the calculation of reaction energies. It can be noted that the QMC method is good in predicting the bond dissociation energies irrespective of the spin states of the reactant and product molecules.

Downloaded by UNIV OF GUELPH LIBRARY on July 4, 2012 | http://pubs.acs.org
Publication Date: December 31, 2006 | doi: 10.1021/bk-2007-0953.ch006

Downloaded by UNIV OF GUELPH LIBRARY on July 4, 2012 | http://pubs.acs.org
Publication Date: December 31, 2006 | doi: 10.1021/bk-2007-0953.ch006

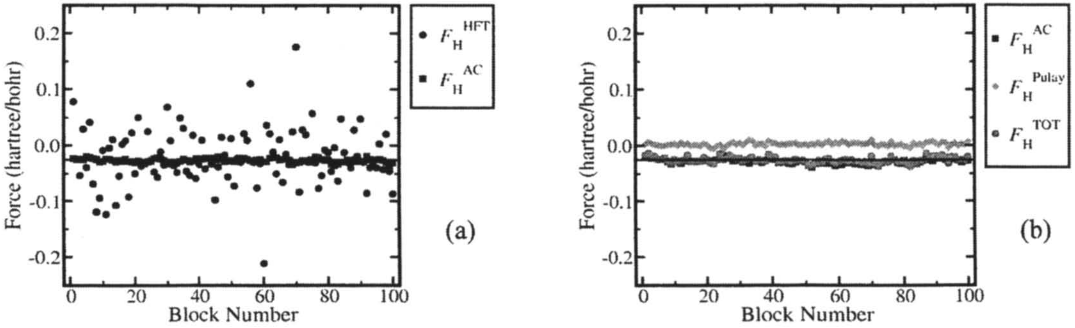

Figure 1. Force on hydrogen atom in the VMC force calculation of LiH molecule. (a) Hellmann-Feynman theorem force and Assaraf-Caffarel force, and (b) Assaraf-Caffarel force, Pulay correction, and total force.

Downloaded by UNIV OF GUELPH LIBRARY on July 4, 2012 | http://pubs.acs.org
Publication Date: December 31, 2006 | doi: 10.1021/bk-2007-0953.ch006

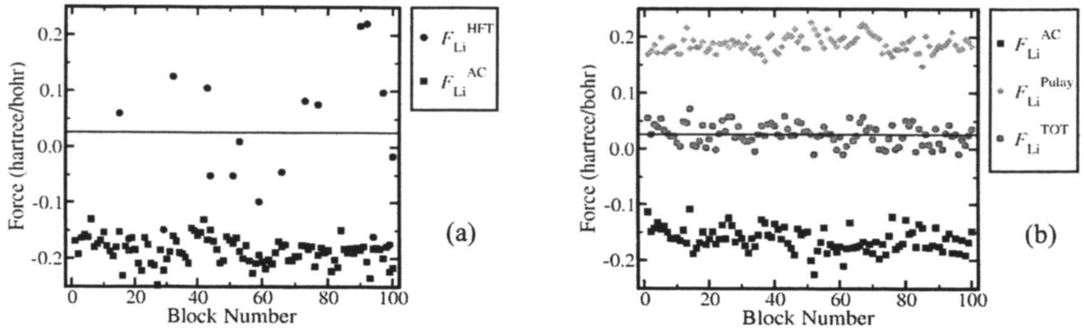

Figure 2. Force on lithium atom in the VMC force calculation of LiH molecule. (a) Hellmann-Feynman theorem force and Assaraf-Caffarel force, and (b) Assaraf-Caffarel force, Pulay correction, and total force.

Downloaded by UNIV OF GUELPH LIBRARY on July 4, 2012 | http://pubs.acs.org
Publication Date: December 31, 2006 | doi: 10.1021/bk-2007-0953.ch006

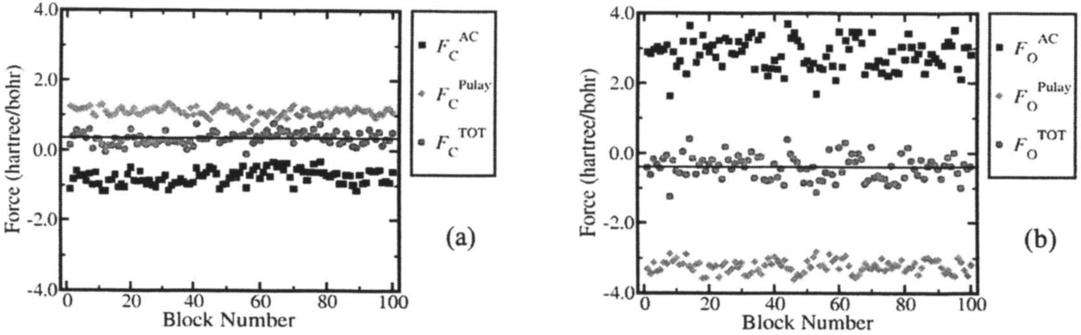

Figure 3. Force calculation of CO molecule. (a) Force on carbon atom, and (b) force on oxygen atom.

Table II. Dissociation energies of some polyatomic molecules in kcal/mol

Process	H-F	VMC	DMC	Exp
$CH_4(g) \rightarrow CH_3(g) + H(g)$	88	109	112	104
$CH_3(g) \rightarrow CH_2(g) + H(g)$	99	122	125	108
$CH_2(g) \rightarrow CH(g) + H(g)$	86	101	103	102

For the singlet methylene radical (CH_2), we calculated the force on each atom at various geometries. The calculated forces were in the direction to restore the experimental geometry, as is the case for the LiH molecule above. The force on each atom is depicted in Figure 4 using an arrow on each atom, whose direction is the same as the direction of the force and the magnitude proportional to the magnitude of the force. At the experimental geometry, each force component was close to zero as expected. For other geometries where the bond lengths or bond angles are changed, the forces we obtained were generally as expected. While the forces on hydrogen atoms look correct in all cases, the force on the carbon atom deviated from the expected direction in some cases. We could calculate the forces on the hydrogen atoms quite accurately, but longer simulation time may be necessary to get more accurate forces on larger atoms.

The preliminary result of our benzene QMC energy calculation at the experimental geometry is shown in Figure 5. The first data point at about -230.8 hartrees is the reproduction of the Hartree-Fock energy. Initially, the steepest descent method was applied (iterations 2-17). We used 4 parameters for iterations 2-6, 40 parameters for iterations 7-10, and 64 parameters for iterations 11-17. Even after these steepest descent steps, the noise in the Hessian was so large that it was difficult to apply Newton's method when we used the equation for the Hessian calculation in our previous work (*7*). So we used the Hessian in the symmetrized covariance form as proposed by Umrigar and Filippi (*9*),

$$\bar{E}_{ij} = 2\left[\left\langle\left(\frac{\psi_{ij}}{\psi}+\frac{\psi_i\psi_j}{\psi^2}\right)(E_{\mathrm{L}}-\bar{E})\right\rangle - \left\langle\frac{\psi_i}{\psi}\right\rangle\bar{E}_j - \left\langle\frac{\psi_j}{\psi}\right\rangle\bar{E}_i\right]$$

$$+\left\langle\frac{\psi_i}{\psi}E_{\mathrm{L},j}\right\rangle - \left\langle\frac{\psi_i}{\psi}\right\rangle\left\langle E_{\mathrm{L},j}\right\rangle + \left\langle\frac{\psi_j}{\psi}E_{\mathrm{L},i}\right\rangle - \left\langle\frac{\psi_j}{\psi}\right\rangle\left\langle E_{\mathrm{L},i}\right\rangle .$$

This scheme reduced the noise considerably and we could apply Newton's method as used for diatomic molecules. After the VMC calculation, we performed a DMC calculation (iterations 23-26), which reduced the energy even more. The final calculated energy for benzene is -232.17 hartrees, which may be compared with the experimentally derived value of -232.26 hartrees.

Downloaded by UNIV OF GUELPH LIBRARY on July 4, 2012 | http://pubs.acs.org
Publication Date: December 31, 2006 | doi: 10.1021/bk-2007-0953.ch006

Downloaded by UNIV OF GUELPH LIBRARY on July 4, 2012 | http://pubs.acs.org
Publication Date: December 31, 2006 | doi: 10.1021/bk-2007-0953.ch006

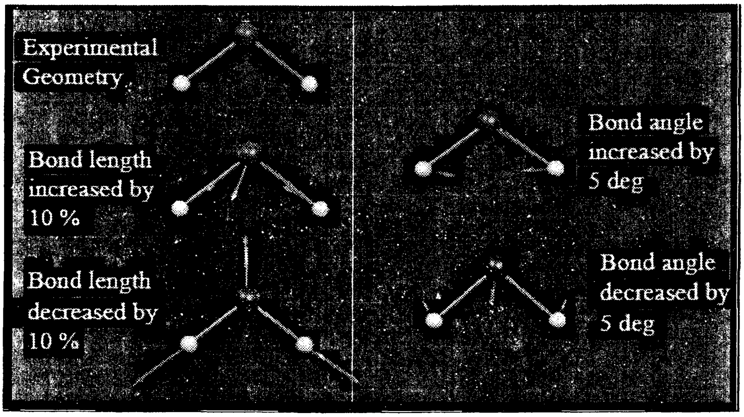
Experimental Geometry
Bond length increased by 10 %
Bond length decreased by 10 %
Bond angle increased by 5 deg
Bond angle decreased by 5 deg

Figure 4. Force calculation of CH_2 radical at various geometries

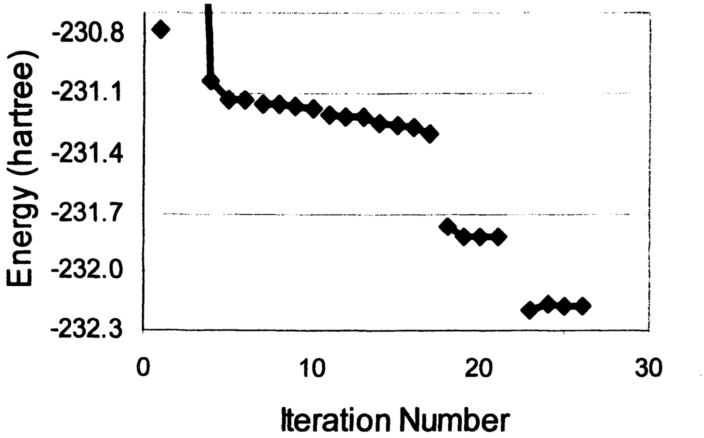

Figure 5. Energy of benzene in the course of QMC calculation

Conclusions

The force calculation method combining energy minimization, a renormalized Hellmann-Feynman estimator, and a Pulay correction worked well with all the first-row hydride molecules, carbon monoxide, and some polyatomic molecules with very little extra effort.

The energy minimization method in VMC is useful, but it requires an effective optimization scheme. The addition of steepest descents to the initial steps and to the subspace neglected by Newton's method with SVD seems to be advantageous for the molecular systems we investigated. For larger systems, the use of the covariance form in the Hessian calculation seems indispensable due to the large noise.

We could calculate accurate harmonic vibrational frequencies and anharmonicity constants of diatomic molecules by fitting QMC results to the Morse potential, achieving good agreement between QMC calculations and experiment for these vibrational parameters.

Acknowledgments

This work was supported by the Air Force Office of Scientific Research, Air Force Material Command, USAF, under Grant No. FA9550-04-1-0077. Computational support was provided by the Defense University Research Instrumentation Program, and by the NSF CRIF program, Grant CHE-0131132.

References

1. Assaraf, R.; Caffarel, M. *J. Chem. Phys.* **2000,** *113,* 4028
2. Assaraf, R.; Caffarel, M. *J. Chem. Phys.* **2003,** *119,* 10536
3. Filippi, C.; Umrigar, C. J. *Phys. Rev. B* **2000,** *61,* R16291
4. Casalegno, M.; Mella, M.; Rappe, A. M. *J. Chem. Phys.* **2003,** *118,* 7193
5. Chiesa, S.; Ceperley, D. M.; Zhang, S. *Phys. Rev. Lett.* **2005,** *94,* 036404
6. Lee, M. W.; Mella, M.; Rappe, A. M. *J. Chem. Phys.* **2005,** *122,* 244103
7. Lin, X.; Zhang, H.; Rappe, A. M. *J. Chem. Phys.* **2000,** *112,* 2650
8. Lüchow, A.; Anderson, J. B. *J. Chem. Phys.* **1996,** *105,* 7573
9. Umrigar, C. J.; Filippi, C. *Phys. Rev. Lett.* **2005,** *94,* 150201

Downloaded by UNIV OF GUELPH LIBRARY on July 4, 2012 | http://pubs.acs.org
Publication Date: December 31, 2006 | doi: 10.1021/bk-2007-0953.ch006

Downloaded by CORNELL UNIV on July 4, 2012 | http://pubs.acs.org
Publication Date: December 31, 2006 | doi: 10.1021/bk-2007-0953.ch007

Chapter 7

The Fixed Hypernode Method for the Solution of the Many Body Schroedinger Equation

F. Pederiva[1], M. H. Kalos[2], F. Reboredo[2]. D. Bressanini[3], D. Guclu[4], L. Colletti[1], and C. J. Umrigar[4]

[1]Dipartimento di Fisica, Universita di Trento, Povo, Trento, Italy
[2]Lawrence Livermore National Laboratory, Livermore, CA 94550
[3]Dipartimento di Scienze Chimiche e Ambientali, Università dell'Insubria, Como, Italy
[4]Cornell Theory Center, Cornell University, Ithaca, NY 14853

We propose a new scheme for an approximate solution of the Schroedinger equation for a many-body interacting system, based on the use of pairs of walkers. Trial wavefunctions for these pairs are combinations of standard symmetric and antisymmetric wavefunctions. The method consists in applying a fixed-node restriction in the enlarged space, and computing the energy of the antisymmetric state from the knowledge of the exact ground state energy for the symmetric state. We made two conjectures: first, that this fixed-hypernode energy is an upper bound to the true fermion energy; second, that this bound is lower than the usual fixed-node energy using the same antisymmetric trial function. The first conjecture is true, and is proved in this paper. The second is not, and numerical and analytical counterexamples are given. The question of whether the fixed-hypernode energy can be better than the usual bound remains open.

In Advances in Quantum Monte Carlo; Anderson, J., et al.;
ACS Symposium Series; American Chemical Society: Washington, DC, 2006.

Introduction

Monte Carlo methods can be used to compute characteristics of many natural processes such as thermodynamic and transport properties of materials and, in particular, diffusion problems. This method is a fundamental tool for studying the many-body problem in quantum mechanics, in particular, the ground state energy of a many-body interacting system. The Schroedinger equation in real time is transformed into a diffusion equation in imaginary time, where the kinetic energy plays the role of a diffusion term and the potential is a source or sink of particles. Indeed, for positive imaginary times, the operator $\exp(-H\tau)$ acting on any state with no null projection c into the ground state $|g\rangle$ converges asymptotically to $c\exp(E_0\tau)\ |g\rangle$.[1] This provides a simple recipe to obtain the ground state energy of a many-body quantum system with a diffusion algorithm. However, there is an important limitation: since the ground state of a many-body system is a symmetric (bosonic) wavefunction, the evaluation of the energy of fermionic systems cannot be obtained only using this technique. Additional constraints must be added to force the wavefunctions to remain antisymmetric in the diffusion process[2]. In practice, the requirement of antisymmetry imposes boundary conditions upon the wavefunction. In this chapter we will describe a possible alternative to the standard fixed node approach based on the use of an extended space which is the product of the configuration space of the system under consideration by itself, in which a diffusion equation for pairs of points in the configuration space is implemented. Additional constraints are added in order to guarantee antisymmetry in the extended space. Such constraints in principle do not correspond to imposing a fixed-node constraint in the configuration space. In the next section we will review the fixed-node approximation. In the third section hypernodal functions in the product space will be introduced. The fourth section is devoted to the proof of upper bound properties for a restricted algorithm using hypernodal functions. The fifth section will present some results and some of the open questions related to this formalism.

Fixed node approximation

One of the earliest and still common approaches to impose antisymmetry is the so called fixed-node (FN) approximation[2]. In the standard FN-DMC, a trial wavefunction $\psi(\mathbf{r})$ is used to impose a fixed-node boundary condition (where $\mathbf{r}$ denotes the $3N$ coordinates of the electrons). The trial wavefunction must satisfy some conditions described below[3]. The walkers that generate the diffusion process are constrained to remain in a volume inside the nodes of $\psi(\mathbf{r})$. Thus, the nodes act as a boundary having an infinite repulsive potential. Any point $\mathbf{r}$

Downloaded by CORNELL UNIV on July 4, 2012 | http://pubs.acs.org
Publication Date: December 31, 2006 | doi: 10.1021/bk-2007-0953.ch007

inside a volume defined by the nodes, has images generated by symmetry operations on other volumes $S_n\mathbf{r}$ (where S_n are all possible permutations of electronic coordinates). Ideally the nodes of $\psi(\mathbf{r})$ must define volumes that expand the complete $3N$ space Ω by applying all the symmetry operations of the group; that is, all the permutations of coordinates. This imposes some restrictions on the nature of the trial wavefunctions that can be used (i.e. for the ground state, they cannot have more nodes than required by symmetry.) Various techniques are used to contract these trial wavefunctions, typically including Slater determinants of appropriate basis functions and two-body correlations by way of Jastrow products. DMC in the fixed-node approximation yields the ground state wavefunction $\psi_{FN}(\mathbf{r})$ inside a volume defined by the nodes of $\psi(\mathbf{r})$ Since $\psi_{FN}(\mathbf{r})$ is obtained by projecting out the high-energy components of the original trial wavefunction compatible with its nodes, the corresponding expectation value of H must be less than or equal to that of the original trial wavefunction.

An antisymmetric wavefunction that expands the full volume Ω can be obtained from $\psi_{FN}(\mathbf{r})$ with the operation:

$$\psi^{*}_{FN}(S_n\mathbf{r}) = \sum_n \chi^F(S_n)\psi_{FN}(\mathbf{r}). \tag{1}$$

The function $\psi^{*}_{FN}(\mathbf{r})$ is, by construction, an antisymmetric wave function because $\chi^{F}(S_n)$ are the characters of the permutations operations in the antisymmetric representations of the symmetric group, *i.e.*, the $\chi^{F}(S_n)=1$ for even permutations and $\chi^{F}(S_n)=1$ for odd permutations. Therefore, the fixed-node approximation limits the search of the fermionic ground state to the subspace of linear combinations of antisymmetric wavefunctions that share the nodes of a trial wavefunction $\psi(\mathbf{r})$. Since the ground state of the true fermion problem $\psi_0(\mathbf{r})$ could have in principle different nodes than $\psi(\mathbf{r})$, we only obtain an upper bound of the fermionic ground state energy. The difference between this upper estimate and the true ground state energy is the *nodal error* of the fixed-node approximation.

Hypernodal functions

Various attempts have been explored to overcome the limitations imposed by the fixed-node approximation. Here we propose an algorithm which in principle should be able to go beyond the highly successful but nevertheless still limited fixed-node diffusion Monte Carlo.

We propose an alternative construction of the nodes in an expanded space that doubles the dimensions of the usual FN-DMC, and we impose fixed-node

Downloaded by CORNELL UNIV on July 4, 2012 | http://pubs.acs.org
Publication Date: December 31, 2006 | doi: 10.1021/bk-2007-0953.ch007

boundary conditions in this 6N-dimensional space. Instead of the usual fixed-node approximation we propose determining the nodes using functions of the form:

$$\begin{aligned}\psi^{b}_{HN}(R) &= \psi_A(\mathbf{r}_1)\psi_S(\mathbf{r}_2)+\psi_S(\mathbf{r}_1)\psi_A(\mathbf{r}_2)\\ \psi^{c}_{HN}(R) &= \psi_A(\mathbf{r}_1)\psi_S(\mathbf{r}_2)-\psi_S(\mathbf{r}_1)\psi_A(\mathbf{r}_2)\end{aligned} \tag{2}$$

where R=($\mathbf{r}_1$,$\mathbf{r}_2$), and the indexes 1 and 2 denote that the wavefunctions act on different subspaces with *3N* coordinates each. It is straightforward to see that, if ε_A and ε_S are the ground state energies of the fermionic and bosonic problem respectively, then

$$H\psi^{b,c}_{HN}(R) = (H_1 + H_2)\psi^{b,c}_{HN} = (\varepsilon_A + \varepsilon_S)\psi^{b,c}_{HN} \tag{3}$$

where H_1 and H_2 are identical except that H_1 acts on the set (1) of *3N* coordinates and H_2 on the set (2). It remains to be shown that the ground state solution within the nodes of functions of the form $\psi^b{}_{HN}$ and $\psi^c{}_{HN}$ have higher energy than $\varepsilon_A+\varepsilon_S$. That implies that the the energy of the lowest energy state of a domain inside the nodes of $\psi^b{}_{HN}$ or $\psi^c{}_{HN}$ is necessarily also the energy of a function with the structure of $\psi^b{}_{HN}$ or $\psi^c{}_{HN}$.

A key step in the standard fixed-node approximation is the selection of an antisymmetric trial wavefunction, that is, an irreducible representation of dimension 1 of the group of all permutations of electronic coordinates[4]. The irreducible representations of dimension 1 are eigenvectors of every operator S_n with eigenvalues $\chi^{\upsilon}(S_n)$ denoted as characters. In general, for any H, if $\psi^{\upsilon}(\mathbf{r})$ belongs to an irreducible representation ν of H of dimension 1 of some group of symmetry operations S_n, the nodes of $\psi^{\upsilon}(\mathbf{r})$ transform as H. That is $S_n H=H$ and if $\psi(\mathbf{r})=0$, then

$$\psi(S_n\mathbf{r}) = \chi^{\nu}(S_n)\psi(\mathbf{r}) = 0 \tag{4}$$

for every S_n. The $\chi^{\upsilon}(S_n)$ are denoted as characters of the operator S_n on the representation ν. Thus all volumes enclosed by the nodes of an irreducible representation of dimension 1 $\psi^{\nu}(\mathbf{r})$ are equivalent by symmetry operations.

Accordingly, and provided that there are no additional accidental nodes, the full volume Ω can be expanded using Eq. (1). On the contrary, if $\psi(\mathbf{r})$ is a mixture of two or more representations i) the nodes and the volumes enclosed are no longer equivalent by symmetry, ii) there is no way to obtain by symmetry operations the value of the ground state wavefunction outside a given volume; iii) since the volume are not equivalent, fixed nodes on different volumes give different energies.

Downloaded by CORNELL UNIV on July 4, 2012 | http://pubs.acs.org
Publication Date: December 31, 2006 | doi: 10.1021/bk-2007-0953.ch007

In summary, in order to obtain an upper bound estimation of a ground state, it is key that the ground state belong to an irreducible representation of dimension 1 of the symmetry group of $H=H_1+H_2$. Using a trial wavefunction of the same irreducible representation will give an upper limit for the energy. Thus in order to prove the upper bound it is necessary and sufficient to demonstrate that functions of the form $\psi^b{}_{HN}$ or $\psi^c{}_{HN}$ are irreducible representations of dimension 1 of some symmetry group that expands the volume Ω⊗Ω. Therefore, in the following section we will i) find the symmetry group ii) demonstrate that $\psi^b{}_{HN}$ or $\psi^c{}_{HN}$ are irreducible representations with dimension 1 of the a group and iii) extend the ground state fixed-hypernode wavefunction in all of the higher-dimensional space Ω⊗Ω.

Downloaded by CORNELL UNIV on July 4, 2012 | http://pubs.acs.org
Publication Date: December 31, 2006 | doi: 10.1021/bk-2007-0953.ch007

The extended Hamiltonian symmetries and some representations

In order to prove that $\psi^b{}_{HN}$ and $\psi^c{}_{HN}$ are irreducible representations of some group, we need to recall some properties of the symmetric group (the group of all possible permutations). Every permutation in the symmetric group commutes with the many-body Hamiltonian of identical particles. In quantum mechanics, irreducible representations are associated with quantum numbers or conserved quantities such as parity, angular momentum, etc. Good quantum numbers appear every time there is an operator that commutes with the Hamiltonian. There are two trivial 1-dimensional representations of the symmetric group. These representations are the identity (symmetric), with character 1 for every member of the group, and the antisymmetric representation, with character 1 for even and -1 for odd permutations. Depending on the order of the group (which is the number of permutations $N!$) there may be many other representations.

In the case of the antisymmetric wavefunctions the quantity conserved can be related to the operator

$$Q^F = \frac{1}{N!}\sum_n \chi^F(S_n)S_n \qquad (5)$$

that has eigenvalue 1 for every antisymmetric wavefunction and zero otherwise. It is possible to define analogously a bosonic operator Q^B which consists of the sum of all permutations with eigenvalue 1. The operators Q^F and Q^B can be rewritten as:

$$Q^F = [1 - S_{ij}][\Sigma E] = [\Sigma E][1 - S_{ij}]$$
$$Q^B = [1 + S_{ij}][\Sigma E] = [\Sigma E][1 + S_{ij}], \tag{6}$$

where S_{ij} is any single pair exchange and $[\Sigma E]$ the sum over all even permutations.

Suppose that $S_{ij}(1)$ is any permutation of two coordinates i,j on the space (1) and $S_{lm}(2)$is another permutation acting on space (2). Since these two operators commute, the character table of the group generated by the product can be factored out as a product of the character tables of the subgroups. Moreover, the irreducible representations of the product group are products of the irreducible representations of the factors. Thus, since we know two irreducible representations of the symmetric group we can trivially guess four irreducible representations of the product group. They are given by:

$$\begin{aligned}
&\psi^a_{HN}(R) = \psi_S(\mathbf{r}_1)\psi_S(\mathbf{r}_2)\\
&\frac{\psi^b_{HN}(R) + \psi^c_{HN}(R)}{2} = \psi_S(\mathbf{r}_1)\psi_A(\mathbf{r}_2)\\
&\frac{\psi^b_{HN}(R) - \psi^c_{HN}(R)}{2} = \psi_A(\mathbf{r}_1)\psi_S(\mathbf{r}_2)\\
&\psi^d_{HN}(R) = \psi_A(\mathbf{r}_1)\psi_A(\mathbf{r}_2)
\end{aligned} \tag{7}$$

There is a symmetry operation of the Hamiltonian that we have not considered so far: the exchange of all coordinates in the subsets (1) and (2) denoted by the operator P. Applying P to the irreducible representations of the product of permutations in Eq. (7) one immediately finds that P mixes the second and third representation of the subgroup of all permutations in Eq.(7). Therefore, functions of the form ψ^b_{HN} and ψ^c_{HN} generate an irreducible representation of dimension 2 of the group all symmetry operations of H, and it is possible to define the operator T,

$$T(b,c) = Q^F(1)\, Q^B(2) + Q^B(1)\, Q^F(2) \tag{8}$$

which is the associated projector into that subspace [see Eq.(6)]. This case is analogous to the group of continuous rotations in spherical symmetry. The representations have dimensions larger than one for angular momentum $l > 0$. Because ψ^b_{HN} and ψ^c_{HN} belong to the same representation they give rise to degenerate states. Eigenfunctions within a representation with dimension larger than 1 can be classified according to a symmetry operation in the group. The

Downloaded by CORNELL UNIV on July 4, 2012 | http://pubs.acs.org
Publication Date: December 31, 2006 | doi: 10.1021/bk-2007-0953.ch007

exchange operator P can be used to assign an additional quantum number to them with eigenvectors of the form $\psi^b{}_{HN}$ and $\psi^c{}_{HN}$. The associated projectors are:

$$T(b) = \frac{(E+P)}{2} T(b,c)$$
$$T(c) = \frac{(E-P)}{2} T(b,c) \tag{9}$$

Physically, one can also remove these degeneracies by breaking the symmetries of the Hamiltonian. We will follow this path to find a group that has $\psi^b{}_{HN}$ and $\psi^c{}_{HN}$ as distinct irreducible representations. For that we consider only the permutations that commute with P, that is, only permutations of the form $S_n(1).S_n(2)$.

The group of all $S_n(1).S_n(2)$ is an isomorphism of the symmetric group of the S_n acting in a single space. Thus they have the same character tables. Multiplying every $S_n(1).S_n(2)$ by E or P defines a larger group of order $2N!$. Taking advantage of the knowledge of two irreducible representations of the symmetric group one can generate the projectors of four representations of the product group. Since, as in the previous case the projectors are the product of the subgroups projectors:

$$\begin{aligned} T(a) &= (P+E)Q(+) \\ T(b) &= (P+E)Q(-) \\ T(c) &= (P-E)Q(-) \\ T(d) &= (P-E)Q(+) \end{aligned} \tag{10}$$

with

$$\begin{aligned} Q(1,2)(\pm) &= \sum_n \chi^{B,F}(S_n) S_n(1).S_n(2) = \\ &= [1 \pm S_{ij}(1) S_{ij}(2)][\Sigma E(1).\Sigma E(2)]/N! \\ &= [\Sigma E(1).\Sigma E(2)][1 \pm S_{ij}(1) S_{ij}(2)]/N! \end{aligned} \tag{11}$$

where $S_{ij}(\sigma)$ is any single pair permutation acting on the set of coordinates σ, $[\Sigma E(1).E(2)]$ is the sum over all the products of even permutations, and $N!$ is the total number of permutations. By construction $Q(\pm)$ are projectors on the symmetric and the antisymmetric representation of the group generated by

Downloaded by CORNELL UNIV on July 4, 2012 | http://pubs.acs.org
Publication Date: December 31, 2006 | doi: 10.1021/bk-2007-0953.ch007

$S_n(1).S_n(2)$. Since the even permutations are a subgroup of the symmetric group one has that $[\Sigma E(1).E(2)][\Sigma E(1).E(2)]=[\Sigma E(1).E(2)]\ N!/2$ and one can therefore show that $Q(1,2)\,Q(1,2) = Q(1,2)$.

It is easy to see that

$$\begin{aligned} T(b,E)\psi^b_{HN} &= \psi^b_{HN} \\ T(b,E)\psi^c_{HN} &= 0 \\ T(c,E)\psi^c_{HN} &= \psi^c_{HN} \\ T(c,E)\psi^b_{HN} &= 0 \end{aligned} \tag{12}$$

Also any symmetry operation outside this reduced group such as $S_n(1).S_m(2) = S_n(1).S_n(2).S_n(2).S_m(2) = S_n(1).S_n(2).S_k(2)$ may be applied to $\psi^b{}_{HN}$:

$$\begin{aligned} S_n(1).S_n(2).S_k(2)\psi^b_{HN} &= \psi^b_{HN} && S_n, S_k \text{ even} \\ S_n(1).S_n(2).S_k(2)\psi^b_{HN} &= -\psi^b_{HN} && S_n \text{ odd}, S_k \text{ even} \\ S_n(1).S_n(2).S_k(2)\psi^b_{HN} &= \psi^c_{HN} && S_n \text{ even}, S_k \text{ odd} \\ S_n(1).S_n(2).S_k(2)\psi^b_{HN} &= -\psi^c_{HN} && S_n, S_k \text{ odd} \end{aligned} \tag{13}$$

Similar rules are found for $\psi^c{}_{HN}$. Therefore, only if $S_k(2)$ is odd are the representations $\psi^b{}_{HN}$ and $\psi^c{}_{HN}$ mixed. In other words, we only need to remove the symmetries $S_n(1).S_n(2).S_k(2)$ when $S_k(2)$ is odd to split $\psi^b{}_{HN}$ and $\psi^c{}_{HN}$. Since we know that $\psi^b{}_{HN}$ is an eigenvector of all $S_n(1).S_n(2).S_k(2)$, and of P for $S_k(2)$ even, and that the eigenvalues are the same for different even $S_k(2)$, we can write the associated projector that includes these symmetries as

$$\frac{1}{2N!}\sum_{S_k \text{ even}} T(b/c,E)S_k(2) = T(b/c)\frac{1}{2N!}[\Sigma E(2)] \tag{14}$$

With a little work it can be shown now that the projectors $T(b)$ and $T(c)$ defined in Eq. (9) and (14) are indeed identical. Therefore, $T(b)$ and $T(c)$ project into a representation of dimension 1 of a group, namely the one formed by all P and all $S_n(1).S_n(2).S_k(2)$ with $S_k(2)$ even. Thus $\psi^b{}_{HN}$ and $\psi^c{}_{HN}$ are irreducible representations of dimension 1 of a subgroup of symmetries of H and the volume enclosed by their nodes can be extended to the complete space by application of the operations of the subgroup. That is what we wanted to prove.

Downloaded by CORNELL UNIV on July 4, 2012 | http://pubs.acs.org
Publication Date: December 31, 2006 | doi: 10.1021/bk-2007-0953.ch007

In other words, just as the permutations are enough to construct an antisymmetric function over the full space, so, in our larger space, the permutations plus interchange of the two sets of coordinates serves the same purpose.

Results

The fixed-hypernode algorithm is a straightforward extension of the standard fixed-node procedure. Instead of working with a single walker, we use pairs of walkers, each one defined in the subspaces 1 and 2 respectively. Each walker is drifted/diffused according to the usual prescription using as importance function either ψ^b_{HN} or ψ^c_{HN}. Moves are rejected whenever the importance function changes sign, and the energy is projected out of the importance function. The outcome is an upper bound for the sum of the energies of the symmetric and antisymmetric ground states. Additionally, one needs to compute the energy of the symmetric state by means of standard Diffusion Monte Carlo. The difference between this quantity and the FHN eigenvalue will give an upper bound for the ground state of the fermionic state.

The important issue is to assess the quality of this upper bound with respect to the standard FN value. In fact, it can be easily seen that walkers subject to the FHN constraint are not in principle constrained within a nodal pocket in the configuration space, and more space can be explored.

However, this fact in itself is not enough to guarantee that the FHN upper bound is better (or worse) than the FN bound.

Numerical experiments were performed on two different systems. The first was a N=6 electrons quantum dot, defined by the Hamiltonian[5]

$$H=\sum_{i=1}^{N}\left(-\frac{\hbar^2}{2m_e m^*}\nabla^2+\frac{1}{2}m_e m^*\omega^2 r_i^2\right)+\frac{e^2}{\varepsilon}\sum_{i<j}\frac{1}{|r_i-r_j|} \qquad (15)$$

where m^* =0.067 and ε=12.4 are the effective mass and effective dielectric constant which approximate electrons in GaAs, and ω=3.32meV is the confinement constant of the dot. For this system the FN energy in effective atomic units (effective Hartrees) is 7.6001(1). The FHN eigenvalue is 14.752(5), and the energy for the equivalent symmetric system is 7.1086(1), giving as an estimate for the antisymmetric ground state 7.643(3), which is higher than the fixed node estimate.

More tests of this procedure have been performed on the Be atom, using different importance functions with different degrees of optimization[6]. The results are summarized in Table I. The wavefunctions labelled as A, B and C in the table are obtained using in the construction of the hypernodal function, antisymmetric functions which are respectively a one-determinant trial

Downloaded by CORNELL UNIV on July 4, 2012 | http://pubs.acs.org
Publication Date: December 31, 2006 | doi: 10.1021/bk-2007-0953.ch007

Table I. Fixed-hypernode results for the Be atom

Wavefunction	*DMC*	*VMC*
Boson	-19.26439(1)	-19.27439(1)
A FN	-14.6578(3)	-14.615(2)
A FHN	-33.9323(3)	-33.890(2)
A FHN-Boson	-14.6579(3)	-14.616(2)
B FN	-14.6571(3)	-14.6400(2)
B FHN	-33.9313(3)	-33.9144(2)
B FHN-Boson	-14.6570(3)	-14.6401(4)
C FN	-14.66721(1)	-14.6665(4)
C FHN	-33.94512(20	-33.94158(2)
C FHN-Boson	-14.66719(3)	-14.6665(2)
Exact[7]	-14.66736	

wavefunction with incorrect cusp and non-optimized parameters (A), a one-determinant wavefunction with correct cusp and optimized parameters (B), and a four-determinant wavefunction with correct cusp and optimized parameters (C).

As it can be seen from the table, the results are in contrast with the conjecture that the FHN upper bound is lower than the standard FN one. In particular, it can be noticed that the FHN estimates for the Fermion eigenvalue (i) do strongly depend on the choice of the *antisymmetric function* used to build the hypernodal function and (ii) are essentially the same as the FN estimates for that particular antisymmetric function. This result would suggest that although the nodal properties of the hypernodal functions are not directly related to the nodes of the antisymmetric function used, some of this information is passed into the doubled space. This point is not completely clarified at present.

It is however possible to show that in general using a good antisymmetric trial function for building an hypernodal function does not lead in principle to better eigenvalues. In fact, let us assume that we know an approximate antisymmetric trial whose nodes are *exact.* For instance, let us consider the problem of a particle in a two dimensional square box of side 1, seeking an estimate of the eigenvalue for the first spatial antisymmetric solution. Let φ_S be an approximation of $\cos(\pi x/2)$. We can build four approximations of the exact degenerate antisymmetric eigenstates, each one with an *exact node*:

Downloaded by CORNELL UNIV on July 4, 2012 | http://pubs.acs.org
Publication Date: December 31, 2006 | doi: 10.1021/bk-2007-0953.ch007

$$\begin{aligned}\psi_1 &= \varphi_S(x)\sin(\pi y)\\ \psi_2 &= \varphi_S(y)\sin(\pi x)\\ \psi_3 &= \varphi_S(y)\sin(\pi x) - \varphi_S(x)\sin(\pi y)\\ \psi_4 &= \varphi_S(y)\sin(\pi x) + \varphi_S(x)\sin(\pi y)\end{aligned} \qquad (16)$$

Obviously, if we used FN-DMC for computing the expectation value of the Hamiltonian using any of these functions, we would obtain the exact eigenvalue. On the other hand, if we build an hypernodal function starting from a symmetric function $\Psi_S = \varphi_S(x)\,\varphi_S(y)$:

$$\Psi_{HN} = \Psi_S(x_1, y_1)\Psi_3(x_2, y_2) - \Psi_S(x_2, y_2)\Psi_3(x_1, y_1) \qquad (17)$$

it is easy to see that the hypernodes are given from the following expression:

$$\frac{\sin(\pi y_1)}{\varphi_S(y_1)} - \frac{\sin(\pi x_1)}{\varphi_S(x_1)} - \frac{\sin(\pi y_2)}{\varphi_S(y_2)} + \frac{\sin(\pi x_2)}{\varphi_S(x_2)} = 0 \qquad (18)$$

which in general has hypernodes which (i) depend on the choice of φ_S and (ii) *do not coincide with the exact hypernode.* Therefore, the estimate of the energy for the antisymmetric state will be *worse* than the corresponding fixed-node estimate. So, in general, it is possible to build hypernodal function with a wrong hypernodal surface starting from functions with the correct nodal surface.

However, in a general case neither the exact nodal structure nor the exact hypernodal structure are known, so it is difficult to assess the relative quality of the two estimates.

In general, a possible strategy for better exploiting the hypernodal functions would be that of optimizing the hypernodal structure (following a variational procedure analogous to that used for standard functions), rather than relying on the optimization of the antisymmetric functions. Some aspects though, like the correspondence between the FN and FHN results in the case of the Be atom, warrant additional study.

Acknowledgements

Acknowledgment is made to the donors of The American Chemical Society Petroleum Research Fund for partial support of this research. This work was performed under the auspices of the U.S. Department of Energy by the University of California, Lawrence Livermore National Laboratory under contract No. W-7405-Eng.-48.

Downloaded by CORNELL UNIV on July 4, 2012 | http://pubs.acs.org
Publication Date: December 31, 2006 | doi: 10.1021/bk-2007-0953.ch007

References

1. J.B. Anderson, J. Chem. Phys. **63**, 1499 (1975).
2. P.J. Reynolds, D.M. Ceperley, B.J. Alder, and W.A. Lester, Jr., J. Chem. Phys. **77**, 5593 (1982).
3. W.M.C. Foulkes, L. Mitas, R. J. Needs and G. Rajagopal, Rev. Mod. Phys. **73**, 33–83 (2001).
4. See e.g. M. Hamermesh, *Group Theory and its Application to Physical Problems*, 1st ed., Addison-Wesley/Dover, 1962.
5. For a QMC treatment of quantum dots see F. Pederiva, C.J. Umrigar, and E. Lipparini, Phys. Rev. **B62**, 8120 (2000).
6. C-J. Huang, C.J. Umrigar, M.P. Nightingale, J. Chem. Phys. **107**, 3007 (1997).
7. S.J. Chakravorty, S.R. Gwaltney, E.R. Davidson, F.A. Parpia, and C.F. Fischer, Phys. Rev. **A47**, 3649 (1993).

Downloaded by CORNELL UNIV on July 4, 2012 | http://pubs.acs.org
Publication Date: December 31, 2006 | doi: 10.1021/bk-2007-0953.ch007

Downloaded by STANFORD UNIV GREEN LIBR on July 3, 2012 | http://pubs.acs.org
Publication Date: December 31, 2006 | doi: 10.1021/bk-2007-0953.ch008

Chapter 8

Recent Progress in Fermion Monte Carlo

M. H. Kalos[1] and F. Pederiva[2]

[1]Lawrence Livermore National Laboratory, Livermore, CA 94550
[2]Dipartimento di Fisica, Università di Trento, Povo, Trento, Italy

Our approach to the solution of the Schrödinger Equation for many-fermion systems has been extensively revised. We have devised a generalization of "acceptance/rejection" that applies to signed random walkers. We have introduced a new class of importance functions for two walkers that better reflects the structure of the enlarged Euclidean space of the pair. For greater flexibility, we no longer rely on the "local energy" of the importance function to determine the dynamics of the walk. We sketch these technical changes and give new results for the two-dimensional electron gas.

Introduction

This paper is a progress report on our research in Fermion Monte Carlo, which is aimed at developing a method for solving many-fermion problems that is efficient in the spirit of Monte Carlo methods, that is polynomial in particle number, and that uses no uncontrolled approximations.

The phrase "no uncontrolled approximations" is often used in a somewhat ambiguous way. We propose the following criteria:

In Advances in Quantum Monte Carlo; Anderson, J., et al.;
ACS Symposium Series; American Chemical Society: Washington, DC, 2006.

1. Any calculation should produce an error estimate. In a Monte Carlo calculation, the statistical error is not sufficient: what is required is an internal estimate of the difference between the expected value and the correct answer to the physical or mathematical model being solved.

2. The results should agree with known exact results or with reliable experimental data if available.

3. The computer time required to reduce the total error by some fraction should be a polynomial of low degree in the ratio of errors.

The criteria deserve further discussion. Criterion 2 can hardly be controversial; perhaps a reminder is needed that experimental results can be wrong or wrongly interpreted.

The desirability of criterion 3 is clear, but often ignored: many computations can be carried through to an apparently satisfactory level of agreement with other results, but can only be further improved at great cost, either because of an approximation essential to the computation, a combinatorial explosion in an expansion or a set of basis functions, or because of the inherent computational complexity of the method. Nevertheless, we restrict the term "no uncontrolled approximations" to methods that satisfy it.

Criterion 3 is clearly the most stringent. Many numerical calculations—and purely theoretical work as well—require physical, mathematical, or numerical approximations to be feasible. We do not assert that such calculations are invalid. Indeed, in the work described below and elsewhere we make two well-known approximations—neglect of relativistic effects and fixing the nuclear positions. The effect of these can be accurately estimated. Our argument is that a numerical solution of the non-relativistic Schrödinger equation for a many-electron system that has no uncontrolled approximations would be a tremendously valuable asset to the theory of electronic structure. Since corresponding methods for the ground state of many-boson systems exist and have also proved valuable, it is natural to seek the analog for many-fermion systems.

It is the notorious "fermion sign problem" that makes the extension difficult. Perhaps another digression is worth while. If one defines a "sign problem" in Monte Carlo as the degradation of statistical efficiency because of the presence of negative signs, then there are many "sign problems." Some are provably intractable; some are clearly trivial or can be transformed away.

Downloaded by STANFORD UNIV GREEN LIBR on July 3, 2012 | http://pubs.acs.org
Publication Date: December 31, 2006 | doi: 10.1021/bk-2007-0953.ch008

Downloaded by STANFORD UNIV GREEN LIBR on July 3, 2012 | http://pubs.acs.org
Publication Date: December 31, 2006 | doi: 10.1021/bk-2007-0953.ch008

The sign problem that arises in treating the Schrödinger equation for many-fermion systems is not trivial, but it is not known to be intractable.

The standard way to treat such systems within the framework of Quantum Monte Carlo[1] is to impose the "fixed-node approximation,"[2] namely to choose an antisymmetric trial function and to follow walkers that diffuse only in domains in which that function does not change sign. If one removes the fixed-node constraint, then the Monte Carlo estimates of the numerator and denominator of the energy quotient degenerate exponentially fast to zero with statistical errors that asymptotically dominate their mean values. This behavior reflects the fact that the distributions of the random walkers converge to that of the symmetric ground state in which the averages of antisymmetric test functions are zero.

The difficulty is not simply technical; it reflects some deep challenges. These can be characterized in several ways that may be clues about how to cure them.

One way of describing the problem is that the random walk that solves the Schrödinger equation is "local." All decisions about the dynamics are based on the position of a walker. But the Pauli principle is global in character; it connects the properties of a physically acceptable solution at distinct points usually well separated in configuration space. Reconciling the random walk with antisymmetry seems to require some action at a distance. In effect, this is what the fixed-node restriction does, at the cost of an uncontrolled approximation.

We introduce walkers with algebraic signs: a positive walker adds its contributions (which may have either sign) to numerator and denominator of the energy quotient. A negative walker subtracts its contributions. The use of such signed walkers does nothing in itself to avoid the asymptotic decay of signal to noise as described above. If these walkers diffuse independently then the distributions of both populations will approach that of the symmetric ground state. But there is now an opportunity to ameliorate that decay by changing the dynamics. Clearly, the two walkers must obey different dynamics; at the least they must follow different guiding functions. If not, then, in the long run the two populations will have the same distributions (corrected for the effect of importance sampling) namely that of the symmetric ground state.

Another opportunity for improvement lies in the possibility of canceling walkers of opposite signs against each other, while leaving unchanged the projections with antisymmetric test functions. While this is straightforward in principle, it is effective only when the walkers are close to each other, and close pairs become exponentially rare in high-dimensional space— i.e. for large particle numbers.

Correlating the dynamics of two random walkers makes it possible to cancel walkers efficiently even for many-body systems.

Our research[3] has been motivated by the expectation that this sign problem can be solved in an effective way, using these and perhaps other techniques.

Downloaded by STANFORD UNIV GREEN LIBR on July 3, 2012 | http://pubs.acs.org
Publication Date: December 31, 2006 | doi: 10.1021/bk-2007-0953.ch008

Importance functions

Let $\varphi_A(\mathbf{R})$ and $\varphi_S(\mathbf{R})$ be approximate wave functions for the antisymmetric and symmetric ground states of our system. Now define

$$\begin{aligned}
&\Phi_G^{\pm}(\mathbf{R}) = \sqrt{\varphi_S^2(\mathbf{R}) + g_1^2\varphi_A^2(\mathbf{R})} \pm g_0\varphi_A(\mathbf{R}) + g_0\,|\,\varphi_A(\mathbf{R})\,|;\\
&\Phi_S(\mathbf{R}) = \sqrt{\varphi_S^2(\mathbf{R}) + g_1^2\varphi_A^2(\mathbf{R})}; \qquad (1)\\
&\Psi(\mathbf{R}^+,\mathbf{R}^-) = \Phi_G^{+}(\mathbf{R}^+)\Phi_S(\mathbf{R}^-) + \Phi_S(\mathbf{R}^-)\Phi_G^{-}(\mathbf{R}^+).
\end{aligned}$$

The parameters g_k are adjusted to achieve stability and minimize the variance of the fermion energy.

Note that $\Phi^{\pm}_G$ and Ψ have cusps at the nodes of $\varphi_A(\mathbf{R})$. An alternative to $\Phi^{\pm}_G$ with no cusps is

$$\begin{aligned}
\Phi_G^{\pm}(\mathbf{R}) = {} & \sqrt{\varphi_S^2(\mathbf{R}) + g_1^2\varphi_A^2(\mathbf{R})} \pm g_0\varphi_A(\mathbf{R})\\
& + \; g_0\sqrt{\varphi_A^2(\mathbf{R}) + g_2^2(\nabla\varphi_A(\mathbf{R}))^2},
\end{aligned} \qquad (2)$$

where $\nabla\,\varphi_A(\mathbf{R})$ measures the change of $\varphi_A(\mathbf{R})$ needed to smooth the cusp.

The following properties hold for any an odd permutation *P*.

$$\Phi_G^{\pm}(P\mathbf{R}) = \Phi_G^{\pm}(\mathbf{R}) \qquad (3)$$

$$\begin{aligned}
&\Psi(P\mathbf{R}^+, P\mathbf{R}^-) = \Psi(\mathbf{R}^-,\mathbf{R}^+)\\
&\Psi(P\mathbf{R}^+, P\mathbf{R}^-) \neq \Psi(\mathbf{R}^+,\mathbf{R}^-).
\end{aligned} \qquad (4)$$

If $\mathbf{R}_0^+$, $\mathbf{R}_0^-$ are such that

$$\begin{aligned}
&\varphi_A(\mathbf{R}_0^+) > 0\\
&\varphi_A(\mathbf{R}_0^-) < 0
\end{aligned} \qquad (5)$$

then

$$\begin{aligned}
&\Psi(\mathbf{R}_0^+,\mathbf{R}_0^-) > \Psi(P\mathbf{R}_0^+,\mathbf{R}_0^-) > \Psi(P\mathbf{R}_0^+,P\mathbf{R}_0^-),\\
&\Psi(\mathbf{R}_0^+,\mathbf{R}_0^-) > \Psi(\mathbf{R}_0^+,P\mathbf{R}_0^-) > \Psi(P\mathbf{R}_0^+,P\mathbf{R}_0^-).
\end{aligned} \qquad (6)$$

These last inequalities state that if both the positive and negative walkers are in their favorable "pockets," then the importance functions Ψ are decreased when odd permutations are applied to either or both sets of coordinates in either order.

In practice, the function Ψ was modified further to reflect the fact that cancellation of close walkers means that the importance must vanish as they approach each other. Consideration of the diffusion process with cancellation suggests the following form:

$$\Psi_C(\mathbf{R}^+,\mathbf{R}^-) = \Psi(\mathbf{R}^+,\mathbf{R}^-)\,erf(g_3 k_F/(2\pi)\,|\,\mathbf{R}^+ - \mathbf{R}^-\,|). \tag{7}$$

As indicated above, in the computations reported here, the drift and branching for the basic diffusion Monte Carlo was carried out using the symmetric trial function $\varphi_S(\mathbf{R})$. This takes care of cusps associated with the physical potentials—here Coulomb potentials. Then after a pair of walkers is advanced by means of drift, correlated diffusion, symmetric branching, cancellation, and " repairing," the new pairs are branched again on the basis of the ratio of Ψ_C before and after.

It is useful to review here the technique involved in correlating the two walkers. The diffusion step for any walker requires generating a 3N-dimensional vector $\mathbf{U}^+$ whose components are drawn independently from a Gaussian distribution of mean zero and variance $\delta\tau$, the increment in imaginary time. That is, a positive walker is moved from $\mathbf{S}^+$ to $\mathbf{R}^+$ by

$$\mathbf{R}^+ = \mathbf{S}^+ + \mathbf{U}^+, \tag{8}$$

and a negative walker by

$$\mathbf{R}^- = \mathbf{S}^- + \mathbf{U}^-, \tag{9}$$

where

$$\mathbf{U}^- = \mathbf{U}^+ - 2\left[\frac{\mathbf{S}^+ - \mathbf{S}^-}{|\,\mathbf{S}^+ - \mathbf{S}^-\,|}\cdot\mathbf{U}^+\right]\frac{\mathbf{S}^+ - \mathbf{S}^-}{|\,\mathbf{S}^+ - \mathbf{S}^-\,|}. \tag{10}$$

Downloaded by STANFORD UNIV GREEN LIBR on July 3, 2012 | http://pubs.acs.org
Publication Date: December 31, 2006 | doi: 10.1021/bk-2007-0953.ch008

Acceptance/Rejection Dynamics

We review here a few basics of DMC dynamics and show how it can be generalized to take into account acceptance/rejection, correlated diffusion, and cancellation. We use the simple unsymmetric short-time propagator

$$G_0(\mathbf{R},\mathbf{S};\delta\tau)=\frac{\exp\left[-(\mathbf{R}-\mathbf{S}-\delta\tau\nabla\varphi_S(\mathbf{S}))/\varphi_S(\mathbf{S}))^2/2\delta\tau\right]}{(2\pi\delta\tau)^{3N/2}} \qquad (11)$$

and define

$$\begin{aligned} E_L(\mathbf{R}) &= \frac{H\varphi_S(\mathbf{S})}{\varphi_S(\mathbf{S})}; \\ B(\mathbf{R}) &= e^{[E_T-E_L(\mathbf{R})]\delta\tau}; \\ G(\mathbf{R},\mathbf{S};\delta\tau) &= B(\mathbf{R})G_0(\mathbf{R},\mathbf{S};\delta\tau). \end{aligned} \qquad (12)$$

Cancellation of walkers means that the algebraic density of walkers of opposite signs that is generated by means of G_0 can be canceled if they are close enough. When importance sampling is used, what is cancelled is the density unweighted by the importance function. So a pair of walkers ($\mathbf{R}_k^+$, $\mathbf{R}_k^-$) generates an unweighted net density at **R** given by

$$\begin{aligned} &\psi_F(\mathbf{R},\tau+\delta\tau)= \\ &\frac{B(\mathbf{R})G_0(\mathbf{R},\mathbf{R}_k^+;\delta\tau))}{\varphi_S(\mathbf{R})}-\frac{B(\mathbf{R})G_0(\mathbf{R},\mathbf{R}_k^-;\delta\tau))}{\varphi_S(\mathbf{R})}. \end{aligned} \qquad (13)$$

Using "acceptance/rejection" means replacing the propagator G by

$$\begin{aligned} G_{AR}(\mathbf{R},\mathbf{S};\delta\tau) &= A(\mathbf{R},\mathbf{S})B(\mathbf{R})G_0(\mathbf{R},\mathbf{S};\delta\tau) \\ &+ p_r(\mathbf{S})B(\mathbf{S})\delta(\mathbf{R}-\mathbf{S}) \end{aligned} \qquad (14)$$

Downloaded by STANFORD UNIV GREEN LIBR on July 3, 2012 | http://pubs.acs.org
Publication Date: December 31, 2006 | doi: 10.1021/bk-2007-0953.ch008

where A(**R**,**S**) is the probability that a move proposed from **S** to **R** is accepted, and p_r is the total probability that moves from **S** are rejected. We separate positive and negative parts of the density by applying the identity

$$x = \max(x,0) - \max(-x,0). \tag{15}$$

We find the following propagators for the positive and negative parts of the future density:

$$\begin{aligned} G^+_{CAR}(\mathbf{R},\mathbf{R}^+_k;\delta\tau) &= A(\mathbf{R},\mathbf{R}^+_k)B(\mathbf{R})G_0(\mathbf{R},\mathbf{R}^+_k;\delta\tau) \\ &\quad \times \max(1-\frac{A(\mathbf{R},\mathbf{R}^-_k)G_0(\mathbf{R},\mathbf{R}^-_k;\delta\tau)}{A(\mathbf{R},\mathbf{R}^+_k)G_0(\mathbf{R},\mathbf{R}^+_k;\delta\tau)},0) \\ &\quad + p_r(\mathbf{R}^+_k)B(\mathbf{R}^+_k)\delta(\mathbf{R}-\mathbf{R}^+_k); \\ G^-_{CAR}(\mathbf{R},\mathbf{R}^-_k;\delta\tau) &= A(\mathbf{R},\mathbf{R}^-_k)B(\mathbf{R})G_0(\mathbf{R},\mathbf{R}^-_k;\delta\tau) \\ &\quad \times \max(1-\frac{A(\mathbf{R},\mathbf{R}^+_k)G_0(\mathbf{R},\mathbf{R}^+_k;\delta\tau)}{A(\mathbf{R},\mathbf{R}^-_k)G_0(\mathbf{R},\mathbf{R}^-_k;\delta\tau)},0) \\ &\quad + p_r(\mathbf{R}^-_k)B(\mathbf{R}^-_k)\delta(\mathbf{R}-\mathbf{R}^-_k). \end{aligned} \tag{16}$$

Results for the two-dimensional electron gas

We have carried out a set of computations for the two-dimensional electron gas at $r_s = 1$. The symmetric trial function, $\varphi_S(\mathbf{R})$, was simply an electron-electron Jastrow product, and the antisymmetric function, $\varphi_A(\mathbf{R})$, was $\varphi_S(\mathbf{R})$ times a Slater determinant of plane waves. Recall that in the present form of our methods, there can be linear dependence in time step and noticeable dependence on population size, so that a substantial computing effort is required. Results are summarized in Table 1 and compared with a calculation by Kwon, Ceperley, and Martin[4] (which included backflow in the determinant basis functions). FMC(1) refers to a set of calculations with importance functions with cusps; FMC(2) to a set without cusps. The fact that these agree with each other and with the reliable released node computation[4] is a strong verification of the correctness of our method.

In Table 2, we show the decline in the computational efficiency as electron number, increases from 10 to 26. The "figure of merit" is the product of the variance of a typical run by the aggregate computing time for that run. It is notable that this measure of efficiency decreases only by a factor of two as the

Downloaded by STANFORD UNIV GREEN LIBR on July 3, 2012 | http://pubs.acs.org
Publication Date: December 31, 2006 | doi: 10.1021/bk-2007-0953.ch008

Table 1. Energy per particle for the two-dimensional electron gas at $r_s = 1$

N_e	FMC(1)	FMC(2)	DMC
10	-0.4582(10)		
26	-0.3910(17)	-0.3908(17)	-0.3910(12)*

* Released node[4]

Table 2. Efficiency vs. electron number

N_e	Computing time per step*	Figure of merit*
10	0.018	0.0077
26	0.101	0.016

* Arbitrary relative units

electron number doubles. Preliminary results show a modest increase for 58 electrons; we are in the process of revising our programs to treat larger electron systems even more efficiently.

Acknowledgements

This work was performed under the auspices of the U.S. Department of Energy by the University of California, Lawrence Livermore National Laboratory under contract No. W-7405-Eng.-48.

References

1. P.J. Reynolds, D.M. Ceperley, B.J. Alder, and W.A. Lester, Jr., J. Chem. Phys. 77, 5593 (1982)
2. J.B. Anderson, J. Chem. Phys. **63**, 1499 (1975)
3. M. H. Kalos and F. Pederiva, Phys. Rev. Lett. **85**, 3457 (2000)
4. Y.Kwon, D..M. Ceperley, and R.M. Martin, Phys. Rev. B. **53**, 7376 (1996)

Downloaded by STANFORD UNIV GREEN LIBR on July 3, 2012 | http://pubs.acs.org
Publication Date: December 31, 2006 | doi: 10.1021/bk-2007-0953.ch008

Chapter 9

Quantum Effects in Loosely Bound Complexes

Meredith J. T. Jordan[1], Deborah L. Crittenden[1,2], and Keiran C. Thompson[1]

[1]School of Chemistry, University of Sydney, Sydney, New South Wales 2006, Australia
[2]Current address: Research School of Chemistry, Australian National University, Canberra, ACT 0200, Australia

This chapter presents the incorporation of vibrational diffusion Monte Carlo (DMC) calculations into the *Grow* algorithm for interpolating and iteratively converging molecular potential energy surfaces (PES). These surfaces are then used as a basis for calculating the ground state properties of loosely bound complexes. DMC calculations are incorporated into *Grow* in two ways. Firstly, DMC walkers are used to sample the configuration space of the complex, providing new geometries to be added to the PES data set. The convergence of the PES with respect to the size of the data set is then monitored with a second DMC calculation which calculates the zero point energy of the complex and/or various bond length distribution functions of interest. The methodology is developed using of an analytic PES for the water dimer, a prototypical loosely bound complex. The method is then applied to gas-phase and monohydrated 1,2-ethanediol, where the nature of intra- and inter-molecular hydrogen bonding is investigated. Although no evidence is found for intramolecular hydrogen bonding in 1,2-ethanediol, DMC calculations demonstrate the presence of intermolecular hydrogen bonds in the 1,2-ethanediol.H_2O complex. A second application is the hydrated glycyl radical, glycyl.$8H_2O$. A 280 point PES is generated and DMC calculations on this surface show that ground state glycyl.$8H_2O$ exists as a neutral molecule and not a zwitterion.

In Advances in Quantum Monte Carlo; Anderson, J., et al.;
ACS Symposium Series; American Chemical Society: Washington, DC, 2006.

DMC calculations are also used to investigate the ground state structure of another hydrated amino acid, γ-aminobutyric acid (GABA). A global PES for the GABA.5H_2O complex is generated based on the 9 local minima on the surface. DMC calculations are then used to investigate the conformational flexibility of ground state GABA.5H_2O.

Introduction

Loosely bound molecular complexes are common in chemistry and can occur as clusters, transition states and reactive intermediates. They are also central to many biological processes, in particular those involving weak interactions and inter- and intra-molecular proton transfer. Typically the molecular potential energy surface (PES) describing a loosely bound complex is characterised by multiple local minima. If the overall zero-point energy (ZPE) of the complex is comparable to or larger than the barriers between these local minima then the ground state molecular wavefunction may be delocalized over two or more minima. In this case the properties of the ground state may differ significantly from those of the lowest energy equilibrium configuration.(1-3)

The degree of nuclear delocalization due to zero-point motion and tunnelling may be determined from the ground state nuclear wavefunction. This wavefunction also allows calculation of any observable ground state properties. The ground state nuclear wavefunction may be calculated from the molecular PES using either variational methods which use expansions of the wavefunction, or Monte Carlo techniques such as quantum Diffusion Monte Carlo (DMC).(4-7) DMC techniques, however, have better scaling properties with increasing dimension than the variational, grid-based, methods which scale exponentially. DMC techniques can therefore be used to characterize large, loosely bound complexes.

DMC has been used previously to study many loosely bound molecular systems or complexes. For example, the intermolecular modes in water clusters, $(H_2O)_n$, have been studied extensively,(8-16) and other systems studied include $(HF)_2$,(17) $(DF)_3$,(18) $(HCl)_2$,(19) $(CO)_2$,(20) Ar_nHF,(21,22) N_2:H_2O(23) and CH_5^+(24) These previous DMC studies have employed either functional forms for the molecular PES, for example $(HF)_2$,(17) $(H_2O)_n$(8,9,11-16) and CH_5^+(24) or the direct *ab initio* calculation of the value of the molecular potential energy at each configuration sampled by the DMC procedure (direct DMC), for example $(H_2O)_2$(10) and phenol:$(H_2O)_n$.(25) Although using a functional form to represent the global PES is computationally inexpensive, the accuracy of the DMC calculation is limited by the parameterization of the surface. Furthermore the number of data points required for the multidimensional parametrization of a PES scales exponentially with dimension. Direct DMC is, in principle, the most accurate method. However, due to the high computational expense of accurate *ab initio* calculations and the large number of energy evaluations required per DMC simulation, this method is currently limited by the quality of the *ab initio* calculation performed. Typically, direct DMC simulations are only feasible using density functional theory with, at most, a double-zeta quality basis.(10,25)

Interpolation is an alternative method for the generation of a PES. A number of interpolation schemes have been proposed(26-38) and here we use the modified Shepard interpolation scheme of Collins and coworkers.(31-38) This scheme provides a method for obtaining a representation of the global PES with higher accuracy than using a functional form and with lower computational cost than direct DMC. The molecular PES is expressed as an interpolation over data that is scattered throughout the chemically relevant regions of conformational space, thus reducing the scaling with dimension that makes functional form PESs prohibitive for large systems. Each data point in the interpolation comprises a set of atomic coordinates, the corresponding energy and the first and second derivatives of the energy with respect to nuclear displacement, as calculated using a density functional or *ab initio* level of theory. For relatively small systems these calculations can be performed at chemically accurate levels of theory.(39) The potential energy at any arbitrary configuration is then expressed as a weighted sum of Taylor series expansions from neighbouring data points. The interpolation procedure is an iterative process in which the relevant configuration space is explored dynamically, providing a set of molecular configurations describing the chemically relevant regions of configuration space. Some of these molecular configurations are then chosen as new data points to create a new, expanded, data set. This procedure is repeated until the PES is converges for a given observable, that is, when the values of the observables calculated from the PES remain constant upon addition of extra data points.

Initially the dynamical sampling procedure used classical trajectory calculations to describe reactive PESs.(31-38,40-51) Bettens,(52) however, has demonstrated that using DMC walkers to sample configuration space is a cost-effective method for constructing a PES for the tightly bound fluoromethane system. In this case approximately 100 *ab initio* data points were required for convergence of the ground state energy of fluoromethane. Loosely bound complexes pose a more difficult problem because the volume of configuration space that needs to be covered by the interpolated PES is much larger. We have therefore optimized the PES iteration procedure to efficiently construct a PES for the water dimer, a prototypical loosely bound complex.(53)

This chapter presents the *Grow* algorithm for generating interpolated PESs and illustrates its optimization to the calculation of ground state properties of loosely bound complexes. Specifically we compare PES iteration schemes on an analytic PES for the water dimer (rather than using more computationally expensive *ab initio* calculations) and we sample new molecular configurations from the distribution of DMC walkers describing the ground state nuclear wavefunction. Having determined the most efficient methods of sampling configuration space, the resulting *Grow* methodology is then applied to three loosely bound systems.

1. 1,2-ethanediol/1,2-ethanediol.water. 1,2-ethanediol (ethylene glycol) serves as a prototypical polyhydroxlated biomolecule and can be used to model more complicated species such as sugars and more complex carbohydrates. It has been the subject of intensive theoretical(54-79) and experimental(55,57,62,79-90) investigation, which has centred on the presence, or lack thereof, of an intramolecular hydrogen bond. Here we generate PESs for ethanediol and the ethanediol.water complex and use DMC bond-length distribution functions to identify hydrogen bonds in the ground state structures of both species.
2. The glycyl radical. Glycine (NH_2–CH_2–COOH) is the smallest amino acid and the glycyl radical is formed from glycine by radical abstraction of a hydrogen atom. The glycyl radical (NH_2–$^{\bullet}$CH–COOH) provides a prototype for the intermediate in radical peptide reactions.(91) Glycine itself, in aqueous solution, exists as a zwitterion,(92) an overall neutral species with distinct, localized regions of positive and negative charge. Solvated glycine has a positively charged amino group on one end and a negatively charged carboxylate group on the other end of the molecule. The solvated glycyl radical, however, may exist as a neutral or zwitterionic species. Here we generate a PES for the glycyl radical loosely bound to 8 water molecules (glycyl.$8H_2O$) and use DMC techniques to describe the ground state structure.
3. γ-amino butyric acid (GABA). GABA (NH_2–CH_2–CH_2–CH_2–COOH) is a larger amino acid than glycine. In the mammalian central nervous system it is the major inhibitory neurotransmitter and plays a key role in regulating the firing of neurons.(93) As such, GABA is implicated in diseases and conditions such as epilepsy, schizophrenia, depression and Huntington's chorea.(93-96) New drugs acting at GABA receptors therefore hold promise in treating these diseases. To design these drugs, however, it is important to know the biologically active form (or forms) of GABA. GABA is known to exist in a variety of zwitterionic conformations in aqueous solution(97,98) and we use DMC to investigate the conformational flexibility of ground state solvated GABA, modelled as a GABA.$5H_2O$ weakly bound complex.

Quantum Diffusion Monte Carlo Calculations

Our focus is on ground state properties of loosely bound complexes. Because many of the systems considered are large (up to 34 atoms in the case of glycine.$8H_2O$), DMC calculations represent the only computationally feasible method for calculating vibrational ground state wavefunctions. In each case the DMC simulations follow the same overall form, as outlined below and as illustrated schematically in Figure 1.

The initial ensemble of M walkers is established by allowing a random fraction of a 0.5 Bohr displacement along each Cartesian axis of each atom from the specified minimum energy geometry (or geometries). The reference potential energy (E_{ref}) of the ensemble of walkers is then calculated as an ensemble average. The DMC simulation then enters the propagation phase, consisting of walking and branching steps. During the walking step the atomic displacements are sampled from a Gaussian distribution with variance:

$$\mathrm{var} = \frac{2\tau}{mass} \tag{1}$$

where τ is the timestep, in atomic units, and *mass* is the mass, in atomic units.

The new potential energy (E_i) of the ensemble of walkers is evaluated before the branching step. During the branching step, the branching weight of each walker:

$$w_i = e^{-\tau(E_i + E_{ref})} + rand \tag{2}$$

is used to determine the number of walkers created, where *rand* is a random number between zero and one. For weights lower than 1.0, the walker is annihilated. For walkers with higher weights, $w_i - 1$ extra replicas are created, to give total population P_{curr}.

The DMC walkers are equilibrated for N_{eq} steps using the walking and branching algorithms as illustrated in Figure 1. After the equilibration steps have been completed, the DMC walkers are propagated for an additional N_{prod} steps. The ensemble average energy, E_{ens}, is accumulated at each step as are the wavefunction histograms.

Finally, the ground state ZPE is calculated by averaging the accumulated E_{ens} values.

The DMC simulations are repeated N times, typically $N = 10$, and the results are quoted with errors corresponding to twice the standard error of the mean, $2\sigma/\sqrt{N}$, where σ is the standard deviation of the N independent DMC runs.

The Grow Algorithm

The *Grow* algorithm is an automated method that iteratively "grows" a molecular potential energy surface using *ab initio* calculations. It is described diagrammatically in Figure 2.

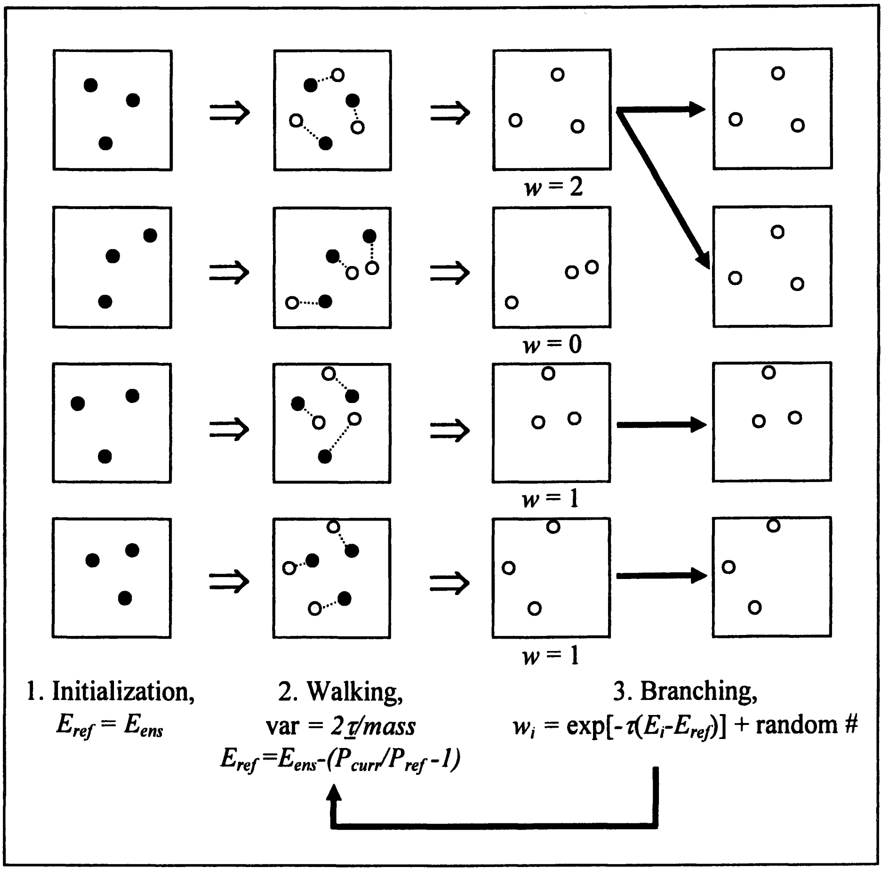
w = 2
w = 0
w = 1
w = 1
1. Initialization,
$E_{ref} = E_{ens}$
2. Walking,
var = $2\tau/mass$
$E_{ref}=E_{ens}-(P_{curr}/P_{ref}-1)$
3. Branching,
$w_i = \exp[-\tau(E_i-E_{ref})]$ + random #

Figure 1. Schematic Representation of the Quantum Diffusion Monte Carlo Simulation

Details of the modified Shepard interpolation scheme and the iteration techniques developed by Collins and coworkers to "grow" a PES may be found elsewhere.(31-38) The essential features of the *Grow* program, however, are summarised in Figure 2.

This Chapter describes the use of DMC in place of "dynamical" calculations to describe the ground state properties of a loosely bound complex and the use of the DMC walker configurations to choose new geometries to add to the PES data set.

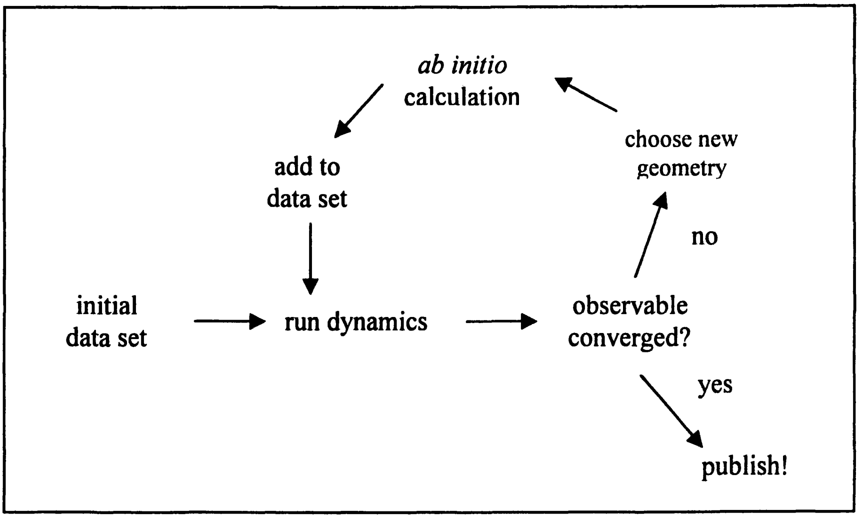
ab initio
calculation
add to
data set
choose new
geometry
no
initial
data set
run dynamics
observable
converged?
yes
publish!

Figure 2. Schematic representation of the Grow *algorithm for "growing" molecular potential energy surfaces.*

Potential Energy Surface Interpolation Scheme

The energy at an arbitrary molecular configuration is expressed, according to the modified Shepard interpolation scheme, as a weighted sum of Taylor polynomials in inverse interatomic distances, $\mathbf{Z} = \{1/R_1, 1/R_2, \ldots, 1/R_{3N-6}\}$, about N_d data points defining the PES data set and their symmetry equivalents:

$$V(\mathbf{Z}) = \sum_{g\in G}\sum_{i=1}^{N_d} w_{g\circ i}(\mathbf{Z})T_{g\circ i}(\mathbf{Z}) \tag{3}$$

$T_i(\mathbf{Z})$ is the Taylor series expansion about the i^{th} data point, typically truncated at second order:

$$\begin{aligned} T_i(\mathbf{Z}) = {} & V[\mathbf{Z}(i)] + \sum_{k=1}^{3N-6}[Z_k - Z_k(i)]\left.\frac{\partial V}{\partial Z_k}\right|_{\mathbf{Z}=\mathbf{Z}(i)} \\ & + \frac{1}{2!}\sum_{k=1}^{3N-6}\sum_{j=1}^{3N-6}[Z_k - Z_k(i)]\times[Z_j - Z_j(i)]\left.\frac{d^2V}{\partial Z_k \partial Z_j}\right|_{\mathbf{Z}=\mathbf{Z}(i)} \end{aligned} \tag{4}$$

and w_i is the normalized weight function, which gives the contribution of the i^{th} Taylor expansion to the potential energy at configuration **Z**. The weight function w_i is normalised by construction:

$$w_i(\mathrm{Z}) = \frac{v_i(\mathrm{Z})}{\sum\limits_{g \in G} \sum\limits_{i=1}^{N} v_{g \circ i}(\mathrm{Z})} \tag{5}$$

with the un-normalised primitive weight function, $v_i(\mathbf{Z})$, given by either a one-part formula:

$$v_i(\mathrm{Z}) = \left\| \mathrm{Z} - \mathrm{Z}_i \right\|^{-p} \tag{6}$$

or a two-part formula:

$$v_i(\mathrm{Z}) = \left\{ \left[\sum_{k=1}^{N(N-1)/2} \left(\frac{\left\| \mathrm{Z} - \mathrm{Z}_i \right\|}{\mathrm{d}_{\mathrm{k}}(i)} \right)^2 \right]^q + \left[\sum_{k=1}^{N(N-1)/2} \left(\frac{\left\| \mathrm{Z} - \mathrm{Z}_i \right\|}{\mathrm{d}_k(i)} \right)^2 \right]^p \right\}^{-1} \tag{7}$$

The un-normalized two-part weight function, Equation (7), includes $d_k(i)$ terms which are confidence lengths derived from Bayesian analysis of the interpolation data.(37) This type of weight function is more complex than the simple *one-part* weight function, Equation (6), but has been shown to give significantly greater accuracy in reactive systems(37,38) and for DMC calculations on the water dimer.(53)

The notation $g \in G$ in Equations (3) and (5) denotes the inclusion of all g elements from the permutation group G, which acts to interchange symmetry equivalent atoms in the system. Accordingly, $g \circ i$ denotes that the i^{th} data point is transformed by the group element g. In this manner, the interpolated PES is guaranteed to possess the correct nuclear permutation and inversion symmetry.

The quality of the PES produced depends on two factors: the *ab initio* theory used to generate the derivative data for the Taylor polynomials and the location of the PES data points in configuration space.

The PES interpolation scheme is illustrated in Figure 3 for two data points in one dimension using a simple one-part weight function, $v_i(Z) = 1/\|Z - Z_i\|^2$. Figure 3(a) shows the exact potential (heavy line) and second-order Taylor expansions about the two data points (×). Figure 3(b) indicates the effect of the weight function. At a point exactly half way between the two data points the interpolated potential weights the Taylor expansions of each equally. If, however, the point is only ¼ of the way from one data point to the next, the weight for the closest data point, using $v_i(Z) = 1/\|Z - Z_i\|^2$, is 0.90 whereas the

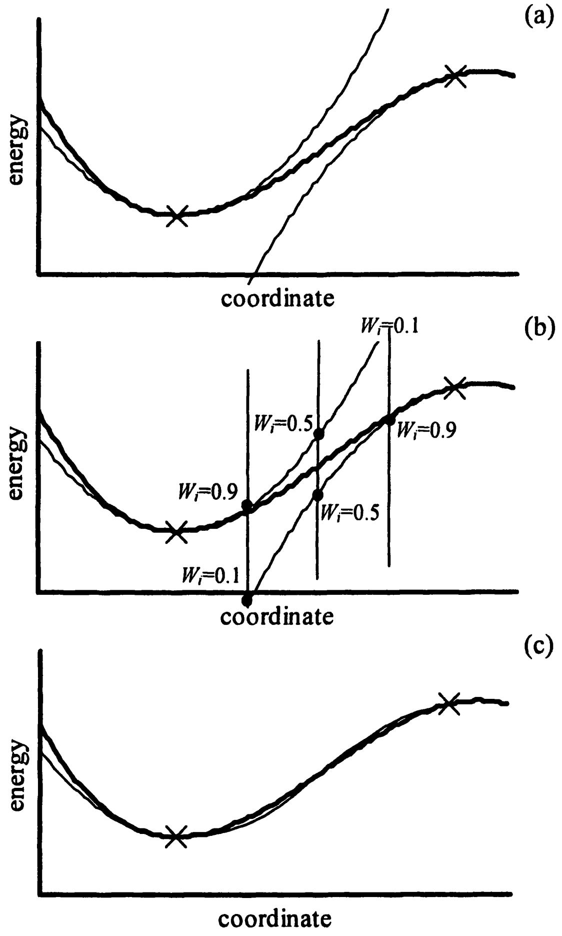

Figure 3. One-dimensional representation of the modified Shepard interpolation scheme for potential energy surfaces. The heavy solid line represents the exact potential. In (a) the light-weight line represents two separate second-order Taylor expansions about the two data points marked (x), in (b) representative weights are indicated between the two data points, using the weight function $v_i(Z) = 1/||Z - Z_i||^2$ and, in (c), the light-weight line indicates the interpolated potential based on the two indicated data points.

weight for the point further away is 0.10. In this way the interpolated potential weights the nearest data points most heavily. The final, interpolated potential is compared to the exact potential in Figure 3(c).

Potential Energy Surface Iteration Scheme

At the outset the interpolated PES is described by an initial set of data points. These may represent the reaction pathway for a reactive system, a set or subset of stationary points for a bound system or even a single point corresponding to the minimum energy configuration. The interpolated PES is then iteratively improved by adding data points to the initial data set. These points are sampled from the appropriate region of configuration space using some dynamical simulation of the system. Classical trajectories and the DMC walkers can both be used to sample the region of configuration space important to the ground state wavefunction. Classical trajectories have been shown to be appropriate for sampling the configuration space of reactive systems for both quantum(41-44) and classical(31-38,40,45-51) calculations of reaction dynamics. Although classical trajectory sampling has been used to grow surfaces for subsequent DMC calculations,(3,52) DMC simulations are more appropriate for sampling the configuration space of bound systems.(53) This is illustrated, in the following section, using the water dimer as a prototypical loosely bound complex.

The Water Dimer: $(H_2O)_2$

The water dimer was chosen as a prototypical loosely bound system because analytic representations of the PES have previously been derived.(99-102) Use of an analytic PES is advantageous in that it allows the *exact* ZPE and ground state properties to be calculated by performing DMC calculations directly on the analytic surface, providing benchmark values for testing PES convergence. Moreover, calculation of the energies, first and second derivatives required for "growing" the PES is trivial and the overall computational expense of constructing sn interpolated PES is determined primarily by the convergence properties of the DMC calculations. Here the water dimer potential of Reimers, Watts, and Klein,(101) denoted SW91, was used in lieu of *ab initio* calculations to provide the data required by the potential surface interpolation algorithm, Equation (3).

DMC simulations were run using the parameters specified in Tables I and II. Table I presents all of the parameters required to grow the PES and Table II the parameters used in the DMC calculations to test whether the interpolated

Table I. Parameters describing *Grow* calculations on the water dimer

Parameter	*Value*
DMC-sampling calculations:	
Number of starting geometries	1
Starting geometry	Global minimum on SW91 PES
Number of replicas, *M*, per starting geometry	1000
Maximum Cartesian displacement	0.5 a_0
Time step, τ	0.1 a.u.
Number of equilibration steps, N_{eq}	6 000
Number of data-accumulating steps, N_{prod}	20 000
Potential Energy Surface Interpolation:	
G	Sym(4)×Sym(2); |G|=48
Taylor Series truncation	2nd order
Weight function:	2-part
P	24
Q	2
Confidence length, $d_k(i)$	Determined by 50 closest data points
Energy tolerance for $d_k(i)$	0.5 kJ/mol

Table II. Parameters used in the DMC calculations to test convergence of the PESs for the water dimer

Parameter	*Value*
Number of starting geometries	1
Starting geometry	Global minimum on SW91 PES
Number of replicas, *M*, per starting geometry	1000
Maximum Cartesian displacement	0.5 a_0
Time step, τ	0.1 a.u.
Number of equilibration steps, N_{eq}	18 000
Number of data-accumulating steps, *N*	90 000
Number of independent DMC calculations, *N*	10

PESs had converged. The DMC parameters used in the iteration procedure were not as "rigorous" as those used for the convergence calculations. This reflects the fact that the DMC walkers provide a representative sampling of the important regions in configuration space long before the DMC calculation itself has converged. As the interpolated PESs were being constructed the configurations accessed by the DMC walkers were printed to file once every 1000 timesteps. These configurations were then sampled according the regimes outlined below, and the chosen points were added to the PES data set.

Two methods were used to determine which points to add from the sampled configuration space:

1. *h*-weight sampling.(32) Using this method the *n* configurations with the largest *h*-weight, Equation (8), are added to the PES data set for the next iteration.

$$h[Z(j)] = \frac{1}{N-1} \frac{\sum_{n=1,n\neq j}^{N} v_j[Z(n)]}{\sum_{g\in G}\sum_{i=1}^{N} v_{g\circ i}[Z(j)]} \tag{8}$$

   That is, the *n* configuration **Z***(j)* that are the "furthest" from the existing data points are added to the PES data set.

2. rms sampling.(35,36) The single sampled configuration with the largest variance in predicted energy, σ_v as calculated in Equation (9), is added to the PES data set.

$$\sigma_v^2(Z) = \sum_{g\in G}\sum_{i=1}^{N} w_{g\circ i}(Z)[T_{g\circ i}(Z) - V]^2 \tag{9}$$

   That is, the configuration **Z** for which the Taylor series estimates of the energy, *T(***Z***)*, from the different existing data points, $\mathbf{Z}_i$, were most variant is chosen for addition to the PES data set. *V* in Equation (9) is the average of the Taylor series predictions of the energy. This method, however, allows only a single configuration to be added to the data set in any iteration.

The two sampling methods have been utilized alone or in combination using a PES constructed using the two-part weight function, Equation (7), which was found to be more efficient than the one-part weight function.(53) The four sampling regimes considered were:

A. 1rms1hwt: add one DMC-sampled rms configuration and one DMC-sampled *h*-weight configuration to the PES data set per iteration. This regime was used by Bettens to develop a PES for CH_3F.(52)
B. 1rms9hwt: add one DMC-sampled rms configuration and 9 DMC-sampled *h*-weight configurations to the PES data set per iteration
C. allrms: add one DMC-sampled rms-sampled configuration to the PES data set per iteration
D. allhwt: add one DMC-sampled *h*-weight configuration to the PES data set per iteration

In calculations on the water dimer PES it was found that the DMC walkers sampled configurations significantly higher in energy than the ZPE. These configurations occurred with low probability and did not contribute significantly to the overall averaged ZPE but were weighted highly by both the *h*-weight and rms-weight methods. To avoid the PES being dominated by such configurations, if a selected DMC-sampled configuration had a predicted energy greater than 0.1 E_h above the global minimum energy it was rejected and the sampling procedure was repeated until an eligible point was added to the PES data set.

The convergence of the water dimer ZPE and the wavefunction histograms were monitored, with respect to the equivalent quantities calculated on the analytic SW91 PES, for the PES iteration schemesoutlines above.

Figure 4 plots the convergence of the water dimer ZPE for each of the 4 regimes as a function of the number of unique data points in the PES data set. From Figure 4 it can be seen that regimes A, B and C all appear to converge the water dimer ZPE upon the addition of 25-50 unique data points to the PES data set. In the case of the water dimer the most computationally efficient of the regimes considered was regime B, the addition of 1 rms and 9 *h*-weight points per sampling run. This regime enabled the addition of 10 PES data points per iteration, thus reducing the number of DMC-sampling runs required and significantly reducing the overall computational expense of the PES iteration procedure. For other systems, however, if the computational cost of the *ab initio* calculations required for each new data point is greater than the cost of the DMC calculations, regime A may be more efficient.

The vibrationally-averaged O-O distance distribution function of the water dimer was also examined for the regime B scheme with the results illustrated in Figure 5 for the initial, 1 point PES and the 100 data point PES. The O-O radial distribution function represents the projection of $(|\psi|/4\pi r^2)^2$ onto the O-O distance. The wavefunction histogram was projected onto the O-O distance and then scaled by $4\pi r^2$ prior to squaring the wavefunction amplitude in order to account for the Jacobian of the transformation from space-fixed to internal coordinates.

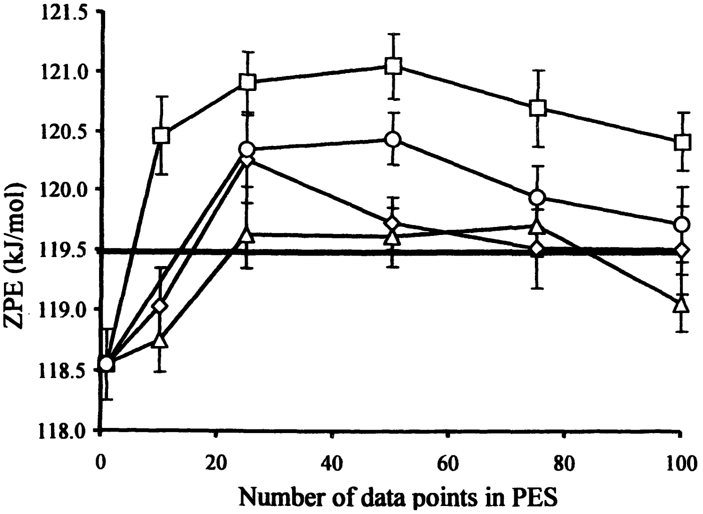

Figure 4. The ZPE of the water dimer as a function of the number of unique data points in the PES data file for PESs determined using iteration regime A (○), regime B (◇), regime C (△) and regime D (□). For reference, the exact result on the SW91 PES is indicated by the heavy solid line and the shaded rectangle. All errors represent two standard errors of the mean as calculated from 10 independent DMC simulations (Figure 3, reprinted with permission in Reference 53. Copyright 2004 American Institute of Physics).

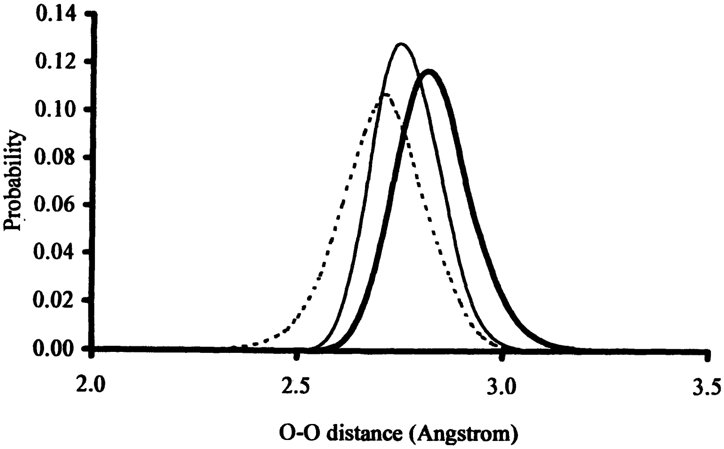

Figure 5. The O-O radial distribution function from the ground state wavefunction of the water dimer as calculated from the SW91 PES (heavy solid line) and using a 1 point PES (dotted line) and a 100 data point PES determined using DMC-sampling (light-weight line).

It can be observed from Figure 5 that the vibrationally averaged O-O bondlength converges more slowly than the ZPE, Figure 4. That is, the radial distribution function is more sensitive to the nature of the PES than the ZPE with the slow convergence of the O-O radial distribution function reflecting the slow convergence of the PES in the O-O coordinate. An examination of the PES along the O-O coordinate reveals that, although the repulsive wall at short O-O distances is well described, it takes longer for the PES iteration scheme to adequately describe the PES at large O-O distances.(53)

The results illustrated in Figures 4 and 5, however, are encouraging. The water dimer PES is a 12-dimensional surface and Figure 4 shows that its ZPE is being reproduced (using the most efficient schemes) when the PES comprises approximately 50 unique data points. The O-O distribution function, however, is a more stringent test of convergence than the ZPE and more than 100 unique data points are needed to converge the water dimer PES with respect to this observable.

The DMC-sampling scheme has been successfully incorporated into the current version of the *Grow* computer program, *Grow2.2,*(103) and this has been used to investigate a number of systems of biological interest.

Intramolecular Hydrogen Bonding in Gas Phase and Hydrated 1,2-Ethanediol

1,2-ethanediol (ethylene glycol) is one of the simplest molecules with two adjacent hydroxyl groups. It therefore acts as a model compound for more complicated biological molecules such as sugars and carbohydrates. The presence of the two adjacent hydroxyl groups also allows the possibility of intramolecular hydrogen bonding. For these reasons there have been many previous theoretical (54-79) and experimental (55,57,63,79-90) studies of 1,2-ethanediol and a smaller number of studies on solvated 1,2-ethanediol.(61,63,64,66,68,75,76,82,84-86)

The 1,2-ethanediol molecule has 10 symmetry distinct rotamers, Figure 6, which, provided at least a valence double-zeta basis and a theoretical method that includes electron correlation (at least density functional theory) have been used, all correspond to local minima on the molecular PES and lie within approximately 15 kJ/mol of the lowest energy structure, the tGg′ isomer. Indeed the two lowest energy structures in the gas phase, the tGg′ and gGg′ conformers, were found by all of the previous investigations to differ in energy by approximately 1.7 kJ/mol.

Because 1,2-ethanediol has a large number of low-lying minima, with low (torsional) barriers to interconversion, quantum nuclear motion may be significant in determining the ground state structure of 1,2-ethanediol. Quantum nuclear motion is also important in describing the nature of light nuclei such as

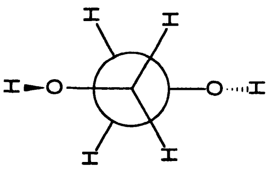

tTt

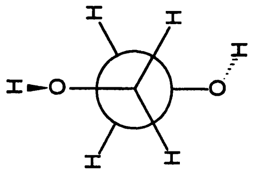

tTg

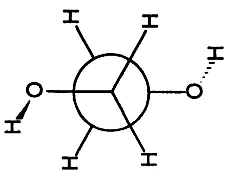

gTg

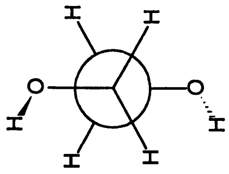

gTg'

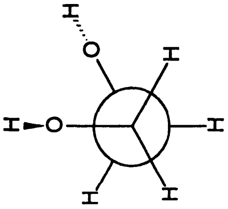

tGt

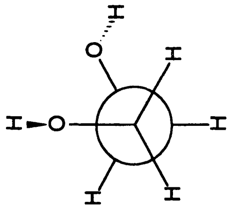

tGg

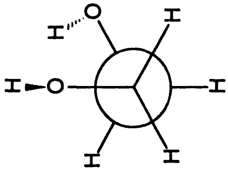

tGg'

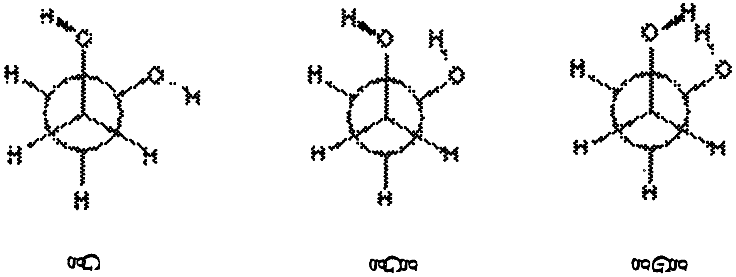

Figure 6. The 10 symmetry-distinct rotamers of 1,2-ethanediol, depicted as Newman projections. The two lowest energy configurations in the gas phase are tGg' and gGg'. (Reproduced with permission from reference 119. Copyright 2004 American Institute of Physics.

hydrogen and an examination of the nuclear motion of the various protons may allow the extent of hydrogen bonding to be determined. Previous theoretical studies of 1,2-ethanediol, however, have characterised the molecule only in terms of its lowest energy structures.(54-61,65-74,77) The relative stabilization of the two gauche conformers, tGg′ and gGg′, has been taken as evidence of an intra-molecular hydrogen bond. Despite this, recent electron density studies(80,91) have concluded that 1,2-ethanediol does not possess an intramolecular hydrogen bond according to the criteria for bonding defined by Popelier.(104) We have used DMC calculations to calculate the ground state wavefunction of 1,2-ethanediol and monohydrated 1,2-ethanediol (1,2-ethanediol.H_2O) in order to examine the extent of delocalization of the O-H distribution function in both species and to use this as an indication of the formation of a hydrogen bond.(105) We have therefore posed the following questions:

1. Does 1,2-ethanediol have an intramolecular hydrogen bond?
2. How is the bonding in 1,2-ethanediol changed upon addition of a water molecule?
3. How sensitive are the results to the level of *ab initio* theory used?

PESs were grown for 1,2-ethanediol and 1,2-ethanediol.H_2O similarly to the water dimer case described above. Here, however, *ab initio* calculations were used to provide the energies and the first and second derivatives of the energy. Three different methods for treating electron correlation were used, second-order Møller-Plesset perturbation theory (MP2)(106) and two common Density Functional Theory methods B3LYP(107,108) and PW91(109-113). In all cases the Huzinaga-Dunning correlation consistent valence double-split basis set (cc-pVDZ)(114) was used and the calculations were performed using the Gaussian 03 program package.(115) Because the *ab initio* calculations were now more computationally expensive than the DMC calculations regime A was used to construct the PESs, that is, at each iteration of the PES one rms-weight and one *h*-weight point was added to the PES data set. The parameters used to construct the various PESs are given in Table III and the parameters used in the converged DMC calculations are given in Table IV. Because of the higher dimensionality of 1,2-ethanediol and 1,2-ethanediol.H_2O as compared to the water dimer it was far less likely that the DMC walkers accessed high energy configurations. As a consequence an energy cutoff was not required, although the DMC-sampling calculations used a significantly smaller timestep than that used for the convergence calculations.

For 1,2-ethanediol the initial set of starting geometries comprised 6 stationary points on the global PES corresponding to the tGg', tGt and tTt local minima and to transition states describing tGg' isomerization, tGt isomerization and conversion of tTt to tGt. Each of these configurations was considered to possess 192 symmetry equivalent structures, defined by permutation of the 2 equivalent carbon atoms,

Table III. Parameters describing *Grow* calculations on 1,2-ethanediol and 1,2-ethanediol.H_2O^a

Parameter	*Value*
DMC-sampling calculations:	
Number of starting geometries	6 (5)
Starting geometries	3 lowest energy minima and 3 interconnecting transition states (5 lowest energy minima)
Number of replicas, M, per starting geometry	150 (200)
Maximum Cartesian displacement	0.5 a_0
Time step, τ	0.1 a.u.
Number of equilibration steps, N_{eq}	1 000
Number of data-accumulating steps, N_{prod}	4 000
Potential Energy Surface Interpolation:	
G	Sym(4)×Sym(2)×Sym(2) ×Sym(2); |G|=192 (Sym(2)×Sym(2)×Sym(2); |G|=8)
Taylor Series truncation	2nd order
Weight function:	2-part
P	24
Q	2
Confidence length, $d_k(i)$	Determined by 50 closest data points
Energy tolerance for $d_k(i)$	0.5 kJ/mol
Choosing scheme	1 rms, 1 hwt

a: if the parameter for 1,2-ethanediol.H_2O differs from that of 1,2-ethanediol it is indicated in parentheses.

the 2 equivalent oxygen atoms, the 4 equivalent carbon-bound hydrogen atoms and the 2 equivalent oxygen-bound hydrogen atoms.

The initial data set for 1,2-ethanediol.H_2O comprised 5 approximately isoenergetic local minima. In this case the permutation symmetry group was defined by considering all atoms distinct except the two hydrogen atoms bound to the water molecule, which are considered equivalent, and the two sets of two carbon-bound hydrogen atoms, where the hydrogen atoms in each set are considered equivalent. Although this symmetry group is minimal, it is expected to contain most of the feasible permutations encountered during the DMC simulation, as the atomic vibrational motion is small and atomic rearrangements are also not expected to occur through torsional motion.

Table IV. Parameters used in the DMC calculations to test convergence of the PESs for 1,2-ethanediol and 1,2-ethanediol.H_2O^a

Parameter	*Value*
Number of starting geometries	6 (5)
Number of replicas, *M*, per starting geometry	150 (200)
Starting geometries	3 lowest energy minima and 3 interconnecting transition states (5 lowest energy minima)
Maximum Cartesian displacement	0.5 a_0
Time step, τ	1.0 a.u.
Number of equilibration steps, N_{eq}	50 000
Number of data-accumulating steps, *N*	50 000
Number of descendent weighting generations	40
Number of timesteps, descendent weighting	20 000
Number of independent DMC calculations, *N*	10

a: if the parameter for 1,2-ethanediol.H_2O differs from that of 1,2-ethanediol it is indicated in parentheses.

The ZPE and nuclear vibrational wavefunction for each species were determined using DMC calculations on the various interpolated PESs. Convergence of the PESs was monitored, in terms of the ZPE and nuclear vibrational wavefunction, after 1, 10, 25, 50, 75 and 100 data points had been added to the PES.

Wavefunction histograms were obtained by binning the interatomic distances into 0.05 bohr bins for each walker at every time step of the simulation run and averaging over the 10 simulation runs. Vibrationally-averaged internal coordinates were obtained using the descendent weighting algorithm.(116) These wavefunction histograms and vibrationally averaged coordinates were constructed without incorporating the complete nuclear permutation (CNP) symmetry. That is, all atoms and interatomic distances were artifically distinguishable to enable each interatomic distance to be monitored separately during the course of the DMC simulation. If required, the distributions could be averaged over the CNP equivalent internal coordinates to give physically relevant observables.

The ZPE of 1,2-ethanediol and 1,2-ethanediol.H_2O is plotted, for the three levels of theory, as a function of the number of unique data points in the PES data set in Figures 7 and 8, respectively.

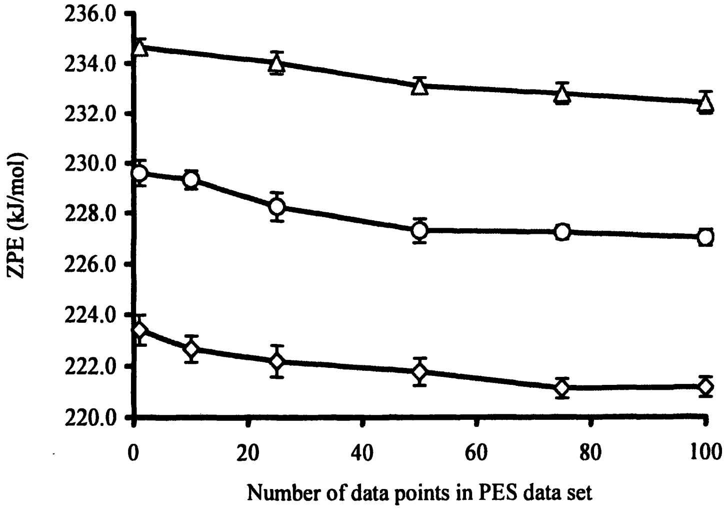

Figure 7. Convergence of the ZPE with respect to the number of unique data points in the PES data set for 1,2-ethanediol PESs grown at the PW91/cc-pVDZ (◇), B3LYP/cc-pVDZ (○) and MP2/cc-pVDZ (△) levels of theory.

From Figures 7 and 8 it can be seen that the ZPE converges to within ± 0.5 kJ/mol, for both molecules, and for all three levels of theory, once approximately 100 data points have been added to the PES data set. From the figures we also observe that the ZPE of all three levels of theory falls within a 11.2 kJ/mol range with the following order:

MP2 > B3LYP > PW91

The differences in ZPE reflect the underlying topology of the three PESs, for example, they suggest that the MP2 surface would, relative to the B3LYP and PW91 surfaces, have either steeper walls, tighter minima, higher barriers, or some combination of these. This can also be seen, to an extent, in the equilibrium bond lengths predicted for 1,2-ethanediol at the three levels of theory. The equilibrium O-H bond lengths at PW91/cc-pVDZ are 0.010 Å longer than those predicted at B3LYP/cc-pVDZ or MP2/cc-pVDZ for 1,2-ethanediol and up to 0.015 Å longer for 1,2-ethanediol.H_2O.(105)

The O-H distribution functions were found to have converged for both 1,2-ethanediol and 1,2-ethanediol.H_2O once 100 unique data points had been added to the PES data set.(105) This convergence is significantly faster than was

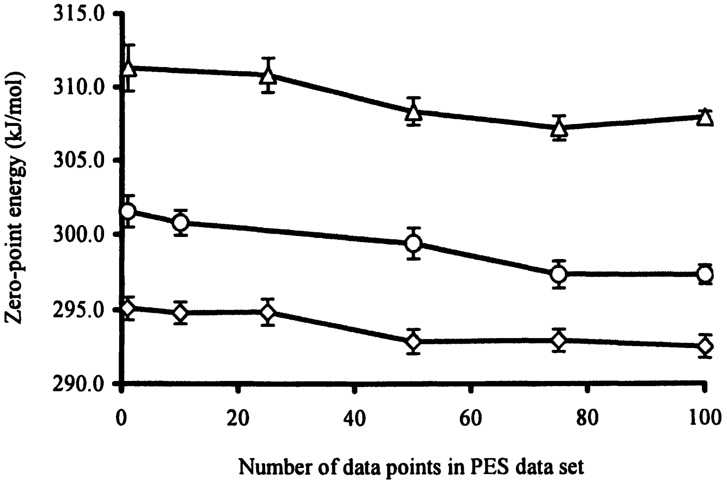

Figure 8. Convergence of the ZPE with respect to the number of unique data points in the PES data set for 1,2-ethanediol.H2O PESs grown at the PW91/cc-pVDZ (◇), B3LYP/cc-pVDZ (○) and MP2/cc-pVDZ (△) levels of theory.

observed for the O-O distribution function. The reason for this is the fact that the PES is significantly steeper in the bonded O-H coordinate than the non-bonded O-O coordinate, for both the water dimer and ethanediol. The shallower PES in the O-O coordinate leads to large amplitude O-O vibrational motion; in 1,2-ethanediol the full width half maximum (FWHM) of the O-O distribution is 1.7 Å whereas the FWHM for the O-H distribution is 1.2 Å.(105) This leads to both greater uncertainty in the O-O distribution and slower convergence. The O-H distribution functions are illustrated in Figures 9 and 10 for 1,2-ethanediol and 1,2-ethanediol.H_2O, respectively. These figures present only the MP2/cc-pVDZ results on the 100 point interpolated PES and the insets are used to indicate the relevant O-H bonds in the two species. If hydrogen bonding occurs we would expect the O-H distribution of the H involved in the hydrogen bond to be shifted to longer distances, that is, hydrogen bonding will lead to a more delocalized proton and a longer, weaker O-H bond. It is difficult, however, to resolve two O-H distributions in Figure 9 for 1,2-ethanediol: the standard error in the distributions is approximately twice the width of the lines. This implies that there is no resolvable proton delocalization, to within the accuracy of the DMC calculation, and therefore no resolvable intra-molecular hydrogen bond in gas phase 1,2-ethanediol. Figure 10, however, indicates two resolvable O-H bond distributions, one at shorter and one at longer O-H distance. These two

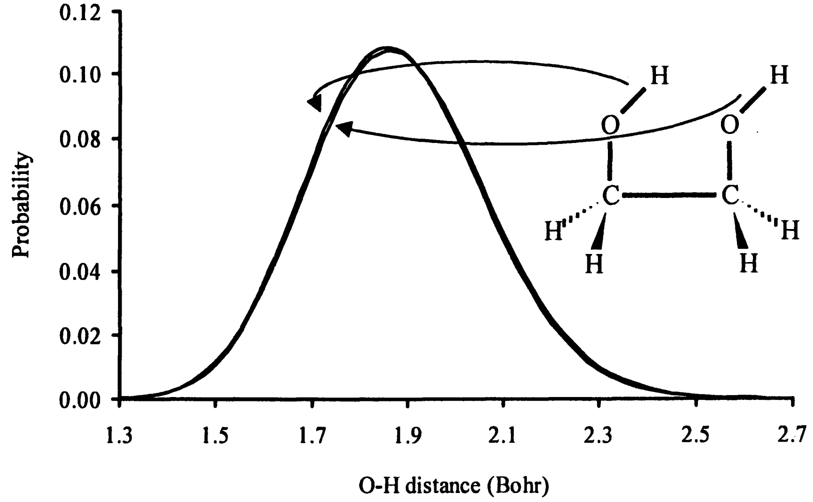

Figure 9. O-H wavefunction histograms for gas-phase1,2- ethanediol calculated from the converged 100 data point PES at the MP2/cc-pVDZ level of theory.

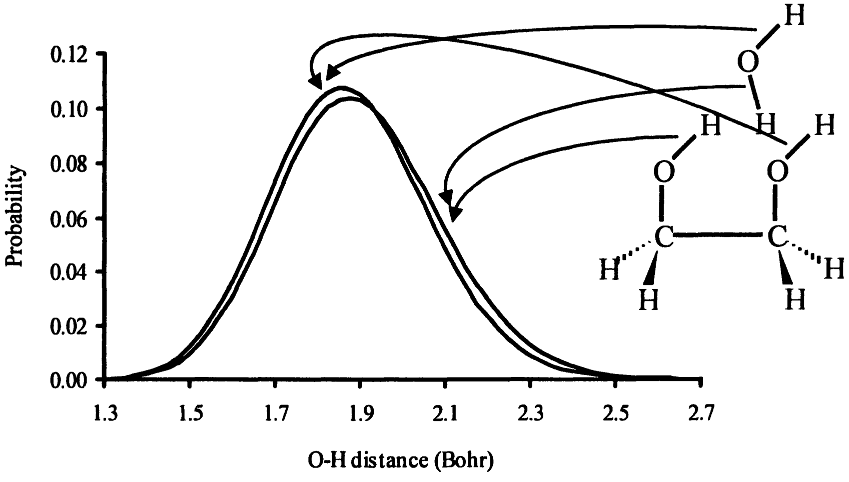

Figure 10. O-H wavefunction histograms for 1,2-ethanediol.H_2O calculated from the converged 100 data point PES at the MP2/cc-pVDZ level of theory.

distributions correspond to the four O-H bonds indicated in the inset of Figure 10, indicating two distinct proton environments. One corresponds to non-hydrogen-bonded protons, and the O-H distribution function for these protons is the same as that in 1,2-ethanediol, Figure 9. The other proton environment corresponds to hydrogen-bonded protons, indicative of intermolecular hydrogen bonding with the oxygen from the water molecule.

The O-O heavy-atom distance is another indicator of hydrogen bonding.(117) This distance contracts upon formation of a hydrogen bond. In 1,2-ethanediol.H_2O the intramolecular O-O distance was found to be approximately 0.3 Å longer than the intermolecular O-O distance for all methods considered. The intermolecular O-O distance was found to be approximately 2.75 Å,(105) consistent with the presence of a weak intermolecular hydrogen bond. Together with the O-H distributions in Figure 10, this is conclusive evidence of intermolecular hydrogen bonding. There is no such conclusive evidence for intramolecular hydrogen bonding in 1,2-ethanediol.H_2O.

Thus, we have shown that the nature of the O-H distribution function can be used to confirm the presence of a hydrogen bond in a molecule like 1,2-ethanediol. Our calculations show that, at the MP2/cc-pVDZ, B3LYP/cc-pVDZ and PW91/cc-pVDZ levels of theory there is no evidence for intramolecular hydrogen bonding in either 1,2-ethanediol or 1,2-ethanediol.H_2O. The hydrated species, 1,2-ethanediol.H_2O, however, has been shown conclusively to have two intermolecular hydrogen bonds with the water molecule. Although the three levels of theory studied exhibited the same overall trends,(105) the values of the ZPE differed significantly and, in particular, the PW91 density functional overestimated the O-H distances with respect to MP2 and B3LYP.

The Nature of the Glycyl Radical

Glycine, $NH_2–CH_2–COOH$, is the smallest amino acid and exists in aqueous solution in its zwitterionic form: $^+NH_3–CH_2–COO^-$. Because of its small size and computational tractability glycine has been used as a model for peptide reactions. The glycyl radical, $NH_2–^\bullet CH–COOH$, therefore serves as a model for the peptide radicals formed in many biological processes.(91) The aqueous phase structure (the predominant biological environment is aqueous) of the glycyl radical is not known experimentally, nor has the vibrationally averaged structure been determined theoretically. Like 1,2-ethanediol, there are multiple local minima on the PES with low energy barriers to interconversion. In this case, however, the glycyl radical PES possesses minima corresponding to both neutral and zwitterionic conformers. In an attempt to model aqueous phase structure we have constructed a PES, using the *Grow* methodology, for the hydrated radical, glycyl.$8H_2O$ using B3LYP/6-31+G* calculations. This method has been previously benchmarked against G3/MP2 calculations and shown to reproduce trends in relative energies. The initial PES data set comprised 8 low energy conformers, 4 neutral and 4 zwitterionic. Similarly to 1,2-ethanediol, torsional motion interconverts many of the neutral and zwitterionic conformers. The tautomerization *between* the neutral and zwitterionic species also occurs with a low barrier through water-facilitated proton transfer. For glycine, this barrier is approximately 9 kJ/mol.(118) The parameters used to "grow" the PES are given in Table V and the parameters for the final converged DMC calculations are given in Table VI.

The DMC calculations were started using 8 "seed" geometries, corresponding to the 4 lowest energy neutral and zwitterionic conformations. The *Grow* algorithm incorporated the nuclear permutation symmetry of the complex, with the two hydrogen atoms on each water molecule considered equivalent as were the two amino hydrogen atoms and the two carboxylate oxygen atoms. The order of the CNP group used was therefore 1024. Thus, for every data point calculated on the glycyl.8H_2O PES the 1024 symmetry equivalent structures were added to the data set. The procedure for the DMC-sampling of configuration space involved using 100 walkers per seed geometry and allowing 500 steps of 1.0 a.u. for equilibration. After equilibration the walkers were propagated for a further 100 steps with all walker configurations saved every 10 steps. Two new configurations were chosen each iteration from these sampled geometries by taking the point of highest rms-weight and the point of highest *h*-weight (regime A, above). After 280 unique data points had been added to the PES the DMC wavefunction was calculated and the N-H and O-H bond length distribution functions were determined using descendent weighting. The "pattern" of these distribution functions was used to determine the nature of ground state glycyl.8H_2O.

Similarly to 1,2-ethanediol the DMC distribution functions were obtained by explicitly labelling the atoms, that is, removing the CNP symmetry. The N-H and O-H bond length distribution functions for the three terminal hydrogen atoms are shown in Figures 11 and 12, respectively. In both figures the three lowest energy structures are indicated as insets, where the 8 water molecules have been omitted for clarity. Structure (a) is the lowest energy zwitterion and structures (b) and (c) represent the lowest energy neutral conformers, the colour code is H=light grey, C=black, N=dark grey and O=mid grey.

The pattern of the distribution functions shown in Figures 11 and 12 is indicative of the structure of the hydrated glycyl radical. There are two distinct N-H distributions shown in Figure 11 and three distinct O-H distributions shown in Figure 12. The zwitterionic structure, structure (a), should have a single (to within the resolution of the figures) N-H distribution at short N-H distance, approximately 2 bohr, and three O-H distributions, all at large O-H distance. The neutral conformers, (b) and (c) should show two peaks in the N-H bond

Table V. Parameters describing *Grow* calculations on the hydrated glycyl radical, glycyl.8H_2O

Parameter	*Value*
DMC-sampling calculations:	
Number of starting geometries	8
Starting geometries	4 lowest energy neutral and 4 lowest energy zwitterionic conformers
Number of replicas, M, per starting geometry	100
Maximum Cartesian displacement	0.5 a_0
Time step, τ	1.0 a.u.
Number of equilibration steps, N_{eq}	500
Number of data-accumulating steps, N	100
Potential Energy Surface Interpolation:	
G	Sym(2)^{10}; $\|G\|=1024$
Taylor Series truncation	2nd order
Weight function:	2-part
P	24
Q	2
Confidence length, $d_k(i)$	Determined by 50 closest data points
Energy tolerance for $d_k(i)$	0.5 kJ/mol
Choosing Scheme	1 rms, 1 hwt

Table VI. Parameters used in the DMC calculations on the hydrated glycyl radical, glycyl.8H_2O

Parameter	*Value*
Number of starting geometries	8
Starting geometries	4 lowest energy neutral and 4 lowest energy zwitterionic conformers
Number of replicas, M, per starting geometry	100
Maximum Cartesian displacement	0.5 a_0
Time step, τ	1.0 a.u.
Number of equilibration blocks, N_{eq}	50 000
Number of data-accumulating blocks, N	50 000
Number of independent DMC calculations, N	10

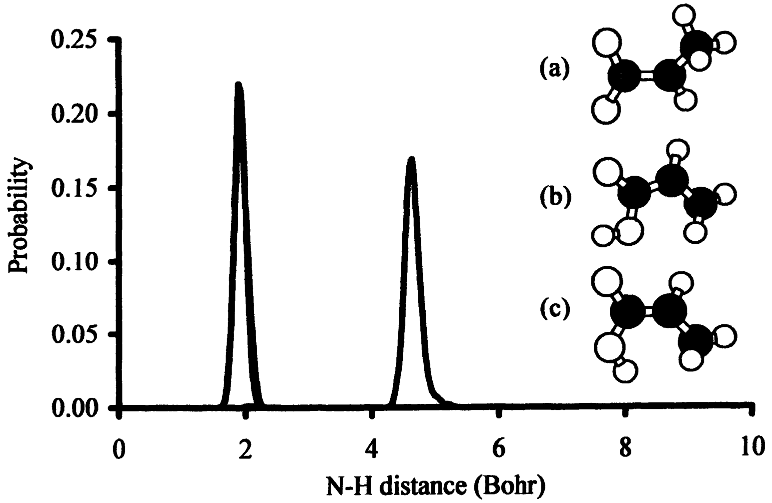

Figure 11. N-H wavefunction histograms for glycyl.8H_2O calculated from a 280 point B3LYP/6-31+G PES, with three low energy conformers inset.*

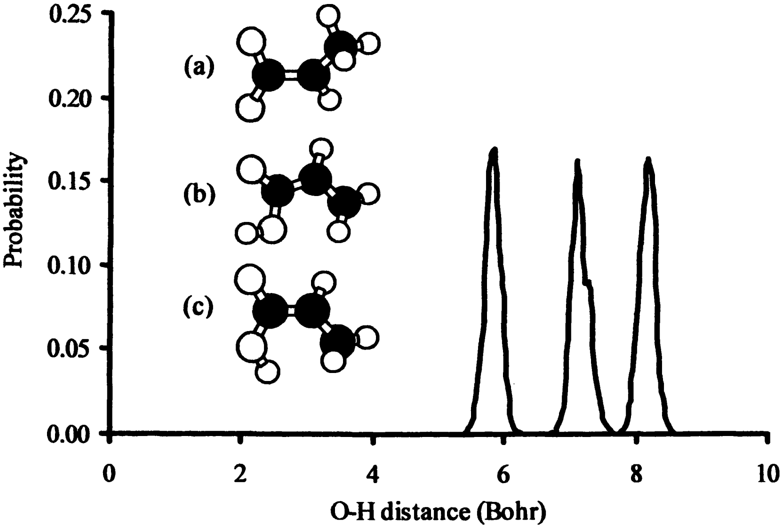

Figure 12. O-H wavefunction histograms for glycyl.8H$_2$O calculated from a 280 point B3LYP/6-31+G PES, with three low energy conformers inset.*

length distribution function, with a single peak at short N-H distance corresponding to the two hydrogen atoms bound to the nitrogen and a second peak at significantly longer N-H distance corresponding to the O-H bound hydrogen. The distribution shown in Figure 11 is therefore consistent with either neutral conformer.

The O-H distribution function in Figure 12 shows three distinct peaks with approximately equal amplitude. The peak at smallest O-H distance occurs at approximately 5.9 bohr (3.1 Å) which is a relatively short non-bonded distance (indeed it corresponds to a very weak hydrogen-bonded distance). This is compatible with the *cis* configuration of the carboylic acid group, structure (c), rather than the *trans* configuration, structure (b), which would have a longer O-H distance, it is not compatible with the zwitterionic structure, structure (a). If there were significant delocalization of the glycyl radical structures we would expect the bond length distribution functions to be significantly broadened and their amplitudes to reflect the extent of delocalization. Neither features are apparent in Figures 11 or 12. Thus we conclude that the glycyl.8H_2O species, at the B3LYP/6-31+G* level of theory, exists as a neutral molecule with a conformation corresponding to structure (c) in Figures 11 and 12. Despite this, we should still be cautious about interpreting the structure of the solvated glycyl radical. Although a solvation sphere consisting of 8 water molecules is a relatively good model for short-range solvation, the 8 water molecules can encircle the glycyl radical and are relatively effective at screening the glycyl radical's charge distribution, long-range solvent effects are omitted. In a dielectric model for long range solvation, for example, the species with the largest dipole moment will be preferentially stabilized by electrostatic interactions with the continuum, thus long-range solvation effects will serve to stabilize the zwitterionic form over the neutral form.

The Structure of Ground State γ-Aminobutyric Acid (GABA)

GABA, $NH_2–CH_2–CH_2–CH_2–COOH$, is a larger amino acid than glycine and has conformational flexibility about the saturated C-C bonds in its backbone. Like glycine, aqueous phase GABA is known to exist as a zwitterion, $^+NH_3–CH_2–CH_2–CH_2–COO^-$, and furthermore NMR experiments suggest that a number of conformers are present at room temperature.(97,98)

Because of its biological significance, the structure of aqueous phase GABA has relevance to the design of neuroinhibitory drugs to treat diseases such as depression, epilepsy and schizophrenia.(93-96) We have modelled aqueous phase GABA using a solvation sphere consisting of 5 water molecules, that is, as GABA.5H_2O. At the MP2/6-31+G* level of theory GABA.5H_2O exists as a zwitterion with 9 local minimum energy structures on the PES.(119)

These structures are illustrated in Figure 13, where the water molecules and the non-terminal hydrogen atoms have been omitted for clarity.

The 9 zwitterionic conformers, Figure 13, can also be characterized in terms of their C–C–C–C and N–C–C–C dihedral angles, which are illustrated diagrammatically in Figure 14. These dihedral angles are given for the 9 minima, zw1-zw9, along with their relative electronic energies, in Table VII.

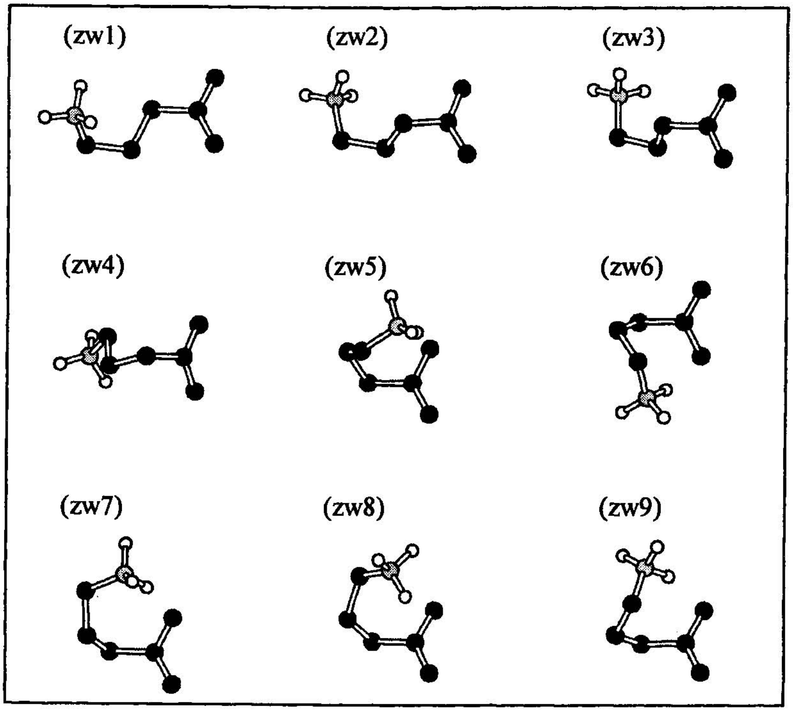

Figure 13. The 9 zwitterionic optimized local minima, zw1-zw9, obtained for $GABA.5H_2O$ at the MP2/6-31+G level of theory. The explicit water molecules have been removed for clarity and only the terminal hydrogen atoms have been displayed. (Reproduced with permission from reference 105. Copyright 2005 American Institute of Physics.)*

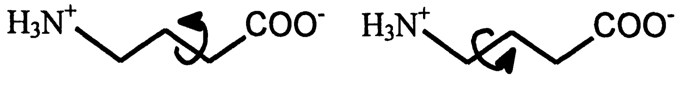

Figure 14. Diagrammatic representation of the C–C–C–C and N–C–C–C dihedral angles in GABA.

Table VII. The 9 local minima on the GABA.5H_2O PES (Figure 13) characterized by their C–C–C–C and N–C–C–C dihedral angles and their relative electronic energies, ΔE.

Structure	*C–C–C–C (°)*	*N–C–C–C (°)*	*ΔE (kJ/mol)*
zw1	174	–55	63
zw2	–176	178	86
zw3	–161	71	60
zw4	–56	148	11
zw5	–47	85	0
zw6	–41	–49	20
zw7	81	–72	17
zw8	60	–90	8
zw9	39	48	7

From Table VII it can be seen that the lowest energy GABA.5H_2O structure is zw5 (Figure 13), although three other conformers lie within 11 kJ/mol in terms of their electronic energy. Again, similarly to 1,2-ethanediol and the glycyl radical, GABA.5H_2O has multiple local minima on its PES with relatively low (torsional) barriers to interconversion. Given the experimental evidence, we expect GABA to be delocalized over two or more structures at room temperature and this may well be reflected in the ground state structure.

Because of its large size we have not “grown” a PES for GABA.5H_2O. Instead we have generated a full, 87-dimensional PES for GABA.5H_2O by interpolating the surface from 9 data points corresponding to the 9 local minima shown in Figure 13. The ground state structure of GABA.5H_2O has then been investigated by performing DMC calculations on this PES. The parameters used in the DMC calculations are given in Table VIII. Due to the large size and conformational flexibility of the GABA.5H_2O complex, the DMC calculations converge slowly and, as a result, we have let the DMC calculation converge over 1 000 000 total time steps. 2 000 DMC walkers were initiated for each of the 9 minimum energy structures. In each of 100 independent DMC simulation runs the DMC walkers all equilibrated to a single well on the PES. Within an individual simulation there was no delocalization observed. The majority of DMC simulation runs equilibrated to the well corresponding to the zw5 structure, however, some simulations also populated the zw4, zw6, zw7, zw8 and zw9 wells. The fact that individual simulation runs were trapped in a single well suggested that the interpolated PES overestimates the barriers to torsional motion.

Table VIII. Parameters used in the DMC calculations on the hydrated GABA, GABA.5H_2O

Parameter	*Value*
Number of starting geometries	9
Starting geometries	9 zwitterionic local minima, zw1-zw9
Number of replicas, M, per starting geometry	2000
Maximum Cartesian displacement	0.5 a_0
Time step, τ	1.0 a.u.
Number of equilibration steps, N_{eq}	500 000
Number of data-accumulating steps, N_{prod}	500 000
Number of independent DMC calculations, N	100

The ground state wavefunction was approximated by combining the results of all 100 independent DMC simulations. Its structure was further investigated by binning the C–C–C–C and N–C–C–C dihedral angles, Figure 14, directly. The resulting dihedral angle distributions provide a measure of the conformational flexibility of the hydrated GABA molecule and the C–C–C–C and N–C–C–C distributions are illustrated in Figures 15 and 16, respectively.

It is important to note that Figures 15 and 16 do not represent probability *densities* but are directly calculated from the wavefunction. Figures 15 and 16, however, do reflect the essential features of the probability density. It can be seen from Figures 15 and 16 that, although the maxima in the dihedral angle distributions occur at angles corresponding approximately to those in the minimum energy conformer (–47° for C–C–C–C and 85° for N–C–C–C) there is significant structure in both distribution functions. There is a second distinct peak in the C–C–C–C dihedral angle distribution at approximately +55° and shoulders at approximately –70° and –10°. These features are consistent with a number of local minima: zw4, zw5, zw6, zw8 and zw9. The N–C–C–C dihedral angle distribution, Figure 16, is even more complex. There are features at approximately –90°, -60°, -20°, 30°, 80°, 110° and 120°. Again these are consistent with a number of local minima. The shapes of the dihedral angle distribution functions, the number of features and their width, are indicative that, when the results are averaged over 100 independent DMC simulation runs there is significant delocalization at 0 K, even though each simulation converged individually to a single well. As mentioned earlier, these results suggest that the interpolated PES overestimates the barriers to torsional motion and it may be worthwhile characterizing the torsional transition states and adding them to the PES data set.

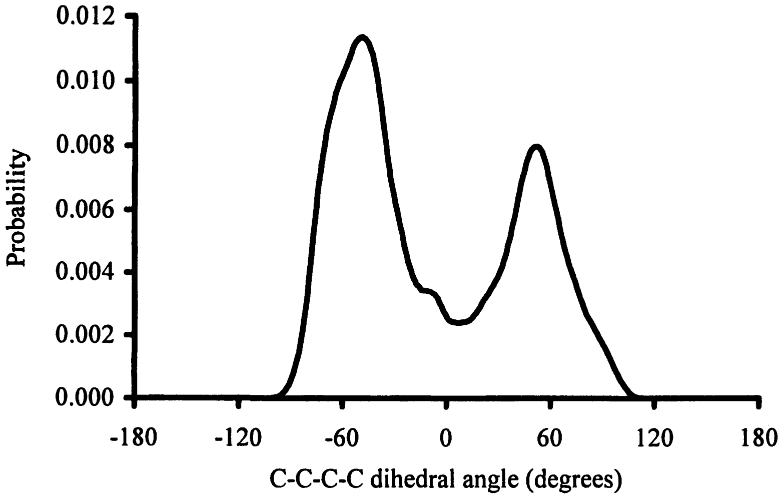

Figure 15. The C–C–C–C dihedral angle distribution in GABA.5H_2O binned directly from the DMC walkers from 100 independent DMC simulations.

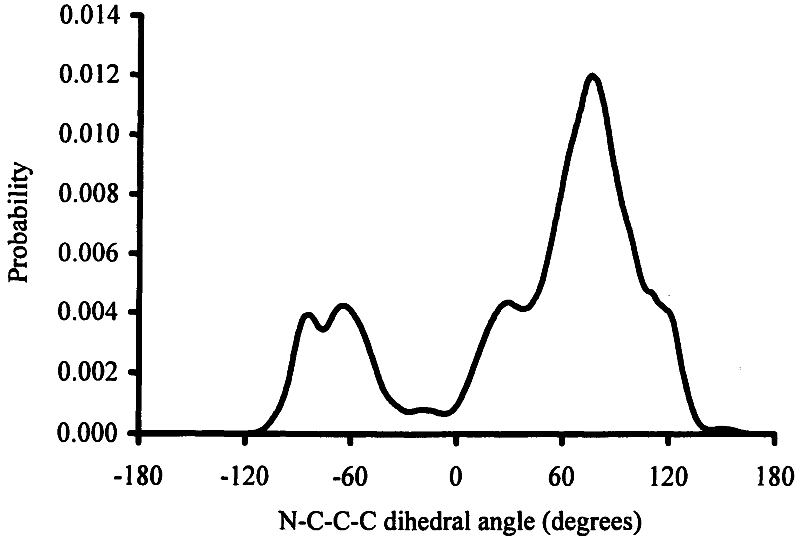

Figure 16. The N–C–C–C dihedral angle distribution in GABA.5H_2O binned directly from the DMC walkers from 100 independent DMC simulations.

In terms of the averaged results we would expect a high degree of torsional flexibility in the ground state of GABA.5H_2O and the increasing presence of additional conformers as the temperature is increased, consistent with the NMR experimental data.(97,98)

Conclusions

This chapter has presented the *Grow2.2*(103) computer package. This package uses a modified Shepard interpolation to interpolate a molecular PES from *ab initio* data at a discrete set of data points. The PES is then iteratively improved by adding additional PES data points until convergence is obtained in any given property or properties of interest. The additional data points are chosen via a dynamical sampling of the configuration space relevant to the particular property of interest. The new implementation of the program allows the use of DMC calculations to both sample the relevant molecular configuration space and to calculate ground state properties of the molecule. We have shown that, for loosely bound complexes, DMC-based sampling provides an efficient means of iteratively building up a PES that describes the ground state properties of the complex. Various PES iteration schemes were tested with respect to an analytic PES for the water dimer and the techniques were then applied to three systems of biological interest.

We first applied the *Grow2.2*(103) methodology to gas-phase and monohydrated 1,2-ethanediol. These molecules are prototypical polyhydroxylated species and we investigated intra and intermolecular hydrogen bonding in the two species by generating converged molecular PESs at the MP2/cc-pVDZ, B3LYP/cc-pVDZ and PW91/cc-pVDZ levels of theory. Although we found no conclusive evidence for an intramolecular hydrogen bond in either species the O-H bond length distribution functions obtained from DMC calculations were used to demonstrate the presence of intermolecular hydrogen bonds in the 1,2-ethanediol.H_2O complex. Upon hydrogen bonding the O-H distribution function was observed to shift to longer O-H distances, indicating delocalization of the hydrogen-bonded proton.

A second application was to the hydrated glycyl radical, glycyl.8H_2O, which serves as a model for radical peptide intermediates. The aqueous phase structure of the glycyl radical is not known and it could exist in either neutral or zwitterionic forms. We investigated the nature of the glycyl.8H_2O complex by growing a 280 point PES at the B3LYP/6-31+G* level of theory. DMC calculations on this surface showed that ground state glycyl.8H_2O exists as a neutral molecule and not a zwitterion.

DMC calculations were also used to investigate the ground state structure of another hydrated amino acid, γ-aminobutyric acid (GABA), a target for new drugs to treat a number of neurological diseases. A global PES was generated for the GABA.5H_2O complex based on the 9 local minima characterized on the MP2/6-31+G* PES. DMC calculations on this PES were then used to demonstrate the conformational flexibility of ground state GABA.5H_2O.

Acknowledgements

DLC would like to acknowledge the financial support of an Australian Postgraduate Research Award. This work has also been supported by Large Grant A00104447 from the Australian Research Council and by grants of computer time from the Australian Partnership in Advanced Computing (APAC) National Merit Allocation Scheme.

References

1. Del Bene, J. E.; Jordan, M. J. T. *Int. Rev. Phys. Chem.* **1999,** *18,* 119.
2. Del Bene, J. E.; Jordan, M. J. T. *J. Am. Chem. Soc.* **2000,** *122,* 4794.
3. Thompson, K. C.; Crittenden, D. L.; Jordan, M. J. T. *J. Am. Chem. Soc.* **2005,** *127,* 4954.
4. Anderson, J. B. *J. Chem. Phys.* **1975,** *63,* 1499.
5. Anderson, J. B. *J. Chem. Phys.* **1976,** *65,* 4121.
6. Anderson, J. B. *J. Chem. Phys.* **1980,** *73,* 3897.
7. Anderson, J. B.; Freihaut, B. H. *J. Comput. Phys.* **1979,** *31,* 425.
8. Coker, D. F; Watts, R. O. *Mol. Phys.* **1986,** *58,* 1113.
9. Suhm, M. A.; Watts, R. O. *Phys. Rep.* **1991,** *204,* 293.
10. Gregory, J. K.; Clary, D. C. *Chem. Phys. Lett.* **1994,** *228,* 547.
11. Gregory, J. K.; Clary, D. C. *J. Chem. Phys.* **1995,** *102,* 7817.
12. Gregory, J. K.; Clary, D. C. *J. Chem. Phys.* **1995,** *103,* 8924.
13. Gregory, J. K.; Clary, D. C. *J. Phys. Chem. A.* **1997,** *101,* 6813.
14. Benoit, D. M.; Clary, D. C. *J. Chem. Phys.* **2000,** *113,* 5193.
15. Miller, R. E.; Coker, D. F.; Watts, R. O. *J. Chem. Phys.* **1985,** *82,* 3554.
16. Coker, D. F; Watts, R. O. *J. Phys. Chem.* **1987,** *91,* 2513.
17. Quack, M.; Suhm, M. A. *J. Chem. Phys.* **1991,** *95,* 28.
18. Quack, M.; Stohner. J.; Suhm, M. A. *J. Mol. Struct.* **1993,** ***294,*** 33.
19. Auer, B. M.; McCoy, A. B. *J. Phys. Chem. A* **2003,** *107,* 4.
20. Meredith, A. W.; Stone, A. J. *J. Phys. Chem. A* **1998,** *102,* 434.
21. M. Lewerenz, J. Chem. Phys. **104,** 1028 (1996).
22. Niyaz, P.; Bacic, Z.; Moskowitz, J.W.; Schmidt, K. E. *Chem. Phys. Lett.* **1996,** *252,* 23.

23. Sandler, P.; Jung, J. O.; Szczniak, M. M.; Buch, V. J. *Chem. Phys.* **1994,** *101,* 1378.
24. Brown, A.; McCoy, A. B.; Braams, B. J.; Jin, Z.; Bowman, J. M. *J. Chem. Phys.***2004,***12,* 4105.
25. Benoit, D. M.; Clary, D. C. *J. Phys. Chem. A* **2000,** *104,* 5590.
26. Ho, T. S.; Rabitz, H. *J. Chem. Phys.* **1996,** *104,* 2584.
27. Hollebeek, T.; Ho, T. S.; Rabitz, H. *J. Chem. Phys.* **1997,** *106,* 7223.
28. Rhee, Y. M.; Lee, T. G.; Park, S. C.; Kim, M. S. *J. Chem. Phys.* **1997,** *106,* 1003.
29. Nguyen, K. A.; Rossi, I.; Truhlar, D. G. *J. Chem. Phys.* **1995,** *103,* 5522.
30. Ishida, T.; Schatz, G. C. *J. Chem. Phys.* **1997,** *107,* 3558.
31. Ischtwan, J.; Collins, M. A. *J. Chem. Phys.* **1994,** *100,* 8080.
32. Jordan, M. J. T.; Thompson, K. C.; Collins, M. A. *J. Chem. Phys.* **1995,** *102,* 5647.
33. Jordan, M. J. T.; Thompson, K. C.; Collins, M. A. *J. Chem. Phys.* **1995,** *103,* 9669.
34. Jordan, M. J. T.; Collins, M. A. *J. Chem. Phys.* **1996,** *104,* 4600.
35. Thompson, K. C.; Collins, M. A. *J. Chem. Soc., Faraday Trans.* **1997,** *93,* 871.
36. Thompson, K. C.; Jordan, M. J. T.; Collins, M. A. *J. Chem. Phys.* **1998,** *108,* 8302.
37. Bettens, R. P. A.; Collins, M. A. *J. Chem. Phys.* **1999,** *111,* 816.
38. Collins, M. A. *Theor. Chem. Acc.* **2002,** *108,* 313.
39. For example, Jensen, F. *Introduction to Computational Chemistry*; Wiley: New York, 1998.
40. Brouard, M.; Burak, I.; Minayev, D.; O'Keeffe, P.; Vallance, C.; Aoiz, F. J.; Bañares, L.; Castillo, J. F.; Zhang D. H.; Collins, M. A. *J. Chem. Phys.* **2003,** *118,* 1162.
41. Zhang, D. H.; Collins, M. A.; Lee, S.-Y. *Science* **2000,** *290,* 961.
42. Yang, M.; Zhang, D. H.; Collins, M. A.; Lee, S.-Y. *J. Chem. Phys.* **2001,** *114,* 4759.
43. R Bettens, R. P. A.; Collins, M. A.; Jordan, M. J. T.; Zhang, D. H. *J. Chem. Phys.* **2000,** *112,* 10162.
44. Moyano, G. E.; Collins, M. A. *J. Chem. Phys.* **2003,** *119,* 5510.
45. Collins, M. A.; Radom, L. *J. Chem. Phys.* **2003,** *118,* 6222.
46. Fuller, R. O.; Bettens, R. P. A.; Collins, M. A. *J Chem. Phys.* **2001,** *114,* 10711.
47. Collins, M. A.; Petrie, S.; Chalk, A. J.; Radom, L. *J. Chem. Phys.* **2000,** *112,* 6625.
48. Bettens, R. P. A.; Hansen, T. A.; Collins, M. A. *J. Chem. Phys.* **1999,** *111,* 6322.
49. Collins, M. A.; Bettens, R. P., A. *J. Chem. Phys.* **1999,** *111,* 939.
50. Bettens, R. P. A.; Collins, M. A. *J. Chem. Phys.* **1998,** *109,* 9728.

51. Bettens, R. P. A.; Collins, M. A. *J. Chem. Phys* **1998**, *108*, 2424.
52. Bettens, R. P. A. *J. Am. Chem. Soc.* **2003**, *125*, 584
53. Crittenden, D.L.; Thompson, K. C.; Chebib, M.; Jordan, M. J. T. *J. Chem. Phys.* **2004**, 121, 9844.
54. Radom, L.; Lathan, W. A.; Hehre, W. J.; Pople, J. A. *J. Am. Chem. Soc.* **1973**, *95*, 693.
55. Ha, T. K.; Frei, H.; Meyer, R.; Günthard, H. H. *Theor. Chim. Acta* **1974**, *34*, 277.
56. Almlöf, J.; Stymne, H. *Chem. Phys. Lett.* **1975**, *33*, 118.
57. Frei, H.; Ha, T. K.; Meyer, R.; Günthard, H. H. *Chem. Phys.* **1977**, *25*, 271.
58. Van Alsenoy, C.; Van Den Enden, L.; Schäfer, L. *J. Mol. Struct. (Theochem)* **1984**, *108*, 121.
59. Pople, J. A.; Head-Gordon, M.; Raghavachari, K. *J. Chem. Phys.* **1987**, *87*, 5968.
60. Cabral, B. J. C.; Albuquerque, L. M. P. C.; Fernandes, F. M. S. S. *Theor. Chim. Acta* **1991**, *78*, 271.
61. Nagy, P. I.; Dunn, W. J.; Alagona, G.; Ghio, C. *J. Am. Chem. Soc.* **1991**, *113*, 6719.
62. Park, C. G.; Tasumi, M. *J. Phys. Chem.* **1991**, *95*, 2757.
63. Alagona, G.; Ghio, C. *J. Mol. Struct. (Theochem)* **1992**, *254*, 287.
64. Hooft, R. W. W.; van Eijck, B. P.; Kroon, J. *J. Chem. Phys.* **1992**, *97*, 3639.
65. Murcko, M. A.; DiPaola, R. A. *J. Am. Chem. Soc.* **1992**, *114*, 10010.
66. Nagy, P. I.; Dunn, W. J.; Alagona, G.; Ghio, C. *J. Am. Chem. Soc.* **1992**, *114*, 4752.
67. Carmichael, I.; Chipman, D. M.; Podlasek, C. A.; Serianni, A. S. *J. Am. Chem. Soc.* **1993**, *115*, 10863.
68. Cramer, C. J.; Truhlar, D. G. *J. Am. Chem. Soc.* **1994**, *116*, 3892.
69. Oie, T.; I.A., T.; Burt, S. K. *J. Phys. Chem.* **1994**, *98*, 1121.
70. Yeh, T.-S.; Chang, Y.-P.; Su, T.-M.; Chao, I. *J. Phys. Chem.* **1994**, *98*, 8921.
71. Bultinck, P.; Goeminne, A.; Van de Vondel, D. *J. Mol. Struct. (Theochem)* **1995**, *357*, 19.
72. Csonka, G. I.; Anh, N.; Ángyán, J.; Csizmadia, I. G. *Chem. Phys. Lett.* **1995**, *245*, 129.
73. Csonka, G. I.; Csizmadia, I. G. *Chem. Phys. Lett.* **1995**, *243*, 419.
74. Chang, Y.-P.; Su, T.-M.; Li, T.-W.; Chao, I. *J. Phys. Chem. A* **1997**, *101*, 6107.
75. Cabral, B. J. C. *Int. J. Quantum Chem.* **1998**, *60*, 1651.
76. Manivet, P.; Masella, M. *Chem. Phys. Lett.* **1998**, *288*, 642-646.
77. Trindle, C.; Crum, P.; Douglass, K. *J. Phys. Chem. A* **2003**, *107*, 6236.
78. Mandado, M.; Grana, A.; Mosquera, R. *Phys. Chem. Chem. Phys.* **2004**, *6*, 4391.

79. Howard, D. L.; Jørgensen, P.; Kjaergaard, H. G. *J. Am. Chem. Soc.* **2005,** *127*, 17096.

80. Bastiansen, O. *Acta. Chem. Scand.* **1949,** *3*, 415.

81. Kuhn, L. P. *J. Am. Chem. Soc.* **1952,** *74*, 2492.

82. Krueger, P. J.; Mettee, H. D. *J. Mol. Spec.* **1965,** *18*, 131.

83. Buckley, P.; Giguère, P. A. *Can. J. Chem.* **1967,** *45*, 397.

84. Pachler, K. G. R.; Wessels, P. L. *J. Mol. Struct.* **1970,** *6*, 471.

85. Busfield, W. K.; Ennis, M. P.; McEwen, I. J. *Spectrochim. Acta* **1973,** *29*, 1259.

86. Maleknia, S.; Friedman, B. R.; Abedi, N.; Schwartz, M. *Spectrosc. Lett.* **1980,** *13*, 777.

87. Walder, E.; Bauder, A.; Günthard, H. H. *Chem. Phys.* **1980,** *51*, 223.

88. Caminati, W.; Corbelli, G. *J. Mol. Spec.* **1981,** *90*, 572.

89. Takeuchi, H.; Tasumi, M. *Chem. Phys.* **1983,** *77*, 21.

90. Christen, D.; Coudert, L. H.; Larsson, J. A.; Cremer, D. *J. Mol. Spec.* **2001,** *205*, 185.

91. For example, Frey, P. A. *Ann. Rev. Biochem.* **2001,** *70*, 121.

92. Maskill, H. *The Physical Basis of Organic* Chemistry, Oxford University Press: Oxford, U.K., 1985; p162.

93 Rang, H. P.; Dale, M. M.; Ritter, J. M. *Pharmacology 4th ed*; Churchill Livingstone: Edinburgh, 1999; p478.

94. Prosser, H. M.; Dill, C. H.; Hirst, W. D.; Grau, E.; Robbins, M.; Calver, A.; Soffin, E. M.; Farmer, C. E.; Lanneau, C.; Gray, J.; Schenck, E.; Warmerdam, B. S.; Clapham, C.; Reavill, C.; Rogers, D. C.; Stean, T.; Upton, N.; Humphreys, K.; Randall, A.; Geppert, M.; Davies, C. H.; Pangalos, M. N. *Mol. Cell. Neurosci.* **2001,** *17*, 1059.

95. Bernard, C.; Cossart, R.; Hirsh, J. C.; Esclapez, M.; Ben-Ari, Y. *Epilepsia* **2000,** *41(Suppl. 6)*, S90.

96. Leo, R. J. *Psychiatric Times* **2001,** *XVII.*

97. Tanaka, K.; Akutsu, H.; Ozaki, Y.; Kyogoku, Y.; Tomita, K.-I. *Bull. Chem. Soc. Japan* **1978,** *51*, 2654.

98. Ham, N.S. *Mol. Quantum Pharmacol,. Proc 7th Jerusalem Symposium* **1974,** *7*, 261.

99. Leforestier, C.; Gatti, F.; Fellers, R. S.; Saykally, R. J. *J. Chem. Phys.* **2002,** *117*, 8710.

100. Matsuoka, O.; Clementi, E.; Yoshimine, M. *J. Chem. Phys.* **1976,** *64*, 1351.

101. Reimers, J. R.; Watts, R. O.; Klein, M. L. *Chem. Phys.* **1982,** *64*, 95.

102. Jorgensen, W. L.; Chandrasekhar, J.; Madura, J. D.; Impey, R. W.; Klein, M. L. *J. Chem. Phys.* **1983,** *79*, 926.

103.The *Grow2.2* package and documetation is available from the authors, please contact m.jordan@chem.usyd.edu.au.

104.Koch, U.; Popelier, P. L. A. *J. Phys. Chem.* **1995,** *99*, 9747.

105.Crittenden, D.L.; Thompson, K. C.; Jordan, M. J. T. *J. Phys. Chem. A* **2005,** *109*, 2971.

106.Møller, C.; Plesset, M. S. *Phys. Rev.* **1934**, *46*, 618

107.Lee, C.; Yang, W.; Parr, R. G. *Phys. Rev. B* **1988**, *37*, 785.

108.Becke, A. D. *J. Chem. Phys.* **1993**, *98*, 5648.

109.*Electronic Structure of Solids '91*; Perdew, J. P.; Ziesche, P., Eschrig, H., Eds.; Akademie Verlag: Berlin, 1991.

110. Perdew, J. P.; Chevary, J. A.; Vosko, S. H.; Jackson, K. A.; Pederson, M. R.; Singh, D. J.; Fiolhais, C. *Phys. Rev. B* **1992**, *46*.

111.Perdew, J. P.; Chevary, J. A.; Vosko, S. H.; Jackson, K. A.; Pederson, M. R.; Singh, D. J.; Fiolhais, C. *Phys. Rev. B* **1993**, *48*.

112. Perdew, J. P.; Burke, K.; Wang, Y. *Phys. Rev. B* **1996**, *54*, 16533.

113.*Electronic Density Functional Theory: Recent Progress and New Directions*; Burke, K.; Perdew, J. P.; Wang, Y.; Dobson, J. F., Vignale, G., Das, M. P., Eds.; Plenum, 1998.

114.Woon, D. E.; Dunning Jr., T. H. *J. Chem. Phys.* **1993**, *98*, 1358.

115. Gaussian 03, Revision C.02, Frisch, M. J.; Trucks, G. W.; Schlegel, H. B.; Scuseria, G. E.; Robb, M. A.; Cheeseman, J. R.; Montgomery, Jr., J. A.; Vreven, T.; Kudin, K. N.; Burant, J. C.; Millam, J. M.; Iyengar, S. S.; Tomasi, J.; Barone, V.; Mennucci, B.; Cossi, M.; Scalmani, G.; Rega, N.; Petersson, G. A.; Nakatsuji, H.; Hada, M.; Ehara, M.; Toyota, K.; Fukuda, R.; Hasegawa, J.; Ishida, M.; Nakajima, T.; Honda, Y.; Kitao, O.; Nakai, H.; Klene, M.; Li, X.; Knox, J. E.; Hratchian, H. P.; Cross, J. B.; Adamo, C.; Jaramillo, J.; Gomperts, R.; Stratmann, R. E.; Yazyev, O.; Austin, A. J.; Cammi, R.; Pomelli, C.; Ochterski, J. W.; Ayala, P. Y.; Morokuma, K.; Voth, G. A.; Salvador, P.; Dannenberg, J. J.; Zakrzewski, V. G.; Dapprich, S.; Daniels, A. D.; Strain, M. C.; Farkas, O.; Malick, D. K.; Rabuck, A. D.; Raghavachari, K.; Foresman, J. B.; Ortiz, J. V.; Cui, Q.; Baboul, A. G.; Clifford, S.; Cioslowski, J.; Stefanov, B. B.; Liu, G.; Liashenko, A.; Piskorz, P.; Komaromi, I.; Martin, R. L.; Fox, D. J.; Keith, T.; Al-Laham, M. A.; Peng, C. Y.; Nanayakkara, A.; Challacombe, M.; Gill, P. M. W.; Johnson, B.; Chen, W.; Wong, M. W.; Gonzalez, C.; and Pople, J. A.; Gaussian, Inc., Pittsburgh PA, 2003.

116.Suhm, M. A.; Watts, R. O. *Phys. Rep.* **1991**, 293.

117.Del Bene, J. E.; Jordan, M. J. T. *Int. Rev. Phys. Chem.* **1999**, *18*, 119.

118.Jensen, J.; Gordon, M. *J. Am. Chem. Soc.* **1995**, *117*, 8157.

119.Crittenden, D. L.; Chebib, M.; Jordan, M. J. T. *J. Phys. Chem. A* **2004**, *108*, 203.

Downloaded by PENNSYLVANIA STATE UNIV on July 3, 2012 | http://pubs.acs.org
Publication Date: December 31, 2006 | doi: 10.1021/bk-2007-0953.ch010

Chapter 10

Ab Initio Biomolecular Calculations Using Quantum Monte Carlo Combined with the Fragment Molecular Orbital Method

Ryo Maezono[1,2], Hirofumi Watanabe[3,4], and Shigenori Tanaka[3,4,*]

[1]National Institute for Materials Science, Tsukuba 305–0047, Japan
[2]PRESTO, Japan Science and Technology Agency, 4–1–8 Honcho,
Kawaguchi City, Saitama 332–0012, Japan
[3]Graduate School of Science and Technology, Kobe University, Rokkodai,
Nada, Kobe 657–8501, Japan
[4]CREST, Japan Science and Technology Agency, 4–1–8 Honcho,
Kawaguchi City, Saitama 332–0012, Japan

A novel computational scheme for the electronic states of biomolecules is proposed on the basis of the quantum Monte Carlo (QMC) method combined with the fragment molecular orbital (FMO) method. The latter provides an accurate and very efficient framework for calculating the molecular orbitals of huge systems through parallel computations for divided subsystems, thus enabling the applications to realistic proteins and nucleic acids with chemical accuracies. The feasibility of the proposed method is illustrated for a small polypeptide, the glycine trimer, as a benchmark test.

Introduction

The quantum Monte Carlo (QMC) method (*1,2*) provides a very accurate computational approach that goes beyond the single-particle or mean-field approximation to solve the Schroedinger equation, taking into account the electron correlation effects appropriately. Simplicity of the methodology is another advantage of the method, which enables the combination with other

In Advances in Quantum Monte Carlo; Anderson, J., et al.;
ACS Symposium Series; American Chemical Society: Washington, DC, 2006.

computational methods with ease. For example, the implementations combined or associated with the variational theories, the Hartree-Fock (HF) approximation and the density functional theory (DFT) approaches have been carried out in the fields of quantum chemistry, solid state physics and condensed matter theories (*1,2*). In this report, we address a problem for which the QMC method would be combined with a novel quantum chemical approach called the fragment molecular orbital (FMO) method (*3-7*) that provides a framework to perform the *ab initio* electronic state calculations for huge biomolecules with high accuracy.

Fragment Molecular Orbital (FMO) Method

Downloaded by PENNSYLVANIA STATE UNIV on July 3, 2012 | http://pubs.acs.org
Publication Date: December 31, 2006 | doi: 10.1021/bk-2007-0953.ch010

The application of quantum mechanical methods to large molecules such as proteins and nucleic acids provides a great challenge in theoretical chemistry. The calculations of electronic states for biomolecules are usually formidable due to their huge size, and some ingenious techniques are required to make them feasible. While the idea of the fragmentation of the whole system is straightforward and appealing for the reduction in computational cost, difficulties always take place concerning the inaccuracies due to the artificial breakage of chemical bonds and the systematic reconstruction of observable properties. Among a number of these approaches, however, the FMO method proposed by Kitaura *et al.* (*3-7*) affords a very promising way to retain the chemical accuracies in energy and other properties in the applications to huge biopolymers.

The FMO method (*3-7*) relies on the division of a large molecular system into a collection of small fragments and on molecular orbital (MO) calculations for the fragments (monomers) and their pairs (dimers) performed to obtain the total energy and other molecular properties. The total electronic energy of molecule can then be calculated as $E=\sum E_I+\sum(E_{IJ}-E_I-E_J)$, where E_I and E_{IJ} represent the energies of fragment monomers {I} and dimers {I,J}, respectively, calculated under the electrostatic potentials from other surrounding fragments (environmental electrostatic potentials). The FMO method thus avoids the costly MO calculation of the whole system of a large molecule and reduces the computational time remarkably. Another advantage of this method is its ease in utilizing parallel processing, since the fragments and the fragment pairs can be treated independently.

A number of test calculations have been already performed (*3-7*) concerning the accuracy and efficiency of the FMO method, providing extremely promising results for the applications to biomolecules. For example, the errors due to the fragmentation in the total energy are less than a few kcal/mol for small proteins. Actual implementations of the FMO method have been carried out in terms of the softwares such as GAMESS (*8-11*), NWChem (*12,13*), and ABINIT-MP

(*14-19*). The FMO calculations beyond the HF approximation are also available on these programs, such as the second-order Moeller-Plesset (MP2) perturbation, the configuration interaction (CI), and DFT calculations.

Combination of QMC with FMO Method

There are several practical considerations in establishing a combined approach of FMO and QMC methods. First, the FMO methodology is essentially amenable to parallel computations (*3-19*). In the case of proteins, one or two amino-acid residues are usually employed as a fragment, which typically contains tens to hundreds of electrons and therefore provides a good target of QMC calculations (*1,2*). Secondly, highly accurate calculations are often required only for the active sites of biomolecules. The capability of divided or hierarchical calculations in the FMO method (*3-19*) would then enable us to focus on some special fragments to which the QMC method should be applied.

The implementation of the coupling between the FMO and QMC methods was carried out by employing the ABINIT-MP (*19*) and CASINO (*20*) codes for the FMO and QMC calculations, respectively. We first perform the FMO calculations usually at the HF level and obtain the MOs for all the fragment monomers and dimers including the contributions of electrostatic fields from the surrounding fragments. We then proceed to the QMC calculations using these MOs, where we rely on the CASINO code. For example, the output files obtained by the HF/FMO calculations are utilized as input files for performing the HF/VMC(variational Monte Carlo) calculations for all the fragment monomers and dimers in which the environmental electrostatic fields are constructed on the basis of the charge distributions of fragments obtained by the FMO and QMC calculations. After the examination that the identical energies are recovered at the HF level by the Monte Carlo calculations, we could proceed to the inclusions of cusp correction (*21*) and electron correlations. For the latter calculations, the VMC method with the Jastrow factors and the diffusion Monte Carlo (DMC) method would be employed. The details of these implementations will be described elsewhere (*22*).

Benchmark Calculation: Glycine Trimer

As a test case, we have applied the QMC/FMO method to the total energy calculation of glycine trimer. In this report, we illustrate the results based on the HF variational calculations (HF/VMC method). The structure of glycine trimer was constructed by the HF optimization with the minimal basis set STO-3G

Downloaded by PENNSYLVANIA STATE UNIV on July 3, 2012 | http://pubs.acs.org
Publication Date: December 31, 2006 | doi: 10.1021/bk-2007-0953.ch010

starting from the α-helix initial structure. We have first carried out the usual HF and HF/FMO calculations for glycine trimer with the basis set STO-3G. In the latter calculation, we employed the ABINIT-MP program (*19*) and the total system was divided into three fragments at the C_α sites. The total energies obtained with the conventional MO and FMO methods agreed with each other within the error of 0.1 kcal/mol (Table I). Using the calculated MOs, we have next performed the HF/VMC calculations for the identical system without the cusp correction using the CASINO code (*20*). We have thus found that the HF/VMC energy without the FMO approximation agreed with the conventional HF energy and with the HF/VMC energy with the FMO approximation within the estimated error bars (Table I). We have also compared the energies for fragment monomers {I} and dimers {I,J} between the HF/FMO and HF/VMC/FMO approximations, which are listed in Table II.

With the inclusion of the cusp correction (*21*), we could expect that the electronic energies would be lowered. The comparisons of the total and fragment energies are illustrated in Tables I and II, showing that the HF/VMC energies decrease by about 5 a.u. both with and without the FMO approximations by including the cusp correction. These total energies with the cusp correction agreed with each other within the estimated error bars.

We have next included the effects of electron correlations in terms of the Jastrow factors. The agreement between the VMC and VMC/FMO energies has been found to be excellent, which will be reported elsewhere (*22*).

Downloaded by PENNSYLVANIA STATE UNIV on July 3, 2012 | http://pubs.acs.org
Publication Date: December 31, 2006 | doi: 10.1021/bk-2007-0953.ch010

Table I. Energies of glycine trimer obtained by various methods

Methods	*HF*	*HF/VMC*	*HF/VMC(cusp)*
Full MO	-687.3875159324	-687.6(6)	-692.69(6)
FMO	-687.3873537360	-687.9(4)	-692.60(7)

NOTE: Units are hartree (a.u.). The number in the parenthesis refers to the estimated error in the last digit. The HF/VMC(cusp) represents the HF/VMC calculation with the cusp correction.

Summary and Perspective

This is a first report concerning a combinatorial approach of QMC and FMO methods for electronic state calculations for biomolecules. We have here proposed the basic concept and strategy, and illustrated them in a benchmark test calculation for glycine trimer. While the example herein is confined to the HF level calculations, the calculations including the electron correlation effects are in progress, which will be shown elsewhere (*22*). We are also attempting the

Table II. Energies of fragment monomers and dimers of glycine trimer obtained by various methods

Fragments	*HF*	*HF/VMC*	*HF/VMC(cusp)*
{1}	-122.7992645203	-122.97(8)	-123.55(1)
{2}	-307.6073508713	-307.6(1)	-309.13(2)
{3}	-683.4622078107	-683.5(3)	-686.32(3)
{1,2}	-518.3118234031	-518.3(1)	-520.59(2)
{1,3}	-885.1526697326	-885.4(2)	-888.83(3)
{2,3}	-1218.9137127138	-1218.9(2)	-1223.40(3)

NOTE: Units are hartree (a.u.). The number in the parenthesis refers to the estimated error in the last digit. The HF/VMC(cusp) represents the HF/VMC calculation with the cusp correction.

Downloaded by PENNSYLVANIA STATE UNIV on July 3, 2012 | http://pubs.acs.org
Publication Date: December 31, 2006 | doi: 10.1021/bk-2007-0953.ch010

calculations for nucleic acid systems such as stacked base pairs in DNA, where the dispersion force associated with the electron correlations is expected to play an important role (*23*). In addition to these benchmark calculations, we will apply this novel QMC/FMO approach to much larger biomolecular systems in terms of parallel computations substantiated in the FMO scheme.

References

1. Foulkes, W.M.C.; Mitas, L.; Needs, R.J.; Rajagopal, G. *Rev. Mod. Phys.* **2001,** *73,* 33.
2. *Recent Advances in Quantum Monte Carlo Methods, Part II;* Lester, Jr., W.A.; Rothstein, S.M.; Tanaka, S., Eds.; World Scientific: Singapore, 2002.
3. Kitaura, K.; Sawai, T.; Asada, T.; Nakano, T.; Uebayasi, M. *Chem. Phys. Lett.* **1999,** *312,* 319.
4. Kitaura, K.; Ikeo, E.; Asada, T.; Nakano, T.; Uebayasi, M. *Chem. Phys. Lett.* **1999,** *313,* 701.
5. Nakano, T.; Kaminuma, T.; Sato, T.; Akiyama, Y.; Uebayasi, M.; Kitaura, K. *Chem. Phys. Lett.* **2000,** *318,* 614.
6. Kitaura, K.; Sugiki, S.; Nakano, T.; Komeiji, Y.; Uebayasi, M. *Chem. Phys. Lett.* **2001,** *336,* 163.
7. Nakano, T.; Kaminuma, T.; Sato, T.; Fukuzawa, K.; Akiyama, Y.; Uebayasi, M.; Kitaura, K. *Chem. Phys. Lett.* **2002,** *351,* 475.
8. Fedorov, D.G.; Olson, R.M.; Kitaura, K.; Gordon, M.S.; Koseki, S. *J. Comput. Chem.* **2004,** *25,* 872.
9. Fedorov, D.G.; Kitaura, K. *J. Chem. Phys.* **2004,** *120,* 6832.
10. Fedorov, D.G.; Kitaura, K. *Chem. Phys. Lett.* **2004,** *389,* 129.

11. Fedorov, D.G.; Kitaura, K. *J. Chem. Phys.* **2004,** *121,* 2483.
12. Sekino, H.; Sengoku, Y.; Sugiki, S.; Kurita, N. *Chem. Phys. Lett.* **2003,** *378,* 589.
13. Sugiki, S.; Kurita, N.; Sengoku, Y.; Sekino, H. *Chem. Phys. Lett.* **2003,** *382,* 611.
14. Mochizuki, Y.; Nakano, T.; Koikegami, S.; Tanimori, S.; Abe, Y.; Nagashima, U.; Kitaura, K. *Theor. Chem. Acc.* **2004,** *112,* 442.
15. Mochizuki, Y.; Koikegami, S.; Nakano, T.; Amari, S.; Kitaura, K. *Chem. Phys. Lett.* **2004,** *396,* 473.
16. Mochizuki, Y.; Koikegami, S.; Amari, S.; Segawa, K.; Kitaura, K.; Nakano, T. *Chem. Phys. Lett.* **2005,** *406,* 283.
17. Mochizuki, Y. *Chem. Phys. Lett.* **2005,** *410,* 165.
18. Mochizuki, Y.; Fukuzawa, K.; Kato, A.; Tanaka, S.; Kitaura, K.; Nakano, T. *Chem. Phys. Lett.* **2005,** *410,* 247.
19. *ABINIT-MP* and *BioStation Viewer* are available from http://www.fsis.iis.u-tokyo.ac.jp/en/result/software/.
20. Needs, R.J.; Towler, M.D.; Drummond, N.D.; Lopez Rios, P. *CASINO version 2.0 User Manual;* University of Cambridge: Cambridge, 2005.
21. Ma, A.; Towler, M.D.; Drummond, N.D.; Needs, R.J. *J. Chem. Phys.* **2005,** *122,* 224322.
22. Maezono, R.; Watanabe, H.; Tanaka, S., in preparation.
23. Fukuzawa, K.; Komeiji, Y.; Mochizuki, Y.; Kato, A.; Nakano, T.; Tanaka, S. *J. Comput. Chem.* **2006,** in press.

Downloaded by PENNSYLVANIA STATE UNIV on July 3, 2012 | http://pubs.acs.org
Publication Date: December 31, 2006 | doi: 10.1021/bk-2007-0953.ch010

Downloaded by STANFORD UNIV GREEN LIBR on July 4, 2012 | http://pubs.acs.org
Publication Date: December 31, 2006 | doi: 10.1021/bk-2007-0953.ch011

Chapter 11

Vibrational Excited States by Diffusion Monte Carlo

Anne B. McCoy

Department of Chemistry, The Ohio State University,
Columbus, OH 43210

Methods for evaluating vibrationally excited states by DMC within the fixed-node approximation are described. Two central issues are identified. The first, and most important, is the identification of the coordinates that will be used to describe the molecular vibrations. The second is the determination of where the node should be placed. Strategies for addressing both of these issues are discussed within the context of the fundamental vibrations in Ne_2OH and $H_3O_2^-$.

Introduction

One of the greatest challenges for and limitations of the Diffusion Monte Carlo (DMC) approach is the treatment of nodes. This is clearly a problem for any application of DMC to electronic structure problems. For vibrational problems, even if the ground state is nodeless, it is unusual for that to be the only state of interest, and excited states all contain nodes.

In cases where the functional form of the N–1 dimensional nodal surface is known, the solution is straightforward, since the behavior of a wave function in the vicinity of a node is identical to that when the potential is forced to be infinite along this surface (*1*). Specifically, the wave function goes to zero at the node, and its first derivative is finite and constant across the node.

This can be readily seen in one-dimension. Consider the first excited state for the harmonic oscillator potential, $V_1(r) = k/2\, r^2$. The energy of this state is the same as the energy of the ground state wave function of potentials that are defined as

$$V_2(r)=\begin{cases}\infty & r\le 0\\ \dfrac{k}{2}r^2 & r>0\end{cases} \tag{1}$$

and

$$V_3(r)=\begin{cases}\dfrac{k}{2}r^2 & r<0\\ \infty & r\ge 0\end{cases} \tag{2}$$

In addition, the wave function that corresponds to the first excited state solution to the Schrödinger equation, where the full harmonic oscillator potential is used, is identical, within a constant factor, to the ground state solution for the potential in Eq. (1) for $r > 0$ and the ground state solution for the potential in Eq. (2) for $r < 0$.

As this example demonstrates, when we know where the node should be located, an excited state calculation reduces to a series of ground state calculations in each of the regions over which the wave function does not change sign. These separate calculations can be readily performed by DMC approaches. Nearly thirty years ago Anderson described an algorithm for evaluating excited state wave functions within a fixed-node approximation (*1*). As we learn from the particle-in-a-box system, the wave function must be zero in regions in configuration space where the potential is infinite. Within DMC, this means that a walker that crosses a node, or tries to cross into a region, in which the potential is infinite, must be removed from the simulation. In the limit of infinitely short time-steps, such a condition is sufficient to ensure that the excited states are properly described. For finite time-steps, the probability that a walker crosses the nodal surface twice must be accounted for. This is achieved through a recrossing correction, which provides the probability that a walker that remains on the same side of a nodal surface has followed a path in which it crossed the node twice (*1*). Specifically, the probability that a walker has crossed a node twice is given by

$$P_{\text{recross}}=\exp\left(-\frac{4x'x''}{2\sigma^2}\right) \tag{3}$$

where x' and x'' provide the distance of the walker from the nodal surface before and after the step was taken and

Downloaded by STANFORD UNIV GREEN LIBR on July 4, 2012 | http://pubs.acs.org
Publication Date: December 31, 2006 | doi: 10.1021/bk-2007-0953.ch011

$$\sigma^2 = \frac{2\Delta\tau}{m} \tag{4}$$

The above procedure is effective and efficient, but it requires knowledge of the position of the nodal surface. This can be argued to be the greatest challenge for applying DMC to electronic states. For vibrational problems, the challenges are more or less severe, depending on the aspect of the problem one focuses on. The challenges come from the smaller energy differences among vibrational states, compared to electronic problems. Therefore it is difficult to make compelling arguments about properties of molecular vibrations with knowledge of only the ground state wave function, although our recent work on CH_5^+ has shown that we can extract considerable information from the ground state wave functions (*2*,*3*). On the other hand, the ground vibrational state is nodeless. Further, in the limit of small amplitude vibrations, the vibrations of an N-atomic molecule can be described in terms of $3N$–6 uncoupled harmonic oscillators. The definition of these coordinates can be readily obtained by diagonalizing the Hessian in mass-weighted Cartesian coordinates. In this limit, the fundamentals correspond to states where the nodal surface is defined by $q_i = \eta_i$. In other words, for a system with n vibrational degrees of freedom, the nodal surfaces that allow us to study each of the fundamentals are defined by n–1 dimensional hyperplanes that are simple functions of only one of the vibrational coordinates. In some cases the value of η_i can be determined by symmetry, as was the case for the one-dimensional harmonic oscillator, described above. In general, this is not the case.

While for many systems we can consider the zero-point motions as small amplitude vibrations about the minimum energy structure, this will not be the case for many systems of interest. In spite of this, in the absence of accidental degeneracies, the vibrations are often separable when the *right set* of coordinates is chosen. As such, this chapter will focus on two issues. First, how do we choose coordinates with which to describe the fundamental excitations? Perhaps even more important, how can we know when we have chosen the *right set* of vibrational coordinates? Once the coordinates are chosen, the second challenge is to determine the value of q_i at which the nodal surface should be placed. In some cases, the value of η_i can be determined by symmetry, but in general this is not the case. To address the issue of determining each of the η_i, we will apply an adiabatic version of DMC, ADMC that was originally introduced by Lee, Herbert and McCoy (*4*,*5*).

The discussion below is focused on the issues that are involved in determining vibrationally excited states. As such, we have not repeated

Downloaded by STANFORD UNIV GREEN LIBR on July 4, 2012 | http://pubs.acs.org
Publication Date: December 31, 2006 | doi: 10.1021/bk-2007-0953.ch011

discussions of our general implementation of the DMC procedures. In brief, our implementations are based on the algorithm that was outlined in the original paper of Anderson (*6*) and which is reviewed in the paper of Suhm and Watts (*7*). Detailed accounts of our implementation of DMC can be found in the original reports of the work on $H_3O_2^-$ and Ne_2OH, discussed below (*8,9*), as well as in a recent review of our work (*10*).

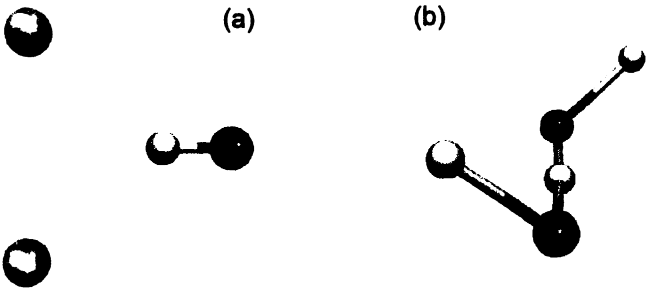

Figure 1. The structures of (a) Ne_2OH *and (b)* $H_3O_2^-$ *in their equilibrium geometries.*

Systems

Before discussing this approach and how we chose our vibrational coordinates, we will introduce the two systems that will serve as examples. These systems are Ne_2OH and $H_3O_2^-$. Our work on these systems is described in greater detail elsewhere (*8,9,11*). They are chosen for the present discussion because they represent examples of two classes of systems that sample large regions of their potentials, even in their ground states. They are also systems for which variational calculations have been performed by us for Ne_2OH (*11*) and by Huang, Carter and Bowman for $H_3O_2^-$ (*8*). These provide points of comparison for our ADMC excited state energies. In the case of $H_3O_2^-$, depicted in figure 1(b), the HOOH structure is fairly rigid, but includes a large amplitude HOOH torsion mode as well as large amplitude excursions of the central hydrogen atom from its position in the minimum. By contrast, Ne_2OH is somewhat more rigid, with the larger amplitude motions corresponding to the rotation of the OH unit. On the other hand, the binding energy of the constituent pieces is small.

Downloaded by STANFORD UNIV GREEN LIBR on July 4, 2012 | http://pubs.acs.org
Publication Date: December 31, 2006 | doi: 10.1021/bk-2007-0953.ch011

The Ne–OH binding energy is only 53 cm^{-1} (*12,13*), while the neon dimer is bound by less than 20 cm^{-1}.

The potential for the Ne_2OH complex is described by a pair-wise sum of the Ne·OH $\tilde{A}$–state potential, which we fit to experimental transition frequencies and rotational constants (*12*) and the HFD-B potential for Ne_2 of Aziz (*14*). The global minimum on this surface has a T-shaped configuration in which the three heavy atoms are nearly equidistant. There is also a low-lying minimum in the linear Ne–OH–Ne geometry that is 37 cm^{-1} higher in energy than the global minimum.

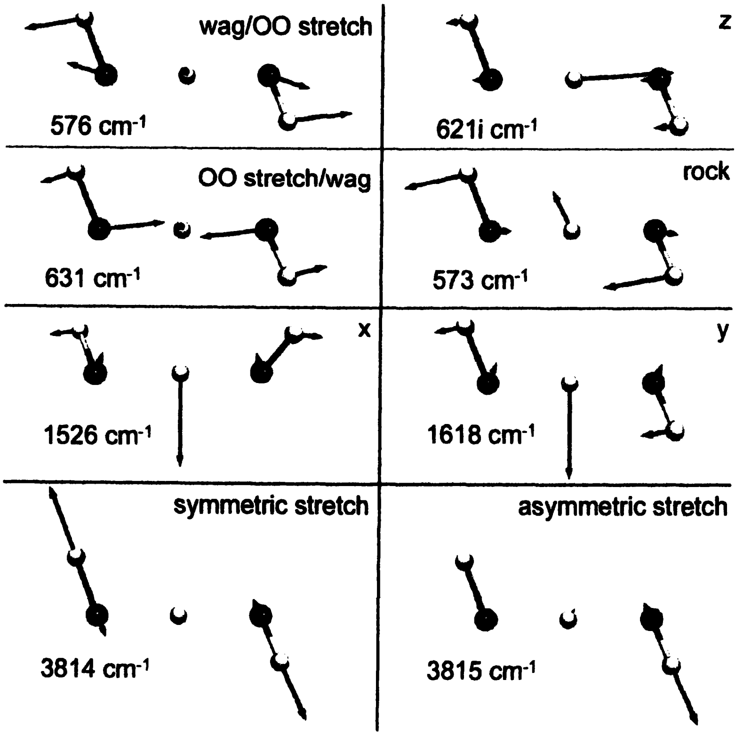
wag/OO stretch
576 cm^{-1}
z
621i cm^{-1}
OO stretch/wag
631 cm^{-1}
rock
573 cm^{-1}
x
1526 cm^{-1}
y
1618 cm^{-1}
symmetric stretch
3814 cm^{-1}
asymmetric stretch
3815 cm^{-1}

Figure 2. Normal mode vectors at the C_2 saddle point in $H_3O_2^-$ *in which the central hydrogen atom lies on the OO axis and equidistant from the two oxygen atoms. The numbers in each panel indicate the corresponding harmonic frequency. Totally symmetric modes are in the left column, modes that have B symmetry are in the right column. (Reprinted with permission from reference 8. Copyright 2005 American Institute of Physics.)*

Downloaded by STANFORD UNIV GREEN LIBR on July 4, 2012 | http://pubs.acs.org
Publication Date: December 31, 2006 | doi: 10.1021/bk-2007-0953.ch011

Downloaded by STANFORD UNIV GREEN LIBR on July 4, 2012 | http://pubs.acs.org
Publication Date: December 31, 2006 | doi: 10.1021/bk-2007-0953.ch011

$H_3O_2^-$ is a chemically more interesting species than Ne_2OH. $H_3O_2^-$ can be thought of as a complex of H_2O and OH^-, with one of the OH bonds in the water molecule forming a hydrogen bond with the oxygen atom in OH^-. Understanding the interactions of OH^- with water is important in investigations of proton transport in basic solution. $H_3O_2^-$ is the simplest example of such a complex. An interesting feature of this complex is that the central hydrogen is closer to one of the OH groups than the other, $r_{O_1H} - r_{O_2H} = 0.3066$ Å, when the ion is in its equilibrium configuration (*15*). In this system, there is a low-lying first-order saddle point in the geometry in which the central hydrogen atom is midway between the two oxygen atoms and a shorter OO distance by 0.050 Å This stationary point lies 68.5 cm^{-1} above the global minimum on the potential surface of Huang, Braams and Bowman, used in the present work (*15*). As this energy is much smaller than the harmonic frequency at the minimum that corresponds to motion toward the transition state, 1569 cm^{-1}, it is anticipated that the most probable geometry will correspond to the hydrogen atom being equidistant from the two oxygen atoms. There are also two low-energy barriers along the HOOH torsion coordinate. The barrier in the *cis*-configuration is 374 cm^{-1}, while the barrier in the *trans*-configuration is 147 cm^{-1} (*8*). If we rotate $H_3O_2^-$ along the torsion coordinate, constraining the central hydrogen atom to be midway between the two oxygen atoms, we find that the magnitudes of the lower frequencies change dramatically, as is seen in figure 2. From this analysis we expect $H_3O_2^-$ to sample large regions of the potential, even in its ground vibrational state. We also expect there to be large couplings among the vibrational modes. These factors make it an excellent system to investigate the choice of coordinates on the effectiveness of the fixed-node approximation in DMC.

Coordinates

As mentioned above, the normal mode picture for molecular vibrations provides an attractive framework for thinking about the nodes. While for strongly bound systems that sample limited ranges of the potential surface in their ground states, the usual normal modes that are defined as linear combinations of mass-weighted Cartesian displacements provide an appropriate choice. Such a set of coordinates is depicted for $H_3O_2^-$ in figure 2. It is clear from the discussion above that these are probably not the optimal coordinates for investigations of floppy systems, like Ne_2 OH or $H_3O_2^-$.

Downloaded by STANFORD UNIV GREEN LIBR on July 4, 2012 | http://pubs.acs.org
Publication Date: December 31, 2006 | doi: 10.1021/bk-2007-0953.ch011

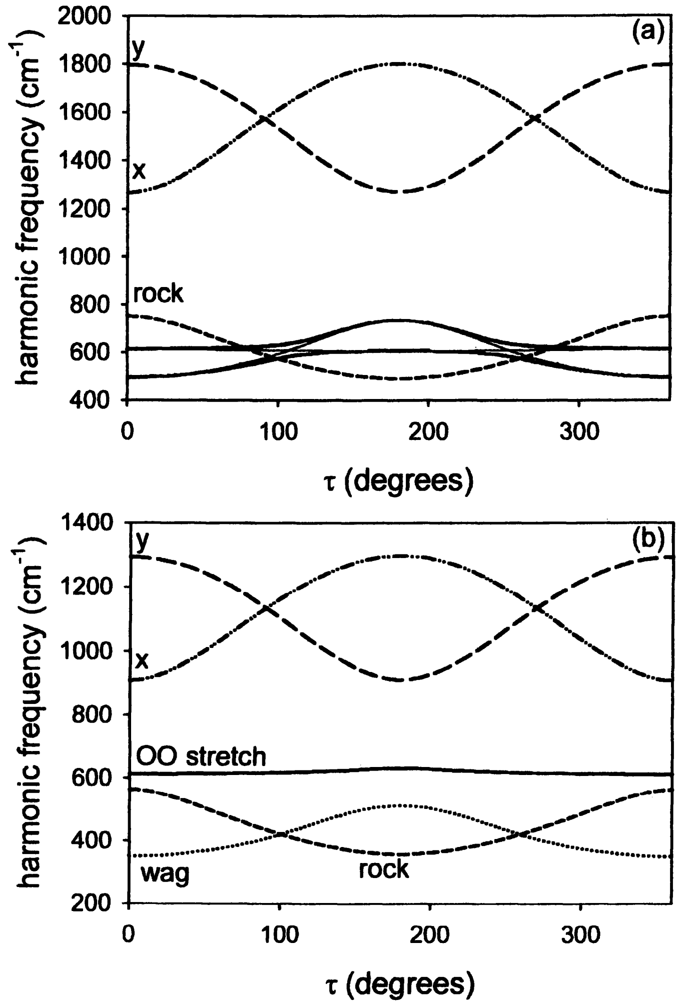

Figure 3. Plot of the dependence of five harmonic frequencies for (a) $H_3O_2^-$ *and (b)* $D_3O_2^-$*. Using the notation in figure 2, the solid line shows the* OO *stretch frequency, dotted and short dashed lines give the wag and rock frequencies while the dot-dot-dashed and long dashed lines give the frequencies of x and y. In* $H_3O_2^-$ *the frequencies of the* OO *stretch and wag flip their energy ordering over this range of angles, and we plotted both frequencies with thick solid lines. To illustrate the underlying, uncoupled (diabatic) frequencies, we have sketched them with thin lines. (Reprinted with permission from reference 8. Copyright 2005 American Institute of Physics.)*

The above definition is the textbook one. As the normal modes are based on the second derivatives of the potential at a stationary point, the extrapolation of these coordinates for larger amplitude displacements is not unique (*16*). In fact *normal coordinates}* may be constructed for any set of linearly independent vibrational coordinates by following the standard *FG* matrix formalism described by Wilson, Decius and Cross (*17*). When normal coordinates are used to expand the Hamiltonian for perturbative treatments of molecular vibrations (*18*), in the absence of resonance interactions, the effective Hamiltonian is independent of the choice of coordinates (*19,20*). In general for variational or DMC calculations, the accuracy of the results for a particular amount of computational effort will depend sensitively on the choice of coordinates. Based on the above discussion, the choice of coordinates in which we place our nodes is critical.

In the case of the Ne_2OH system, we follow the work of Cooper and Hutson (*21*) and use the sum and differences of the two Ne–OH angles, $\theta_\pm$, the distance between the center of masses of OH and Ne_2, R, the angle between the Ne–Ne axis and R, and the rotation of OH off of the plane that contains the heavy atoms.

For $H_3O_2^-$, we use the symmetry adapted linear combinations of the six internal coordinates of H_2O_2, neglecting the central hydrogen atom. Specifically, we use sums and differences of the two OH distances and HOO angles, the OO distance and the HOOH torsion angle. We also use the three Cartesian displacements of the central hydrogen atom from the center of the OO bond, x, y and z. The OO bond is used to define the z–axis.

We have explored two ways to check the separability of these coordinates. The first involves diagonalization of the *FG* matrix in these coordinates. Following Wilson *et al.* (*17*),

$$s_i = \sum_{j=1}^{3N-6} L_{ij} q_j \tag{5}$$

where s_i represents one of the symmetry coordinates and q_j is a normal mode coordinate that is constructed from a linear combination of the s_i's. In this way, $\{L^{-1}\}_{ji}L_{ij}$ provides a rough measure of the contribution of s_i to q_j. This is only approximate because the *FG*-matrix is not symmetric, and $\{L^{-1}\}_{ji}L_{ij}$ need not be positive. The above prescription provides a measure of the separability of the motions near the equilibrium configuration. As is seen in figure 3, in $H_3O_2^-$ there are large changes in the harmonic frequencies with the torsion coordinate, τ, and the relatively low barrier to free rotation along this coordinate in $H_3O_2^-$ leads one to expect that such a measure of separability may be misleading. A second measure, which is more appropriate for systems like $H_3O_2^-$ that undergo large amplitude motions, is the cross correlation (*22*),

Downloaded by STANFORD UNIV GREEN LIBR on July 4, 2012 | http://pubs.acs.org
Publication Date: December 31, 2006 | doi: 10.1021/bk-2007-0953.ch011

$$S_{ij} = \frac{\langle s_i s_j \rangle - \langle s_i \rangle \langle s_j \rangle}{\sigma_i \sigma_j} \tag{6}$$

where

$$\sigma_i = \sqrt{\langle s_i^2 \rangle - \langle s_i \rangle^2} \tag{7}$$

This quantity will take on values between −1 and 1 with values near zero indicating that the modes are uncorrelated and values near ±1 indicating that they are highly correlated. The S_{ij} have the advantage that they are based on the ground state probability amplitude and will reflect the increased or decreased separability among the symmetry coordinates upon large amplitude excursions from the equilibrium geometry, exhibited by the ground state wave function.

Both of the above treatments have been applied to $H_3O_2^-$ (*8*). Because of the low barrier for hydrogen exchange between the two OH groups, we use the saddle point at 68.5 cm^{-1} as our reference geometry for the normal mode analysis. When we do this, we find that for all but two of the normal modes, shown in figure 2, one of the symmetry adapted linear combinations of the internal displacements has a value of $\{L^{-1}\}_{ji}L_{ij}$ that is larger than 0.84. The exceptions involve the modes at 576 and 631 cm^{-1}. This is not surprising based on the plots in figure 3, which show that at the equilibrium configuration, where $\tau = 101°$, the frequencies of these two modes undergo an avoided crossing. In the case of the S_{ij} values, only five pairs are larger than 0.03, and four of these involve displacements of the central hydrogen atom perpendicular to the OO axis.

Once the coordinates have been chosen, we need to determine the appropriate mass factor for the recrossing probability in Eqs. (3) and (7). For Ne_2OH, we use the procedure outlined in Ref. (*5*). Alternatively, the associated masses may be defined using Wilson *G*-matrix elements, or the appropriate linear combination of these effective masses (*17*).

Positioning the Nodes

Once the coordinates have been identified, the second challenge becomes the determination of the value of η_i for the fundamental that corresponds to excitation along q_i. Often symmetry considerations may be used to define the position of the nodal plane. An example of this is the harmonic oscillator, described above. In many situations, this is not the case.

Downloaded by STANFORD UNIV GREEN LIBR on July 4, 2012 | http://pubs.acs.org
Publication Date: December 31, 2006 | doi: 10.1021/bk-2007-0953.ch011

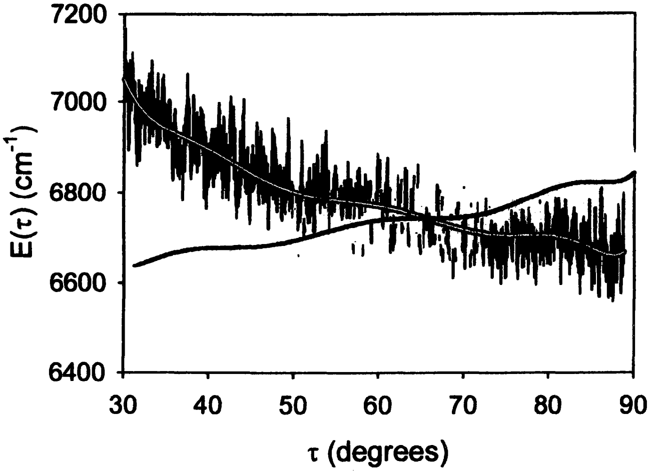

Figure 4. Plot of the energies of the torsion fundamental of $H_3O_2^-$ as a function of the position of the node, obtained from DMC.

As was illustrated, when the node is correctly placed, the energies that are calculated from a pair of simulations, one for each side of the nodal surface, are identical. We use this condition to optimize the position of the nodal surface. If we shift the value of η_i, the energy obtained from a calculation on one side of the node will increase, while the energy from the other calculation will decrease. This can be understood by the relationship between the width of the potential (confinement) and zero-point energies. We developed ADMC based on this property (*4,5*). In this procedure, we first equilibrate a DMC simulation for a particular value of η_i. Once the simulation has equilibrated, we shift η_i by an amount, dη, at each time step, where dη is chosen so that the change in the zero-point energy that is caused by this shift is small compared to the statistical fluctuations in the DMC simulation. The procedure is repeated for a second simulation that is run over the same range of η_i, but for the other side of the nodal surface. A representative energy profile for a pair of simulations of the energy of the fundamental in the HOOH torsion in $H_3O_2^-$ is plotted in figure 4. While there are fluctuations in the energies, we can fit the two curves to polynomials in the torsion angle, τ, using a linear least squares fitting procedure. We then find the point of intersection of the two fit curves. The value of τ provides the position of the node. In this case it is 65.17°. The value of $E(\tau)$ gives the energy of the fundamental, 6740 cm^{-1}. When we repeat this procedure five times and average the quantities, we get an average position of the node of η_t = 64.6° and an average energy of 6736 cm^{-1} (*8*). This procedure has been

Downloaded by STANFORD UNIV GREEN LIBR on July 4, 2012 | http://pubs.acs.org
Publication Date: December 31, 2006 | doi: 10.1021/bk-2007-0953.ch011

used for studies of the fundamentals in Ne_2SH (*5*), Ne_2OH (*9*), $H_5O_2^+$ (*23,24*) and $H_3O_2^-$ (*8,25*).

For a coordinate in which the position of the node is known by symmetry, the amplitude of the wave function on both sides of the node must be equal. This is not the case, in general. In order to obtain the relative amplitudes on the two sides of the nodal surface, additional information is needed. For this, we take advantage of the orthogonality of the ground and excited states and require that the overlaps of the two parts of the excited state wave function with the ground state wave function must be equal.

Calculating overlaps among wave functions is not straightforward in DMC since the information that comes directly from a DMC simulation is a Monte Carlo sampling of the wave function. In other words, DMC does not provide an explicit method to evaluate the magnitude of the wave function at a specific configuration. They are obtained by evaluating the density of walkers in a certain region of configuration space (*10,26*). Within this approach, we calculate the number of walkers in the excited state wave function that are inside of a hypersphere centered on each of the walkers that represent the ground state wave function. Numerically, this procedure is equivalent to convoluting each walker with a Gaussian and representing each of the wave functions as a sum of Gaussians. Obtaining the optimal width for the Gaussian, or equivalently the radius of the hypersphere, requires a balance of having it large enough to generate reasonable statistics, while keeping it small enough so as not to broaden the wave function. We find that for $H_3O_2^-$, $r^2 = 0.375\ a_0^2$ provides a good compromise. This can be checked by investigating variations in the overlaps with changes in this radius as well as by evaluating the overlap of the two contributions of the excited state wave function. The latter quantity should be zero.

In the present investigations, we use this procedure to obtain overlaps between the ground state wave function and the two wave functions that represent the excited state. Since the overlap between the ground and excited state wave functions should be zero, we scale the amplitudes of the two parts of the excited state wave function to ensure that this is indeed the case. Once we have evaluated this scaling factor, expectation values of quantities of interest are obtained using the descendent weighting approach (*7,27*).

Based on the above discussion, it should be apparent that the evaluation of excited state energies and wave functions is not inexpensive as each state must be evaluated independently. We have investigated several overtones and combination bands for $H_3O_2^-$. The simplest situation occurs for states with one quantum of excitation along each of two coordinates of two different symmetries, neither of which is totally symmetric. In this case, a simple fixed node simulation can be performed. For combination bands for which only one of the coordinates is totally symmetric, the two nodes are treated independently,

Downloaded by STANFORD UNIV GREEN LIBR on July 4, 2012 | http://pubs.acs.org
Publication Date: December 31, 2006 | doi: 10.1021/bk-2007-0953.ch011

and the node in the non-totally symmetric coordinate is treated within a fixed-node approach, while the totally symmetric one is found using the ADMC procedure, described above. We have not treated the case of excitation in two different totally symmetric modes.

For overtones, a similar hierarchy exists. Since the first overtone of a mode that is not totally symmetric is an even function of that coordinate, the positions of the two nodes will be related by symmetry. As a result there is only one parameter that needs to be optimized, and this can be readily achieved by the ADMC procedure where instead of considering the parts of the wave function for which $q_i > \eta_i$ and $q_i < \eta_i$, we focus on $| q_i | > \eta_i$ and $| q_i | < \eta_i$.

For totally symmetric modes, such a symmetry does not exist. Here we divide the potential into three pieces, denoted regions I, II and III, that are separated by two nodal surfaces, η_I separates regions I and II while η_III separates regions II and III. In the first step, we perform ADMC simulations in regions I and III. this gives two functions $\eta_\text{I}(E)$ from region I and $\eta_\text{III}(E)$ from region III. We invert these equations to find the values of η_I and η_III that correspond to the same energy. We then perform an ADMC simulation in region II in which we vary the positions of η_I and η_III so that the energies in regions I and III are equal. We use the $E(\eta)$ profiles from regions I and II to obtain the overtone energies as we did in the ADMC simulations for the fundamentals.

As the above illustrates, the forms of the nodal surfaces become increasingly complex as we increase the number of nodes. While the procedure may be extended beyond overtones, to date we have not pursued this in part because the assumption that the nodal surfaces take on simple functional forms is unlikely to remain appropriate for higher levels of vibrational excitation.

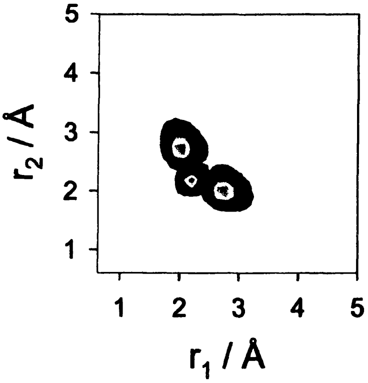

Figure 5. Plot of the probability amplitude for the variational eigenstate of Ne_2OH with one quantum in the Ne–OH stretch, plotted as a function of the two Ne–OH distances, r_1 and r_2.

Downloaded by STANFORD UNIV GREEN LIBR on July 4, 2012 | http://pubs.acs.org
Publication Date: December 31, 2006 | doi: 10.1021/bk-2007-0953.ch011

Results

Ne_2OH

We start by considering Ne_2OH. For these studies we used the rigid body variant of DMC (RBDMC), developed by Buch (*28*), and consider only the five intermolecular molecular vibrations. The results of these simulations are given in Table I and are compared to the energies that were obtained by variational calculations that were converged to better than 0.1 cm^{-1}. Overall, the agreement is excellent. The zero-point energy differs by less than 0.2 cm^{-1}, while for all but one state, the frequencies of the fundamental are within 1.0 cm^{-1} of each other. As noted above, this is a potentially very floppy system and the extent of these motions is illustrated in the plots of the wave function slices and projections, reported in Refs. (*9*) and (*11*). The two exceptions to the excellent agreement are seen in the in-plane bend and the Ne_2OH stretch. We will return to the bend in our discussion of problems with coordinate choices, below. In the case of the stretch, the disagreement can be understood in terms of a poor choice of the nodal surface. This can be seen in the plot of the projection of the probability amplitude for this state onto the r_1/r_2 plane, shown in figure 5. Clearly the nodal surface does not lie along a line that can be defined as $r_1 + r_2 = const.$ Rather there is curvature in the nodal surface. We will return to this point, below.

Table I. Comparison of Diffusion Monte Carlo [DMC] and variational [var] energies for low-lying vibrational states in the T-shaped minimum of the Ne_2OH potential.

State	*DMC*[a]	*var*
Ground state	-112.4	-112.2
Ne—OH—Ne bend	18.2	17.8
Ne_2 bend	22.1	20.8
Ne_2—OH stretch	33.5	28.4
In-plane bend	*b*	*b*
Out-of-plane bend	77.6	78.5

[a] All energies are reported in cm^{-1}. The ground state energy is reported relative to the Ne+Ne+OH dissociation limit while all other energies are reported relative to the ground state energy.

[b] The in-plane bend fundamental does not exist in Ne_2OH.

Downloaded by STANFORD UNIV GREEN LIBR on July 4, 2012 | http://pubs.acs.org
Publication Date: December 31, 2006 | doi: 10.1021/bk-2007-0953.ch011

$H_3O_2^-$

We recently reported DMC energies for all nine fundamentals in $H_3O_2^-$ and $D_3O_2^-$, along with the tunneling splittings along the torsion (*8*). They are reproduced in Table II. As is seen, excellent agreement is obtained with the results of vibrational configuration-interaction (VCI) calculations of Huang, Carter and Bowman. Due to the large number of vibrational degrees of freedom, nine, compared to the five in Ne_2OH, the VCI energies for $H_3O_2^-$ are not as well converged as those for the Ne_2OH system. This can be seen in the larger difference between the zero-point energies, for which the DMC simulations are "exact" within statistical uncertainties. Since the frequencies of the excited states represent differences between energies, rather than absolute energies, the errors should be smaller. Overall, the agreement between the two sets of energies, reported in Table II, is excellent. Notable exceptions are seen for the displacements in x and y, which will be discussed below.

As in Ne_2OH, there is a sensitivity of the OH stretch frequency to how the node is defined. In the case of $H_3O_2^-$, both experiment (*29*) and VCI calculations (*15*) indicate that the OH stretches behave as local modes, rather than normal modes. Evidence for this can also be found in the near degeneracy of the two fundamentals, which can be seen in the harmonic frequencies in figure 2. Further evidence is seen in the fact that the frequencies obtained when one node is placed in the asymmetric and the local mode stretches are nearly equal, within statistical uncertainties, while the symmetric stretch energy obtained by DMC is larger. This is discussed in greater detail in Ref. (*8*).

A related example can be found in the OO stretch. Here one can imagine two definitions. One is the OO bond length, as in HOOH. The other is the symmetric linear combination of the distances of the central hydrogen atom from the two oxygen atoms. Likewise, the z-component of the central hydrogen displacement may be described by either the displacement from the center of the OO bond or the difference between the distances of the central hydrogen atom from the two oxygen atoms. Needless to say, the coupling among modes will depend on this choice, as in one case the so-called OO stretch is treated as a symmetric stretch of two HO bonds, while in the other it is defined explicitly as an OO stretch. We have performed fixed-node DMC and ADMC calculations for both pairs of coordinates. The energies for the OO stretch and displacement of the central hydrogen atom from the center of the OO bond are reported in Table II. The energies for the states obtained from antisymmetric linear combinations of the two HO distances in $H_3O_2^-$ and $D_3O_2^-$ are 644 and 401 cm^{-1}, respectively. These are both within statistical uncertainties of the results reported in Table II.

Downloaded by STANFORD UNIV GREEN LIBR on July 4, 2012 | http://pubs.acs.org
Publication Date: December 31, 2006 | doi: 10.1021/bk-2007-0953.ch011

Table II. Energies of the fundamentals of $H_3O_2^-$ and $D_3O_2^-$. (Reprinted with permission from reference 8. Copyright 2005 American Institute of Physics.)

	VCI		*DMC*[a]	
$H_3O_2^-$	+[b]	−	+	−
ground[c]	6625	22	6605	14
Torsion	132	215	131	224
OO stretch	515	540	505	521
Wag	576	606	588	602
Rock	465	528	479	517
z	741	785	644	665
y	1299	1426	1102	1110
x	1473[d]	1518	*e*	1019
OH-sym[f]	3641	3666	3631	3641
OH-asym[f]	3634	3666	3609	3625
OH-local			3610	3632

	VCI		*DMC*[a]	
$D_3O_2^-$	+[b]	−	+	−
ground[c]	4882	6	4877	4
Torsion	108	143	103	145
OO stretch	493	509	491	495
Wag	398	406	437	437
Rock	319	349	354	368
z	484	512	402	408
y	982	1020	792	797
x	1094	1110	*e*	713
OH-sym[f]	2681	2689	2678	2682
OH-asym[f]	2681	2699	2664	2667
OH-local			2668	2673

[a] All DMC results contain a 5 cm^{-1} statistical uncertainty.

[b] The + and −states represent the lower and upper states of the tunneling doublets.

[c] The ground state energy is reported relative to the potential minimum. All other energies are reported relative to the ground state.

[d] Several states between 1320 and 1618 cm^{-1} contain significant character of this fundamental.

[e] This state could not be identified from the fixed-node DMC calculations.

[f] For these states there is at least one other state with significant OH or OD stretch character within 10 cm^{-1} (OH) or 3 cm^{-1} (OD) of the reported energy.

Downloaded by STANFORD UNIV GREEN LIBR on July 4, 2012 | http://pubs.acs.org
Publication Date: December 31, 2006 | doi: 10.1021/bk-2007-0953.ch011

In contrast, the energies obtained for the symmetric combinations of the two HO distances are 521 and 587 cm^{-1}, which are statistically larger than those reported in Table II. We believe that the true OO distance provides the better description of this mode for several reasons. First, the frequency of this mode should be relatively insensitive to deuteration, as is seen in Table II. In addition, we find that the value of S_{ij} between the OO stretch and the wag is larger when it is defined as the symmetric combination of the two HO distances. We continue to work on identifying independent measures of to use to determine the optimally separable coordinates.

Downloaded by STANFORD UNIV GREEN LIBR on July 4, 2012 | http://pubs.acs.org
Publication Date: December 31, 2006 | doi: 10.1021/bk-2007-0953.ch011

Pathological Cases

In our work, we have found several coordinates for which fixed-node DMC simulations behaved in a way that deviated from our expectations. The first example of this is in the in-plane bend in Ne_2OH. Here we found that when we placed a node in this coordinate, which is basically setting the two Ne–OH angles to be equal, the simulation appeared to be converging to one energy, but at longer times, the energy dropped significantly and the state was clearly not the one we were after. Further analysis showed that the state we were calculating was a state in the Ne–OH–Ne minimum with non-zero total angular momentum. This was later verified by the variational calculations (*11*).

In $H_3O_2^-$ we encountered a similarly large deviation from the variational calculations when we considered the fundamentals in the displacements of the central hydrogen perpendicular to the OO axis. From analysis of the DMC probability amplitudes and calculations of combination bands, it seems that these modes are strongly coupled to the OOH wag and rock motions. From our analysis, we believe that the states that we obtain by putting a node in the *x*- and *y*-displacement coordinates of the central hydrogen atom are approximations to combination bands and overtones of the wag and rock, perhaps with some OO stretch or *z*-displacement of the central hydrogen atom. This is a point that we are continuing to investigate.

The above discussion serves to illustrate that while the fixed node or ADMC simulations may be used to obtain excited states, they must be coupled with careful analysis of the wave functions in order to ensure that the state that was calculated is the one of interest.

Summary and Outlook

A lot may be learned by performing simulations of vibrationally excited states. By careful comparison of the DMC results with accurate variational treatments, we are able to benchmark fixed node approaches and check our intuition and understanding of the nature of vibrationally excited states. Having demonstrated this, the next challenge is to probe the dynamics of these intriguing and important systems. While we have shown that one can obtain excited state energies and wave functions, and from them properties of these states, challenges remain. These include methods for obtaining energies and wave functions for highly excited states, intensities and information about molecular rotations. In spite of this, at this point in time, if one is primarily interested in low-lying vibrationally excited states of a molecular that undergoes large amplitude vibrational motions, ADMC provides an attractive approach for such investigations.

Downloaded by STANFORD UNIV GREEN LIBR on July 4, 2012 | http://pubs.acs.org
Publication Date: December 31, 2006 | doi: 10.1021/bk-2007-0953.ch011

Acknowledgements

Support through grants from the Chemistry Division of the National Science Foundation as well as the Petroleum Research Fund, administered by the American Chemical Society is gratefully acknowledged. I am also grateful to two former students, Dr. Hee-Seung Lee and Dr. John M. Herbert who were responsible for the DMC development and the work on Ne_2OH system. I also thank Professor Joel M. Bowman for providing us with the potentials used in the studies of $H_3O_2^-$ and for many stimulating discussions and suggestions.

References

1. Anderson, J. B. *J. Chem. Phys.* **1976,** *65,* 4121.
2. Huang, X.; McCoy, A. B.; Bowman, J. M.; Johnson, L. M.; Savage, C.; Dong, F.; Nesbitt, D. J. *Science* **2006,** *311,* 60.
3. Johnson, L. M.; McCoy, A. B. *J. Phys. Chem. A* (submitted).
4. Lee, H.-S.; Herbert, J. M.; McCoy, A. B. *J. Chem. Phys.* **1999,** *110,* 5481.
5. Lee, H.-S.; Herbert, J. M.; McCoy, A. B. *J. Chem. Phys.* **1999,** *111,* 9203.
6. Anderson, J. B. *J. Chem. Phys.* **1975,** *63,* 1499.
7. Suhm, M. A.; Watts, R. O. *Physics Reports* **1991,** *204,* 293.
8. McCoy, A. B.; Huang, X.; Carter, S.; Bowman, J. M. *J. Chem. Phys.* **2005,** *123,* 064317.
9. Lee, H.-S.; McCoy, A. B. *J. Chem. Phys.* **2001,** *114,* 10278.
10. McCoy, A. B. *Int. Rev. in Phys. Chem.* (in press).
11. Lee, H.-S.; McCoy, A. B. *J. Chem. Phys.* **2002,** *116,* 9677.
12. Lee, H.-S.; McCoy, A. B.; Harding, L. B.; Carter, C. C.; Miller, T. A. *J. Chem. Phys.* **1999,** *111,* 10053.
13. Lee, H.-S.; McCoy, A. B.; Toczylowski, R. R.; Cybulski, S. M. *J. Chem. Phys.* **2000,** *113,* 5736.

14. Aziz, R. A.; Salaman, M. J. *Chem. Phys.* **1989**, *130*, 187.
15. Huang, X.; Braams, B. J.; Carter, S.; Bowman, J. M. *J. Am. Chem. Soc.* **2004**, *126*, 5042.
16. Mayrhofer, R.; Sibert, E. L. *Theor. chim. Acta* **1995**, *92*, 107.
17. Wilson, E. B.; Decius, J. C.; Cross, P. C. *Molecular Vibrations*; Dover: New York, 1955.
18. Nielsen, H. H. *Rev. Mod. Phys.* **1951**, 23, 90.
19. McCoy, A. B.; Sibert, E. L. *J. Chem. Phys.* **1991**, *95*, 3476.
20. McCoy, A. B.; Sibert, E. L. *J. Chem. Phys.* **1992**, *97*, 2938.
21. Cooper, A. R.; Jain, S.; Hutson, J. M. J. Chem. Phys. **1993**, *98*, 2160.
22. Cho, H. M.; Singer, S. J. *J. Phys. Chem. A* **2004**, *108*, 8691.
23. Hammer, N. I.; Diken, E. G.; Roscioli, J. R.; Myshakin, E. M.; Jordan, K. D.; McCoy, A. B.; Huang, X.; Carter, S.; Bowman, J. M.; Johnson, M. A. *J. Chem. Phys.* **2005**, *123*, 044308.
24. McCoy, A. B.; Huang, X.; Carter, S.; Landeweer, M. Y.; Bowman, J. M. *J. Chem. Phys.* **2005**, *122*, 061101.
25. Diken, E. G.; Headrick, J. M.; Roscioli, J. R.; Bopp, J. C.; Johnson, M. A.; McCoy, A. B.; Huang, X.; Carter, S.; Bowman, J. M. *J. Phys. Chem. A* **2005**, *109*, 171.
26. Sandler, P.; Buch, V.; Sadlej, J. *J. Chem. Phys.* **1996**, *105*, 10387.
27. Langfelder, P.; Rothstein, S. M.; Vrbik, J. *J. Chem. Phys.* **1997**, *107*, 8526.
28. Buch, V. *J. Chem. Phys.* **1992**, *97*, 726.
29. Price, E. A.; Robertson, W. H.; Diken, E. G.; Weddle, G. H.; Johnson, M. A. *Chem. Phys. Lett.* **2002**, *366*, 412.

Downloaded by STANFORD UNIV GREEN LIBR on July 4, 2012 | http://pubs.acs.org
Publication Date: December 31, 2006 | doi: 10.1021/bk-2007-0953.ch011

Downloaded by UNIV OF GUELPH LIBRARY on July 3, 2012 | http://pubs.acs.org
Publication Date: December 31, 2006 | doi: 10.1021/bk-2007-0953.ch012

Chapter 12

Rotations and Exchange in Doped Helium Clusters: Insight from Imaginary-Time Correlation Functions

Nicholas Blinov and Pierre-Nicholas Roy

Department of Chemistry, University of Alberta, Edmonton, Alberta T6G 2G2, Canada

We analyze the behavior of doped helium clusters in terms of imaginary time correlation functions. Illustrative examples are presented in order to highlight the importance of the inclusion of quantum exchange effects in the path integral Monte Carlo calculation of imaginary time orientational correlation functions. We relate the oscillatory behavior of the rotational constant to the variation of the minimum value of the orientational correlation functions for Bose-Einstein statistics.

Introduction

Doped helium clusters provide a feature-rich environment for the study of quantum statistical effects over a broad range of size scales. In the nano-scale regime, rovibrational spectra of doped helium nanodroplets show sharp spectral lines and a renormalized moment of inertia of the dopant species (*1,2,3*). In the case of small to medium size doped helium clusters, a non-monotonic size evolution of the effective rotational constant has been observed experimentally

In Advances in Quantum Monte Carlo; Anderson, J., et al.;
ACS Symposium Series; American Chemical Society: Washington, DC, 2006.

for N_2O (*4,5*) and CO_2 (*6*) impurities, for instance, and predicted via theoretical simulations for OCS (*7,8*) and N_2O (*5,9,10*), and CO_2 (*6,11,12*) dopant species. The observed features have been attributed to quantum exchange effects associated with the bosonic character of the helium environment. Theoretically, the importance of exchange effects on the rotational dynamics of a doped cluster can be assessed with the help of path-integral Monte Carlo (PIMC) simulations (*5,9,12,14*). One of the most interesting results which so far can only be obtained from PIMC simulations is a qualitatively correct prediction of size evolution of the rotational constant for small clusters (in the range of cluster sizes corresponding to the completion of the first solvation shell) based on a two-fluid hydrodynamic model (*5,11*). The approach allows one to relate the superfluid response of helium to the rotational dynamics of the doped cluster but relies on some assumptions (such as a rigid coupling between the normal fraction of helium and the dopant). It is therefore interesting to provide evidence for the importance of exchange effects without invoking these assumptions. The ultimate test would be based on the energy spectrum of the doped cluster, but such an approach is impractical even for small (more than three helium atoms) clusters due to exponential scaling of the complexity of the problem. We discuss here some aspects of the extraction of rotational constants from imaginary-time orientational correlation functions.

Downloaded by UNIV OF GUELPH LIBRARY on July 3, 2012 | http://pubs.acs.org
Publication Date: December 31, 2006 | doi: 10.1021/bk-2007-0953.ch012

Formal aspects and practical considerations

The most practical (numerically exact) approach to treat the rotational dynamics of relatively large clusters is based on the analysis of imaginary time dipole-dipole correlation functions. These functions can be evaluated using ground state quantum Monte Carlo (QMC) (*7,8*) or PIMC approaches (*9,13,14*). In the rigid rotor approximation, the dipole-dipole correlation function is proportional to an orientational correlation function defined as

$$\left\langle \hat{\mathbf{n}}(\tau)\cdot\hat{\mathbf{n}}(0)\right\rangle = \frac{1}{Z} Tr\left\{ e^{-\beta H} e^{\tau H} \hat{\mathbf{n}} e^{-\tau H} \cdot \hat{\mathbf{n}} \right\}, \qquad (1)$$

where the unit vector **n** represents the orientation of the molecule, β is the reciprocal temperature, Z is the partition function, and $\hat{H}$ is the Hamiltonian of the system.

In the path-integral picture the difference between the ground state and the finite temperature (canonical) average in the above equation appears as a difference in topology of the Feynman paths. In the ground state, open paths are involved, while at finite temperature, only closed paths contribute to the physical properties (other than the Green's functions). There are also important differences in the eigenstate (spectrum) representation of the correlation functions. In the ground state, the correlation functions are represented by the sum of decaying exponential functions $C_g(\tau) = \sum_i A_i e^{-\tau\varepsilon_i}$, where ε_i is an energy eigenstate of the Hamiltonian: $\hat{H}\psi_i = \varepsilon_i\psi_i$, i is a composite index that labels the eigenstates, and $A_i = \left|\mathbf{n}_{gi}\right|^2$. Here $\mathbf{n}_{gi}$ is a matrix element of the operator $\hat{\mathbf{n}}$ taken between the ground state, g, and the ith eigenstate. For long enough projection times ($\tau \to \infty$) the contribution of the highly excited states to the correlation function can be projected out. The excitation energies corresponding to the transitions involving the ground and few (usually, one or two) excited sates can then be extracted from the imaginary time propagation via the use of a multi-exponential fit or from maximum entropy approaches (*7,8*).

For finite temperatures, the spectral representation of the correlation function of Eq. (1) is: $C_\beta(\tau) = \frac{1}{Z}\sum_{ij} e^{-\beta\varepsilon_i} A_{ij} e^{-\tau\omega_{ij}}$, where $\omega_{ij} = \varepsilon_j - \varepsilon_i$ is the transition frequency and τ varies in the interval $[0, \beta]$. The important difference with the ground state is that each decaying exponential function is matched here by a growing exponential function associated with the corresponding reverse transition. This guarantees the periodicity of the correlation function in imaginary time. This is made especially clear using the following representation of the correlation function

$$C_\beta(\tilde{\tau}) = \sum_{i,j} (2 - \delta_{i0}\delta_{j0}) e^{-\beta(\varepsilon_i + \varepsilon_j)/2} A_{ij} \cosh(\tilde{\tau}\omega_{ij}), \tag{2}$$

where $\tilde{\tau} \in [-\beta/2, \beta/2]$. In contrast to ground state simulations, the correlation function cannot be propagated long enough in imaginary time in order to project out excited states for an arbitrary temperature. Still, in the low temperature regime ($\beta \to \infty$), transitions involving only the ground and the first excited states will dominate. In this case, a time interval, $\tau \in [0, \beta/2]$, should exist where the evolution of the correlation function will be determined by the low lying energies (just as in the ground state case). A multi-exponential fitting procedure can then be applied on such an interval in order to extract the excitation energies, again, as in ground state applications. It should be advantageous to take into account the explicit spectral form of the correlation function in Eq. (2) in the fitting procedure at finite temperature (*13*). If the temperature is low enough, and the amplitudes of transitions are treated as fitting parameters along with the

Downloaded by UNIV OF GUELPH LIBRARY on July 3, 2012 | http://pubs.acs.org
Publication Date: December 31, 2006 | doi: 10.1021/bk-2007-0953.ch012

transition frequencies, such a procedure should give exact excitation energies (and intensities).

The challenge of fitting

The low temperature regime required to obtain accuracies on par with ground state calculations demands a large number of discretizations in the path-integral representation for the density matrix. Such an implementation is currently impractical for the bosonic case. The actual temperatures used in previous PIMC calculations (0.15-0.4K) are too high to single-out the contribution of a single excited state to the multi-exponential sum in the expression for the correlation function. For relatively high temperatures, i.e. $\beta B \sim 1$, (where B is the effective rotational constant of the complex) the above fitting may become extremely unreliable because many exponential functions contribute simultaneously to the correlation function for any τ. In this case a model fit can be used as a qualitative way to analyze the rotational dynamics of doped helium clusters. The difference here, when comparing to the above multi-exponential fit, is that one uses a specific model of the transition amplitudes and excitation energies. Rigid top and ro-vibrational Hamiltonian models are possible. If the actual rotational dynamics can be accurately described by a rigid top model, this procedure provides quantitative results for the rotational constant. The accuracy of the fit also provides some insight into the accuracy of the model, and so provides useful information (*12*). We analyze this type of approach in the following section.

Downloaded by UNIV OF GUELPH LIBRARY on July 3, 2012 | http://pubs.acs.org
Publication Date: December 31, 2006 | doi: 10.1021/bk-2007-0953.ch012

Illustrative examples

To circumvent the technical difficulties associated with the contribution of many transitions to the Monte Carlo sampling in the low temperature regime, we first choose to illustrate the above considerations using basis-set calculations for the He-OCS dimer. The approach and results have been partially discussed in Ref. (*13*). The method allows us to obtain (exact) bound energy levels and related eigenfunctions of the He-OCS Hamiltonian. We can then evaluate canonical averages for any physical observable including imaginary time correlation functions. We present the ro-vibrational energies obtained using parity-adapted basis functions by Lanczos diagonalization (*15*,*16*) in Table I.

The energy levels are labeled by the total angular momentum J, the parity, p, and the vibrational quantum number, n. These energies are degenerate in M

Table I. Energy levels (cm^{-1}) for ^{4}He-OCS dimer

n	J_0p_0	J_1p_0	J_1p_1	J_2p_0	J_2p_1
0	-18.6	-18.0	-18.3	-17.7	-17.3
1	-10.3	-7.8	-18.1	-17.5	-16.6
2	-9.2	-6.5	-10.1	-16.6	-7.1
3	-6.5	-4.0	-9.0	-9.6	-6.7

(the projection of the total angular momentum on the z-axis in the laboratory fixed frame). The imaginary time orientational correlation function can now be calculated as follows,

$$\langle \hat{n}_Z(\tau)\hat{n}_Z(0)\rangle = \frac{1}{Z}\sum_{n,J,M,p} e^{-E_n^{Jp}/k_BT} e^{\tau E_n^{Jp}} \sum_{n',J',p'} e^{-\tau E_{n'}^{J'p'}} \left|\langle nJMp|\hat{n}_Z|n'J'Mp'\rangle\right|^2, \quad (3)$$

where the matrix elements of the direction cosines are,

$$\langle nJMp|\hat{n}_Z|n'J'Mp'\rangle = \sum_{\alpha,j,k} c_{\alpha,j,k}^{nJMp} c_{\alpha,j,k}^{n'J'Mp'} \langle JkMp|\hat{n}_Z|J'kMp'\rangle, \quad (4)$$

where $c_{\alpha,j,k}^{nJMp}$ is an element of the eigenvectors for state $|nJMp\rangle$ in the parity adapted ro-vibrational basis (See Refs. (*13*) and (*17*) for details). The non-zero matrix elements of the direction cosine in the parity adapted rotational basis are,

$$\langle JkMp|n_z|JkMp'\rangle = \frac{Mk}{J(J+1)}(1-\delta_{pp'}), \quad (5)$$

$$\langle JkMp|n_z|J+1kMp'\rangle = \frac{\sqrt{(J+1)^2-M^2}\sqrt{(J+1)^2-k^2}}{(J+1)\sqrt{(2J+1)(2J+3)}}(1-\delta_{pp'}), \quad (6)$$

$$\langle JkMp|n_z|J-1kMp'\rangle = \frac{\sqrt{J^2-M^2}\sqrt{J^2-k^2}}{J\sqrt{4J^2-1}}(1-\delta_{pp'}). \quad (7)$$

Note that the above matrix elements are diagonal in *M*, and that the contributions from the other two direction cosines to the correlation function are the same. The

Downloaded by UNIV OF GUELPH LIBRARY on July 3, 2012 | http://pubs.acs.org
Publication Date: December 31, 2006 | doi: 10.1021/bk-2007-0953.ch012

correlation function from Eq. (3) is plotted in Figure 1 for some representative temperatures. We can observe that the lower the temperature, the lower the amplitude of the correlation function at $\tau=\beta/2$. To illustrate the contribution of individual energy levels to the canonical averages in Eq. (3), we show in Figure 2 the Boltzmann factors (including degeneracy), $(2J+1)e^{-\beta E_n^{Jp}}$, for some of the lowest energies.

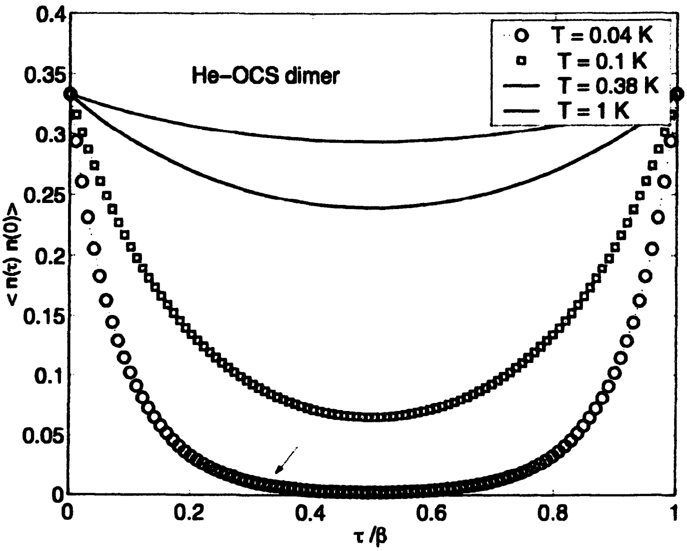

Figure 1. Orientational imaginary time correlation functions for the He-OCS dimer. Results for different temperatures are presented.

It is clear from the above picture (Figure 2) that at T=0.04 K (and even at T=0.1 K), the ground state contribution dominates. A multi-exponential fit would therefore yield results with accuracies comparable to that of a ground state analysis in this low temperature regime. On the other hand, at T=0.38 K, the temperature of actual nanodroplets experiments, the populations of the excited states are relatively high. Under these conditions, a multi-exponential fit could be unreliable, but one can use a model fit to obtain the information regarding the rotational dynamics. Because many excited states (with temperature dependent populations) contribute to the correlation function, the resulting effective rotational constant obtained from the model fit will depend on temperature. For larger clusters, the rotational constant will be renormalized and the Boltzmann weight distribution will be different.

Downloaded by UNIV OF GUELPH LIBRARY on July 3, 2012 | http://pubs.acs.org
Publication Date: December 31, 2006 | doi: 10.1021/bk-2007-0953.ch012

Downloaded by UNIV OF GUELPH LIBRARY on July 3, 2012 | http://pubs.acs.org
Publication Date: December 31, 2006 | doi: 10.1021/bk-2007-0953.ch012

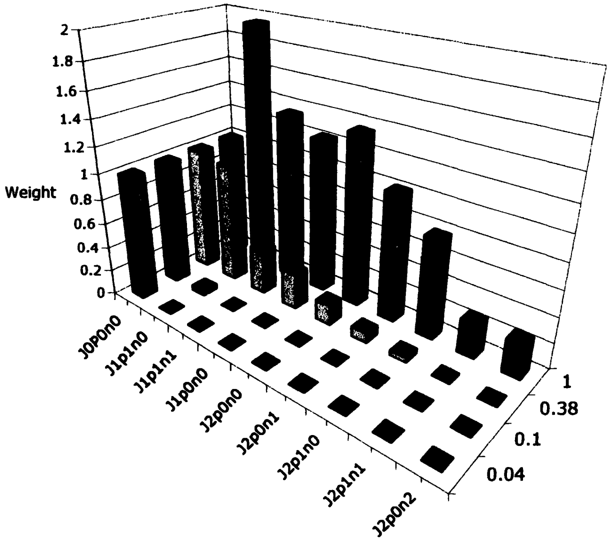

Figure 2. Boltzmann weights for the lowest states of the He-OCS dimmer at $T = 0.04$ K, 0.1 K, 0.38 K and 1.0 K.

Path integral Monte Carlo calculations

We illustrate the above considerations in Figure 3, where we plot the effective rotational constants obtained from fits to linear rotor and symmetric top models (*13*). The temperature dependence of the effective rotational constants for the He-OCS complex indicates a deviation from the rigid rotor models. This fact should not be surprising since the presence of the helium atom hinders the free rotation of the OCS monomer and this floppy complex should not be expected to behave as a simple free linear rotor.

We present orientational correlation functions for He_N-N_2O clusters of varying sizes in Figure 4. The calculations are related to those presented in Ref. (*5*) and include Bose-Einstein statistics (exchange). The figure shows that the size evolution of the minimum value of the correlation functions at $\tau=\beta/2$ exhibits an oscillatory behavior. This pattern is very similar to the size evolution of the *B* rotational constant. To explore this further, we show in Figure 5 the size evolution of the reciprocal value of the correlation function at $\tau=\beta/2$ for Bose-Einstein and Boltzmann statistics. We observe that Bose-Einstein statistics are required in order to capture the experimentally observed two turnarounds in the size evolution. For comparison, we also show in the inset of Figure 5 the actual experimental and PIMC *B* constants as reported in Ref. (*5*). The $1/C(\beta/2)$ values and the *B* rotational constants clearly have a similar behavior. We explore this connection in Figure 6 and observe that the result of the fit is directly correlated

Downloaded by UNIV OF GUELPH LIBRARY on July 3, 2012 | http://pubs.acs.org
Publication Date: December 31, 2006 | doi: 10.1021/bk-2007-0953.ch012

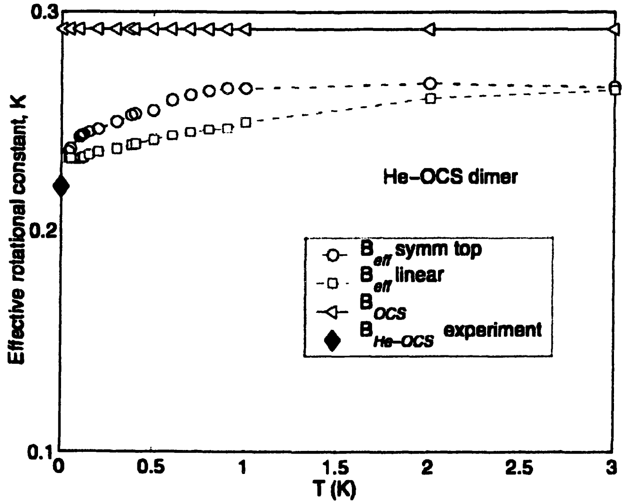

Figure 3. Effective rotational constants obtained from symmetric top (open circles) and linear molecule (open squares) model fits of the PIMC orientational correlation function. The experimental value (18) of the B constant (filled diamond) is also presented along with the free OCS B value (open triangles). (Reproduced with permission from Path Integral Monte Carlo Approach for Weakly Bound van der Waals Complexes with Rotations: Algorithms and Benchmark Calculations *by Nicholas Bilnov. Copyright American Institute of Physics.)*

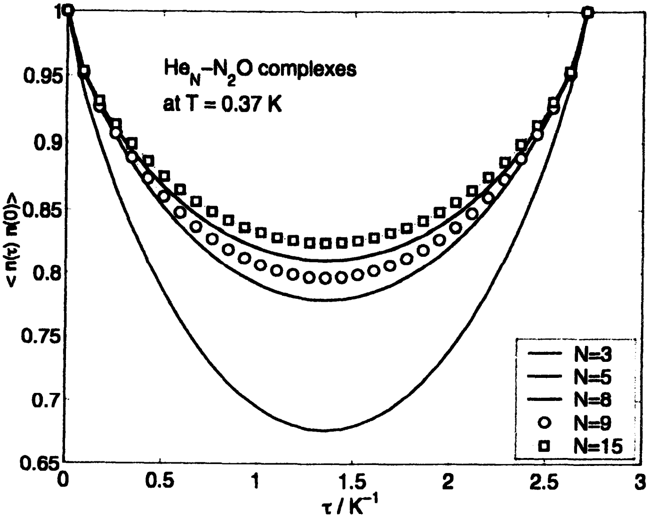

Figure 4. Orientational correlation functions for various cluster sizes.

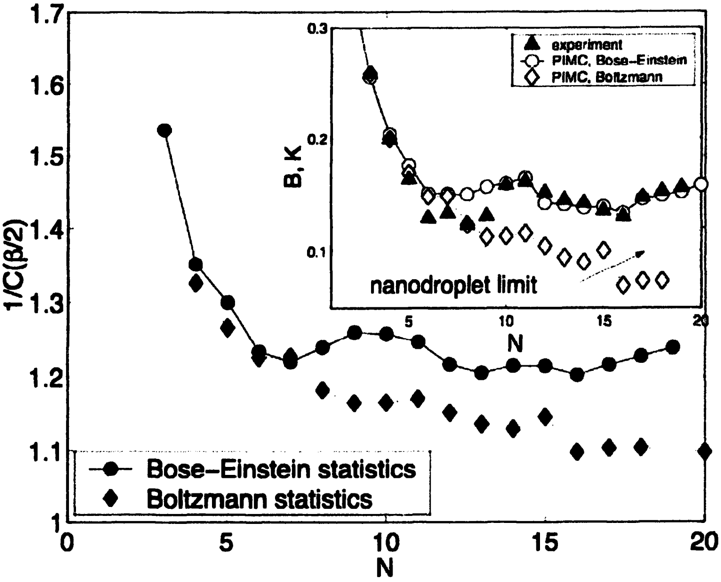

Figure 5. Size evolution of 1/C(β/2) for two statistics. Inset: experimental (filled triangles) and PIMC (open symbols) B versus N (Ref. (5)).

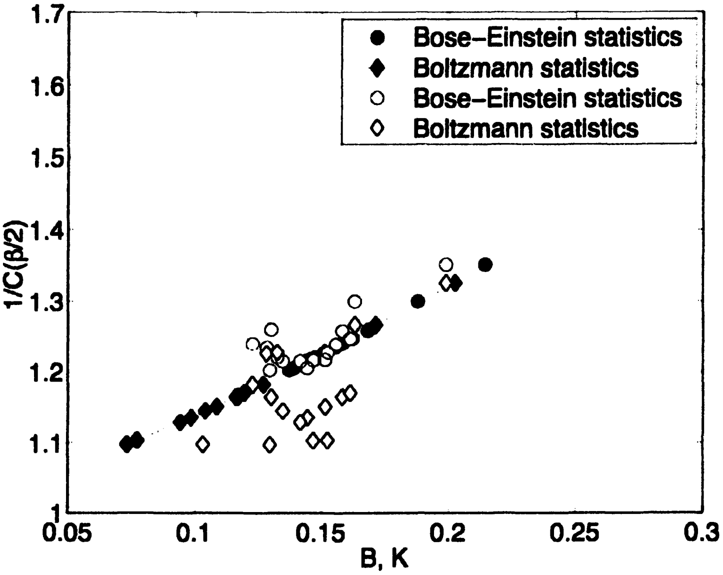

Figure 6. Correlation between 1/C(β/2) and the PIMC (filled symbols) and experimental (open symbols) B constants.

Downloaded by UNIV OF GUELPH LIBRARY on July 3, 2012 | http://pubs.acs.org
Publication Date: December 31, 2006 | doi: 10.1021/bk-2007-0953.ch012

to the $1/C(\beta/2)$ value. We also present the correlation between $1/C(\beta/2)$ and the experimental B values. The analysis shows that the $1/C(\beta/2)$ values obtained for Bose-Einstein statistics correlate much better with experiment than results where exchange has been neglected (i.e., Boltzmann statistics). The bosonic results still deviate from experiment since the height of the correlation function cannot simply be connected to the B constant because of thermal excitations.

Concluding Remarks

We have shown how the analysis of orientational imaginary time correlation functions obtained from PIMC simulations can provide insight into the size evolution of the B rotational constants in doped helium clusters. We noted that for the case of an N_2O dopant, exchange effects (Bose-Einstein staitistics) must be included in order to reproduce the experimentally observed oscillatory behavior of the B constants. This oscillatory behaviour has been connected to the onset of superfluidity where decoupling between a rotor and its environment is observed. The oscillation of the value of the correlation function at $\beta/2$ directly follows the trend in B constants and therefore provides a measure of decoupling that is free from a fit. We note that a connection between $C(\beta/2)$ and B has recently been used by Miura (*19*) for a particular cluster size.

Acknowledgments

We thank the Natural Sciences and Engineering Research Council of Canada and the Canada Foundation for Innovation for financial support.

References

1. Grebenev, S; Toennies, J.P.; Vilesov, A.F. *Science* **1998**, *279*, 2083.
2. Toennies, J.P.; Vilesov, A.F., *Annu. Rev. Phys. Chem.* **1998**, *49*, 1.
3. Reinhard, I.; Callegari, C.; Conjusteau, C.; Lehmann, K. K.; Scoles, G. *Phys. Rev. Lett.* **1999**, *82*, 5036.
4. Xu, Y.; Jäger, W.; Tang, J.; McKellar, A. R. W. *Phys. Rev. Lett.* **2003**, *91*, 163401.
5. Xu, Y.; Blinov, N.; Jäger, W.; Roy, P.-N.; *J. Chem. Phys.* **2006**, *124*, 081101.
6. Tang, J.; McKellar, A. R. W.; Mezzacapo, F.; Moroni, S. *Phys. Rev. Lett.* **2004**, *92*, 145503.

Downloaded by UNIV OF GUELPH LIBRARY on July 3, 2012 | http://pubs.acs.org
Publication Date: December 31, 2006 | doi: 10.1021/bk-2007-0953.ch012

7. Moroni, S.; Sarsa, A.; Fantoni, S.; Schmidt, S. K. E.; Baroni, S. *Phys. Rev. Lett.* **2003,** *90,* 143401.
8. Paesani, F.; Viel, A.; Gianturco, F.A.; Whaley, K.B. *Phys. Rev. Lett.* **2003,** *90,* 073401.
9. Moroni, S.; Blinov, N.; Roy, P.-N. *J. Chem. Phys.* **2004,** *121,* 3577.
10. Paesani F.; Whaley, K. B. *J. Chem. Phys.* **2004,** *121,* 5293.
11. Paesani, F.; Kwon, Y.; Whaley, K. B. *Phys. Rev. Lett.* **2005,** *94,* 153401.
12. Blinov, N.; Roy, P.-N. *Low Temp. Phys.* **2005,***140,* 255.
13. Blinov, N.; Song, X.; Roy, P.-N. *J. Chem. Phys.* **2004,** *120,* 5916.
14. Zillich, R.; Paesani, F.; Kwon, Y.; Whaley, K.B. *J. Chem. Phys.* **2005** *123,* 114301.
15. Cullum, J.K.; Willoughby, R.A. *Lanczos Algorithms for Large Symmetric Eigenvalue Computations*; Birkhäuser: Boston, MA, 1985.
16. Carrington, T. Jr., *Encyclopedia of Computational Chemistry,* edited by P. von Ragué Schleyer; Wiley: New York, NY, 1998; Vol. 5.
17. Song, X.; Xu, Y.; Roy, P.-N.; Jäger, W. *J. Chem. Phys.* **2004,** *121,* 12308.
18. Higgins, K.; Klemperer, W. *J. Chem. Phys.* **1999,** *110,* 1383.
19. Miura, S.; *J. Phys.: Condens. Matter* **2005,** *17,* S3259.

Downloaded by UNIV OF GUELPH LIBRARY on July 3, 2012 | http://pubs.acs.org
Publication Date: December 31, 2006 | doi: 10.1021/bk-2007-0953.ch012

Author Index

Alexander, S. A., 15
Anderson, James B., 1
Aspuru-Guzik, Alán, 55
Austin, Brian, 55
Bande, Annika, 42
Blinov, Nicholas, 165
Bressanini, D., 81
Coldwell, R. L., 15
Colletti, L., 81
Crittenden, Deborah L., 101
Guclu, D., 81
Jordan, Meredith J. T., 101
Kalos, M. H., 81, 93
Lee, Myung Won, 69
Lester, William A., Jr., 55
Lu, Shih-I, 29
Lüchow, Arne, 42
Maezono, Ryo, 141
McCoy, Anne B., 147
Mella, Massimo, 69
Pederiva, F., 81, 93
Rappe, Andrew M., 69
Reboredo. F., 81
Rothstein, Stuart M., ix
Roy, Pierre-Nicholas, 165
Salomón-Ferrer, Romelia, 55
Tanaka, Shigenori, 141
Thompson, Keiran C., 101
Umrigar, C. J., 81
Watanabe, Hirofumi, 141
Wilson, Matthew C., 1

Downloaded by 89.163.35.42 on July 3, 2012 | http://pubs.acs.org
Publication Date: December 31, 2006 | doi: 10.1021/bk-2007-0953.ix001

Subject Index

A

Ab initio calculations
  biomolecular, quantum Monte Carlo with fragment molecular orbital methods, 141–146
  molecular potential energy surface, 1,2-ethanediol and 1,2-ethanediol.H_2O, 118
  molecular potential energy surface with *Grow2.2*(103) computer package, 105–110
Acceptance-rejection dynamics in techniques with signed random walkers, 98–99
Adiabatic diffusion Monte Carlo, 149, 160–161
Amino acids. *See* GABA; Glycine
γ-Aminobutyric acid. *See* GABA
Amsterdam Density Functional package, wave functions expanded on STO basis, 60
Antisymmetric function, two-dimensional electron gas, 99
Antisymmetry, wavefunctions 85–86
  in fixed-node approximation, 82–83, 84
Approximations, criteria for no uncontrolled, 93–94
Aqueous phase, GABA, ground state structure, *Grow* methodology, 129–135
Aqueous phase structure, glycyl.$8H_2O$, potential energy surface, *Grow* methodology, 124–129
Assaraf-Caffarel expression, variational Monte Carlo atomic force calculation, 71
Assaraf-Caffarel force on lithium hydride molecule components, 73–75*f*
Asymptotic decay of signal to noise, 95
Atomic Rydberg states, excitation nodes, 45
Axilrod-Teller-Muto expression for helium trimer, 2, 3–4, 12

B

Bacteriochlorophyll, linear-scaling evaluation, local energy, 62–65*f*
Basis set superposition error, 2
Benzene, quantum Monte Carlo, force calculations 77–78*f*
Beryllium atom, fixed-hypernode results, 90
Biological system applications, linear-scaling evaluation, local energy, 62–66*f*
Boltzmann compared to Bose-Einstein (exchange) statistics for He_N-N_2O clusters, correlation function, reciprocal value, 171, 173*f*–174
Boltzmann weights, helium-OCS dimer, lowest states, 170–171*f*
Born-Oppenheimer approximation, diagonal energy correction, 17–20
Born-Oppenheimer potential energy, hydrogen molecular ion, 17, 18*t*–19*t*
Bose-Einstein (exchange) compared to Boltzmann statistics for He_N-N_2O clusters, correlation function, reciprocal value, 171, 173*f*–174
Branching factor, random walkers in Monte Carlo simulation, 33

In Advances in Quantum Monte Carlo; Anderson, J., et al.;
ACS Symposium Series; American Chemical Society: Washington, DC, 2006.

Downloaded by 89.163.35.42 on July 3, 2012 | http://pubs.acs.org
Publication Date: December 31, 2006 | doi: 10.1021/bk-2007-0953.ix002

C

Carbon atom excitation, ^3P and ^1P Rydberg states, 46–52
Carbon atom nodal regions, Rydberg states, 47–49
Carbon monoxide molecule components, atomic force calculations, 73, 76*f*
Compressed matrix representation, grid generation, 58–59
Computational cost reduction for Slater determinant evaluation and correlation functions, 55–68
Computational efficiency versus electron number, 99–100*f*
Conformational flexibility, ground state GABA.5H_2O, 130–135
Coordinates, choice in node placement, 152–155
Correlated molecular wave function form, 56
Correlation function
  linear-scaling evaluation, 61–62
  reciprocal value, Bose-Einstein compared to Boltzmann statistics, 171, 173*f*–174
Cut-off values, fixed sample, 60, 62

D

Determinate evaluation algorithm, Slater determinant, 59–60
Diagonal energy correction, Born-Oppenheimer approximation, 17–20
Diatomic radicals, first-row, doublet, equilibrium bond lengths and harmonic frequencies, 29–41
Diffusion quantum Monte Carlo approach, vibrational excited states, 147–164
Diffusion quantum Monte Carlo calculations
  dissociation energies, methane molecule, methylene radical, and methyl radical, 73, 77
  1,2-ethanediol and 1,2-ethanediol.H_2O, 119–124
  fixed node, helium dimers and trimers, 1–14
  GABA, 131–132
  glycyl.8H_2O, 125–129
  ground state properties, loosely bound complexes, overview, 104–140
Diffusion quantum Monte Carlo method, fixed node, equilibrium bond lengths and harmonic frequencies, doublet first-row diatomic radicals, 29–41
Direct diffusion Monte Carlo, feasibility, 102–103
Dissociation energies for diatomic molecules by Hartree-Fock, variational Monte Carlo, diffusion Monte Carlo, 72
Dissociation energies for methane molecule, methylene radical, and methyl radical, 73, 77
Doped helium clusters, rotations and exchange, 165–175

E

Effective rotational constants, He-OCS complex, 171–172*f*
Electron correlation methods, 118
Equilibrium bond lengths for some doublet first-row diatomic radicals, calculated compared to experimental, 36, 39*t*
Error estimate and reduction, 94
1,2-Ethanediol, gas phase and hydrated
  hydrogen bonding, 115–124
  model for more complex species, 104

Downloaded by 89.163.35.42 on July 3, 2012 | http://pubs.acs.org
Publication Date: December 31, 2006 | doi: 10.1021/bk-2007-0953.ix002

Excitation energies for carbon atom results, comparison among methods, 51–52

F

Fermion sign problem, 94–95
Finite difference technique for energy gradient determination, 33
Fitting challenge, imaginary time dipole-dipole correlation functions, 168
Fixed hypernode algorithm, extension fixed-node procedure, 89–91
Fixed node approximation, algorithm 148, 160–161
Fixed node approximation in diffusion quantum Monte Carlo method, 82–83, 95
Fixed node boundary conditions in expanded space, 83–84
Fixed-node diffusion quantum Monte Carlo method
  for helium dimers and trimers, calculation procedure, 3–4
  random walk approach to equilibrium bond lengths and harmonic frequencies, 29–41
  Rydberg states, calculations, 44–53
Floating spherical Gaussian orbitals and spherical Gaussian geminals for trial wave function, 30–32, 35–36, 39
Fokker-Planck equation, 36–38
Fragment molecular orbital method, 142–143
  with quantum Monte Carlo method, 143–145

G

GABA (γ-aminobutyric acid)
  ground state structure, aqueous phase, 129–135
  neurotransmitter, 104
Geometry optimization procedures, 33–35
Glycine trimer, fragment molecular orbital method combined with quantum Monte Carlo method, 143–145
Glycyl.8H_2O, potential energy surface by *Grow* methodology, 124–129
Glycyl radical, 104, 124–129
Grid generation in Slater determinant evaluation, 58–59
Ground state properties, loosely bound complexes, 101–140
Grow computer package for molecular potential energy surface using *ab initio* calculations, 105–110
Grow method applications
  aqueous phase structure, glycyl.8H_2O, potential energy surface, 124–129
  1,2-ethanediol, gas phase and hydrated, potential energy surface, 118–120
  GABA, ground state structure, aqueous phase, 129–135
  water dimer, potential energy surfaces, 110–115

H

$H_3O_2^-$ system
  coordinate placement, 152–155
  diffusion Monte Carlo energies for fundamentals, 160–162
  equilibrium geometry, 150*f*
  node positioning, 155–158
Hamiltonian symmetries and representations, 85–89
Harmonic frequencies for some doublet first-row diatomic radicals, calculated compared to experimental, 35, 40*t*

Downloaded by 89.163.35.42 on July 3, 2012 | http://pubs.acs.org
Publication Date: December 31, 2006 | doi: 10.1021/bk-2007-0953.ix002

Hartree-Fock calculated dissociation energies, methane molecule, methylene radical, and methyl radical, 73, 77
Hartree-Fock-variational Monte Carlo calculations for glycine trimer, 143–145*t*
Helium clusters, doped, rotations and exchange, 165–175
Helium dimers, interaction energies relative to exact value for pair, separated atoms, 4–6*t*
Helium fixed-node diffusion quantum Monte Carlo calculations for dimers and trimers, 1–14
Helium$_N$-N_2O clusters, correlation function, reciprocal value, Boltzmann compared to Bose-Einstein (exchange) statistics, 171, 173*f*–174
Helium-OCS dimer
  basis-set calculations, 168–171
  path integral Monte Carlo calculations, 171–174
Helium trimers, equilateral triangle form, interaction energies, 4, 7*f*–9*t*
  pairwise-additive energy calculations, correction, 12–13*t*
Helium trimers, symmetric linear form, interaction energies, 9*f*–11*t*
  pairwise-additive energy calculations, correction, 12–13*t*
Hellmann-Feynman force estimator modification, 34
Hellmann-Feynman theorem force, lithium hydride molecule components, 73–75*f*
Hydrogen bonding formation in 1,2-ethanediol, gas phase and hydrated, 115–124
Hydrogen molecular ion
  energies and properties, 15–28
  energy by variational Monte Carlo method, 16–20
Hydrogen molecular ion ground state
  potential energy surface with statistical error, 18*t*–19*t*
  rovibrational energies, 20, 22–25
Hypernodal functions in product space, 83–85

I

Imaginary time dipole-dipole correlation functions, analysis, 166–168
Interaction energies for equilateral triangle helium trimers, 4, 7*f*–9*t*
  pairwise-additive energy calculations, correction, 12–13*t*
Interaction energies for helium dimers relative to exact value, separated atom pair, 4–6*t*
Interaction energies for symmetric linear helium trimers, 9*f*–11*t*
  pairwise-additive energy calculations, correction, 12–13*t*
Intermolecular hydrogen bonding, 1,2-ethanediol, gas phase and hydrated, 124
Interpolation methods for potential energy surface generation, 103, 106, 107–110

J

Jastrow factors, variational quantum Monte Carlo calculations, 44, 45, 46
Jastrow-Slater wave function, 30

K

Kohn-Sham orbitals, open-shell localized Hartree-Fock method as Rydberg orbitals, 43, 46

Downloaded by 89.163.35.42 on July 3, 2012 | http://pubs.acs.org
Publication Date: December 31, 2006 | doi: 10.1021/bk-2007-0953.ix002

Downloaded by 89.163.35.42 on July 3, 2012 | http://pubs.acs.org
Publication Date: December 31, 2006 | doi: 10.1021/bk-2007-0953.ix002

L

Lee-Yang-Parr correction functional, 46
Linear-scaling evaluation, correlation function, 61–62
Lithium hydride molecule, force components, 73–75*f*
London dispersion forces between helium atoms, 2
Loosely bound complexes, ground state properties, 101–140

M

Markov procedure implementation, diffusion quantum Monte Carlo simulation, 37–38
Methylene radical, force calculations at various geometries, 77–78*f*
Molecular properties, hydrogen molecular ion, 20–21*t*
Monohydrides, first row, energies and atomic forces, dissociation energies, 72–75*f*
Morse potential fitting, 72

N

Ne_2OH system
  coordinate placement, 152–155
  diffusion Monte Carlo and variational energies, low-lying vibrational states, 159
  equilibrium geometry, 150*f*
  in-plane bend, fixed-node diffusion Monte Carlo, 162
  node positioning, 155–158
Newton's method
  application to benzene energy calculations, 77
  parameter optimization in variational Monte Carlo trial wave function, 71
Nodal error, fixed-node approximation, definition, 83
Nodal regions, carbon atom, Rydberg states, 47–49
Nodal surfaces, N-1 dimensions, wave function, 147–148
Node definition, sensitivity of O–H stretch frequency, 160
Nodes, positioning, 155–158
Nonhydrogen atom force calculations, Pulay correction, 73
Numerical threshold cutoff for fast evaluation, Slater determinant, 58–59

O

O–H distribution function, 1,2-ethanediol and 1,2-ethanediol.H_2O, 121–124
O–H stretch frequency, sensitivity, node definition, 160
O–H wavefunction for glycyl.$8H_2O$, 128*f*–129
O–O stretch energies, fixed-node DMC and ADMC calculations, 160–161
Open-shell localized Hartree-Fock wave function for Rydberg excited states, 46–49
Orientational correlation functions, He_N-N_2O clusters, 171–172*f*
Ornstein-Uhlenbeck random walk, fixed-node diffusion quantum Monte Carlo approach to equilibrium bond lengths and harmonic frequencies, 29–41

P

Path integral Monte Carlo approaches to rotational dynamics, relatively large clusters, 166–168
Path integral Monte Carlo calculations, helium-OCS dimer, 171–174
Pauli principle, 95
Peptide radical model, 124
Potential energy surface, interpolating surface for GABA.5H_2O, 131
Potential energy surface interpolation scheme, *Grow* algorithm, 107–110
Potential energy surface iteration scheme, *Grow* algorithm, 110
Primitive basis functions, rapid evaluation, 60
Pulay correction, diatomic molecule forces, 73–76*f*

Q

Quantum Monte Carlo. *See* Diffusion quantum Monte Carlo; Fixed node quantum Monte Carlo; Variational Monte Carlo
Quantum nuclear motion in ground state structure, 1,2-ethanediol, 115, 118

R

Radiative correction, hydrogen molecular ion, ground state, 18*t*–19*t*, 20
Random walkers, branching control, 33
Recrossing correction, walkers, 148–149
Reimers, Watts, and Klein, water dimer potential, 110
Relativistic corrections, hydrogen molecular ion, ground state, 17–20
Rigid body variant of diffusion Monte Carlo, 159
Rovibrational energies, hydrogen molecular ion, ground state, 20, 22–25, 26*t*–27*t*
Rydberg excitations, carbon atom, 49–52
Rydberg states, quantum Monte Carlo methods, 44–53

S

Sampling methods
  configuration space, water dimer, 112–113
  efficiency, 103–104
Schmidt-Moskowitz-Boys-Handy correlation function, linear scaling, 61–62
Schroedinger equation for many body systems, fixed hypernode method, 81–92
Schroedinger equation for many fermion systems, revised solution, 93–100
Shepard interpolation method for potential energy surface generation, 103, 106, 107–110
Signed walkers, 95–99
SIMPLEX technique, 31–32
Singlet-triplet splitting for carbon atom results, method comparison, 51–52
Sparse representation, Slater matrix, 58
Spheroidene molecule, linear-scaling evaluation, local energy, 62–66*f*
Spurious regions, 44
Statistical error reduction in quantum Monte Carlo calculations, helium trimer, 12

Downloaded by 89.163.35.42 on July 3, 2012 | http://pubs.acs.org
Publication Date: December 31, 2006 | doi: 10.1021/bk-2007-0953.ix002

Symmetric trial function, two-dimensional electron gas, 99
Symmetry distinct rotamers, 1,2-ethanediol, 115–117*f*
Symmetry operations, extended Hamiltonian symmetries, 85–89

T

Tautomerization, neutral and zwitterionic species, glycine, 124–125
Tilting theorem, Ceperley's proof, 44
Torsional flexibility in GABA.5H_2O, 132–135
Trial wave function
  floating spherical Gaussian orbitals and spherical Gaussian geminals, 30–32, 35–36, 39
  variational quantum Monte Carlo method, 44, 70–71
Trial wave functions in geometry optimization procedure, 34–35
Turbomole, program package, 46
Two-dimensional electron gas, results, 99–100

U

Uncontrolled approximations, criteria for limiting, 93–94
Upper bound properties for a restricted algorithm using hypernodal functions, proof, 85–89

V

Variational quantum Monte Carlo calculations, dissociation energies, methane molecule, methylene radical, and methyl radical, 73, 77
Variational quantum Monte Carlo method, calculations and corrections, hydrogen molecular ion, 16–20
Variational quantum Monte Carlo method for Rydberg states, 44–46, 50–52
Vibrational configuration-interaction calculations, $H_3O_2^-$, 160–162
Vibrational diffusion Monte Carlo calculations in *Grow* algorithm, 105–110
Vibrational excited states by diffusion Monte Carlo approach, 147–164
Vibrationally averaged O–O bond length in water dimer, 113–115

W

Walker distribution sampling in fixed node diffusion Monte Carlo method, 45–46, 49
Walkers
  algebraically signed, 95–99
  for calculating vibrational ground state wavefunctions, 105, 113
  for GABA.5H_2O ground state investigation, 131
  pairs, in fixed-hypernode algorithm, 89
  recrossing correction, 148–149
Water dimer, potential energy surfaces with *Grow* computer program, 110–115
Wave functions for antisymmetric and symmetric ground states with signed walkers, 96–97

Downloaded by 89.163.35.42 on July 3, 2012 | http://pubs.acs.org
Publication Date: December 31, 2006 | doi: 10.1021/bk-2007-0953.ix002

Z

Zero point energy convergence, potential energy surface
  1,2-ethanediol and 1,2-ethanediol.H_2O, 120–124
  water dimer, 113–115
Zwitterionic species
  GABA.$5H_2O$, 129–131
  glycyl radical conformer, 124

Downloaded by 89.163.35.42 on July 3, 2012 | http://pubs.acs.org
Publication Date: December 31, 2006 | doi: 10.1021/bk-2007-0953.ix002